Interfaces in Metal Halide Perovskite Photovoltaics



Robert Oliver

St Anne's College

A thesis submitted for the degree of

Doctor of Philosophy

at the University of Oxford

Trinity Term 2022

To Polly,

For being the best grandma and encouraging me to

be the best version of myself, always.

Contents

Acknowledgements **v**

Abstract **ix**

List of Publications **xii**

1 Introduction **1**

1.1 Motivation - the Need for Sustainability 1

1.2 Solar Energy 4

1.2.1 A brief history of solar 5

1.2.2 The need for tandem solar cells 8

1.3 Aims of this Thesis 10

2 Background and Theory **14**

2.1 Semiconductors 14

2.1.1 Band theory 15

2.1.2 Semiconductor under illumination 21

2.1.3 Charge-carrier recombination 27

2.2 Solar Cell Operation 51

2.2.1 Ideal solar cells 51

2.2.2 Theoretical maximum efficiency 54

2.2.3 Practical limitations 65

2.3 Metal Halide Perovskites 71

2.3.1 Methylammonium-free Wide Bandgap Perovskites 78

3 Experimental Methods **101**

3.1 Device fabrication . . . 101

3.1.1 Materials . . . 101

3.1.2 Deposition protocols . . . 105

3.2 Photophysical characterisation . . . 108

3.2.1 Optical-pump terahertz-probe spectroscopy (OPTPS) . . . 108

3.2.2 Time-correlated single photon counting (TCSPC) . . . 112

3.2.3 Photoluminescence quantum yield (PLQY) . . . 113

3.2.4 UV-Vis absorption . . . 114

3.2.5 Ellipsometry . . . 114

3.2.6 Time-resolved emission spectroscopy (TRES) . . . 114

3.3 Structural Characterisation . . . 115

3.3.1 X-ray diffraction . . . 115

3.4 Electronic characterisation . . . 115

3.4.1 Ultraviolet photoemission sprectroscopy (UPS) . . . 115

3.4.2 X-ray photoemission spectroscopy (XPS) . . . 115

3.5 PV Device Characterisation . . . 116

3.5.1 JV characteristics . . . 116

3.5.2 Ageing experiments . . . 117

3.5.3 External quantum efficiency (EQE) . . . 118

3.5.4 Intensity dependent open-circuit voltage measurements . . . 118

3.5.5 Pseudo JV-curve (pJV) determination . . . 119

3.5.6 Photoluminescence imaging . . . 119

3.6 Drift-diffusion simulations . . . 120

4 Thermally Stable Passivation **128**

4.1 Summary of results . . . 128

4.2 Introduction . . . 129

4.3 Results and Discussion . . . 131

4.3.1 Optoelectronic properties . . . 131

4.3.2 Structural and chemical characterisation 139
4.3.3 Photovoltaic device performance 144
4.4 Conclusion 149

5 Nonradiative losses in wide bandgap perovskites 154
5.1 Summary of results 155
5.2 Introduction 156
5.3 Results and discussion 158
5.3.1 Bulk optoelectronic properties 158
5.3.2 Interface recombination 169
5.3.3 Photovoltaic device performance 174
5.3.4 Recombination analysis in full devices 179
5.4 Conclusions 186

6 Optimised Hole Transport Layer Through Blended Polymers 193
6.1 Summary of results 193
6.2 Introduction 194
6.3 Results and discussion 196
6.3.1 Photovoltaic device performance 202
6.3.2 Polymer blend / metal halide perovskite heterostructures 208
6.3.3 Physics of the blended polymer system 210
6.4 Conclusion and Future Work 216

7 Conclusions and Future Work 223

Acknowledgements

There are so many people without whom the work presented here simply would not have been possible. I can't possibly do them all justice, but that's no reason not to try anyway.

First and foremost, I would like to express my immense gratitude to Prof. Henry Snaith FRS. Working with you has been an absolute pleasure these past four years. Your enthusiasm for science is infectious, and some of my fondest memories in the group have been our discussions, getting carried away by 'what-if's or 'if we could just's. This passion and genuine excitement makes long days in the lab more enjoyable. I also want to thank you for the vast intellectual freedom you have provided over the course of my DPhil. While not always easy, this has meant that I have always worked on the areas that I find most interesting and has made me a far better scientist because of it. In short, thank you.

Another enormous thank you must go to Prof. Michael Johnston who has been there from the very start of my academic career. I can never thank you enough for everything you have done for me these past eight years. You have helped me feel like I belonged first in Oxford, and then in academia as well. Your dedication to undergraduate teaching and passion for the material was an enormous inspiration and one that I have tried to pass on to my students. Working in your group has been a real pleasure and I have learned so many things from you. I would not be the same scientist without your tireless help and outstanding example to aspire towards. I will always be grateful for everything you have done for me.

I have been immensely lucky to have benefited from Prof. Laura Herz's seemingly endless wisdom about science, academia and life. Your unerring commitment to the highest standards is an inspiration and drives me to make sure my work as good as I can make it. The quality of your advice on how to navigate the often murky waters of academia is unparalleled and I can not thank you enough for all the help and guidance you have given me – I could not have asked for a better mentor.

I owe an immense debt of gratitude to Nick Greenwood for making this all possible. Thank you so much for your generous and selfless endowment of my Studentship. As we have discussed several times at this point, I think it is important to maximise

any opportunity given to me, and I hope you agree I have done my best here. This opportunity has been genuinely life-changing and I will be forever grateful.

My DPhil would have been infinitely harder without Clare Moloney. You are the kindest person and I always left your office happier from our chats and with any issue instantly solved. You really are the glue that holds the group together and I will miss you very much. I'll make sure everyone knows to get you a silk scarf as a leaving gift to say thank you.

No experimental work is done in isolation, and I am incredibly thankful to have had such amazing colleagues across the Snaith, Johnston and Herz groups these past four years. Some people in particular have been instrumental in helping me to become the scientist I am today. First and foremost, I was so lucky when Henry asked Yen to be my mentor in my first year. Not only is Yen an outstandingly talented scientist, but a wonderful person too. I can't thank Yen enough for teaching me his wizardry with perovskites and always being willing to get excited about science with me. No one deserved a faculty job more than you, I can't wait to see what awesome work your new group will do! I was equally lucky that Clare (yet another example for her being the absolute best) sat me in G30 – the cool office. Melissa, Ashley, Harry, and Fengning made the office such a wonderful and happy place to be. I will miss our chats, gossip, teas and teasing of Harry (when he bothered to show up) very much. You guys are the best. A huge thank you to James Ball for always leading the charge, thoroughly earning his nickname as Mr Maximum Power Pints. Seriously though, thank you for always being willing to help me whenever I asked. I learned so much from you and I am very grateful. Suhas, you are simply a genius and the loveliest person. You taught me so much about the thermodynamics of solar cells, though it took me several years longer to fully understand! I owe Jonny hugely for helping me to spot and dodge (for the most part) the traps PhD students usually fall into. You were a brilliant mentor and saved me so many sad months in the lab! A massive thank you to Augustin for being far too helpful for his own good. The lab would have been so much worse without you, and many of my experiments simply wouldn't have been possible. I am also very grateful for your love of feeding people, your food was always delicious and the evenings spent at your house were always so fun. I am very grateful for Akash being so kind and never complaining when I grab him as he walks past my office to debug my code for sometimes days on end and somehow making it fun. It is a shame that I had to write this thesis before we (and James of course) could finish the optical modelling project. It just means you're stuck debugging code with me for some time yet! My time in the group would have been so much less fun without Derek. You are such a gem of a person and make every situation full of laughter and joy. I have never laughed as hard or as long as during the Fruit and Veg bop. A huge thank you to Leo, Karim and Silvia who were always willing to show me the dark arts of spectroscopy,

and made it very fun, and they were always happy to help whenever I tipped up at their offices with data I didn't understand yet. You succeeded in converting me into a spectroscopist for my postdoc! Alan is a huge unsung hero of the department and deserves far more credit for keeping everything working. Thank you for being so incredibly helpful, and for making any trip to stores so enjoyable. Finally, huge thank yous to Mike, Kelly, Philippe, Anna, Olivia, Flo, Rouhan, Jake, Pietro, Joel, Emil, Manuel, Grey, Esthy, Eli, Seongrok, Spencer, Benny, Xinyi, Saq, Ben, Zhongcheng, Nicky, Heon, Suer, Giulia, Laura, Pabitra, Bernard, Tong, Nobuya; Kun, Chelsea, Kilian, Qimu, Ford, Siyu, Juliane, Sabrina, Djamshid, Jay; Snigdha, Jae, Vincent, Full Stack Ulatowski, Alex K, Marcello, Mathias, Kimberley, Adam, Hannah and Tim who all made the Snaith, Johnston and Herz groups such a fun place to work. I am sorry there isn't space here for you each to have a few sentences!

I was lucky to have the opportunity to teach extensively during my PhD. I am really grateful to Neville, Pat, Norman and Sneha for instantly making me feel part of the team of tutors and making the whole experience so enjoyable. Another thank you to my students for making the tutorials themselves fun, and for your consistently great feedback. It really makes all the effort worth it.

SCRFC played an enormous role in my whole time in Oxford. I made some amazing friends, Russell, Jamie, Meryem, Barney, Ewan, Joe, Dan, Xav, Aaron and so many more who I don't have space to list. I am incredibly proud of what we achieved, going from nowhere to winning the league and then making the cuppers final in just a few short years. I loved my whole time with SCRFC and many of my best memories in Oxford are with you guys. Similarly, I am grateful to OURFC for reminding me, regularly, that the best progress is made when outside of your comfort zone.

James Turner has been a great friend since we were 11 but sadly the quality of his jokes has been downhill since then. Thank you for being our Sheffield tour guide and I hope you get all the Spaghetti Bolognese your heart desires – you deserve it.

So many people at home supported and encouraged me to get to this point. All the practical work I did with Kevin and my brother growing up was surprisingly invaluable over the course of my PhD. My parents have always encouraged me to follow my passions and been extremely supportive of my academic journey, even if they just smile and nod when I try to explain why something is super cool. Not to be outdone, my mum started a Masters at Oxford during my PhD – it has been incredibly fun, and a little surreal, to be students together at the same time! A huge thank you for always being excited whenever "I found a finding". Polly, this thesis is dedicated to you. You are the best grandma anyone could ever hope for. You're kind and generous and, you probably don't realise that you, as much as anyone, have encouraged me to pursue science and teaching. This stems from our chats in the kitchen 20 years ago about how/why spoons get hot when making teas.

Ben, you might as well be family and I am very lucky to have you as my best friend. You've been there from the start and have made my time in Oxford packed with fun and happiness. Thank you as well for always being willing to tell me my figures look nice and you're a fan of my colour schemes. It hasn't quite sunk in yet that we will be living in different cities for the first time since we met (if you ignore the pandemic) and so can't have our Wednesday dinners or impromptu Nando's. You're the best and we will visit each other often.

Finally, Alex who, in her own words, is the best person ever and I couldn't agree more. You helped me more than I can say with my PhD and inspire me to be the best scientist and person I can. I am sure you will be more relieved than me that this thesis is finished. I love you and our rapidly expanding family of fruits more than I can say. I am struggling to express how much I love you, and so I scoured all of the great works for inspiration. Finally, I found something that was fitting: *We ride together, we die together, bad boys for life.*

Abstract

Metal halide perovskite (MHP) semiconductors are an extremely promising class of materials for photovoltaic (PV) applications. The outstanding optoelectronic properties of MHPs and their relative ease of manufacture have caused much excitement in the PV research and industrial communities alike. In turn, the solar-to-electrical power conversion efficiencies of PV devices based on MHPs have continued to soar over the past decade. Typically, and throughout this thesis, these are hybrid organic-inorganic semiconductors which combine many of the best aspects of both inorganic and organic semiconductors. Namely, their high charge-carrier mobility, long charge-carrier lifetimes and diffusion lengths are typical of inorganic semiconductors, whereas their low temperature processability and tunable optoelectronic properties are more typical of organic semiconductors.

It has become apparent that the interfaces between the MHP semiconductor and the organic semiconductors required as charge transport layers for full photovoltaic devices are the limiting factor constraining the performance of perovskite solar cells. These interfaces introduce additional, rapid non-radiative recombination pathways which are detrimental to the open-circuit voltage of PV devices. Therefore, the highest efficiency devices to-date are delivered via a process known as 'passivation' wherein an additional chemical treatment is applied between the perovskite and the charge transport layer to reduce non-radiative recombination at these interfaces. This process has pushed the performance of single junction perovskite solar cells towards their radiative limit. Regrettably, these passivation treatments can often introduce additional instabilities into the device structure and hence are not suitable for long-term applications.

More recently, as single-junction perovskite solar cells have neared their maximum attainable efficiency, an increasing focus has been dedicated to wide ($> 1.7\,\mathrm{eV}$) perovskites which are suitable for tandem solar cells. Tandem solar cells significantly raise the thermodynamic limit and so are able to deliver much higher power conversion efficiencies. However, the wide bandgap perovskites perform significantly poorly compared to their single junction counterparts. The reasons for this had been unclear and are studied in detail herein.

In this thesis, I focus on understanding and improving the interfaces present within MHP solar cells. In the first instance, a novel passivation strategy is implemented for single junction devices and its influence on the optoelectronic properties of the perovskite semiconductor and full devices is investigated in detail. Importantly, the benefit of this passivation strategy is maintained over the course of harsh ($85\,^{\circ}\mathrm{C}$, full spectrum AM1.5 illumination) ageing, a major advance in the field.

Following these investigations, the technologically relevant (for stable tandem solar cells) methylammonium-free wide bandgap perovskite is investigated in detail. Compared to their lower bandgap (≤ 1.6 eV) counterparts, these types of perovskites suffer from higher levels of non-radiative losses constraining their efficiencies far below their thermodynamic potential. The energy losses in MA-free high-bromide-content wide bandgap perovskites are studied in detail. These perovskites are found to be characterised by large non-radiative recombination losses in the bulk material and especially that the interfaces with transport layers in solar cell devices strongly limit their open-circuit voltage. In particular, the interface with the hole transport layer is discovered to perform particularly poorly, in contrast to $1.6\,\mathrm{eV}$ bandgap MHPs which are generally limited by the interface with the electron transport layer. To overcome these losses, we incorporate and investigate the recombination mechanisms present with perovskites treated with the ionic additive 1-butyl-1-methylpiperidinium tetrafluoroborate ($[\mathrm{BMP}]^{+}[\mathrm{BF_4}]^{-}$). We find that this additive not only improves the radiative efficiency of the bulk perovskite, but also reduces the non-radiative recombination at both the hole and electron transport layer interfaces of full photovoltaic devices. The recombination

processes in full devices are studied in detail, and directions for further enhancements are suggested.

Finally, following the discovery that the hole transport layer is the limiting factor in these wide bandgap devices, I focus on improving this interface in detail. I create a novel hole transporting material developed by blending two commercially available polymers. For certain blend ratios, the PV device performance is significantly enhanced and the PV device physics of this system is investigated in detail. The structure and basic optoelectronic properties of the MHP semiconductor is found to be insensitive to the different polymer blends onto which it was deposited. The photophysical properties of these polymer blend systems themselves are investigated in detail. While substantial changes to the photophysics are observed, the reason for enhanced device performance remain elusive and ought to be the focus of future research.

List of Publications

1. Vincent J-Y Lim, Alexander J Knight, **Robert DJ Oliver**, Henry J Snaith, Michael B Johnston, Laura M Herz, '*Impact of Hole-Transport Layer and Interface Passivation on Halide Segregation in Mixed-Halide Perovskites*', *Advanced Functional Materials*, 2204825, (2022).

2. Akash Dasgupta, Suhas Mahesh, Pietro Caprioglio, Yen-Hung Lin, Karl-Augustin Zaininger, **Robert DJ Oliver**, Philippe Holzhey, Suer Zhou, Melissa M McCarthy, Joel A Smith, Maximilian Frenzel, M Greyson Christoforo, James M Ball, Bernard Wenger, Henry J Snaith, '*Visualizing Macroscopic Inhomogeneities in Perovskite Solar Cells*', *ACS Energy Letters*, **7**, 7, 2311–2322, (2022).

3. Ke Xiao, Yen-Hung Lin, Mei Zhang, **Robert DJ Oliver**, Xi Wang, Zhou Liu, Xin Luo, Jia Li, Donny Lai, Haowen Luo, Renxing Lin, Jun Xu, Yi Hou, Henry J Snaith, Hairen Tan, '*Scalable Processing for Realizing 21.7%-Efficient All-Perovskite Tandem Solar Modules*', *Science*, **376**, 6594, 762–767, (2022).

4. Yinan Chen, Silvia G Motti, **Robert DJ Oliver**, Adam D Wright, Henry J Snaith, Michael B Johnston, Laura M Herz, Marina R Filip, '*Optoelectronic Properties of Mixed Iodide–Bromide Perovskites from First-Principles Computational Modeling and Experiment*', *The Journal of Physical Chemistry Letters*, **13**, 18, 4184–4192, (2022).

5. Kilian B Lohmann, Silvia G Motti, **Robert DJ Oliver**, Alexandra J Ramadan, Harry C Sansom, Qimu Yuan, Karim A Elmestekawy, Jay B Patel, James M Ball, Laura M Herz, Henry J Snaith, Michael B Johnston, '*Solvent-Free Method for*

Defect Reduction and Improved Performance of pin Vapor-Deposited Perovskite Solar Cells', *ACS Energy Letters*, **7**, 6, 1903–1911, (2022).

6. **Robert DJ Oliver**, Pietro Caprioglio, Francisco Peña-Camargo, Leonardo RV Buizza, Fengshuo Zu, Alexandra J Ramadan, Silvia G Motti, Suhas Mahesh, Melissa M McCarthy, Jonathan H Warby, Yen-Hung Lin, Norbert Koch, Steve Albrecht, Laura M Herz, Michael B Johnston, Dieter Neher, Martin Stolterfoht, Henry J Snaith, '*Understanding and Suppressing Non-Radiative Losses in Methylammonium-Free Wide-Bandgap Perovskite Solar Cells*', *Energy & Environmental Science*, **15**, 2. 714–726, (2022).

7. Silvia G Motti, Jay B Patel, **Robert DJ Oliver**, Henry J Snaith, Michael B Johnston, Laura M Herz, '*Phase Segregation in Mixed-Halide Perovskites Affects Charge-Carrier Dynamics While Preserving Mobility*', *Nature Communications*, **12**, 1, 1–9, (2021).

8. Alexander J Knight, Juliane Borchert, **Robert DJ Oliver**, Jay B Patel, Paolo G Radaelli, Henry J Snaith, Michael B Johnston, Laura M Herz, '*Halide Segregation in Mixed-Halide Perovskites: Influence of A-site Cations*', *ACS Energy Letters*, **6**, 2, 799–808, (2021).

9. **Robert DJ Oliver**, Yen-Hung Lin, Alexander J Horn, Chelsea Q Xia, Jonathan H Warby, Michael B Johnston, Alexandra J Ramadan, Henry J Snaith, '*Thermally Stable Passivation Toward High Efficiency Inverted Perovskite Solar Cells*', *ACS Energy Letters*, **5**, 11, 3336–3343, (2020).

10. Yen-Hung Lin, Nobuya Sakai, Peimei Da, Jiaying Wu, Harry C Sansom, Alexandra J Ramadan, Suhas Mahesh, Junliang Liu, **Robert DJ Oliver**, Jongchul Lim, Lee Aspitarte, Kshama Sharma, PK Madhu, Anna B Morales-Vilches, Pabitra K Nayak, Sai Bai, Feng Gao, Chris RM Grovenor, Michael B Johnston, John G Labram, James R Durrant, James M Ball, Bernard Wenger, Bernd Stannowski, Henry J Snaith, '*A Piperidinium Salt Stabilizes Efficient Metal-Halide Perovskite Solar Cells*', *Science*, **369**, 6499, 96–102, (2020).

11. Jonathan H Warby, Bernard Wenger, Alexandra J Ramadan, **Robert DJ Oliver**, Harry C Sansom, Ashley R Marshall, Henry J Snaith, '*Revealing Factors Influencing the Operational Stability of Perovskite Light-Emitting Diodes*', *ACS Nano*, **14**, 7, 8855–8865, (2020).

12. Kilian B Lohmann, Jay B Patel, Mathias Uller Rothmann, Chelsea Q Xia, **Robert DJ Oliver**, Laura M Herz, Henry J Snaith, Michael B Johnston, '*Control Over Crystal Size in Vapor Deposited Metal-Halide Perovskite Films*', *ACS Energy Letters*, **5**, 3, 710–717, (2020).

13. Suhas Mahesh, James M Ball, **Robert DJ Oliver**, David P McMeekin, Pabitra K Nayak, Michael B Johnston, Henry J Snaith, '*Revealing the Origin of Voltage Loss in Mixed-Halide Perovskite Solar Cells*', *Energy & Environmental Science*, **13**, 1, 258–267, (2020).

Manuscripts in preparation

1. P. Caprioglio, J. A. Smith, **R. D. J. Oliver**, A. Dasgupta, S. Choudhary, M. D. Farrar, A. J. Ramadan, Y-H. Lin, M. G. Christoforo, J. Diekmann, J. Thiesbrummel, K-A. Zaininger, X. Shen, D. Neher, M. Stolterfoht, H. J. Snaith,'*Open-circuit and short-circuit loss management in inverted wide-gap perovskite pin solar cells*', Under review, *Nature Materials*.

2. H. Song, J. Yang, W. H. Jeong, J. Lee, T. H. Lee, J. W. Yoon, H. Lee, A. J. Ramadan, **R. D. J. Oliver**, S. C. Cho, S. G. Lim, J. W. Jang, Z. Yu, J. T. Oh, E. D. Jung, M. H. Song, S. H. Park, J. R. Durrant, H. J. Snaith, S. U. Lee, B. R. Lee, H. Choi, '*A universal perovskite nanocrystal ink for high-performance optoelectronic devices*', Under Review, *Energy and Environmental Science*.

3. **R. D. J. Oliver**, A. J. Ramadan, Y-H. Lin, K. Elmestekawy, M. M. McCarthy, A. Marshall, S. Motti, J. A. Smith, L. M. Herz, M. B. Johnston, H. J. Snaith, '*Broadly Tunable Hole Transport Material Based on Polymer Blends Enables High*

Performance Wide Bandgap Perovskite Solar Cells', *Manuscript in Preparation*

4. **R. D. J. Oliver**, J. M. Ball, A. J. Ramadan, A. Dasgupta, M. Kober-Czerny, F. Yang, Y-H. Lin, S. Mahesh, H. J. Snaith, M. B. Johnston, '*Understanding Charge-Carrier Recombination in Perovskite Solar Cells by Voltage-Dependent External Quantum Efficiency*', *Manuscript in Preparation*

List of Figures

1.1 (a)Energy generation from different sources. (b) Carbon intensity of different electricity generation technologies. 3

1.2 Projected and historical installed solar capacity 5

1.3 Schematic showing benefit of tandem solar cells 9

2.1 Schematic of a modified plane wave from Bloch's theorem 21

2.2 Schematic showing the effect of doping on the Fermi level position . . . 26

2.3 Schematic describing charge-carrier recombination processes within a semiconductor. 30

2.4 Recombination rate of free carriers in a semiconductor as a function of charge carrier density. 32

2.5 Influence of defects on the quasi-Fermi level splitting 34

2.6 Schematic describing the rates involved capture and release of charge-carriers from a trap state. 35

2.7 Radiative efficiency as a function of charge carrier density for different monomolecular decay rates. 46

2.8 Diagram showing the relationship between the quasi-Fermi level splitting and device V_{OC} for perfect and lossy interfaces. 50

2.9 Schematic of the bands within a p-i-n solar cell at short- and open-circuit conditions. 52

2.10 Annotated JV curve of describing key device parameters 53

2.11 Schematic showing importance of atmospheric effects on the solar spectrum 57

2.12 Intrinsic losses occurring in a device with optimal $E_g = 1.31$ eV (a) and an optimal tandem device (b) under one sun illumination. 64
2.13 Influence of R_{series} and R_{shunt} on solar cell performance. 66
2.14 Equivalent circuit of a solar cell including shunt and series resistance . 67
2.15 Ideality factor dependence on the open-circuit voltage as energetic alignment, surface and bulk non-radiative recombination are varied 70
2.16 Schematic of the cubic MHP crystal structure. 72
2.17 Comparison of research solar cell record efficiency development. 74

4.1 Photoluminescence quantum yield (PLQY) measurements for pristine and benzylammonium bromide (BenABr) treated thin films on glass and with device-relevant contacts. The increased in quasi-Fermi level splitting (QFLS) following the treatment is shown for each condition. The steady-state photoluminescence (PL) spectra for each condition show no peak shape change following BenABr treatment. 133
4.2 Time-resolved photoluminescence (TRPL) transients for pristine (purple) and benzylammonium bromide treated (orange) films and Real part of THz photoconductivity spectra induced by photoexcitation. 136
4.3 a) Dark conductivity spectra measured using THz spectroscopy without photoexcitation. b) the absorption coefficient at THz frequencies. These measurements and analysis were performed by Dr. Chelsea Q. Xia. . . 137
4.4 X-ray photoemission spectroscopy (XPS) and X-ray diffraction (XRD) data for pristine and benzylammonium bromide treated perovskite thin-films 141
4.5 X-ray photoemission spectroscopy (XPS) fittings and scanning electron microscopy (SEM) images for pristine and benzylammonium bromide treated samples 143
4.6 Photovoltaics device statistics for the optimisation of the benzylammonium bromide treatment 144

4.7 Stabilised power output (SPO) and external quantum efficiency (EQE) measurements for champion PV devices with and without benzylammonium bromide treatment 146
4.8 Stability assessment of perovskite solar cells with and without the benzylammonium bromide (BenABr) treatment at 85 °C under simulated AM 1.5 irradiance in an open-circuit condition 148

5.1 Absorption coefficient, steady-state photoluminescence spectra and X-ray diffraction patterns for $FA_{0.83}Cs_{0.17}Pb(I_{0.6}Br_{0.4})_3$ with and without 1-butyl-1-methylpiperidinium tetrafluoroborate ($[BMP]^+[BF_4]^-$) modification. 159
5.2 Optical-pump terahertz-probe spectroscopy (OPTPS) and time-correlated single photon counting (TCSPC) measurements on control and $[BMP]^+[BF_4]^-$-modified perovskite thin films 162
5.3 Time-resolved photoluminescence (TRPL) modelling using unbalanced electron and hole trapping rates assuming uniform initial charge carrier distribution. 165
5.4 Modelled electron and hole populations for control and $[BMP]^+[BF_4]^-$ modified perovskite thin films. 166
5.5 Remaining charge carrier density at the time of arrival of photoexcitation pulse for control and ionic additive-modified perovskite thin films . . . 168
5.6 Influence of repetition rate on the time-correlated single photon counting (TCSPC) transients for control and ionic additive-modified perovskite thin films. 169
5.7 (a) Interfacial recombination photophysical characterisation for control and ionic additive (IA) modified perovskite thin films. 170
5.8 Photovoltaic device performance for control, ionic additive (IA)-modified and ionic additive (IA)-modified with LiF interlayer. 175

5.9 JV scan-rate dependence and maximum power point tracked efficiencies for control, ionic additive-modified and ionic additive-modified with a LiF interlayer solar cells. 177
5.10 External quantum efficiency and optical constants investigating the short-circuit current density (J_{SC}) increase in ionic additive (IA)-modified devices 178
5.11 Comparison between the measured JV curve of a solar cell and the reconstructed pseudo JV-curves (pJVs) from intensity dependent measurements on the same solar cell device or respective thin-film. 181
5.12 Open-circuit voltage intensity-dependent measurements and ideality factors for solar cell devices implementing control, ionic additive (IA)-modified, and ionic additive (IA)-modified with additional LiF interlayer before the C60. V_{OC} and fill factor (FF) energy loss summaries. 182
5.13 Ultraviolet photoemission sprectroscopy (UPS) measurements on methylammonium-free wide bandgap perovskties with sequential C60 deposition 184

6.1 Photoluminescence quantum yield measurements of a wide bandgap perovskite processed on a range of hole transport layers. 197
6.2 a) Comparison of representative JV curves comparing devices with PTAA as the hole transport layer and TFB as the direct replacement for poly[bis(4-phenyl)(2,4,6-trimethylphenyl)amine] (PTAA). Comparison of the stabilised open-circuit voltage for control (PTAA), $[BMP]^+[BF_4]^-$-passivated (as in **Chapter 5**) and devices with a bilayer PTAA/TFB hole transport layer. 200
6.3 JV curves for representative control (PTAA as the hole transport layer), the initial polymer blend and the final, fully optimised polymer blend. . 202
6.4 Statistical summary of the photovoltaic device parameters are presented for devices based on $FA_{0.83}Cs_{0.17}Pb(I_{0.6}Br_{0.4})_3$ processed on different polymer hole transport layers. 203

6.5 Maximum power point tracking (MPPT) efficiencies for poly[bis(4-phenyl)(2,4,6-trimethylphenyl)amine] (PTAA) and polymer blend hole transport layer devices, comparison of JV-curves after 6 months of shelf storage, and ageing of the polymer blend unencapsulated at 65 °C under full spectrum AM1.5 illumination. 205

6.6 Spatial distribution of the quasi-Fermi level splitting (QFLS) and 'charge collection quality' across an entire device active area (0.25 cm^2) for devices employing PTAA, polymer blend and TFB as the hole transport layer. 206

6.7 Absorption coefficient and steady state photoluminescence (bold curves) of $FA_{0.83}Cs_{0.17}Pb(I_{0.6}Br_{0.4})_3$ processed on each polymer hole transport layer investigated. X-ray diffraction (XRD) patterns of the perovskite semiconductors processed on the polymer HTLs. 209

6.8 Normalised absorption of the PTAA, TFB and 3:1, 2:1, 1:1 and 1:2 PTAA:TFB blends. Comparison between the measured absorption and a 'linear combination' of the poly[bis(4-phenyl)(2,4,6-trimethylphenyl)amine] (PTAA) and poly(9,9-dioctylfluorene-alt-N-(4-sec-butylphenyl)-diphenylamine) (TFB) absorption for 3:1, 2:1, 1:1. and 1:2 blend ratios. 210

6.9 Atomic force microscopy (AFM) images for pure poly[bis(4-phenyl)(2,4,6-trimethylphenyl)amine] (PTAA), poly(9,9-dioctylfluorene-alt-N-(4-sec-butylphenyl)-diphenylamine) (TFB) and the 2:1 PTAA:TFB blend. . . 212

6.10 Photoluminescence spectra for polymer and blended polymer thin films on quartz. 214

6.11 Time-resolved emission spectroscopy of the blended polymer systems. . 215

6.12 Photoluminescence transients for emission between $425 - 455$ nm and $555 - 605$ nm for the polymer blend systems. 216

List of Tables

3.1 FACs 1.8 eV perovskite precursor solution recipe 104

3.2 Input parameters for the drift-diffusion simulations presented in **Chapter 5**. If no explanation for a value is provided, the values used are consistent with SCAPS simulations presented in the literature [14, 15]. In particular, ref [14] provides detailed information from each parameter is determined. 126

4.1 PLQY values for pristine and passivated samples processed on glass (glass), with the additional coating of PCBM (PCBM) and processed on polyTPD coated FTO (polyTPD). Also shown are the ΔQFLS from the radiative limit $\Delta QFLS_{rad}$ and the ΔQFLS between the passivated and non-passivated films. 134

4.2 Fitted parameters for a stretched exponential fit to the time-resolved photoluminescence (TRPL) 135

4.3 Average (champion) device parameters for the benzylammonium bromide (BenABr) concentrations investigated. 145

5.1 Surface recombination velocity (SRV) 173

5.2 Reported values of the open-circuit voltage and power conversion efficiency for methylammonium-free p-i-n solar cells. 176

5.3 Comparing the device performance parameters of actual devices without (control) and with ionic additive (IA) modification (IA) with those determined using drift-diffusion simulations, taking the mobility, bulk lifetimes and surface recombination velocitys (SRVs) values that were determined in the main text. A full list of the device simulation inputs can be found in **Table 3.2**. 179

5.4 Estimated power conversion efficiency (PCE) (in the absence of interfacial and/or transport losses) obtained from the pseudo JV-curve (pJV) of cells and isolated thin films for the materials investigated in the study. The short-circuit current density (J_{SC}) used here to estimate the efficiency potentials are calculated by assuming 95 % of the thermodynamic limit corresponding to the bandgap. 182

Acronyms

pJV pseudo JV-curve

FF fill factor

J_{SC} short-circuit current density

n_{id} ideality factor

R_{series} series resistance

R_{shunt} shunt resistance

V_{OC} open-circuit voltage

$[\mathbf{BMP}]^{+}[\mathbf{BF}_4]^{-}$ 1-butyl-1-methylpiperidinium tetrafluoroborate

AFM atomic force microscopy

ALD atomic layer deposition

AM air mass

BCP bathocuproine

BenABr benzylammonium bromide

CB chlorobenzene

CO_2 carbon dioxide

CTL charge transport layer

EQE external quantum efficiency

ETL electron transport layer

F8BT poly(9,9-dioctylfluorene-alt-benzothiadiazole)

FA formamidinium

FTO fluorine-doped tin oxide

GDP gross domestic product

HOMO highest occupied molecular orbital

HTL hole transport layer

IA ionic additive

IEA International Energy Acency

IPCC Intergovernmental Panel on Climate Change

ITO indium tin oxide

LUMO lowest unoccupied molecular orbital

MA methylammonium

MHP metal halide perovskite

MPPT maximum power point tracking

OPTPS optical-pump terahertz-probe spectroscopy

$PC_{61}BM$ [6,6]-phenyl-C61-butyric acid methyl ester

PCE power conversion efficiency

PFN-Br poly(9,9-bis(3'-(N,N-dimethyl)-N-ethylammoinium-propyl-2,7-fluorene)-alt-2,7-(9,9-dioctylfluorene))dibromide

PL photoluminescence

PLQY photoluminescence quantum yield

polyTPD poly(4-butyl-N,N-diphenylaniline)

PSCs perovskite solar cells

PTAA poly[bis(4-phenyl)(2,4,6-trimethylphenyl)amine]

PV photovoltaics

QFLS quasi-Fermi level splitting

SAM self-assembled monolayer

SEM scanning electron microscopy

Spiro-OMeTAD 2,2',7,7'-Tetrakis[N,N-di(4-methoxyphenyl)amino]-9,9'-spirobifluorene

SPO stabilised power output

SRV surface recombination velocity

TCSPC time-correlated single photon counting

TFB poly(9,9-dioctylfluorene-alt-N-(4-sec-butylphenyl)-diphenylamine)

THz-TDS terahertz time-domain spectroscopy

TISE time-independent Schrödinger equation

TRES time-resolved emission spectroscopy

TRPL time-resolved photoluminescence

UN United Nations

UPS ultraviolet photoemission sprectroscopy

VB valence band

WBG wide bandgap

XPS X-ray photoemission spectroscopy

XRD X-ray diffraction

Chapter 1

Introduction

1.1 Motivation - the Need for Sustainability

The world is on the precipice of a climate emergency. If humanity is to avoid the worst effects of climate change, it is imperative that, by the year 2050, average global temperature rises are constrained below 1.5 °C compared to preindustiral levels [1]. It has been known for decades that changes to the climate are caused by human industrial activity, most notably by the large-scale emission of 'greenhouse' gases such as carbon dioxide (CO_2) and methane. Despite this causal link being well-established, CO_2 emissions have continued to rise dramatically, with a 50% increase between the years 2000 and 2019 [2]. This is because energy consumption is vital to economic advancement and hence human prosperity. Indeed, the energy consumed by a country is closely linked to the gross domestic product (GDP) of that country [3].

According to the fifth assessment report of the Intergovernmental Panel on Climate Change (IPCC), there are four major factors affecting global CO_2 emissions, namely population size, economic growth, energy intensity and emissions per unit energy generated [1]. I briefly summarise each of these factors below. Population growth is clearly a driving force for increased emissions – basic human requirements such as food, clothing and heating all contribute to the production of greenhouse gases. Simply put, more

people requires more emissions. This is particularly striking given that the United Nations (UN) predicts that the world's population will be increased by $\sim 40\%$ to 11 billion people by the year 2100 [4]. As a result of this increasing population, global CO_2 emissions will rise over the coming decades. Economic growth is hugely beneficial for society but is another key driving factor of emissions. Despite being drastically far from evenly distributed, global GDP per capita is at its highest level ever [5], and the proportion of those living in extreme poverty has concomitantly fallen to the lowest value on record [6]. Economic growth is a key priority of all the world's governments, but it is especially important for developing countries. By growing their economies, developing countries would be able to raise the standard of living for their citizens, potentially lifting millions from poverty [6]. It would be massively unjust to expect developing countries to cut their emissions, and hence stagnate their economies and condemn their citizens to continued poverty. This is especially true since the wealthy nations who would be demanding such an action are only wealthy because of historical emissions. Therefore, in my opinion at least, economic growth, particularly in the developing world, must not be constrained to avoid wide-spread suffering. It is worth noting that there are some indications that growth can be decoupled from emissions in some well-developed countries (e.g. Sweden and the United Kingdom) [1, 7]. While this bodes well for the long term, the link between economic growth and increased greenhouse gas emissions remains strong.

The final two factors identified by the IPCC (energy intensity and emissions per unit energy generated) describe how we can slow and eventually reduce CO_2 emissions without compromising on economic development or standard of living. Energy intensity is a measure of how efficiently we use energy. Developing technologies that use energy more efficiently, as well as organising society in such a way as to reduce waste, is a priority to reduce greenhouse gas emissions. This encompasses everything from the electrification of the transport network to more efficient insulation of homes and more. Regrettably, however, simply reducing energy intensity will not be sufficient. No matter how efficient a technology is, for as long as it needs power, it will generate emissions

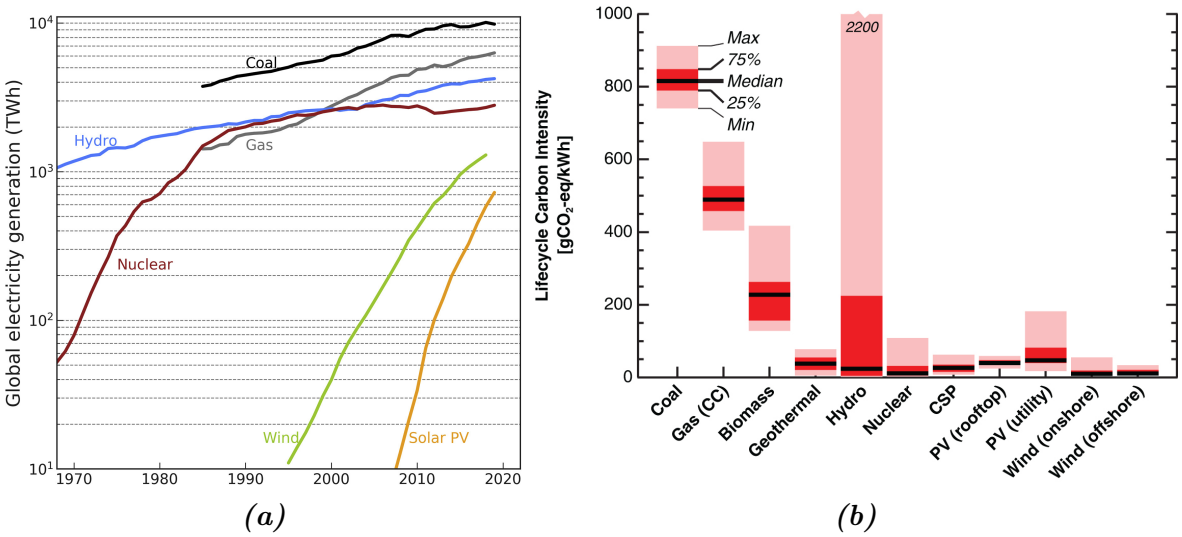


Figure 1.1: ***(a)*** *Energy generation from different sources over time. Energy generated from solar, despite rising exponentially, is still far behind energy generated using fossil fuels. Reproduced with permission from Victoria et al. [9].* ***(b)*** *The carbon intensity is given in grams of CO_2-equivalent emissions per kWh of electricity generated during the lifetime of a typical type of generator (CSP = concentrated solar thermal power), as per the IPCC protocol [1]. It is evident that renewables use far less carbon over their lifecycle compare to fossil fuels which, despite recent progress, still dominate the world's energy generation. Figure and caption adapted from [10], © IOP Publishing. Reproduced with permission. All rights reserved.*

given the current methods in which energy is generated. Therefore the final factor, emissions per unit energy, is vital and must be brought to zero as soon as possible. Currently, the vast majority of the world's power demand is satisfied by burning fossil fuels such as coal, oil or natural gas, which are not only increasingly scarce, but also generate significant CO_2 emissions for each unit of energy generated [1]. Therefore, reducing the world's dependence on fossil fuels, and most especially coal, is the most effective way of reducing CO_2 emissions whilst preserving human prosperity. Regrettably, the world is not doing nearly enough to keep fossil fuels, and the carbon they contain, in the ground and as such the increase in global energy demand continues to outpace decarbonisation efforts [8]. In the short term, reducing the world's power demand is not feasible as it would undoubtedly result in a significant downturn in GDP across all economies and therefore a lower quality of life for potentially billions of people. The solution, therefore, is meet the world's energy demand by low- or zero-carbon routes.

1.2 Solar Energy

Solar energy is an extremely promising technology that has great potential to substantially reduce the 'emissions per unit energy' factor, even being negative over the lifetime of an installation. The solar resource is so abundant that in fact only 90 minutes of solar radiation, if perfectly harvested, would be sufficient to satisfy the planet's energy demands. Even with the constraints of real technology, land area and materials abundance, there are not expected to be any more bottlenecks for solar installation [9, 11]. In addition, silicon-based solar panels are a mature technology and so are ready to be rolled out on a world-scale. Despite these factors, energy generated from photovoltaics (PV) lags significantly behind energy generated by fossil fuels, as can be seen in **Figure 1.1a**. This is particularly troubling when comparing the 'lifecycle carbon intensity' of fossil fuels with their renewable counterparts. **Figure 1.1b** shows renewable energy is roughly 10× less carbon intense over the lifetime of production than energy generated from burning fossil fuels.

The good news is that the installed solar capacity, as seen in **Figure 1.1a**, is rising exponentially. In fact, solar installations continue to outpace the predictions of the International Energy Acency (IEA), as is shown in **Figure 1.2**. This is exciting – not only is the rate of PV installations increasing, but it is increasing more rapidly, consistently, than could have been predicted by the International Energy Acency. This increasing rate of installation is driven by the price of solar energy falling precipitously over the past decade. The so-called 'learning rate' describes how much cheaper new installations of solar energy are as a function of the total installed capacity. Typically this is described in cost reduction for every doubling of total installed capacity, and this is the definition we use here. Since the mid-1970s, solar has maintained a learning rate of over 25 % [9, 12]. Maintaining such a steep learning rate for so long is remarkable, and was driven largely by improvements to the technology itself (i.e. efficiency enhancements), the economy of scale and industry implementing research laboratory developments [9, 13], as well as increased market competition driving down profit margins [14]. What is yet more remarkable, is that this learning rate is accelerating further,

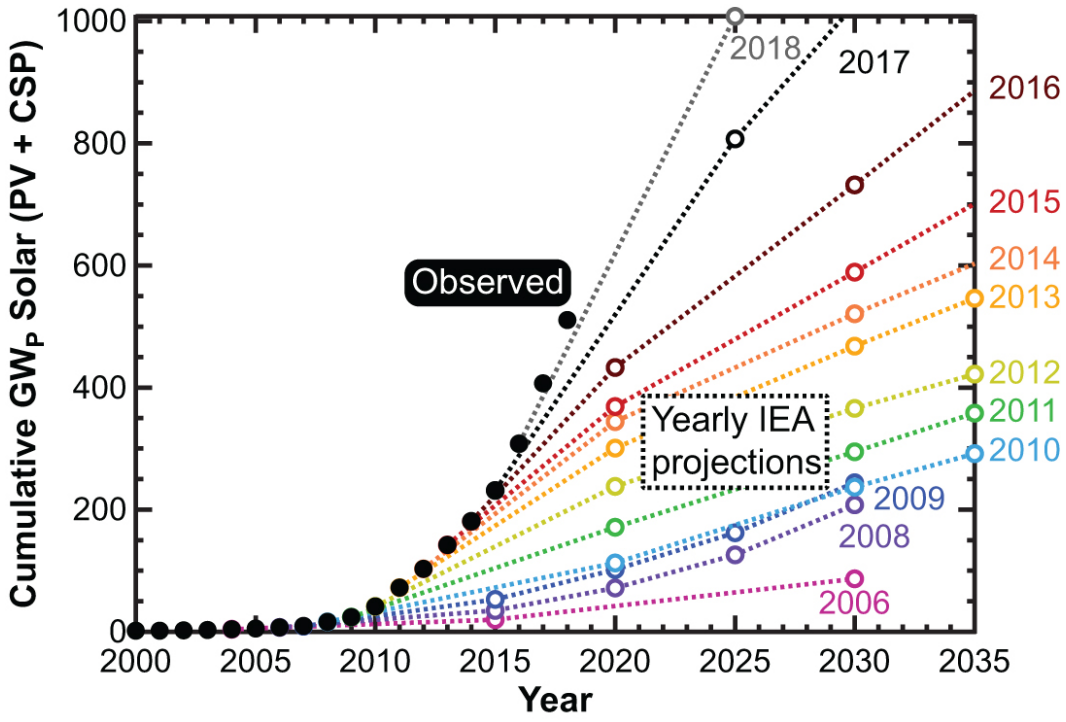


Figure 1.2: *International Energy Acency (IEA) predictions for installed solar capacity (accounting for both photovoltaics (PV) and concentrated solar thermal power (CSP) installations) from 2006 to 2018 are shown in coloured open circles. Consistently, the actual installed solar capacity (black circles) has dramatically outstripped the IEA's predictions. Figure taken from [10] with permission. © IOP Publishing. Reproduced with permission. All rights reserved.*

and is estimated to be $\sim 40\,\%$ since 2007, driven largely by standardisation, lifetime enhancements to modules and reduced balance of systems costs [13]. In the following, we briefly discuss how solar energy got here, and what the most crucial next steps are.

1.2.1 A brief history of solar

The history of photovoltaic cells is far longer than most realise. The common misconception is that PV burst onto the scene in the 1980s, however the first (reported) solar cell was fabricated a century earlier in the 1880s. Scientists had noticed that selenium had a very peculiar property – its resistance changed under light *and* this depended on the kind and 'strength' of the light. Understanding this phenomenon proved to be too challenging even for some of the greatest minds of the 19$^{\text{th}}$ century including James Clerk Maxwell. Seemingly unperturbed by the mystery of it all, Charles Fritts sandwiched selenium between two metal plates, the uppermost of which was semi-

transparent gold. Just like that, the very first photovoltaic solar cell was made and this was installed on a New York rooftop in the early 1880s [15] – astonishingly early. It would be nearly 100 years before a mature understanding of the operating principle of this pioneering cell would be understood. The solar cell installed by Fritts was, unsurprisingly, dismally inefficient at converting solar energy into electricity ($< 0.5\,\%$), nevertheless, a seed was sown from which a zero-carbon future would begin to bloom.

Solar energy generation would be largely dormant for decades until a serendipitous simultaneous arrival of the development of silicon and the space race which provided the expertise and the funding necessary to make substantial developments. Perhaps unsurprisingly, the first silicon based solar cell was developed at Bell labs, and achieved an efficiency of $\sim 6\,\%$ [16, 17]. However, despite this order of magnitude increase in performance, meaningful power production for the average American was still a distant dream. However, the US space program possessed, for all practical purposes, infinite funds and was where solar saw its first 'real world' application in satellites. Battery-powered satellites could only survive for, at most, a few weeks before losing power and becoming unoperational 'space junk'. However, if power could be continuously generated by solar panels, the lifetime of satellites could be extended for, in principle, arbitrarily long times. Indeed, despite PV still being very much in its infancy, the first satellite incorporating solar panels was operational for 6 years [18]!

While solar was firmly establishing itself in space-based applications, it took much longer for the cost of producing power from PV to becoming feasible on Earth. Perhaps ironically, it was the fossil fuel industry who first took a major interest in the use of solar cells to reduce the maintenance costs for their oil platforms in the 1970s, more detail can be found within Ref. [19]. At a similar time, PV was starting to be used to help electrify developing nations which lacked grid-connectivity and where personal diesel generators proved too unreliable. It was the French that pioneered the use of solar for rural electrification by installing, in 1978, solar panels on all huts in French Polynesisa [20]. However, main stream adoption of solar was hampered by successive American administrations. John Perlins describes the situation of the relative neglect towards

solar research well: *"Although the President's Materials Commission had proposed an equally weighted research effort for solar and nuclear, the American government under the incoming Eisenhower Administration and until Obama took office remained biased towards the nuclear option. The discovery of previously unseen documents reveal the strong support for solar, especially solar photovoltaics, by expert advisory groups to various presidential administrations from Eisenhower to Reagan, only to be rejected and suppressed by them to perpetuate support for fossil fuels and nuclear energy"* [21]. Despite this neglect, the cost of generating power from solar continued to fall rapidly [9]. The US would never manage to regain world-leadership in the solar industry due to this multi-administration-long dismissal of the vast solar resource (over $30,000\,\text{TW}$ are available on land alone!), and this leadership was taken on by Japan, then Germany and now China.

A particularly important innovation in solar was made by Markus Real, a Swiss engineer. He realised that solar need not compete with centralised fossil fuel plants, and could instead make the dispersed nature of solar energy work to the PV industry's benefit. He was one of the major pioneers behind rooftop installations such that each building could generate its own power, in his own words: "*It makes sense, absolute sense. The roof is there. The roof is free. The electrical connections are there*" [20]. This culminated with the installation of over 1 MW of solar across rooftops in Zurich. This approach was taken up to immense success by Germany in the late 1990s and early 2000s. Germany required energy providers to 'buy-back' the surplus energy generated by individuals at *at least* 457 euro/MWh for 20 years. This provided unprecedented confidence in PV, with consumers more happy to cover the high upfront costs knowing that they were guaranteed a long term return on their investment. This huge uptick in demand lead to a surge in companies selling photovoltaic panels and investors poured billions into this thriving industry. Regrettably, the PV industry was hit hard by the financial crisis of 2008 when the demand for new installations dropped dramatically, and many companies went bust. The loss on investment means that many are still reluctant to invest in the industry, even to this day.

Today, the solar industry has become largely based in China. It is now the case that solar is the cheapest way to produce energy for many countries [9, 10]. Indeed, the IEA Photovoltaic Roadmap predicts that solar will be the dominant source of electricity by 2050 [22]. Indeed, if the trend in **Figure 1.2** continues, one might be hopeful that we can achieve this milestone earlier.

1.2.2 The need for tandem solar cells

While there is undoubted cause for optimism, it is important to keep in mind that the entire industrial system must be overhauled. The concept of a personal 'carbon footprint' was popularised by BP in 2005, shifting the responsibility from the large emitters (such as themselves) to the average person. This propaganda was, and continues to be, highly effective. However the scale of the problem simply does not support this narrative. Back-of-the-envelope calculations show that if the average person in a well-developed country caused no emissions across their entire life, it would reduce less than 1 second of the current global emissions. This is not to say individual, and particularly societal, efforts are not important, but to demonstrate that a larger overhaul is necessary. The most vital contribution we can make is to influence governmental policy and to make a greener future a priority for those in positions to influence large scale change. This includes the funding of existing technologies, but also investment in research and development of new strategies to accelerate decarbonisation of the entire industrialised world, and particularly help developing nations achieve prosperity without large-scale emissions.

With the overhaul of the industrial system as our goal, energy generated from zero-carbon strategies needs to be plentiful, and far cheaper than current fossil-fuel based strategies. With this strong economic incentive, industry will naturally make the transition to energy generated from renewables. 'Tandem solar cells', wherein two suitable solar absorbers are electronically coupled to more efficiently harvest the solar spectrum, have great potential in this area. They can, at a relatively low addition cost, dramatically boost the efficiency attainable from PV modules, to over comfortably

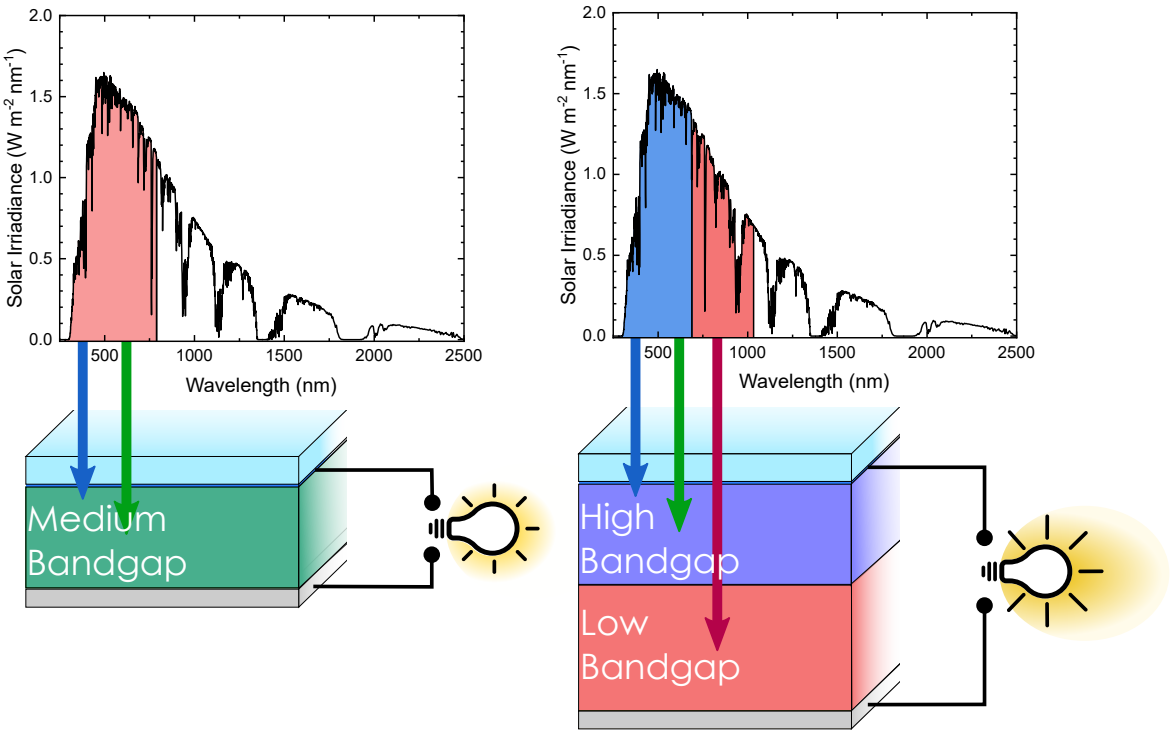


Figure 1.3: *Schematic showing the light harvested by a single junction solar cell (left), and a tandem solar cell (right). The use of tandem solar cells extends the solar spectrum absorbed, and gives more energy per absorbed photon. These factors combined enable far higher efficiencies from tandem solar cells than their single junction counterparts.*

30 % [23]. The reason for this is shown schematically in **Figure 1.3**, which shows that a tandem solar cell is able to make use of a wider proportional of the available solar energy. Moreover, for reasons discussed in detail in **Chapter 2**, one actually harvests more energy for each photon absorbed. These two factors combined result in the dramatic efficiency boost afforded by tandem solar cells. This increased efficiency means that significantly less land needs to be used or solar farms, while maintenance and the balance of systems costs remain unchanged. This dramatically drives down the cost to produce energy from solar. Tandem solar cells are not a new concept, with their roots in the 1970s, but fabricating them was prohibitively expensive since it required near perfect (epitaxial) growth conditions of suitable III-V semiconductors. Recently, a new class of semiconductors, metal halide perovskites (MHPs), has emerged with immense potential in this area. They are both suitable with the incumbent c-Si technology, but have potential to be used in a so called 'all-perovskite' tandem. The benefits of multijunction PV and metal halide perovskites is discussed in detail in the

following chapter.

1.3 Aims of this Thesis

This thesis aims to provide a comprehensive overview of the motivation behind this research and the physics underpinning the results. Earlier in this Chapter, we explored the need for sustainability, described why solar was such an attractive source of zero-carbon electricity generation and how perovskites fit into the developing picture of the solar industry.

In **Chapter 2**, I provide detailed background of the physics which underpins to results presented later in this thesis. It is intended that someone with little knowledge of band structure and PV device physics will gain sufficient knowledge to understand the experimental developments presented later in this thesis. I describe basic band theory, charge-carrier generation and recombination, the thermodynamics of solar cells, and practical limitations that reduce this efficiency. I then describe in detail the material class of metal halide perovskite (MHP) from its first use in solar cells in 2009 to the current state of the art. In particular, I provide an in-depth review of the literature describing technologically-relevant (owing to their superior stability and suitability for tandem solar cells) methylammonium-free wide bandgap (> 1.7 eV) perovskites.

Chapter 3, describes the experimental procedures used throughout the work presented within this thesis. A wide range of techniques were used, and this chapter gives enough detail that the results in the later chapters could be reproduced.

In **Chapter 4**, the development and understanding of a thermally stable passivation treatment is presented. Thermal stability, coupled with high performance, is a key requirement for perovskite solar cells. The highest efficiencies to date are delivered when the polycrystalline perovskite thin-film is 'passivated' by the addition of a new chemical treatment. These treatments are designed to overcome the limiting interfacial losses present within these devices. Regrettably, the influence of the vast majority these passivation treatments is short lived, particularly under accelerated ageing conditions.

In this chapter, I overcome this barrier by developing the use of benzylammonium bromide (BenABr) as a surface passivation treatment which enabled perovskite solar cells with power conversion efficiencies up to 19.5 %. Crucially, while the overall device stack suffered from instability, the influence of the BenABr treatment was not lost over the course of harsh (85 °C , AM1.5 illumination) ageing.

Chapter 5 describes in detail the recombination processes present within the most stable wide bandgap (> 1.7 eV) perovskite solar cells. Explicitly, this concerns the methylammonium (MA)-free perovskites fabricated in a p-i-n device architecture. The V_{OC} of devices based on these perovskites did not increase with the bandgap as you would expect, and instead plateaued at $\sim$ 1.2 V. The reason for this had been elusive, but in this chapter, I uncover the reasons for the voltage loss, descovering that the hole transport layer interface performs particularly poorly. Following this discovery, I implement an effective mitigation strategy to overcome these losses. In addition, I elucidate the next steps necessary for the field to make further advances.

Chapter 6 picks up on the developments made in the previous Chapter. In particular, I work extensively on developing a novel strategy for the hole transport layer layer for methylammonium-free wide bandgap perovskites. This strategy involves the blending of two commercially available polymers which yields outstanding enhancements compared to the control case, as predicted from the major results within **Chapter 5**. Whilst an in-depth PV device optimisation process was undertaken, this is not discussed in detail. Instead, the physics of this new hole transport layer layer is investigated in detail, along side the polymer blend / metal halide perovskite heterostructures.

Finally, concluding remarks and suggestions for areas of future work are given in **Chapter 7**.

References

[1] Blanco, G. *et al.* Drivers, Trends and Mitigation. In: Climate Change 2014: Mitigation of Climate Change. Contribution of Working Group III to the Fifth Assessment Report of the Intergovernmental Panel on Climate Change (2014).

[2] Friedlingstein, P. *et al.* Global carbon budget 2019. *Earth System Science Data* **11**, 1783–1838 (2019).

[3] Soytas, U. & Sari, R. Energy consumption and GDP: causality relationship in G-7 countries and emerging markets. *Energy Economics* **25**, 33–37 (2003).

[4] of Economic, U. N. D. & Social Affairs, U. N. World Population Prospects 2019 (2019).

[5] Bolt, J., Inklaar, R., de Jong, H. & van Zanden, J. L. Maddison Project Database, version 2018. *Rebasing 'Maddison': new income comparisons and the shape of long-run economic development* (2018).

[6] Bank, W. Poverty and shared prosperity 2018: Piecing together the poverty puzzle (2018).

[7] Global Carbon Project. Supplemental data of Global Carbon Budget 2021 (Version 1.0) (2021). URL `https://doi.org/10.18160/gcp-2021`.

[8] Jackson, R. *et al.* Gloabal Energy Growth is Outpacing Decarbozation .

[9] Victoria, M. *et al.* Solar photovoltaics is ready to power a sustainable future. *Joule* **5**, 1041–1056 (2021).

[10] Jean, J. & Brown, P. R. The climate challenge and the solar solution. In *Emerging Photovoltaic Technologies*, 2053-2563, 1–1 to 1–9 (IOP Publishing, 2020). URL `https://dx.doi.org/10.1088/978-0-7503-2152-5ch1`.

[11] Jean, J., Brown, P. R., Jaffe, R. L., Buonassisi, T. & Bulović, V. Pathways for solar photovoltaics. *Energy & Environmental Science* **8**, 1200–1219 (2015).

[12] Group, S. P. *et al.* International technology roadmap for photovoltaic (2017).

[13] Chen, Y. *et al.* From laboratory to production: learning models of efficiency and manufacturing cost of industrial crystalline silicon and thin-film photovoltaic technologies. *IEEE Journal of Photovoltaics* **8**, 1531–1538 (2018).

[14] Green, M. A. How did solar cells get so cheap? *Joule* **3**, 631–633 (2019).

[15] Siemens, W. On the electro motive action of illuminated selenium, discovered by mr. fritts, of new york. *Journal of the Franklin Institute* **119**, 453–IN6 (1885).

[16] Fraas, L. M. History of solar cell development. In *Low-cost solar electric power*, 1–12 (Springer, 2014).

[17] Chapin, D. M., Fuller, C. S. & Pearson, G. L. A new silicon p-n junction photocell for converting solar radiation into electrical power. *Journal of Applied Physics* **25**, 676–677 (1954). URL `https://doi.org/10.1063/1.1721711`. `https://doi.org/10.1063/1.1721711`.

[18] Easton, R. L. & Votaw, M. J. Vanguard i igy satellite (1958 beta). *Review of Scientific Instruments* **30**, 70–75 (1959). URL https://doi.org/10.1063/1.1716492. https://doi.org/10.1063/1.1716492.

[19] Hsu, A. How Big Oil Of The Past Helped Launch The Solar Industry Of Today (2019). URL https://www.npr.org/2019/09/30/763844598/how-big-oil-of-the-past-helped-launch-the-solar-industry-of-today?t=1655890837119.

[20] Perlin, J. Chapter 28 within 'let it shine' (2013). URL https://john-perlin.com/let-it-shine.html.

[21] Perlin, J. Chapter 24 within 'let it shine' (2013). URL https://john-perlin.com/let-it-shine.html.

[22] International Energy Agency (IEA). Technology Roadmap - Solar Photovoltaic Energy 2014, IEA, Paris (2014). URL https://www.iea.org/reports/technology-roadmap-solar-photovoltaic-energy-2014.

[23] Hirst, L. C. & Ekins-Daukes, N. J. Fundamental losses in solar cells. *Progress in Photovoltaics: Research and Applications* **19**, 286–293 (2011).

Chapter 2

Background and Theory

In this chapter, the fundamental of semiconductor physics is discussed and how this relates to photovoltaic device applications. Following this introduction to solar cells in general, the emergence of metal halide perovskites is discussed, and a short summary of notable developments is given. Finally, the developments in the sub-field of methylammonium-free wide bandgap (> 1.7 eV) metal halide perovskites are discussed in detail. This chapter is informed by 'The Oxford Solid State Basics' – Steve Simon [1], 'The Physics of Solar Cells' – Jenny Nelson [2], and 'Physics of Solar Cells: From Basic Principles to Advanced Concepts' – Peter Würfel and Uli Würfel [3].

2.1 Semiconductors

Semiconductors are the backbone for the modern world. They are the crucial element in transistors, enabling efficient computation, light-emitting diodes, lasers and solar cells to name but a few. The immense versatility and power of semiconductors comes from the remarkable property, under certain circumstances, that they can switch between being a good electrical conductor or an electrical insulator. At first glance, this property might not seem overly significant, but it has profound consequences and has enabled so much of the technological advancements the world had enjoyed over the past few decades. Indeed, it has been so revolutionary that some say we are living in the so-

called 'silicon age'. In the following, I discuss the basics of semiconductor physics, starting from a basic quantum mechanical treatment.

2.1.1 Band theory

To understand electronic devices, an in-depth understanding of band theory is required. In an atomic system, electrons can only occupy certain allowed states, or discrete *energy levels*. When two atoms are brought close together, the wavefunctions of the electrons on the individual atoms can 'spread out', or delocalise, across the two atoms. Each electron feels the influence of the others in the two atom states, and so new states form and the wavefunctions (orbitals) are said to hybridise. These hybridised states have slightly different energies, spatial distributions *etc* to the original atomic orbitals. A similar process occurs in a crystalline material, in which there are $\sim 10^{23}$ atoms per cubic centimetre and so the wavefunction of the electron can spread out over many atoms. This leads to new energy levels with a tiny difference $< 10^{-23}$ eV. This energy difference is so small that it has a negligible effect for an electron moving between one state and the next, and so these many, finely spaced orbitals form a continuum of states. This is the process whereby atomic orbitals are said to spread out to form 'bands'. A band describes the allowed states (energy and momentum) an electron can have in the solid. The shape (i.e. curvature) and location of the bands is directly informed by the constituent atoms, and crucially, has profound implications for the material properties. In the following, we will show how bands arise, and see how these inform electronic properties.

Free electrons

In free space, the energy of an electron is purely from its kinetic energy. Quantum mechanically, this means the Hamiltonian, $\hat{H}$, is given by

$$\hat{H} = \frac{\hat{p}^2}{2m_e}, \tag{2.1}$$

where m_e is the free electron mass, and $\hat{p}$ is the momentum operator given by $\hat{p} = -i\hbar\nabla$ where $\hbar$ is Planck's reduced constant [1]. In free space, the energy, E of the electron is not changing in time (in steady-state) and as such we can use the time-independent Schrödinger equation (TISE),

$$\hat{H}|\psi\rangle = E|\psi\rangle, \tag{2.2}$$

where $|\psi\rangle$ is the electron's wavefunction. We can substitute the Hamiltonian from **Equation 2.1** into the TISE to solve the electron wavefunction. In one dimension, this gives

$$-\frac{\hbar^2}{2m_e}\frac{\partial^2}{\partial x^2}\psi(x) = E\psi(x), \tag{2.3}$$

which can be easily solved to give

$$\psi(x) \propto \mathrm{e}^{-ikx}, \quad \text{where } k = \sqrt{2m_eE/\hbar^2}. \tag{2.4}$$

While this above is a simple analysis, it reveals some crucial insights on which we will build. Firstly, that free electrons, a particle, are behaving like plane waves – we have recovered wave-particle duality! Secondly, we have seen that the electron energy scales quadratically with its momentum, which we will be important later when discussing electrons in crystals. It is important that the wavefunction is normalisable (i.e. the chance of finding the electron somewhere is 1). This is achieved by including a normalisation prefactor of $1/\sqrt{L}$, which assumes our system is of size L. The normalised wavefunction is therefore given by $\psi(x) = \frac{1}{\sqrt{L}}\mathrm{e}^{-ikx}$ [1, 4].

Nearly-free electron model

Now we are interested in what happens in the presence of a small periodic potential, such as that which an electron might feel inside a crystal. To understand its effect we need to include a potential $V(\mathbf{x})$ into the Hamiltonian, which gives,

$$\hat{H} = \frac{\hat{p}^2}{2m_e} + V(\mathbf{x}). \tag{2.5}$$

Crucially, this potential is periodic, meaning that translation by any direct lattice vector $\mathbf{R}$ (a vector that takes you from one lattice point to another in the direct lattice) does not change the potential. Mathematically this is expressed as $V(\mathbf{x}+\mathbf{R}) = V(\mathbf{x})$. Since we are treating the potential as small, we can use perturbation theory to understand its influence on the electron within the crystal. Therefore we will need the Fourier components, which are given by

$$\begin{aligned} V_{k-k'} = \langle k'|V|k\rangle &= \frac{1}{L}\int \mathrm{d}x\, \mathrm{e}^{-i(k-k')x}\, V(x) \\ &= \frac{1}{L}\int \mathrm{d}x\, \mathrm{e}^{-i(k-k')x}\, V(x+R), \end{aligned}$$

where $|k\rangle$ labels the state with momentum k, we have started from free-electron wavefunctions (since we are treating the problem perturbatively), we have reduced the problem to 1 dimension to make the analysis more straightforward and in the final step we have used the periodicity of the potential. Now we can make a simple substitution of $y = x + R$, which then gives

$$V_{k-k'} = \langle k'|V|k\rangle = \frac{1}{L}\int \mathrm{d}y\, \mathrm{e}^{-i(k-k')(y-R)}\, V(y) \tag{2.6}$$

$$= \mathrm{e}^{i(k-k')R}\frac{1}{L}\int \mathrm{d}y\, \mathrm{e}^{-i(k-k')y}\, V(y), \tag{2.7}$$

$$= \mathrm{e}^{i(k-k')R}\langle k'|V|k\rangle. \tag{2.8}$$

For this equation to be true, we require $\mathrm{e}^{i(k-k')R} = 1$, which is only true if $k - k' = G$, where G is a reciprocal lattice vector (Laue condition) [1]. Therefore, the influence of the crystal potential can only scatter an electron between momentum states that are separated by a reciprocal lattice vector.

Now, we need to make use of perturbation theory to understand how this potential

has affected the energy eigenstates of the system. Remember, the unperturbed energy is given by

$$E(k) = \frac{\hbar^2 k^2}{2m_e}, \tag{2.9}$$

to which the first order shift is given by

$$\delta E^{(1)} = \langle k|V|k\rangle = \frac{1}{L}\int \mathrm{d}x V(x) = V_0.$$

This is just a constant energy shift and is the same for each eigenstate, and so is not particularly interesting. In fact, we will set this equal to 0 in the following to simplify the mathematics. We can go further to find the second order shift in energy levels using [4]

$$\delta E^{(2)} = \sum_{\substack{k'=k+G,\\ G\neq 0}} \frac{|\langle k'|V|k\rangle|^2}{E(k) - E(k')}. \tag{2.10}$$

Now, since the energies of states $E(k)$ and $E(k')$ can be extremely close, or even precisely equal, the denominator in **Equation 2.10** can go to 0 and invalidate this perturbative approach. To avoid this issue, we need to use degenerate perturbation theory, in which we ensure the numerator in **Equation 2.10** is 0 whenever the denominator is too, which removes this problem. As such, we need to 'diagonalise the degenerate subspace', which occurs when

$$E(k) = E(k') \tag{2.11}$$

$$k = k' + G. \tag{2.12}$$

Since we have $E \propto k^2$, the solution to the above equations occurs when $k = -k' = n\pi/a$ where n is an integer. This precisely describes the Brillouin zone boundaries. The subspace to diagonalise is described by

$$\langle k|\hat{H}|k\rangle = E(k) \tag{2.13}$$

$$\langle k'|\hat{H}|k'\rangle = E(k') \tag{2.14}$$

$$\langle k'|\hat{H}|k\rangle = V_{k-k'} = V_G \tag{2.15}$$

$$\langle k|\hat{H}|k'\rangle = V_{k'-k} = V_G^* \tag{2.16}$$

where we have made use of **Equations 2.8 & 2.12**, and we know that $V_{-G} = V_G^*$ because the potential $V(x)$ is real (see **Equation 2.8**).

Now, since $|k\rangle$ and $|k'\rangle = |k+G\rangle$ are linearly independent, we know that *any* state within this this degenerate subspace can be described by any linear combination of the two states, or $|\psi\rangle = \alpha|k\rangle + \beta|k+G\rangle$ with $|\alpha|^2 + |\beta|^2 = 1$ to ensure the state is normalised correctly. Now the system of equations we need to solve is

$$\begin{pmatrix} E(k) & V_G^* \\ V_G & E(k+G) \end{pmatrix} \begin{pmatrix} \alpha \\ \beta \end{pmatrix} = \varepsilon \begin{pmatrix} \alpha \\ \beta \end{pmatrix} \tag{2.17}$$

where ε is the perturbed energy state. This system of equations has non-trivial solutions when the determinant of the matrix is zero, which gives the secular equation

$$(E(k) - \varepsilon)\,(E(k+G) - \varepsilon) - |V_G|^2 = 0. \tag{2.18}$$

Precisely on the Brillouin zone boundary, we have $E(k) = E(k+G)$ (**Equation 2.11**). This then simplifies to

$$\boxed{\varepsilon_\pm = E(k) \pm |V_G|}. \tag{2.19}$$

Equation 2.19 reveals some really powerful physics: the presence of a periodic potential has caused a gap between allowed energy states of $2|V_G|$ at the Brillouin zone boundary! This very simple model of a weak perturbation by a potential is sufficient to give rise to a *bandgap* (a region with no available states), which has profound impli-

cations which we explore later in this thesis. In fact, it is the presence of this bandgap that enables the immense technological developments discussed briefly earlier in this thesis. In this model, we can understand how this gap arises. For the higher energy band, the wavefunction has its maxima (i.e. highest probability of finding an electron in this region) at the position of maximum potential. This raises the energy compared to the case with no potential. The lower energy branch has its maxima between the periodic potential and so has a lower energy.

Bloch's Theorem

However, in real crystals, the interaction between the electrons in the bands and the atoms giving rise to the periodic potential may not always be considered as weak, and so this perturbation approach should not, at first glance, be valid (certainly only going to second-order perturbation is extremely unlikely to be sufficient).

One important property about electrons in crystals to stress is that 'plane wave momentum' of electrons is not a conserved quantity, and instead the 'crystal momentum' is. The crystal momentum is only known up to a factor of G, i.e. electron with momentum $\hbar k$ and $\hbar(k+G)$ are physically identical. This arises from Noether's theorem [5]: in the crystal, we no longer have arbitrary translational symmetry (as in free-space), but instead the translation symmetry has the periodicity of the unit cell. Therefore the conserved quantity (momentum) associated with this symmetry also has the periodicity of the unit cell. This is true regardless of the strength of the periodic potential.

Bloch's theorem states that for each electron in a system, there is a basis of wavefunctions such that

- each of these wavefunctions is an eigenstate, and
- each of these wavefunctions can be written as $\Psi(r) = \mathrm{e}^{ikr}u_k(r)$, where k is the crystal momentum, and u_k is a function with the same periodicity as the unit cell. u_k is called the 'Bloch function' and Ψ the 'modified plane wave'.

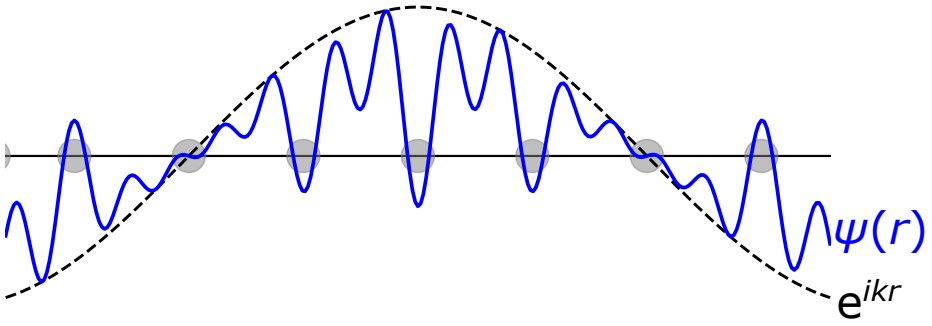


Figure 2.1: *Schematic of a modified plane wave from Bloch's theorem in one dimension. The grey circles are the atomic positions, the black dashed line is the (real part) of the plane wave, and the blue line shows the modified plane wave* $\Psi(r) = e^{ikr}u_k(r)$ *from Bloch's theorem.*

The power of Bloch's theorem is that it tells us that even if the potential that the electron experiences from each atom is large (and it is likely to be!), the electrons still behave almost as if they do not see the atoms at all! They still almost form plane wave eigenstates, with the only modification being the periodic Bloch function u_k and the fact that momentum is now crystal momentum [1]. This is what justifies a lot of our future analysis pertaining to plane-like waves for electrons moving through crystals.

2.1.2 Semiconductor under illumination

We have seen how bands can arise in a semiconducting material, and in their most basic form they describe the allowed states (energy, momentum combinations) that an electron can have in a system. However, the bands have a profound effect on the resulting electronic properties of the material. The distribution and occupation of the bands in a material determine whether a material is an insulator, semiconductor, semimetal, or metal and the curvature of the bands describes how easily electrons can move, quantified through the effective mass, m^*. We explore these properties below.

In the following, we are going to assume parabolic bands, and a 3D material. Further, we are going to consider the valence and conduction bands only. This is justified since, in all cases investigated in this thesis, all bands below the conduction band will be fully occupied (these are called 'core levels'), and so electrons are not free to travel within these bands. Any band above the conduction band is assumed to be entirely

empty since, for the materials investigated in this thesis, there are few photons within the solar spectrum that have sufficient energy to promote an electron from the valence band to any other band than the conduction band. Moreover, any electrons generated in a higher band than the conduction band are likely to rapidly relax back to the conduction band minimum. However, even this simplified picture yields deep and rich physics. Furthermore, when an electron is promoted from the valence band into the conduction band it leaves behind a 'hole', an abstraction, or quasi-particle, which possesses the same energy and momentum as electron in the same location in the valence band, but has positive charge. In semiconductor physics, it is often much more convenient to consider holes as fully fledged charge-carriers rather than tracking the unpromoted electrons left in the valence band. I will adopt this approach throughout this thesis.

An extremely important property of a semiconductor – especially for solar applications – is its bandgap, E_{g}, defined as the difference between the maximum energy of the valence band (ε_{v}), and the minimum energy of the conduction band (ε_{c}), expressed mathematically as

$$E_{\mathrm{g}} = \varepsilon_{\mathrm{c}} - \varepsilon_{\mathrm{v}}. \tag{2.20}$$

Next, it is important to determine the occupation of bands at a given absolute temperature T. Several factors are important during this derivation, including the chemical potential μ (sometimes called the 'Fermi level' in the context of semiconductors), which describes how much energy is required to add/remove an electron to/from the system and the density of states within the conduction and valence bands. In the following, we will use an effective mass for holes m_{h}^* in the valence band and electrons m_{e}^* in the conduction band. Since we have assumed that the bands are parabolic, the effective mass is a constant in each of the bands. However, it is worth noting that this is not true in reality and the effective mass is a function of k (i.e. where in the band an electron is), and can be anisotropic. More fully the effective mass for electrons would be a tensor whose ij^{th} component is given by $\hbar^2 \left[\left(m_{\mathrm{e}}^*\right)^{-1}\right]_{ij} = \partial^2 E/\partial k_i \partial k_j$ [1].

The density of states per unit volume as a function of energy in the conduction and valence bands are given by, respectively [1],

$$g_{\mathrm{c}}(E > \varepsilon_{\mathrm{c}}) = \frac{(2m_{\mathrm{e}}^*)^{3/2}}{2\pi^2\hbar^3}\sqrt{E - \varepsilon_{\mathrm{c}}} \tag{2.21}$$

$$g_{\mathrm{v}}(E < \varepsilon_{\mathrm{v}}) = \frac{(2m_{\mathrm{h}}^*)^{3/2}}{2\pi^2\hbar^3}\sqrt{\varepsilon_{\mathrm{v}} - E}. \tag{2.22}$$

It is in these expressions that we have assumed that the bands are parabolic (i.e. $E \propto k^2$). Given electrons are fermions, they 'stack up' following the Fermi occupation factor (n_{F}) to occupy a band, since they are subject to the Pauli expulsion principle. However, this is only relevant for extremely low temperatures, and for the most part Boltzmann statistics suffice. Quantitatively, this is the statement that

$$n_{\mathrm{F}}(E, \mu, T) = \frac{1}{\mathrm{e}^{\beta(E-\mu)} + 1} \approx \mathrm{e}^{-\beta(E-\mu)}, \tag{2.23}$$

where $\beta = 1/k_{\mathrm{B}}T$. The approximation within **Equation 2.23** holds for $\beta(E-\mu) \gg 1$, or for temperatures that are sufficiently low so there are only few electrons in the conduction band. We can now work out the density of electrons in the conduction band ($n(T)$) and holes in the valence band ($p(T)$) according to

$$n(T) = \int_{\varepsilon_{\mathrm{c}}}^{\infty} n_{\mathrm{F}}(E, \mu, T)\, g_{\mathrm{c}}(E)\, \mathrm{d}E, \tag{2.24}$$

$$p(T) = \int_{-\infty}^{\varepsilon_{\mathrm{v}}} [1 - n_{\mathrm{F}}(E, \mu, T)]\, g_{\mathrm{v}}(E)\, \mathrm{d}E, \tag{2.25}$$

The one minus the Fermi occupation factor in **Equation 2.25** (factor in square brackets) originates from the probability a state is occupied by a hole is in fact the probability it is *not* occupied by an electron. In the following, I will continue with **Equation 2.24**, but a perfectly analogous analysis is possible for the case with holes. Next, we will utilise the approximation in **Equation 2.23**, and assume a fixed chemical potential, yielding

$$n(T) = \int_{\varepsilon_c}^{\infty} \mathrm{e}^{-\beta(E-\mu)}\, g_c(E)\, \mathrm{d}E = \frac{(2m_e^*)^{3/2}}{2\pi^2\hbar^3} \int_{\varepsilon_c}^{\infty} \mathrm{e}^{-\beta(E-\mu)} \sqrt{E-\varepsilon_c}\mathrm{d}E. \tag{2.26}$$

Next, we can make a substitution $\xi = E - \varepsilon_c$, so we arrive at

$$n(T) = \frac{(2m_e^*)^{3/2}}{2\pi^2\hbar^3}\, \mathrm{e}^{-\beta(\varepsilon_c-\mu)} \int_0^{\infty} \mathrm{e}^{-\beta\xi} \sqrt{\xi}\, \mathrm{d}\xi. \tag{2.27}$$

The integral in this equation can be readily evaluated, giving $\frac{1}{2}\beta^{-3/2}\sqrt{\pi}$. With this, we are now in a position to calculate the density of electrons in the conduction band

$$n(T) = \frac{1}{4}\left(\frac{2m_e^* k_B T}{\pi\hbar^2}\right)^{3/2} \mathrm{e}^{-\beta(\varepsilon_c-\mu)}, \tag{2.28}$$

and the analogous expression for holes in the valence band is

$$p(T) = \frac{1}{4}\left(\frac{2m_h^* k_B T}{\pi\hbar^2}\right)^{3/2} \mathrm{e}^{\beta(\varepsilon_v-\mu)}. \tag{2.29}$$

The prefactors in these equations are often written as N_c and N_v respectively to denote the so called 'effective density of states' in the conduction and valence bands. Things to notice are, firstly that N_c and N_v vary relatively slowly with temperature, whereas the populations n or p have an exponential dependence on temperature, which strongly impacts solar cell performance, as will be discussed later. Secondly, the effective density of states encoded within N_c and N_v is determined from the effective mass of charge carriers within that band. The effective mass is determined from the curvature of the bands, and so the shape of the bands directly informs the density of states, and so number of carriers within a band and the physics of the system as a whole.

A critical parameter in semiconductor physics is the 'np product' which is constant regardless of doping density, which is also called the Law of Mass Action. This is given by

$$n_i^2 = n(T)p(T) = N_c N_v\, \mathrm{e}^{-\beta E_g} \tag{2.30}$$

where n_i is the intrinsic carrier-density and is related solely to the effective density of states in the valence and conduction bands, the bandgap of the material and the temperature.

For the special case of an intrinsic (undoped) semiconductor, we have that each electron in the conduction band 'left behind' a hole in the valence band, so $n(T) = p(T)$, which means that

$$n(T) = \sqrt{n(T)p(T)} = \sqrt{N_\mathrm{c}N_\mathrm{v}}\mathrm{e}^{-\beta E_\mathrm{g}/2}, \tag{2.31}$$

or equivalently

$$1 = \frac{n(T)}{p(T)} = \left(\frac{m_\mathrm{e}^*}{m_\mathrm{h}^*}\right)^{3/2} \mathrm{e}^{-\beta(\varepsilon_\mathrm{c}+\varepsilon_\mathrm{v}-2\mu)}. \tag{2.32}$$

This allows us calculate the chemical potential of an intrinsic semiconductor as a function of temperature as

$$\mu(T) = \frac{1}{2}(\varepsilon_\mathrm{c} + \varepsilon_\mathrm{v}) + \frac{3}{4}(k_\mathrm{B}T)\ln\left(\frac{m_\mathrm{h}^*}{m_\mathrm{e}^*}\right), \tag{2.33}$$

which is typically very close to the middle of the bandgap. Doping the semiconductor with electrons shifts the chemical potential nearer the conduction band, and similarly doping with holes shifts the chemical potential nearer the valence band. This effect is shown schematically in **Figure 2.2**.

With this knowledge, we can understand how a semiconductor behaves under illumination. So far all of our analysis has concerned a semiconductor in thermal equilibrium and in the dark. It is important for photovoltaic applications to consider the case of a system out of equilibrium. This is because the basic premise of a solar cell is to convert solar energy into electrochemical energy (i.e. electrons in an excited state) which is then harvested. Detailed discussion concerning absorption and charge carrier recombination processes are not required in the following, but more detail is given in **Section 2.1.3**.

When a photon is absorbed promoting an electron to the conduction band, the

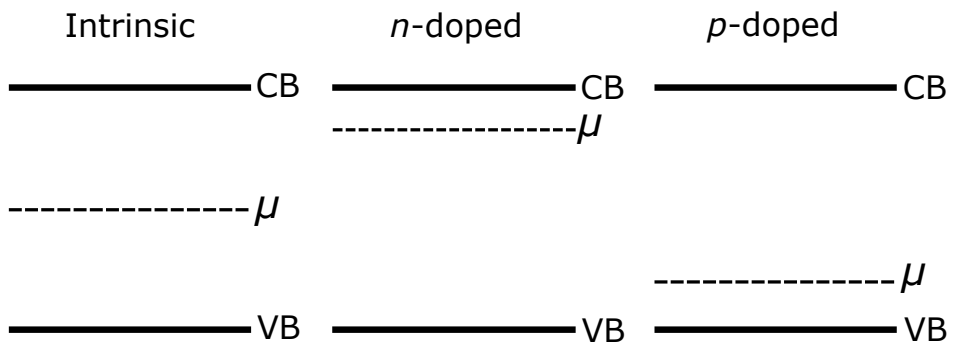


Figure 2.2: *Schematic showing the effect of doping on the chemical potential (Fermi level) position, μ. The solid lines donate the location of the conduction band (CB) minimum and valence band (VB) maximum. For an undoped, intrinsic, semiconductor the chemical potential lies very close to mid-bandgap according to* ***Equation 2.33*** *(left panel). Doping with electron donors results in n-doping and the chemical potential is shifted towards the conduction band (middle panel). Similarly, doping with electron acceptors results in p-doping and the chemical potential is shifted towards the valence band (right panel).*

free energy of this electron has been raised. We will assume that the electrons in the conduction band and holes in the valence band form a quasi-thermal equilibrium, but each with a different chemical potential or quasi-Fermi level. The increase in the electrochemical potential of such a system is given simply by the Gibbs free energy, $N\Delta\mu$, where N is the number of electrons promoted and $\Delta\mu$ is the difference in chemical potential for holes in the valence band and electrons in the conduction band. $\Delta\mu$, which is zero at equilibrium as per our previous analysis, is often called the quasi-Fermi level splitting (QFLS), which is the terminology I will use for the rest of this thesis.

In more detail, under above-bandgap illumination, the population of electrons in the conduction band is higher than in the dark. As discussed later in **Section 2.1.3**, this population will be in a (quasi)thermal equilibrium near the band edge, but about a new chemical potential, or quasi-Fermi level. This quasi-Fermi level for electrons in the conduction band ($E_{\mathrm{F_n}}$), will be closer to the conduction band than the chemical potential in equilibrium. In much the same way, the populations of holes in the valence band will be increased, and this population will also be in a quasi thermal equilibrium near the valence band edge with a new chemical potential. This is the quasi-Fermi level for holes in the valence band ($E_{\mathrm{F_p}}$), and will be closer to the valence band edge compared with the chemical potential in equilibrium. Mathematically, we can express

the populations of excited electrons in the conduction band ($n_{\mathrm{exc}}(T)$) as

$$n_{\mathrm{exc}}(T) = N_{\mathrm{c}}\, \mathrm{e}^{-\beta(\varepsilon_{\mathrm{c}} - E_{\mathrm{F_n}})}, \tag{2.34}$$

and excited holes in the valence band ($p_{\mathrm{exc}}(T)$) as

$$p_{\mathrm{exc}}(T) = N_{\mathrm{v}}\, \mathrm{e}^{-\beta(E_{\mathrm{F_p}} - \varepsilon_{\mathrm{v}})}. \tag{2.35}$$

The product of the excited electron and hole populations is

$$n_{\mathrm{exc}} p_{\mathrm{exc}} = N_{\mathrm{c}} N_{\mathrm{v}}\, \mathrm{e}^{-\beta(\varepsilon_{\mathrm{c}} - \varepsilon_{\mathrm{v}})}\, \mathrm{e}^{\beta(E_{\mathrm{F_n}} - E_{\mathrm{F_p}})} = n_i^2\, \mathrm{e}^{(E_{\mathrm{F_n}} - E_{\mathrm{F_p}})/k_{\mathrm{B}}T}. \tag{2.36}$$

The quantity $E_{\mathrm{F_n}} - E_{\mathrm{F_p}}$ is precisely the QFLS. Its importance arises since it is directly related to the population of free carriers within the semiconductor and the electrochemical potential energy that these carriers possess. By rearranging **Equation 2.36**, we can see how the QFLS is related to the charge carrier population within the semiconductor as

$$QFLS = E_{\mathrm{F_n}} - E_{\mathrm{F_p}} = k_{\mathrm{B}}T \ln\left(\frac{n_{\mathrm{exc}} p_{\mathrm{exc}}}{n_i^2}\right) = k_{\mathrm{B}}T \ln\left(\frac{n^2}{n_i^2}\right), \tag{2.37}$$

where in the last step we have set $n_{\mathrm{exc}} = p_{\mathrm{exc}} = n$, which is valid for high level injection and low doping density.

2.1.3 Charge-carrier recombination

Understanding recombination of charge carriers in semiconductors is vital since recombination underpins the working principles of many (opto)electronic devices. For example, the charge carrier lifetime describes the time in which a carrier must be extracted in a solar cell before a competing recombination process occurs and the excitation is lost. In this Section, I will focus on how charge-carrier recombination affects solar cell operation. This Section is inspired by Refs. [1, 2, 6, 7].

Absorption can occur when an above bandgap photon is incident on a semiconduc-

tor. The absorption coefficient, $\alpha(\lambda)$, determines how likely a photon of wavelength λ is to be absorbed within a certain depth. As stated earlier, but repeated here for completeness: the absorption of an above bandgap photon promotes an electron from the valence band into the conduction band. This leaves behind a 'hole', an abstraction, or quasi-particle, which possesses the same energy and momentum an electron in same location in the valence band, but has positive charge. In semiconductor physics, it is often much more convenient to consider holes as fully fledged charge-carriers rather than tracking the un-promoted electrons left in the valence band. I will adopt this approach throughput this thesis. Several processes can occur following absorption we I discuss briefly below.

Excitons

If the Coulombic attraction between the electron and the positively charge hole is sufficiently large, an exciton could form. An exciton is a quasi-particle that can transport energy, but no net-charge. Forming an exciton is a stabilising process in that it requires slightly less energy to form an exciton than it does to generate free electrons and holes. The electron-hole pair in an exciton have a hydrogen-like wavefunction, but modulated for the electron and hole effective masses, $m_{\mathrm{e}}^*, m_{\mathrm{h}}^*$ respectively, and the electrostatic screening within the semiconductor, characterised by the relative dielectric permittivity, ϵ_{r}. The exciton binding energy is given by

$$E_{\mathrm{X}} = Ry \times \frac{\mu'}{m_{\mathrm{e}}} \times \frac{1}{\epsilon_{\mathrm{r}}^2}, \tag{2.38}$$

where $Ry = 13.6$ eV is the Rydberg energy, $\mu' = m_{\mathrm{e}}^* m_{\mathrm{h}}^* / (m_{\mathrm{e}}^* + m_{\mathrm{h}}^*)$ is the reduced mass of the electron-hole pair (the prime is to be distinct from the mobility), and m_{e} is the free electron mass. The radius of the exciton is given by

$$a_{\mathrm{X}} = a_{\mathrm{B}} \times \frac{m_{\mathrm{e}}}{\mu'} \times \epsilon_{\mathrm{r}} \tag{2.39}$$

where $a_{\mathrm{B}} = 0.529$ nm is the Bohr radius. Since most MHPs possess relatively high

dielectric permittivity and low effective masses, by considering **Equations 2.38 & 2.39** we can conclude that there will be low exciton binding energies and the exciton radius is large. Critically, the exciton binding energy is below the thermal energy at room temperature (and well below normal operating temperatures for solar cells). As such, electron-hole pairs quickly dissociate into free carriers and the role of excitons is minimal in most of these materials at one sun carrier-densities [6–8]. I note that this is not the case for all MHP semiconductors, i.e. 2D or nanocrystalline perovskites [8]. However, these classes of MHP semiconductors are not the focus of this thesis and so are not discussed in more detail.

Thermalisation

Thermalisation is a process wherein the an excited electron in the conduction band (or hole in valence band) rapidly relaxes to the band edge. During this relaxation process, the electron (or hole) loses energy by generating one or more phonons – quasiparticles of crystal vibration that carry energy and momentum. The emission of phonons is equivalent to heating a system, hence the term 'thermalisation'. Strictly speaking, thermalisation is the process of reaching thermal equalibirum, and so can include cooling processes as well. This process is extremely rapid (fs time scale), and hence carriers typically lose their excess energy due to thermalisation before other processes occur. Indeed, these so-called thermalisation losses are a major consideration in the thermodynamic, detailed balance upper limit for the efficiency of a solar cell, as discussed in **Section 2.2.2**.

Following thermalisation, there will be a population of free charge carriers near the band edge. This concentration of excess free carriers, $n(t)$, will recombine through different competing mechanisms. Some of these recombination pathways are avoidable, e.g. trap-mediated due to imperfect materials, and others are unavoidable including Auger and radiative recombination [2]. For the special case of MHPs, the recombination of the excess charge carrier density can be accurately described by the volumetric rate equation [6, 7, 9, 10]

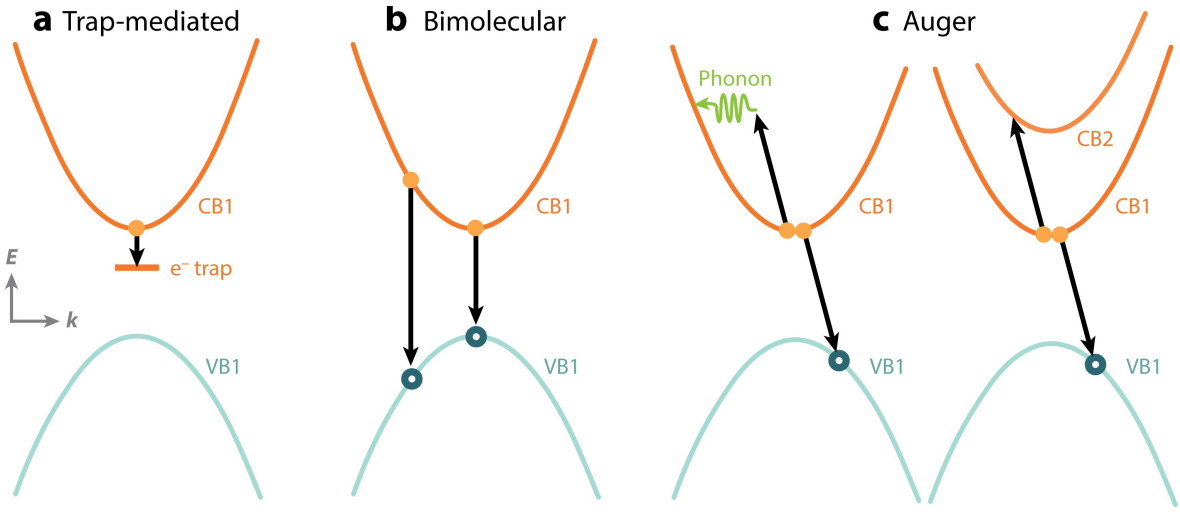


Figure 2.3: *Schematic describing charge-carrier recombination processes within a semiconductor. (a) Schematic of the trap-mediated recombination process depicting an electron-trapping process. This process only involves a single carrier, and a 'trap', explaining the dependence on n only. Once captured, the electron will either be de-trapped (perhaps by thermal effects), or will return to the valence band (where it annihilates a hole) by emitting a series of phonons. I note detrapping is not included in the simplified rate equation used here which assumes trapped carriers recombine instantly. (b) Bimolecular recombination is a radiative process in which an electron from the conduction band recombines with a hole in the valence band – hence the n^2 dependence. This excess energy is emitted as a photon, explaining why this is often called 'radiative recombination'. (c) Auger recombination is a 'many body' process and is nonradiative (a loss process). Auger recombination involves either two electrons and a hole (as shown) or two holes and an electron, and so depends on n^3. In this process, an electron recombines with a hole in the valence band, but the energy is transferred to a third charge-carrier instead of being emitted as a photon. This third carrier can be promoted into a higher band (right), or interact with a phonon to transfer momentum. Figure taken from [6] with permission.*

$$\frac{\mathrm{d}n}{\mathrm{d}t} = -k_1 n - k_2 n^2 - k_3 n^3, \tag{2.40}$$

where k_1 is the monomolecular, trap-mediated recombination rate, k_2 is the radiative, bimolecular band-to-band recombination rate, and k_3 is the Auger recombination rate. In this equation, we have assumed that there is an equal population of electrons and holes ($n_\mathrm{e} = n_\mathrm{h} = n$), which is valid for an undoped semiconductor with a low thermal population of carriers compared to photogenerated carriers, and we have neglected excitons as justified earlier. Later in this Section, derivations and more detailed discussion is provided to justify the form of **Equation 2.40**. These three processes together

all contribute to a total recombination rate $R(n(t))$ which is described by

$$R(n) = k_1 + k_2 n + k_3 n^2. \tag{2.41}$$

This recombination rate describes how long an excited charge-carrier persists in a semiconductor. In **Figure 2.4**, the separate contributions to the recombination rate are plotted. At low charge-carrier densities ($n < k_2/k_1$), monomolecular recombination (shown in blue) dominates. In this regime, $R \approx k_1$ for a wide range of charge carrier densities and most recombination is trap-assisted (which is most likely non-radiative). At intermediate charge carrier densities ($k_2/k_1 < n < k_3/k_2$), most recombination is bimolecular, and the Auger recombination becomes dominate at high charge carrier densities.

The recombination rate and the charge carrier mobility, μ_{mob}, will determine how far a charge-carrier can diffuse on average. This is called the diffusion length (L_{D}), and can be estimated as

$$L_{\text{D}} = \sqrt{\frac{\mu_{\text{mob}} k_{\text{B}} T}{R(n) e}}, \tag{2.42}$$

with e being the charge of an electron [6, 9, 10]. Increasing the charge carrier diffusion length is a key strategy to improved solar cell performance since charges become more likely to reach the correct electrode and so can be extracted as current.

In solar cells under typical working conditions, i.e. under AM1.5 illumination (discussed in **Section 2.2.2**), the charge carrier densities within the semiconductor are of the order $10^{15} - 10^{16}$ cm^{-3} [6, 7]. In such a regime, for most MHPs, we have $k_1 \gg k_2 n, k_3 n^2$, and as such k_1 is the dominant contributor the recombination rate in **Equation 2.41**, as can be seen in **Figure 2.4**. Therefore, minimising k_1, or more precisely the severity of trap-mediated recombination, is critical to enhance optoelectronic properties and solar cell device performance [2, 3].

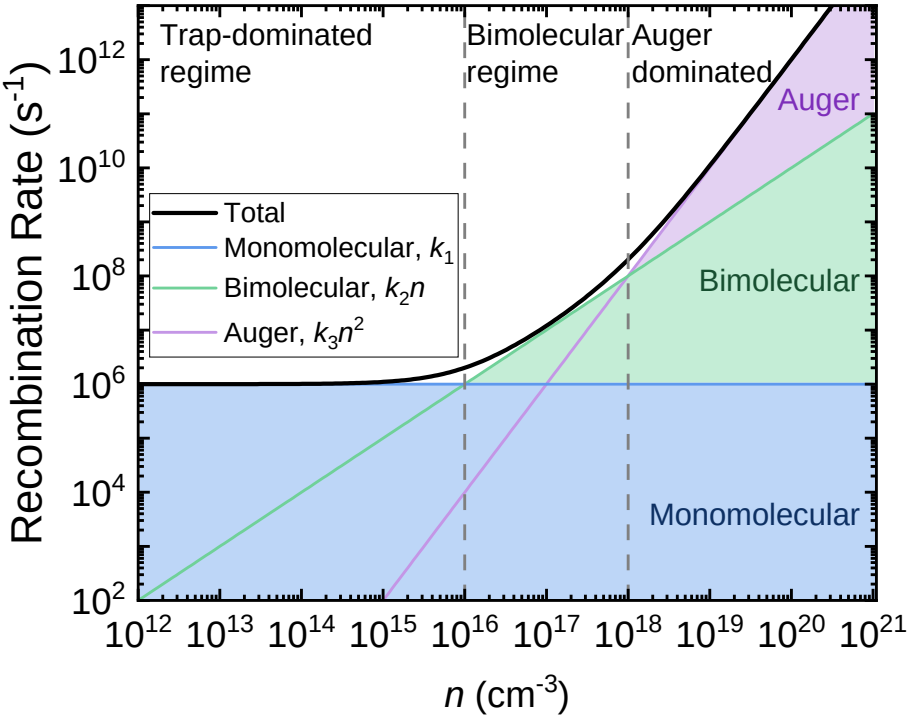


Figure 2.4: *Recombination rate, $R(n)$ (**equation 2.41**), of free carriers in a semiconductor as a function of charge carrier density, n. The monomolecular (blue), bimolecular (green) and Auger (purple) contributions have been plotted separately and their sum is plotted in black. At low charge carrier densities ($n < k_2/k_1$), trap-mediated (monomolecular) recombination dominates and $R(n) \approx k_1$. At intermediate charge carrier densities ($k_2/k_1 < n < k_3/k_2$), most recombination is bimolecular, and the Auger recombination becomes dominant at high charge carrier densities. $k_1 = 10^6\ s^{-1}$, $k_2 = 10^{-10}\ cm^3 s^{-1}$, $k_3 = 10^{-28}\ cm^6 s^{-1}$ were used as inputs as they are typical for MHP semiconductors [7].*

Recombination via a trap state[1]

A schematic of a trap-assisted process is shown schematically in **Figure 2.3a**. The nomenclature of 'trap' arises since the previously delocalised conduction band electron or valence band hole are captured by a spatially localised defect. The terminology 'monomolecular' and trap-assisted recombination are largely used interchangeably in the field of MHP semiconductors, but this is not strictly accurate, since trap-mediated recombination always an electron and a hole as we will see later in this section. The nomenclature 'monomolecular' really refers to the process being linear in n which can

[1]This is often called the 'Shockley Read Hall' recombination. However, due to Shockley being a well-documented racist and eugenicist [11, 12], I refuse to associate his name with the physics throughout this thesis, and I encourage anyone reading this to do likewise, as is becoming more commonplace in the field [12]. I will use alternative names for any formulae, or similar, named after him throughout this work.

be the case for trap-assisted recombination as will be demonstrated later in this section. The rate of trap-assisted recombination, k_1, is determined by the density, depth, distribution, and capture cross-section of traps within the semiconductor. These traps are assumed to be related to defects (vacancies, interstitials, impurities etc.) within the perovskite structure [13]. This trap-assisted recombination is *non-radiative*, so-called since it does not involve the emission of a photon. Non-radiative recombination is they key limiting factor limiting the efficiency obtained from perovskite solar cells. Encouragingly, k_1 is a largely extrinsic property since factors such as processing route and handling can influence, for example, the density of defects and hence trap states. The trap-mediated recombination rate can be further reduced by a process known as passivation, wherein an additional chemical treatment is applied to mitigate the influence of traps on the perovskite [14]. Passivation will be discussed in detail later in this thesis, especially in **Chapter 4**.

The presence of traps has a strong effect on the quasi-Fermi level splitting (QFLS) within a semiconductor. If there are rapid non-radiative decay channels, the population of excited electrons n_{exc} and holes p_{exc} will be depleted compared to the case with few defects. By examining **Equation 2.37**, we can see that this means a system with a lower $n_{\text{exc}}p_{\text{exc}}$ product can maintain a lower QFLS compared to a system with relatively few defects. This is shown schematically in **Figure 2.5**.

Derivation of trap-mediated recombination rate In the following, I will follow the derivation provided within '*The Physics of Solar Cells: from basic principles to advanced concepts*' by Würfel and Würfel [3], as well as inspiration from '*The Physics of Solar Cells*' by Nelson [2].

As alluded to earlier, trap-assisted recombination is extremely important in semiconductors in general, and is often the most important energy-loss process in PV devices and therefore will be discussed in detail. These 'traps' are states within the bandgap of the semiconductor in which an electron and/or hole can become localised. This localisation is what gives rise to the trapping nomenclature as briefly mentioned ear-

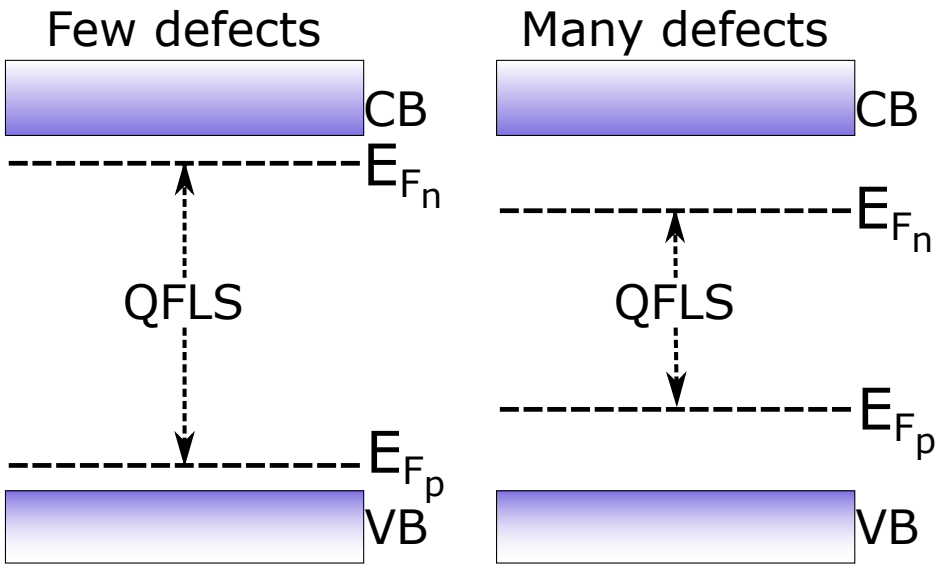


Figure 2.5: *In a semiconductor with many defects, the population of excited electrons (n_{exc}) and holes (p_{exc}) will be depleted compared to the case with few defects. By examining* ***Equation 2.37****, we can see that this means a system with a lower $n_{exc}p_{exc}$ product can maintain a lower QFLS compared to a system with relatively few defects.*

lier. Once a charge-carrier has been localised in one of the states, two major processes can occur. Firstly, the carrier can become 'detrapped', the energy often provided by thermal activation, and returns to the band whence it came. The excitation can be lost if not de-trapped rapidly enough. For example, a trapped electron could return to the valence band by emitting one or more phonons, where it would recombine with a hole. Alternatively, the carrier of the opposite polarity could become localised on the same site, and the electron and hole recombine in this *trap-assisted* manner. The first kind of state often forms near (or even within) the bands, which means thermal energy is sufficient depopulate the traps, and the capture cross section is higher for one carrier than the other. For the second case, these localised states would tend to be deeper in the bandgap, which means that once a carrier has been localised there, it is unlikely to be released. In these states, the capture cross section for electrons and holes tends to be more similar. Sometimes a distinction is drawn between these two kinds of localised states. The first, which supports the trapping and release of one carrier-type is often called a trap. The other, which captures both types of carrier, are called recombination centres. However, in the field of MHP semiconductors, the distinction is rarely made.

In the following analysis, we are considering a device at open-circuit conditions

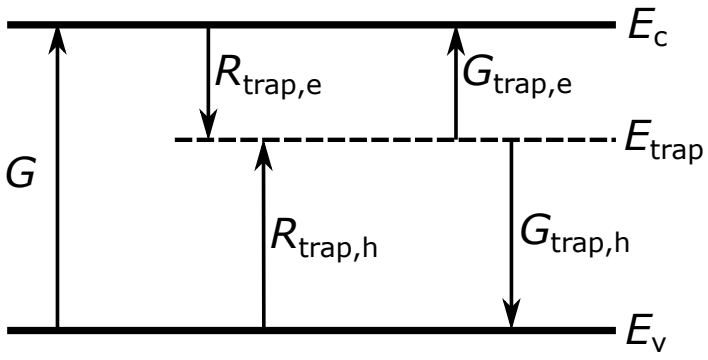


Figure 2.6: *Schematic showing that free electrons and holes are generated at a rate G. These charge-carriers are captured by traps with the rates $R_{\mathrm{trap,e}}$ and $R_{\mathrm{trap,h}}$ respectively. Due to thermal energy, the traps can empty by emitting electrons in to the conduction band at rate $G_{\mathrm{trap,e}}$ and holes into the valence band at rate $G_{\mathrm{trap,h}}$.*

so no current flows and all excited carriers must eventually recombine. Since charge-carrier recombination via a trap state is often the dominant process in PV devices, in the following radiative recombination and Auger recombination are neglected, and only the (volumetric) rates shown in **Figure 2.6** are considered. We will consider a density n_{trap} of trap state with energy E_{trap} that lies within the bandgap. This state has a capture cross-section for electrons and holes of σ_{e} and σ_{h} respectively. Electrons and holes are generated at a rate G, and electrons and holes are captured by the trap state at rates $R_{\mathrm{trap,e}}$ and $R_{\mathrm{trap,h}}$ respectively. Due to thermal energy, the traps can empty by emitting electrons in to the conduction band at rate $G_{\mathrm{trap,e}}$ and holes into the valence band at rate $G_{\mathrm{trap,h}}$. These are volumetric rates and take into account the concentration of carriers in the bands or trap state. Therefore, we can write down the rate of change of the charge-carrier density of electrons in the conduction band (n), holes in the VB (p) and electrons on the trap state ($n_{\mathrm{trap,e}}$) as

$$\frac{\partial n}{\partial t} = G - R_{\mathrm{trap,e}} + G_{\mathrm{trap,e}}, \tag{2.43}$$

$$\frac{\partial p}{\partial t} = G - R_{\mathrm{trap,p}} + G_{\mathrm{trap,p}}, \tag{2.44}$$

$$\frac{\partial n_{\mathrm{trap,e}}}{\partial t} = R_{\mathrm{trap,e}} - R_{\mathrm{trap,p}} - G_{\mathrm{trap,e}} + G_{\mathrm{trap,p}}. \tag{2.45}$$

Unfortunately, these three equations are not sufficient to uniquely define the three

unknowns n, p and $n_{\text{trap,e}}$ since they are not linearly independent. The final condition we need is from charge-neutrality, i.e. while the concentrations may be changing, overall the charge in the semiconductor must not be.

We can get additional information about the rates from kinetic arguments. Firstly, we can write an expression for the rate at which conduction band electrons are captured by the trap state. The average thermal velocity of the electrons in the conduction band is $v_{\text{th,e}}$. Whenever such an electron comes within a capture cross section of an empty trap, σ_{e}, it will be captured. Traps may not become 'doubly charged' by capturing more than one charge carrier in this analysis. The justification for this is that energy for the second electron state in the trap is likely to be much higher. We can consider a trap not occupied by an electron as being occupied by a hole. Therefore, we can write the electron capture rate as

$$R_{\text{trap,e}} = v_{\text{th,e}}\, \sigma_{\text{e}}\, n\, n_{\text{trap,h}}, \tag{2.46}$$

where $n_{\text{trap,h}} = n_{\text{trap}} - n_{\text{trap,e}}$ is the density of traps occupied by holes. An analogous argument gives the recombination rate for holes as

$$R_{\text{trap,h}} = v_{\text{th,h}}\, \sigma_{\text{h}}\, p\, n_{\text{trap,e}}. \tag{2.47}$$

By way of an aside, a particular trap state unlikely to have the same capture cross sections for electrons and holes. For example, an unoccupied donor-type impurity is positively charged and consequently has a large capture cross section for electrons and small capture cross section for holes.

The emission rate of electrons from the trap state of back into the conduction band must depends on the density of electrons in the trap state, or

$$G_{\text{trap,e}} = \beta_{\text{e}}\, n_{\text{trap,e}}, \tag{2.48}$$

and similarly for holes with

$$G_{\mathrm{trap,h}} = \beta_{\mathrm{h}}\, n_{\mathrm{trap,h}} = \beta_{\mathrm{h}}(n_{\mathrm{trap}} - n_{\mathrm{trap,e}}), \tag{2.49}$$

where β_{e} and β_{h} are coefficients that determine the rate of emission that will be determined. We can calculate them by considering the occupation of trap states in the dark (i.e. $G = 0$) and using the principle of detailed balance. We use **Equations 2.43, 2.46 & 2.48** in steady-state which gives

$$\frac{\partial n}{\partial t} = 0 = -v_{\mathrm{th,e}}\, \sigma_{\mathrm{e}}\, n\, (n_{\mathrm{trap}} - n_{\mathrm{trap,e}}) + \beta_{\mathrm{e}}\, n_{\mathrm{trap,e}}, \tag{2.50}$$

from which we can calculate $n_{\mathrm{trap,e}}$. Since the system is in equilibrium in this state, we know that the occupation of traps must be described by a Fermi-Dirac distribution. Together, we arrive at

$$n_{\mathrm{trap,e}} = n_{\mathrm{trap}} \frac{1}{1 + \beta_{\mathrm{e}}/v_{\mathrm{th,e}}\, \sigma_{\mathrm{e}}\, n} = n_{\mathrm{trap}} \frac{1}{\mathrm{e}^{(E_{\mathrm{trap}} - \mu)/k_{\mathrm{B}}T} + 1}. \tag{2.51}$$

Recalling the electron density is given by $n = N_{\mathrm{c}} \left(\mathrm{e}^{(E_{\mathrm{c}} - \mu)/k_{\mathrm{B}}T} + 1\right)^{-} 1$, we can write an expression for the emission coefficient of trapped electrons back into the conduction band as

$$\beta_{\mathrm{e}} = v_{\mathrm{th,e}}\, \sigma_{\mathrm{e}}\, N_{\mathrm{c}} \mathrm{e}^{-(E_{\mathrm{c}} - E_{\mathrm{trap}})/k_{\mathrm{B}}T}, \tag{2.52}$$

and similar analysis leads to the coefficient of emission of trapped holes back to the valence band as

$$\beta_{\mathrm{h}} = v_{\mathrm{th,h}}\, \sigma_{\mathrm{h}}\, N_{\mathrm{v}} \mathrm{e}^{-(E_{\mathrm{trap}} - E_{\mathrm{v}})/k_{\mathrm{B}}T}. \tag{2.53}$$

While this analysis has been conducted for a semiconductor in the dark, to a good approximation, these emission coefficients are unchanged under illumination. This is because of the rapid thermalisation of electrons and holes to a quasi-thermal equilibrium at the band edges, meaning they have the same energy and velocity distributions under illumination as in the dark.

Given this information, we can now solve **Equations 2.43 – 2.45** as a function of the electron-hole volumetric generation rate G which depends on the external illumination conditions. Furthermore, it is possible to solve these equations away from steady-state, albeit only numerically. However, in this further analysis, we consider only the steady-state case. In the steady-state, the net rate of electron ($R_{\text{trap,e}} - G_{\text{trap,e}}$) and hole ($R_{\text{trap,p}} - G_{\text{trap,p}}$) capture must be equal. This condition gives

$$
\begin{aligned}
R_{\text{trap,e}} - G_{\text{trap,e}} &= R_{\text{trap,p}} - G_{\text{trap,p}} \\
v_{\text{th,e}}\,\sigma_{\text{e}}\,n\,(n_{\text{trap}} - n_{\text{trap,e}}) - \beta_{\text{e}}\,n_{\text{trap,e}} &= v_{\text{th,h}}\,\sigma_{\text{h}}\,p\,n_{\text{trap,e}} - \beta_{\text{h}}(n_{\text{trap}} - n_{\text{trap,e}}) \\
n_{\text{trap,e}}\left[v_{\text{th,h}}\,\sigma_{\text{h}}\,p + v_{\text{th,e}}\,\sigma_{\text{e}}\,n + \beta_{\text{h}} + \beta_{\text{e}}\right] &= v_{\text{th,e}}\,\sigma_{\text{e}}\,n\,n_{\text{trap}} + \beta_{\text{h}} n_{\text{trap}} \\
\implies n_{\text{trap,e}} &= n_{\text{trap}} \frac{v_{\text{th,e}}\,\sigma_{\text{e}}\,n + \beta_{\text{h}}}{v_{\text{th,h}}\,\sigma_{\text{h}}\,p + v_{\text{th,e}}\,\sigma_{\text{e}}\,n + \beta_{\text{h}} + \beta_{\text{e}}}. \qquad (2.54)
\end{aligned}
$$

While this result is not important in and of itself, it is very useful when plugged into **Equation 2.43**, giving

$$
\begin{aligned}
-G &= \beta_{\text{e}}\,n_{\text{trap,e}} - v_{\text{th,e}}\,\sigma_{\text{e}}\,n\,(n_{\text{trap}} - n_{\text{trap,e}}) \\
&= n_{\text{trap,e}}\,(\beta_{\text{e}} + v_{\text{th,e}}\,\sigma_{\text{e}}\,n) - v_{\text{th,e}}\,\sigma_{\text{e}}\,n_{\text{trap}} n \\
&= n_{\text{trap}}\left[\frac{(v_{\text{th,e}}\,\sigma_{\text{e}}\,n + \beta_{\text{h}})\,(\beta_{\text{e}} + v_{\text{th,e}}\,\sigma_{\text{e}}\,n)}{v_{\text{th,h}}\,\sigma_{\text{h}}\,p + v_{\text{th,e}}\,\sigma_{\text{e}}\,n + \beta_{\text{h}} + \beta_{\text{e}}} - v_{\text{th,e}}\,\sigma_{\text{e}} n\right] \\
&= n_{\text{trap}}\left[\frac{(v_{\text{th,e}}\,\sigma_{\text{e}}\,n + \beta_{\text{h}})\,(\beta_{\text{e}} + v_{\text{th,e}}\,\sigma_{\text{e}}\,n) - v_{\text{th,e}}\,\sigma_{\text{e}} n(v_{\text{th,h}}\,\sigma_{\text{h}}\,p + v_{\text{th,e}}\,\sigma_{\text{e}}\,n + \beta_{\text{h}} + \beta_{\text{e}})}{v_{\text{th,h}}\,\sigma_{\text{h}}\,p + v_{\text{th,e}}\,\sigma_{\text{e}}\,n + \beta_{\text{h}} + \beta_{\text{e}}}\right] \\
&= n_{\text{trap}}\left[\frac{\beta_{\text{h}}\beta_{\text{e}} - v_{\text{th,e}}\,\sigma_{\text{e}} n(v_{\text{th,h}}\,\sigma_{\text{h}}\,p)}{v_{\text{th,h}}\,\sigma_{\text{h}}\,p + v_{\text{th,e}}\,\sigma_{\text{e}}\,n + \beta_{\text{h}} + \beta_{\text{e}}}\right] \\
&= n_{\text{trap}} v_{\text{th,e}}\,\sigma_{\text{e}}\,v_{\text{th,h}}\,\sigma_{\text{h}}\left[\frac{N_{\text{c}} N_{\text{v}} \text{e}^{(E_{\text{c}} - E_{\text{v}})/k_{\text{B}}T} - np}{v_{\text{th,h}}\,\sigma_{\text{h}}\,p + v_{\text{th,e}}\,\sigma_{\text{e}}\,n + \beta_{\text{h}} + \beta_{\text{e}}}\right] \\
\implies G &= n_{\text{trap}} v_{\text{th,e}}\,\sigma_{\text{e}}\,v_{\text{th,h}}\,\sigma_{\text{h}}\left[\frac{np - n_i^2}{v_{\text{th,h}}\,\sigma_{\text{h}}\,p + v_{\text{th,e}}\,\sigma_{\text{e}}\,n + \beta_{\text{h}} + \beta_{\text{e}}}\right]. \qquad (2.55)
\end{aligned}
$$

This expression can be simplified by introducing a few definitions. Firstly, the minimum lifetime of, for example, electrons is given by $\tau_{\text{min,e}} = 1/n_{\text{trap}} v_{\text{th,e}}\,\sigma_{\text{e}}$, since this is the denominator in this expression is the rate of electron capture if all traps

were full of holes. Since not all traps will be available to trap an electron, the actual lifetime will be longer than this value. Therefore, our expression becomes

$$G = \frac{np - n_i^2}{\tau_{\mathrm{min,n}}(p + N_{\mathrm{v}}\mathrm{e}^{-(E_{\mathrm{trap}}-E_{\mathrm{v}})/k_{\mathrm{B}}T}) + \tau_{\mathrm{min,p}}(n + N_{\mathrm{c}}\mathrm{e}^{-(E_{\mathrm{c}}-E_{\mathrm{trap}})/k_{\mathrm{B}}T}))}$$

$$\boxed{G = \frac{np - n_i^2}{\tau_{\mathrm{min,n}}(p + p_{\mathrm{t}}) + \tau_{\mathrm{min,p}}(n + n_{\mathrm{t}})} = R_{\mathrm{trap}}}. \tag{2.56}$$

In this equation, n_{t} and p_{t} are the electron and hole concentrations when the quasi-Fermi level for electrons or holes is equal to the trap energy respectively (e.g. for $E_{\mathrm{F_n}} = E_{\mathrm{trap}}$). Since we have considered a system at open-circuit the generation rate G must be entirely balanced by recombination, which is the boxed expression in **Equation 2.56**. Here we have derived the recombination rate via a trap-state, R_{trap}, with many fewer approximations than are present in the form of **Equation 2.41**.

We are now in a position to recover the approximate form of trap-mediated recombination given in **Equation 2.40**, namely $k_1 n$. To recover, this rate, we require that $n = p \gg n_i$, which is valid for an undoped semiconductor at high injection. Further, we would require $n \gg n_{\mathrm{t}}$, p_{t}, which again should be valid for high injection. By making these approximations, trap-mediated recombination becomes linear in n and k_1 would be given by $k_1 = 1/(\tau_{\mathrm{min,n}} + \tau_{\mathrm{min,p}})$. I note that for highly doped systems, trap-mediated recombination is also linear in charge-carrier density. For example, in a heavily n-doped system, $n \gg p$, n_i, n_{t}, p_{t}, and so the recombination rate becomes $p/t_{\mathrm{min,p}}$, that is the recombination rate depends on the *minority* carrier lifetime and concentration. One can understand this be considering that in such a heavily doped system, the traps would be predominantly full of electrons and so there is no bottleneck for holes to recombine via the traps.

Surface recombination In the following, I will again be following the derivation provided within '*The Physics of Solar Cells*' by Jenny Nelson [2].

The trap-mediated recombination rate which we derived in **Equation 2.56** can

vary across the semiconductor. These spatial variations can be caused by variations in the electron and/or hole concentrations, or by variations in the nature (depth, capture cross-section etc.) or number density of the dominant traps.

In real materials, defects are far more likely to occur at the surfaces of the semiconductor, or at interfaces. This is why there is such an emphasis on *surface passivation* wherein an additional procedure is utilised to reduce the influence of these surface defects on, for example, the carrier lifetimes. These localised states can arise from the period crystal structure abruptly ending at a surface which leaves broken, or 'dangling', bonds. Additionally, impurities can be introduced from the external environment (this is why high-quality semiconductor growth requires cleanrooms), or impurities during growth can accumulate at surfaces, giving rise to localised states. Therefore, it can be, and often is, the case that the trap states responsible for recombination are concentrated at the surface. Therefore, it is more meaningful to consider the traps in a 2D, and not 3D, space when considering surface recombination in particular (i.e. number of traps per unit area of surface/interface rather than traps per unit volume). Therefore, the rate recombination will be expressed as a flux, the number of carriers recombining per unit area per unit time, rather than the volumetric recombination rates we have previously considered.

If the surface has N_{surf} traps per unit area, then within a very thin layer to the surface of thickness δx, we can write the surface recombination flux as

$$R_{\text{trap}}^{\text{surf}} \delta x = \frac{n_{\text{surf}} p_{\text{surf}} - n_{\text{i}}^2}{\frac{1}{S_{\text{e}}} \left(p_{\text{surf}} + p_{\text{t}}\right) + \frac{1}{S_{\text{h}}} \left(n_{\text{surf}} + n_{\text{t}}\right)}, \tag{2.57}$$

where n_{surf} and p_{surf} are the electron and hole concentrations at the surface respectively. S_{e} is the surface recombination velocity of electrons which is defined by

$$S_{\text{e}} = N_{\text{surf}}\, v_{\text{th,e}}\, \sigma_{\text{e}}, \tag{2.58}$$

and similarly for the surface recombination velocity for holes

$$S_{\mathrm{h}} = N_{\mathrm{surf}}\, v_{\mathrm{th,h}}\, \sigma_{\mathrm{h}}. \tag{2.59}$$

Note that these are velocities, and so have a direction associated with them. Here, both S_{e} and S_{h} are directed from the bulk towards the surface.

In a doped semiconductor, we can simplify the expression for R_{trap}^{surf}. For example, in a p-doped semiconductor, the expression collapses to

$$R_{\mathrm{trap}}^{\mathrm{surf}} \delta x = S_{\mathrm{e}} \left(n_{\mathrm{surf}} - n_0 \right), \tag{2.60}$$

where $n_0 = n_{\mathrm{i}}^2 / p_{\mathrm{surf}}$. This lets use characterise the recombination of the minority carrier at the surface in terms of a surface recombination current. This arises from considering the Poisson equation in the absence of generation (i.e. in the dark), and in steady-state ($\partial n / \partial t = 0$) [2]. Explicitly, this is the condition $\nabla \cdot J_{\mathrm{e}} = q R_{\mathrm{trap}}^{\mathrm{surf}}$. We can integrate this across the interface layer to calculate the difference in the electron current density on either side of the interface. The interface is at position x_{surf}, and we integrate a region of width δx centred on the interface. This is given by

$$\Delta J = J(x_{\mathrm{surf}} + \delta x/2) - J(x_{\mathrm{surf}} - \delta x/2) = q \int_{x_{\mathrm{surf}} - \delta x/2}^{x_{\mathrm{surf}} + \delta x/2} R_{\mathrm{trap}}^{\mathrm{surf}} \mathrm{d}x = q S_{\mathrm{e}} \left(n_{\mathrm{surf}} - n_0 \right). \tag{2.61}$$

If this interface is a surface (and not a grain boundary or heterostructure), no current flows out of the semiconductor, meaning $J(x_{\mathrm{surf}} + \delta x/2) = 0$. Therefore we can calculate the current density at the surface of the semiconductor as

$$J_{\mathrm{e}}(x_{\mathrm{surf}}) = -q S_{\mathrm{e}} \left(n_{\mathrm{surf}} - n_0 \right). \tag{2.62}$$

An identical analysis can be performed for an n-doped semiconductor. The surface recombination velocity is an important parameter in solar cells, since it characterises the rate at which minority carriers are depleted at an interface. This concept is explored in detail in **Chapter 5**.

Radiative recombination

Radiative recombination is a bimolecular process which occurs between electrons and holes, and results in the emission of a photon. For direct bandgap semiconductors (like MHPs) this process is intrinsic – it depends on the shape and position of the valence and conduction bands. For these reasons, radiative bimolecular recombination is often called band-to-band recombination. Often in the MHP PV research field, the terms radiative and bimolecular recombination are used interchangably. However, this is not accurate since there exists non-radiative bimolecular recombination pathways. The process is shown schematically in **Figure 2.3b**. This process is the reverse process of light absorption – this has an important role in determining the efficiency a solar cell can achieve and will be discussed later. Since the bimolecular recombination rate should be an intrinsic material property, k_2 should exhibit minimal sample-to-sample variations and ought to be insensitive to the processing routes through which the material was grown, provided one can be certain that the same material has been formed [7].

Derivation of the radiative recombination rate Once again, in the following, I will follow the derivation provided within '*The Physics of Solar Cells*' by Jenny Nelson [2].

We start with an electron in the conduction band with momentum k_c and energy E_c. We can represent this initial state as $|c\rangle = |k_\mathrm{c}, E_\mathrm{c}\rangle$. The electron will return to a position in the valence band with momentum k_v and energy E_v, and so this final state can be described as $|v\rangle = |k_\mathrm{v}, E_\mathrm{v}\rangle$. The probability of radiative recombination (spontaneous emission) per unit time will be based on Fermi's Golden Rule [1, 2] (strictly this is only a first-order perturbative result, but this suffices for the semiconductors discussed in this thesis). As already mentioned, Fermi's Golden Rule, the derivation of which is outside of this scope of this thesis, gives the probability of a transition occurring per unit time. Herein, we are interested in the *rate* of radiative recombination, and so we must take into account the probability of that the initial state is occupied, and the final state is available. Taking these together, gives the transition rate from the initial

state $|i\rangle$ to the final state $|f\rangle$ as

$$\Gamma_{i\to f} = \frac{2\pi}{\hbar}|\langle i|\hat{H}'|f\rangle|^2 f_{\mathrm{i}}(1-f_{\mathrm{f}}), \tag{2.63}$$

where f_{i} and f_{f} are the probability that initial and final states are occupied respectively, and $\hat{H}'$ is the perturbing Hamiltonian [1–3]. For an electromagnetic field of strength E_0, with polarisation vector $\boldsymbol{\varepsilon}$, angular frequency ω (such that the wavelength is much larger than the interatomic spacing, as is the case for PV cells), $\hat{H}'$ can be expressed as

$$\hat{H}' = \frac{iqE_0}{2m_e\omega}\boldsymbol{\varepsilon}\cdot\hat{\mathbf{p}},$$

where $\hat{\mathbf{p}}$ is the momentum operator introduced in **Equation 2.1**. Bringing returning to the case of the conduction band electron introduced earlier, we can write that the rate of spontaneous emission Γ_{spon} is given by

$$\Gamma_{\mathrm{spon}} = \frac{2\pi}{\hbar}|\langle c|\hat{H}'|v\rangle|^2\, n_{\mathrm{F}}(E_{\mathrm{c}}, E_{\mathrm{F_n}}, T)(1-n_{\mathrm{F}}(E_{\mathrm{v}}, E_{\mathrm{F_p}}, T)), \tag{2.64}$$

with n_{F} defined in **Equation 2.23**. This relies on the populations of electrons and holes being in quasi thermal equilibrium in their respective bands with chemical potentials $E_{\mathrm{F_n}}$ and $E_{\mathrm{F_p}}$ respectively. As a shorthand, hereafter I will write $f_{\mathrm{c}} = n_{\mathrm{F}}(E_{\mathrm{c}}, E_{\mathrm{F_n}}, T)$ and a similar expression for holes. The rate of absorption, Γ_{abs}, can be expressed in a similar form as

$$\Gamma_{\mathrm{abs}} = \frac{2\pi}{\hbar}|\langle c|\hat{H}'|v\rangle|^2\, f(f_{\mathrm{v}}-f_{\mathrm{c}}), \tag{2.65}$$

where f is the probability there is a photon with energy $E = E_{\mathrm{c}} - E_{\mathrm{v}}$. In (quasi) thermal equilibrium, the rate of spontaneous emission and absorption should be the same. This leads to an expression for f which is obtained as follows

$$\begin{aligned}
\frac{2\pi}{\hbar}|\langle c|\hat{H}'|v\rangle|^2 f_{\mathrm{c}}(1-f_{\mathrm{v}}) &= \frac{2\pi}{\hbar}|\langle c|\hat{H}'|v\rangle|^2 f(f_{\mathrm{v}}-f_{\mathrm{c}}),\\
f_{\mathrm{c}}(1-f_{\mathrm{v}}) &= f(f_{\mathrm{v}}-f_{\mathrm{c}})\\
f &= \frac{f_{\mathrm{c}}(1-f_{\mathrm{v}})}{f_{\mathrm{v}}-f_{\mathrm{c}}},\\
&= \frac{\mathrm{e}^{\beta(E_{\mathrm{v}}-E_{\mathrm{F_p}})} f_{\mathrm{c}} f_{\mathrm{v}}}{\left[\mathrm{e}^{\beta(E_{\mathrm{c}}-E_{\mathrm{F_n}})} - \mathrm{e}^{\beta(E_{\mathrm{v}}-E_{\mathrm{F_p}})}\right] f_{\mathrm{c}} f_{\mathrm{v}}},\\
f &= \frac{1}{\mathrm{e}^{(E-\Delta\mu)/k_{\mathrm{B}}T}-1},
\end{aligned} \tag{2.66}$$

where $\Delta\mu$ is the quasi-Fermi level splitting introduced previously (recall **Equation 2.37**). We will make use of this equation later in this section when discussing the detailed balance limit for solar cell efficiency.

By utilising the Boltzmann approximation, **Equation 2.36** and the approach described in detail later, in particular **Section 2.2.2**, in the derivation of **Equation 2.92**, we can now calculate the radiative recombination rate. The detailed derivation can be found in Ref. [2]. By using this approach, we arrive at

$$R_{\mathrm{rad}} = k_2(np - n_{\mathrm{i}}^2), \tag{2.67}$$

where the materials properties are contained within k_2 as

$$k_2 = \frac{1}{n_{\mathrm{i}}^2}\frac{n_{\mathrm{index}}}{4\pi^2\hbar^3c^2}\int_0^\infty \alpha(E)\,E^2\,\mathrm{e}^{-E/k_{\mathrm{B}}T}\,\mathrm{d}E. \tag{2.68}$$

n_{index} is the refractive index of the semiconductor and $\alpha(E)$ is the absorption coefficient. As mentioned earlier, k_2 is a property of the material and is not dependent on the excited charge carrier density.

We can now see under which conditions R_{rad} matches with the bimolecular term in **Equation 2.40**. For this to be the case, we require $np \gg n_{\mathrm{i}}^2$ and $n = p$. This is true for an undoped semiconductor, under illumination conditions such that the excess carriers far exceed the background carriers. These assumptions are often well justified for the MHP semiconductors studied in this thesis under standard AM1.5 illumination

conditions. I note that for a highly doped semiconductor, radiative recombination is linear, depending on the minor carrier concentration and lifetime. This can be understood since both carriers are required for radiative recombination, and in a highly doped system, the doped carrier is always present, therefore the rate would depend just on the lifetime and concentration of the 'other' carrier.

Auger recombination

Auger recombination within a semiconductor is the analogue of the Auger process of an atomic system [15]. It is non-radiative process which involves either two electrons and a hole, or two holes and an electron. Assuming the semiconductor is intrinsic (or high charge-carrier injection), where $n = p$, Auger recombination scales as n^3. A schematic of the process is shown in **Figure 2.3c**. In this process, an electron recombines with a hole in the valence band, but the energy is transferred to a third charge-carrier instead of being emitted as a photon. This third carrier can be promoted into a higher band (right), or interact with a phonon to transfer momentum. As shown in **Figure 2.4**, Auger recombination only becomes significant at high charge-carrier densities where $n > k_3/k_2$.

Radiative efficiency

The radiative efficiency of a material for a solar cell is a crucial parameter. In an ideal solar cell, all the recombination would be radiative. Naïvely, one might assume that an ideal solar cell would have no recombination present at all. Regrettably, the principle of detailed-balance states that if the process of absorbing a photon to create an electron-hole pair is possible, so too must the reverse process, in which the electron and hole recombine, emitting a photon. In fact, at thermal equilibrium the rate of absorption and emission must be equal. This is unavoidable and is a property of the semiconductor, temperature, and excitation conditions. However, we can limit all the other recombination processes, and try to engineer our device such that all recombination is through these (unavoidable) radiative channels. The fraction of absorbed photons

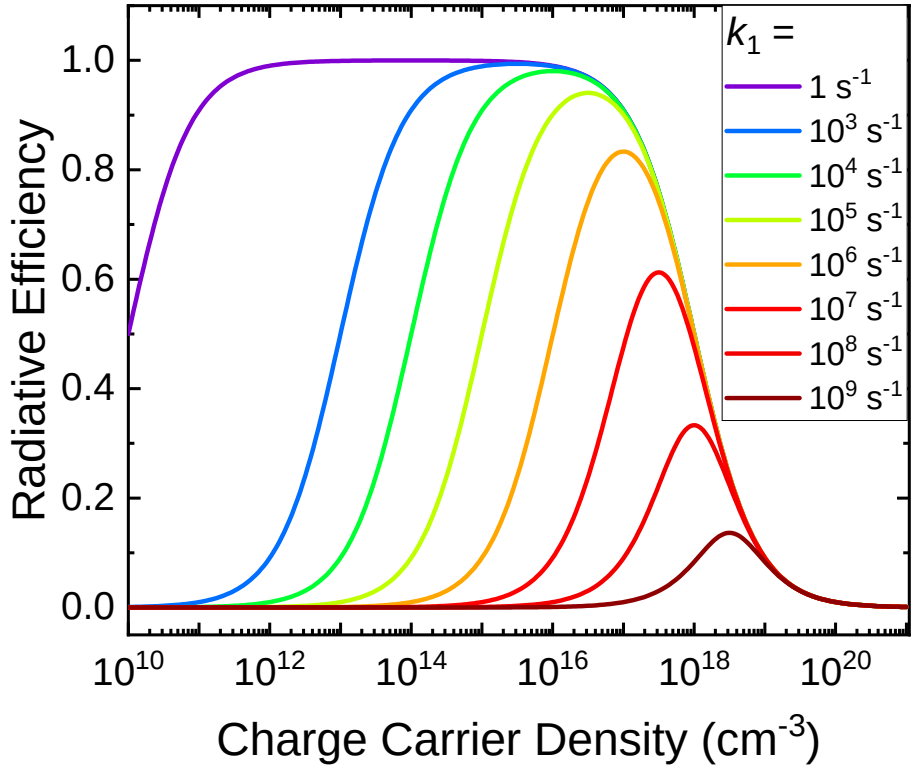


Figure 2.7: *Radiative efficiency, as given in* ***equation 2.69*** *as a function of charge carrier density for different monomolecular decay rates. k_1 is varied from 1 s^{-1} (purple) to 10^9 s^{-1} (brown). As k_1 is increased, the maximum of the radiative efficiency is reduced in magnitude and shifted to larger charge carrier density. Again, $k_2 = 10^{-10}\,\mathrm{cm^3 s^{-1}}$, $k_3 = 10^{-28}$ $cm^6 s^{-1}$ were used as inputs as they are typical for MHP semiconductors. Similar analysis can be found in [7].*

which generate an electron-hole pair recombining to emit a photon is characterised using the 'radiative efficiency', η_{rad}, which is given by

$$\eta_{\mathrm{rad}}(n) = \frac{\text{photons emitted}}{\text{photons absorbed}} = \frac{k_2 n}{k_1 + k_2 n + k_3 n^2}. \tag{2.69}$$

$\eta_{\mathrm{rad}}(n)$ is also called the photoluminescence quantum yield (PLQY), a term which I will use throughout this thesis. If measured on full PV devices, **Equation 2.69** is only valid under open-circuit conditions where no charge-carriers are extracted and so must recombine within the device via one mechanism or another. Since k_2 and k_3 are properties of the material, we have very little control over them for a given system. Instead, we should focus on reducing k_1, the trap-mediated recombination rate, as this can be readily controlled using improved processing routes and/or passivation techniques.

Figure 2.7 shows how $\eta_{\text{rad}}(n)$ varies for different trap-mediated recombination rates, k_1. At low charge carrier density, k_1 dominates over all other recombination process, resulting in low radiative efficiency. As n is increased, $\eta_{\text{rad}}(n)$ also increases as the system enters the bimolecular dominated regime, as described in **Figure 2.4**. In fact, the peak of radiative efficiency can be determined by differentiating **Equation 2.69** with respect to n. Performing this analysis gives $n_{\text{peak}} = \sqrt{k_1/k_3}$, which is clearly strongly dependent on k_1. The peak radiative efficiency occurs at this charge carrier density, and is given by $\eta_{\text{rad}}(n_{\text{peak}}) = \left(1 + 2\sqrt{k_1 k_3/k_2^2}\right)^{-1}$, which again is strongly dependent on k_1. The radiative efficiency falls past this peak due to the effects of Auger recombination, which is non-radiative and scales like n^3. For typical MHP materials, the charge-carrier density is $10^{14} - 10^{16}$ cm^{-3} and $k_1 = 10^5 - 10^7$ s^{-1}. In this regime, the radiative efficiency is strongly dominated by the effects of trap-mediated monomolecular recombination, which is clearly evident from **Figures 2.4 & 2.7**. To improve the radiative efficiency, and hence solar cell performance, it is imperative to reduce the influence of traps on the charge-carrier recombination. Further discussion on the relationship between device performance and radiative efficiency is given below.

Radiative efficiency and the quasi-Fermi level splitting

We are now in a position to connect the radiative efficiency of a semiconductor, with the QFLS that must correspond to. At first glance, it is not clear why these quantities (an ultimately device open-circuit voltage) ought to be related. In the following, we bring these quantities together to understand how one informs the other.

It is not possible to access directly the individual quasi-Fermi levels, E_{F_n} or E_{F_p}. However, the difference (or *splitting*) between them is possible to access through photoluminescence quantum yield (PLQY – radiative efficiency) or electroluminescence quantum yield (ELQY) measurements. In the following, I will only discuss photoluminescence quantum yield (PLQY) measurements. In brief, the relationship originates since both radiative recombination and the QFLS depends on n^2. Starting from the PLQY, we know that this is a ratio of the emitted photon flux (ϕ_{emit}), to the absorbed

photon flux (ϕ_{abs}). These quantities can be converted into current densities by a simple scaling by the charge of an electron. Therefore, one can think of the PLQY as the ratio of a radiative current J_{rad} to a generation current J_{G}. In isolated semiconductors (or devices at open-circuit), all charges that were generated must recombine, either radiatively or non-radiatively, so $J_{\text{G}} = J_{\text{rec}}$. These steps are summarised below

$$\text{PLQY} = \frac{\phi_{\text{emit}}}{\phi_{\text{abs}}} = \frac{J_{\text{rad}}}{J_{\text{G}}} = \frac{J_{\text{rad}}}{J_{\text{rec}}}. \tag{2.70}$$

A simple rearrangement of **Equation 2.70** gives $J_{\text{rad}} = J_{\text{G}} \times \text{PLQY}$. Now, we know the emitted photon flux from radiative recombination is proportional to the np product in the semiconductor, or $\phi_{\text{emit}} \propto k_2 n^2$, and so $J_{\text{rad}} \propto q k_2 n^2$, where we have written $n_{\text{exc}} = p_{\text{exc}} = n$. Similarly, there will be a radiative recombination current not under illumination due to the thermal population of carriers in the band. We call this the 'dark radiative recombination current' and is given by $J_{0,\text{rad}} \propto q k_2 n_i^2$, where n_i^2 is the intrinsic carrier concentration, as defined in **Equation 2.30**. The proportionality constants are identical for each '$\propto$' relationship. We now take the ratio of these quantities, giving

$$\frac{J_{\text{rad}}}{J_{0,\text{rad}}} = \frac{q k_2 n^2}{q k_2 n_i^2} \tag{2.71}$$

which rearranges simply to give

$$\ln\left(\frac{J_{\text{rad}}}{J_{0,\text{rad}}}\right) = \ln\left(\frac{n^2}{n_i^2}\right). \tag{2.72}$$

Now, we recall **Equation 2.37**, which allows us to replace the right-hand side of the above equation with a factor containing the QFLS. This then is rearranged to give

$$\text{QFLS} = k_{\text{B}} T \ln\left(\frac{J_{\text{rad}}}{J_{0,\text{rad}}}\right). \tag{2.73}$$

We are now able to relate QFLS with the PLQY, by combining **Equations 2.70 & 2.73**. This gives [16]

$$\mathrm{QFLS} = k_\mathrm{B}T \ln\left(\mathrm{PLQY}\frac{J_\mathrm{G}}{J_{0,\mathrm{rad}}}\right) \tag{2.74}$$

$$\boxed{\mathrm{QFLS} = \mathrm{QFLS}_\mathrm{rad} + k_\mathrm{B}T \ln\left(\mathrm{PLQY}\right)}. \tag{2.75}$$

Where we define $\mathrm{QFLS}_\mathrm{rad} = \ln\left(J_\mathrm{G}/J_{0,\mathrm{rad}}\right)$. **Equation 2.75** (boxed) is extremely important and used throughout this thesis. Several important things to notice are that, for a perfect material, we would expect the radiative efficiency to be unity, and in this case we do indeed recover that the QFLS is that in the radiative limit. Secondly, that the QFLS has a logarithmic dependence on PLQY. At room temperature, we can therefore calculate that the QFLS is reduced by ~ 60 meV for every order of magnitude drop in the PLQY. The lost QFLS always scales like this with radiative efficiency regardless of the bandgap of the semiconductor in question. This is because all details of the bandgap of the semiconductor are contained within $\mathrm{QFLS}_\mathrm{rad}$. Calculating $\mathrm{QFLS}_\mathrm{rad}$ requires more knowledge of solar cell operation, **Section 2.2**, however the relevant equations are provided below without justification for completeness of this section. The justification and/or derivation of the below can be found in **Section 2.2**. Calculating $\mathrm{QFLS}_\mathrm{rad}$ requires knowing the generation current, which can be approximated as the J_SC, using

$$J_\mathrm{G} \approx J_\mathrm{SC} = q\int_0^\infty EQE(\lambda)AM1.5(\lambda)\mathrm{d}\lambda, \tag{2.76}$$

where $EQE(\lambda)$ is the external quantum efficiency of the solar cell, and $AM1.5$ is the photon flux associated with the AM1.5 solar spectrum, and λ is wavelength. Finally, the radiative recombination current in the dark can be approximated as

$$J_{0,\mathrm{rad}} = q\int_0^\infty EQE(\lambda)\varphi_\mathrm{BB}^{300\,\mathrm{K}}(\lambda)\mathrm{d}\lambda, \tag{2.77}$$

where $\varphi_\mathrm{BB}^{300\,\mathrm{K}}(\lambda)$ is the black body photon flux at 300 K.

In principle, the QFLS should be precisely the V_OC achieved by a solar cell based

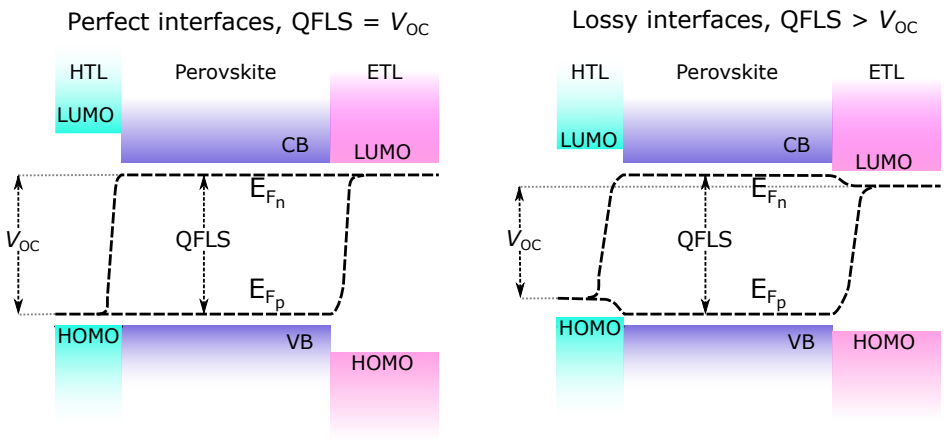


Figure 2.8: *Diagram showing the relationship between the quasi-Fermi level splitting and device V_{OC} for perfect (left) and lossy (right) interfaces. With perfect interfaces, there are no selectivity losses and no energetic misalignment between the perovskite and charge transport layers, and so the QFLS = V_{OC}. For lossy interfaces, however, quasi-Fermi level for electrons and/or holes is not maintained throughout the transport layer and as such QFLS > V_{OC}. For this reason, the QFLS is often seen as the upper bound, or 'best case scenario' for the achievable device V_{OC}.*

on that material system, as will be discussed in the following. However, in MHP solar cells, a so-called 'QFLS-V_{OC}' mismatch is often observed [16, 17]. A cause for this can be 'lossy interfaces', wherein the quasi-Fermi level for electrons and/or holes is not maintained throughout the transport layer which is shown schematically in **Figure 2.8**.This means the V_{OC} measured on the device's terminals is reduced compared to the QFLS within the solar absorber material. For this reason, the QFLS is often seen as the upper bound, or 'best case scenario' for the achievable device open-circuit voltage.

2.2 Solar Cell Operation

2.2.1 Ideal solar cells

At its most basic, a solar cell is a device that converts energy from light (photons) and coverts it into electrical energy. We have seen in the previous section how a semiconductor behaves under external illumination, and this underpins solar cell operation. In the following, we will instead be focused on the macroscopic properties of solar cells. Previously, we have seen that a splitting in the quasi-Fermi levels arises in a semiconductor under illumination, and that this is a form of electrochemical potential energy. This can be considered as forming a voltage (related just by the elementary charge), and is indeed the origin of *photovoltage*, this is called the photovoltaic effect. However, to extract any energy from the solar cell, charge must be extracted (a *photocurrent*). In an idealised scenario, we can model the current within the solar cell using the diode equation[2]

$$J(V) = J_{\mathrm{G}} - J_0 \left[\mathrm{e}^{qV/k_{\mathrm{B}}T} - 1 \right], \tag{2.78}$$

where V is the applied bias to the solar cell, and J_0 is the total recombination current in the dark. Here, J_0 is assumed to have no bias dependence (as is common throughout the literature), but this is unlikely to be true [2, 3]. From **Equation 2.78**, we can extract a few important parameters for solar cell operation. Firstly, the short-circuit current density (J_{SC}) is obtained for $V = 0$, which means that, in this idealised case, $J(0) = J_{\mathrm{SC}} = J_{\mathrm{G}}$. In other words, the short-circuit current achievable for an optimal case is precisely the generation current. Internally within the solar cell, we might imagine steeply tilted bands, whereby the internal electric field is extremely strong ($\sim 10^6\,\mathrm{V/m}$), and oriented in such a way to drive charge-separation and so removes (in the ideal case) all the generated charges as current. As such, the J_{SC} can be thought

[2]This is often called the 'Shockley diode equation'. As mentioned earlier, but I believe it is worth repeating, due to Shockley being a well-documented racist and eugenicist [11, 12], I refuse to highlight his name throughout this thesis, and I encourage anyone reading this to do likewise, as is becoming more commonplace in the field [12]. I will use alternative names for any formulae, or similar, named after him throughout this work.

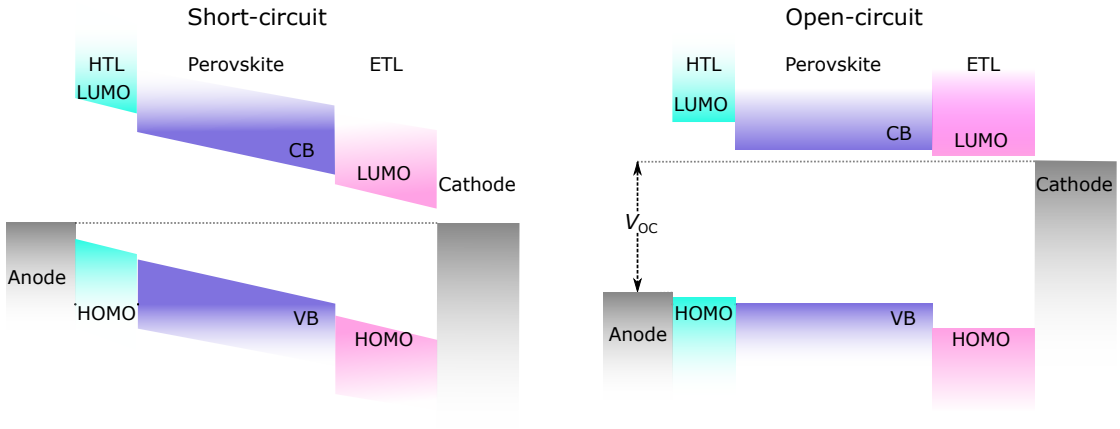


Figure 2.9: *A schematic of the bands within a p-i-n solar cell at short- (left) and open-circuit (right) conditions. At short-circuit, the bands are steeply tilted which rapidly drives charge separation and collection. At open-circuit, the bands are flat and no charges are extracted. Due to the lack of charge extraction, all generated charges must recombine within the solar cell itself.*

of as the maximum current a solar cell could deliver.

Next, we can determine the V_{OC}, that is the voltage in the cell at which no current flows, or

$$J(V_{\mathrm{OC}}) = 0 = J_{\mathrm{G}} - J_0 \left[\mathrm{e}^{qV_{\mathrm{OC}}/k_{\mathrm{B}}T} - 1\right] \tag{2.79}$$

$$\implies V_{\mathrm{OC}} = \frac{k_{\mathrm{B}}T}{q} \ln\left(\frac{J_{\mathrm{G}}}{J_0} + 1\right). \tag{2.80}$$

At open-circuit, no charges are (by definition) extracted to the external circuit. At such conditions, we can imagine the bands to be 'flat' (neither promoting or hindering charge separation), and so the internal electric field is at its minimum, but the voltage the cell can output is at its highest. A schematic of the bands at short- and open-circuit conditions is shown in **Figure 2.9**.

Power is defined as the current-voltage product. In the case of solar cells, we are most often working with current densities (current per unit area), and so we are instead measuring a power density (e.g. $\mathrm{mW/cm^2}$), however the terms are often used interchangeably. At the two special conditions highlighted above, the power generated by the solar cell is 0 – no current flows at open-circuit, and there is no voltage at

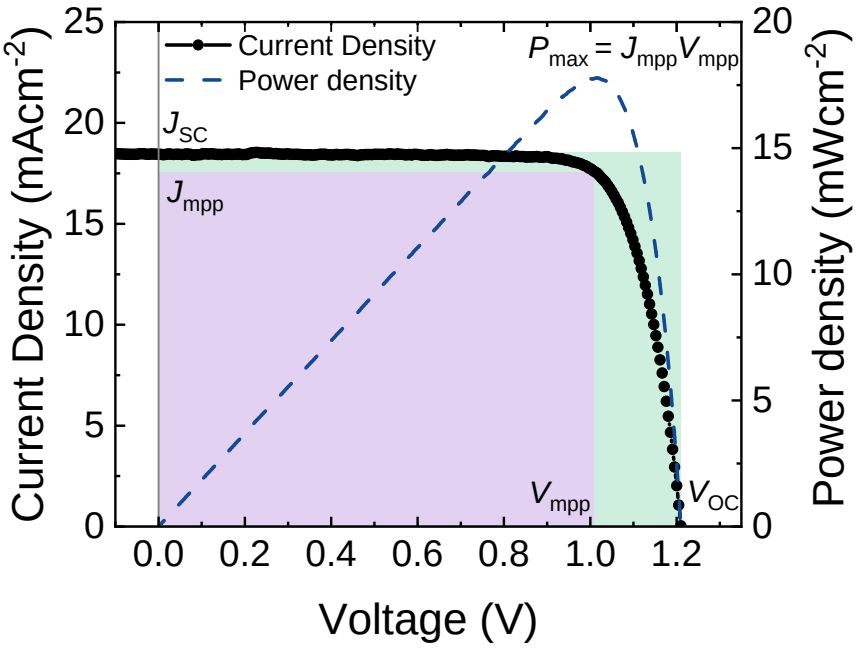


Figure 2.10: *Annotated JV curve (black) of represenative* 1.7 eV *perovskite solar cell. The labels describe key device parameters. The* J_{SC} *is the current-density at 0 applied voltage, and the* V_{OC} *is the voltage when no current flows through the cell. The green rectangle has an area of* $V_{OC} \times J_{SC}$*. The power extracted from the cell at each point is calculated (by* $J \times V$*), and is plotted as a blue dashed line. The maximum in the power (*P_{max}*) gives this location of* V_{mpp} *and* J_{mpp}*. The purple rectangle has an area* $V_{mpp} \times J_{mpp}$*. The fill factor can be thought of as the ratio of the purple and green rectangles.*

short-circuit so the JV product in both cases is 0. Somewhere along the JV curve, there is a current density-voltage pair at which a maximum in the power is achieved. These points are called, for obvious reasons, the maximum power point current-density (J_{mpp}), and maximum power point voltage (V_{mpp}). These must each be lower than J_{SC} and V_{OC} respectively for the reasons discussed earlier. Another important solar cell performance parameter can now be defined. It is called the fill factor (FF), and is given by

$$FF = \frac{J_{mpp}V_{mpp}}{J_{SC}V_{OC}}. \tag{2.81}$$

The FF can be understood graphically by examining **Figure 2.10**, as the ratio of the largest rectangle you can fit 'underneath' the curve to the smallest rectangle you can fit 'around' the curve. For this reason, the FF is often said to describe the 'squareness'

of the JV curve. The FF describes the ease with which charges can move through the solar cell, as will be discussed in more detail later. Understanding the FF of realistic solar cells is extremely complicated, and more details can be found here [18].

From rearranging **Equation 2.81**, we can see that the maximum power extracted from the cell is $P_{\text{max}} = J_{\text{SC}} V_{\text{OC}} FF$. If we compare this to the power incident upon the solar cell (P_{in}), we can calculate the solar-to-electrical power conversion efficiency (PCE) through

$$PCE = \frac{J_{\text{SC}} V_{\text{OC}} FF}{P_{\text{in}}}. \tag{2.82}$$

For AM1.5 illumination, $P_{\text{in}} = 100$ mWcm^{-2} .

2.2.2 Theoretical maximum efficiency

Given the above discussion, a very natural question is what is the maximum PCE achievable for a particular solar absorber material. For this we need to use the principle of detailed balance.

It is extremely challenging to accurately model a realistic multi-layer solar cell architecture, since this requires detailed knowledge of, for example, energetic alignment between each layer, doping densities and charge-carrier mobilities within each layer, bulk and surface defect densities, depth, emission rates, capture cross-section etc., as well as quantitative charge-carrier generation profiles within each layer – all of which are required as inputs to a drift-diffusion simulator. Knowledge of these parameters is particularly challenging for emerging semiconductors such as MHPs. However, it is possible to consider a perfect solar cell material using a thermodynamic treatment. Indeed, this has been widely studied in the literature, and much more detail than I present in this this can be found in the following publications for solar cells in general [19–24], and for MHPs [25, 26].

As can be seen from **Equations 2.78, 2.80 & 2.82**, the J_{SC}, V_{OC} and PCE and of a solar cell material are not an intrinsic properties, and depend strongly on the

incident illumination. This is because not all wavelengths are harvested with the same efficacy due to rapid thermalisation losses discussed earlier in this thesis. Indeed, the reduction of thermalisation losses is a key motivating factor for tandem solar cells and hence the work presented in **Chapters 5 & 6**. Therefore, before undertaking any thermodynamic treatment of solar cells, we must first be explicit with the incident spectrum.

Solar Spectrum

As a first approximation, we can consider the sun to be a black-body emitter, with a temperature $T_{\text{sun}} \approx 5800\,\text{K}$. This means that the emission would follow the expression given by Planck's law [27]:

$$\varphi_{\text{sun}}(E) = \frac{1}{4\pi^3\hbar^3c^2}\frac{E^2}{\mathrm{e}^{E/k_{\text{B}}T_{\text{sun}}}-1}, \tag{2.83}$$

where $\varphi_{\text{sun}}(E)$ is the flux of photons from the sun at energy E, and all other terms have their usual meaning. However, the atmospheres of the sun and, predominantly, the Earth absorb some of this irradiation. In particular, the Earth's atmosphere is particularly good at 'filtering' the high energy UV photons in the ozone layer, and the substantial amount of water vapour in the atmosphere absorbs the near infrared photons effectively. The greater the distance light from the sun must propagate through the Earth's atmosphere, the more substantial this 'filtering' effect becomes. Therefore, it is important that a thickness of atmosphere be universally accepted to ensure that solar cell performance parameters can be reliably compared between laboratories. The schematic in **Figure 2.11(a)** demonstrates the increased thickness of atmosphere that light must travel nearer the poles versus the equator. This is characterised by the air mass (AM) factor, which depends on the angle θ between the equator and latitude at which the light as incident (also called the 'solar zenith angle'). To a first approximation, the air mass scales as

$$AM = \frac{1}{\cos\theta}, \tag{2.84}$$

so $AM = 1$ for light incident at the equator, and $AM = 1.5$ for $\theta =\sim 48°$ [2]. The effect of the different air mass is shown in **Figure 2.11 (b)**, wherein the spectral irradiance as a function of wavelength is shown for the blackbody spectrum at 5778 K (black), AM0 (blue) and AM1.5 (purple) conditions. The absorption of different molecules in the Earth's atmosphere are marked. The AM1.5 spectrum is the standard for solar cell research, and is the standard used throughout this thesis. By integrating beneath the red curve in **Figure 2.11(b)**, one finds the available power from AM1.5 sunlight is $100\,\mathrm{mWcm^{-2}}$.

Detailed Balance limit

The detailed-balance limit a solar cell was first derived in the mid 20^{th} century, and gives the maximum efficiency for single-junction PV [29]. In general, the principle of detailed balance states that, in thermal equilibrium, a process must be precisely balanced by its inverse. In the case of solar cells, this would be that for every photon absorbed, there must be one emitted. However, as we discussed in **Section 2.1.1**, a semiconductor under illumination is not in thermal equilibrium with its surroundings! Importantly, as we showed in **Equation 2.36**, the difference between emission (remember this is proportional to the *np* product) at thermal equilibrium and under illumination is just a scaling factor of $\mathrm{e}^{(E_{\mathrm{F_n}}-E_{\mathrm{F_p}})/k_{\mathrm{B}}T}$ – i.e. it is exponentially related to the QFLS. This observation is crucial, the consequences of which we will see shortly.

To briefly summarise the major findings from the detailed-balance limit of solar cell operation is that the maximum efficiency of 33 % occurs for a solar absorber bandgap of $\sim$ 1.33 eV. At this bandgap, there is a compromise between thermalisation losses (which limits the voltage), and harvesting as much of the solar spectrum as possible (which determines the current). In the following, I will outline the derivation of the detailed-balance limit.

In the detailed-balance limit, 5 major assumptions are made [20, 29] which can be separated into optical (assumptions 1 & 2), thermal (assumption 3), and electronic (assumptions 4 & 5) categories which are summarised by Guillemoles *et al.* [20] and

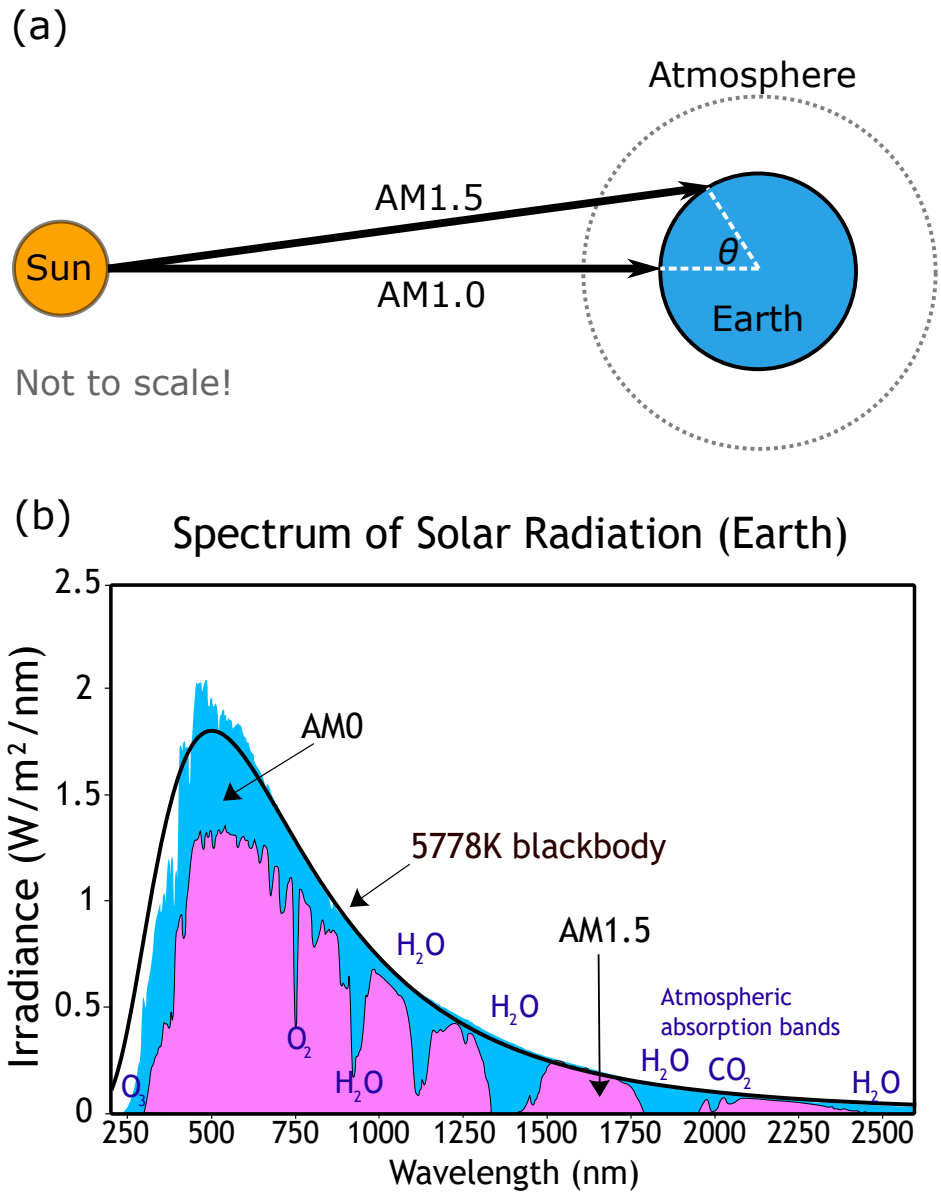


Figure 2.11: *(a) Schematic of the sun-Earth system (not to scale!). The greater the distance light has to travel through the Earth's atmosphere the more will be absorbed, which is characterised by the air mass (AM) through which the light has to travel. The air mass light travels through depends on the angle θ which is 0 for the equator, and 90° for the equator. The air mass scales as $AM = 1/\cos\theta$, which gives AM1.0 for $\theta = 0$, and AM1.5 for $\theta = \sim 48°$. (b) Spectral irradiance as a function of wavelength for the blackbody spectrum at 5778 K (black), AM0 (blue) and AM1.5 (purple) conditions. The absorption of different molecules in the Earth's atmosphere are marked. The area under each curve gives the solar power. This figure is freely usable and taken from [28].*

given below.

1. The absorptance of the solar cell is a step-function: 0 below the bandgap, and 1 for photons above the bandgap.

2. Each photon creates one (and only one) electron hole pair. All electron-hole pairs are collected at short-circuit.

3. The heat generated due to thermalisation is rapidly dissipated, and so the solar cell is at the same temperature as the surroundings ($T_{\text{cell}} = T_{\text{ambient}}$).

4. All recombination is radiative. There are no traps, and Auger recombination is neglected.

5. The contacts are perfectly selective for either electrons or holes, and so no Ohmic losses occur.

A further important property rarely explicitly mentioned is that there can exist no spatial gradients within the quasi-Fermi levels. With these assumptions holding, the QFLS within the solar absorber is the voltage at the terminals of the device, shown schematically in the left panel of **Figure 2.8**. As such, we shall write $E_{\text{F}_\text{n}} - E_{\text{F}_\text{p}} = V$ for brevity hereafter. Moreover, in the following derivation, I will be following the procedure taken by Louise Hirst in Ref. [30].

Next, it is important to know the photon flux incident on the solar cell 'in the dark' (at thermal equibrium with its surroundings). To do this, we need to calculate the black body spectrum. This is commonly just stated, and there is often confusion where this comes from (myself included). Therefore, in the following, I provide a brief derivation. This density of states with wavevectors in a range between k and $k + \mathrm{d}k$ in 3D space is given by

$$g'(k)\mathrm{d}k = \underbrace{\left(\frac{L}{2\pi}\right)^3}_{1/\text{volume of 1 state}} \underbrace{4\pi k^2 \mathrm{d}k}_{\text{volume of shell width d}k} \underbrace{p}_{\text{polarisations}} . \tag{2.85}$$

Rearranging to find the density of states per unit volume, and simplifying, we arrive at

$$g(k)\mathrm{d}k = \left(\frac{p}{2\pi^2}\right) k^2 \mathrm{d}k. \tag{2.86}$$

Next, we need to convert into energy. To do this, we need the dispersion relationship that connects energy and wavevector for a photon. This is given by $E = \hbar ck$, so $\mathrm{d}k = \mathrm{d}E/\hbar c$. Using this yields,

$$\tilde{g}(E)\mathrm{d}E = \left(\frac{p}{2\pi^2\hbar^3c^3}\right) E^2 \mathrm{d}E. \tag{2.87}$$

We are now in a position to determine how many photons there are per unit volume, in an energy interval between E and $E + \mathrm{d}E$, in thermal equilibrium at temperature T. To do that we need to combine **Equation 2.87** (the number of available states) with the Bose occupation factor (how these states are occupied), which gives us the density of photons with energy between E and $E + \mathrm{d}E$

$$\mathrm{d}N_{\mathrm{BB}} = \left(\frac{p}{2\pi^2\hbar^3c^3}\right) \frac{E^2\mathrm{d}E}{\mathrm{e}^{E/k_BT} - 1}. \tag{2.88}$$

Equation 2.88 accounts for *all* photons, regardless of their momentum ($\hbar k$). The direction of travel for these blackbody photons is isotropic, equally likely in any direction. Therefore the fraction travelling to within a small element of solid angle ($\mathrm{d}\Omega$) will be given by $\mathrm{d}\Omega/4\pi$, where 4π is the maximum solid angle. Together, this gives us Planck's law of radiation which gives the number of photons per volume, with an energy between E and $E + \mathrm{d}E$, travelling within a solid angle $\mathrm{d}\Omega$:

$$\frac{\mathrm{d}N_{\mathrm{BB}}}{\mathrm{d}E} = \left(\frac{E^2\mathrm{d}\Omega}{4\pi^3\hbar^3c^3}\right) \frac{1}{\mathrm{e}^{E/k_BT} - 1}, \tag{2.89}$$

where we have substituted $p = 2$ for the number of polarisation directions. Since all photons are travelling at c, we can now calculate the flux of photons from the blackbody spectrum, known as Planck's law, as

$$\phi(E,T,\Omega) = \left(\frac{1}{4\pi^3\hbar^3c^2}\right)\frac{E^2\,\mathrm{d}E\mathrm{d}\Omega}{\mathrm{e}^{E/k_BT}-1}. \tag{2.90}$$

Now, as mentioned earlier, the emission of a solar cell can be related to that in the dark by $\mathrm{e}^{(E_{\mathrm{F_n}}-E_{\mathrm{F_p}})/k_{\mathrm{B}}T}$ (recall **Equation 2.66**), and this then leads us to the generalised Plank's law, first derived by Würfel [24, 31, 32], as

$$\varphi(E,T,\mu,\Omega) = \left(\frac{1}{4\pi^3\hbar^3c^2}\right)\frac{E^2\,\mathrm{d}E\mathrm{d}\Omega}{\mathrm{e}^{(E-\mu)/k_BT}-1}. \tag{2.91}$$

$\varphi(E,T,\mu,\Omega)$ gives the total photon flux per energy interval, per solid angle, at a particular chemical potential and temperature. As discussed previously, in thermal equilibrium, $\mu = 0$ and under illumination $\mu = qV$ where V is the QFLS, which (in this model) is equivalent to the voltage across the solar cell.

We can now calculate the photocurrent generated by the solar cell (J) as the difference between absorbed and emitted photons, or

$$J(V) = q\int_0^\infty \varphi(E,T_{\mathrm{sun}},\mu=0,\Omega_{\mathrm{abs}})A(E)\mathrm{d}E - q\int_0^\infty \varphi(E,T_{\mathrm{cell}},\mu=qV,\Omega_{\mathrm{emit}})A(E)\mathrm{d}E, \tag{2.92}$$

where $A(E)$ is the absorptance of the cell, and Ω_{abs} and Ω_{emit} are the solid angles of absorption and emission respectively. The electrical power is given, as always, by the JV product, and so in theory **Equation 2.92** is sufficient to completely define the efficiency of a solar cell. However, this is quite opaque, and we are able to calculate some important parameters of solar cells from here. Firstly, at open-circuit, no photocurrent is extracted from the cell, and so all absorbed photons must be remitted into the ambient. For simplicity, we will assume a step absorbtance that is 0 below the bandgap, and 1 above it. Mathematically, this is expressed as

$$\int_{E_g}^{\infty} \varphi(E, T_{\text{sun}}, \mu = 0, \Omega_{\text{abs}}) \mathrm{d}E = \int_{E_g}^{\infty} \varphi(E, T_{\text{cell}}, \mu = qV_{\text{OC}}, \Omega_{\text{emit}}) \mathrm{d}E, \tag{2.93}$$

$$\int_{E_g}^{\infty} \Omega_{\text{abs}} \frac{E^2 \, \mathrm{d}E}{\mathrm{e}^{E/k_B T_{\text{sun}}} - 1} = \int_{E_g}^{\infty} \Omega_{\text{emit}} \frac{E^2 \, \mathrm{d}E}{\mathrm{e}^{(E - qV_{\text{OC}})/k_B T_{\text{cell}}} - 1}, \tag{2.94}$$

and now we make the Boltzmann approximation that $\left(\mathrm{e}^{E/k_{\text{B}}T} - 1\right)^{-1} \approx \mathrm{e}^{-E/k_{\text{B}}T}$. With this approximation, we can simplify our expression to

$$\int_{E_g}^{\infty} \Omega_{\text{abs}} E^2 \, \mathrm{e}^{-E/k_B T_{\text{sun}}} \, \mathrm{d}E = \int_{E_g}^{\infty} \Omega_{\text{emit}} E^2 \, \mathrm{e}^{-(E - qV_{\text{OC}})/k_B T_{\text{cell}}} \, \mathrm{d}E, \tag{2.95}$$

$$\Omega_{\text{abs}} \int_{E_g}^{\infty} E^2 \, \mathrm{e}^{-E/k_B T_{\text{sun}}} \, \mathrm{d}E = \Omega_{\text{emit}} \mathrm{e}^{qV_{\text{OC}}/k_B T_{\text{cell}}} \int_{E_g}^{\infty} E^2 \, \mathrm{e}^{-E/k_B T_{\text{cell}}} \, \mathrm{d}E, \tag{2.96}$$

which can be rearranged to give

$$\mathrm{e}^{qV_{\text{OC}}/k_B T_{\text{cell}}} = \frac{\Omega_{\text{abs}}}{\Omega_{\text{emit}}} \frac{\displaystyle\int_{E_g}^{\infty} E^2 \, \mathrm{e}^{-E/k_B T_{\text{sun}}} \, \mathrm{d}E}{\displaystyle\int_{E_g}^{\infty} E^2 \, \mathrm{e}^{-E/k_B T_{\text{cell}}} \, \mathrm{d}E}. \tag{2.97}$$

The integrals in the fraction within **Equation 2.97** can be readily integrated by parts, which gives

$$\mathrm{e}^{qV_{\text{OC}}/k_B T_{\text{cell}}} = \frac{\Omega_{\text{abs}}}{\Omega_{\text{emit}}} \frac{\left(E_{\text{g}}^2 k_{\text{B}} T_{\text{sun}} + E_{\text{g}} (k_{\text{B}} T_{\text{sun}})^2 + 2(k_{\text{B}} T_{\text{sun}})^3\right) \mathrm{e}^{-E_{\text{g}}/k_{\text{B}} T_{\text{sun}}}}{\left(E_{\text{g}}^2 k_{\text{B}} T_{\text{cell}} + E_{\text{g}} (k_{\text{B}} T_{\text{cell}})^2 + 2(k_{\text{B}} T_{\text{cell}})^3\right) \mathrm{e}^{-E_{\text{g}}/k_{\text{B}} T_{\text{cell}}}}. \tag{2.98}$$

In the following, we will write $\gamma(E_{\text{g}}, T) = \left(E_{\text{g}}^2 k_{\text{B}} T + E_{\text{g}} (k_{\text{B}} T)^2 + 2(k_{\text{B}} T)^3\right)$ for simplicity. This gives

$$\mathrm{e}^{qV_{\text{OC}}/k_B T_{\text{cell}}} = \frac{\Omega_{\text{abs}}}{\Omega_{\text{emit}}} \frac{\gamma\left(E_{\text{g}}, T_{\text{sun}}\right)}{\gamma\left(E_{\text{g}}, T_{\text{cell}}\right)} \exp\left(\frac{-E_{\text{g}}}{k_{\text{B}}} \left[\frac{1}{T_{\text{sun}}} - \frac{1}{T_{\text{cell}}}\right]\right), \tag{2.99}$$

and taking the logarithm gives

$$qV_{\mathrm{OC}} = k_{\mathrm{B}}T_{\mathrm{cell}} \ln\left(\frac{\Omega_{\mathrm{abs}}}{\Omega_{\mathrm{emit}}}\right) + k_{\mathrm{B}}T_{\mathrm{cell}} \ln\left(\frac{\gamma\left(E_{\mathrm{g}}, T_{\mathrm{sun}}\right)}{\gamma\left(E_{\mathrm{g}}, T_{\mathrm{cell}}\right)}\right) + E_{\mathrm{g}}\left(1 - \frac{T_{\mathrm{cell}}}{T_{\mathrm{sun}}}\right). \quad (2.100)$$

The final term in **Equation 2.100** is the Carnot factor, and has its origin in the fact that solar cells are essentially heat engines with the source being at the temperature of the sun's surface, and the sink being the temperature of the solar cell. With this in mind, it is perhaps less surprising that a Carnot factor is included [33]. The prefactor of E_{g} is due to carrier-thermalisation, and so charge-carriers have lost any excess energy and are at the band edge in this model. The first term within **Equation 2.100** is the so-called Boltzmann factor. It arises from the 'étendue expansion' between the incident sunlight (the sun subtends just $\Omega_{\mathrm{abs}} = 6.8 \times 10^{-5}$ Sr on the Earth's surface), and the emitted photons (into an entire hemisphere, so $\Omega_{\mathrm{emit}} = 2\pi$). The relative contribution of each of these terms can be seen in **Figure 2.12a**. The middle term in **Equation 2.100** actually boosts the V_{OC}, though its effect is minor – about 5 times less significant than the Carnot term at a bandgap of ~ 1.3 eV. Its origin in the difference in the temperature between the absorbed and emitted photon populations [30, 34]. This is because during thermalisation, entropy, as well as heat, is transferred to the lattice. This reduced entropy of the excited charge carrier population actually means the available energy, the Helmholtz free energy, F, is increased. (Recall $F = U - TS$, where U is the internal energy of the carrier distribution, S is the entropy of the carrier distribution.) [30]. As an aside, while the entropy of the charge carrier population is reduced, the entropy of the charge carriers *and* lattice has increased overall, and so we haven't violated any thermodynamic laws!

Above we have investigated the maximum voltage achievable in the detailed balance limit. The maximum current is somewhat easier to calculate. We make use of assumptions 2, 4 and 5 which, in this context, state that charge-carrier extraction is perfect and that it happens on much faster timescales than radiative recombination. Therefore the short-circuit current is given by

$$J_{\mathrm{SC}} = q \int_0^\infty \varphi(E, T_{\mathrm{sun}}, \mu = 0, \Omega_{\mathrm{abs}}) A(E) \mathrm{d}E. \tag{2.101}$$

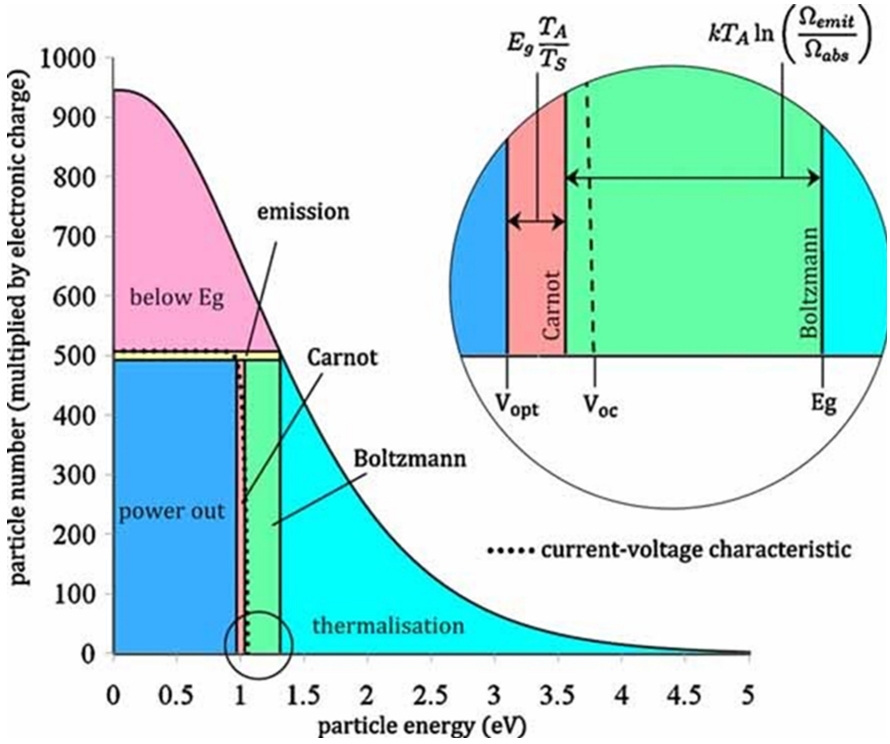
The information about the bandgap of the solar cell is encoded in $A(E)$. In real solar cells, an adapted version of **Equation 2.101** is used where φ is replaced by the AM1.5 spectrum, and $A(E)$ by $EQE(E)$, where the external quantum efficiency (EQE) gives the ratio of incident photons to extracted electron-hole pairs.

Interesting, there is no analytical expression for the ideal fill factor (FF), but there exists many very accurate approximate expression for the FF exist [35]. The simplest of these expressions is given by

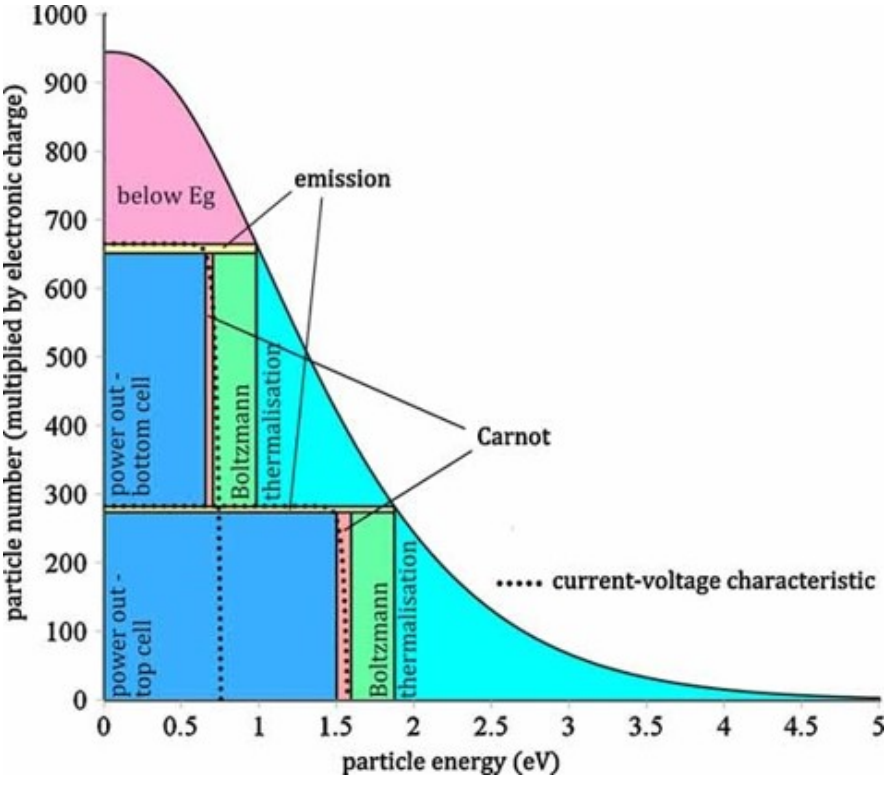
$$FF_{\mathrm{max}} = \frac{\nu_{\mathrm{OC}} - \ln(\nu_{\mathrm{OC}} + 0.72)}{\nu_{\mathrm{OC}} + 1}, \tag{2.102}$$

where $\nu_{\mathrm{OC}} = V_{\mathrm{OC}}/k_{\mathrm{B}}T$ is the 'reduced V_{OC}'. This expression is accurate to at 4 significant figures for even modest reduced open-circuit voltages ($\nu_{\mathrm{OC}} > 10$) [35].

While the losses presented in **Figure 2.12a** are intrinsic and unavoidable, higher efficiencies are, surprisingly, achievable. To do this, we need to violate the first assumption we made in the detailed balance limit. Explicitly, if we couple two absorbers together with different bandgaps, we can create a tandem solar cell. The intrincic losses of the tandem are presented in **Figure 2.12b**. By creating a tandem, the theoretical maximum efficiency leaps to $\sim 44\,\%$, mainly driven by reduced thermalisation losses, and greatly increased absorption range (there are now fewer photons with energy below the bandgap). This is the power of multijunction solar cells, by 'splicing' up the solar spectrum in this way, we have raised the maximum achievable efficiency by over a third. This hugely increased power generation for the same footprint is what gives multijunction solar so much potential for widespread, grid-scale energy generation.



(a)



(b)

Figure 2.12: *(a) Intrinsic losses occurring in a device with optimal* $E_g = 1.31$ *eV under one sun illumination. (b) Intrinsice losses for an optimal tandem device with bandgaps* $E_g = 1.87$ *eV and* $E_g = 0.98$ *eV for the top and bottom cells respectively. In each case, different loss pathways are shown and how they impact on the current and/or voltage of working solar cell. Reproduced with permission from Hirst et al., [30].*

2.2.3 Practical limitations

Thus far, we have discussed the ideal performance of a solar cell. In reality, recombination losses – as described in **Section 2.1.3** – play a significant role, as do parasitic resistances within the solar cell. These mean that solar cells in the real world violate many of the assumptions in the detailed balance derivations discussed above. For example, **assumption 1** is violated since there will always be some disorder in real materials which 'smears out' the band edge. This means there will be absorption of photons with energies below the bandgap, which will increase $J_{0,\mathrm{rad}}$, and so reduce the open-circuit voltage (V_{OC}) achievable. Further, as discussed in **Section 2.1.3**, not all recombination in metal halide perovskite solar cells is radiative, and in fact, at charge carrier densities comparable to operating solar cells, MHPs are often dominated by trap-mediated recombination. This violates **Assumption 4** and reduces the quasi-Fermi level splitting and hence device open-circuit voltage. In fact, each of the 5 assumptions are violated in real life scenarios, and this has significant implications on the V_{OC}, J_{SC}, and/or FF. Therefore it is important to understand how real-world effects influence the device performance of solar cells.

Transport losses

In a real solar cell, there will be resistance to charges flowing through the cell, contributing to the series resistance (R_{series}), and pathways through which charges bypass the external load, giving rise to the shunt resistance (R_{shunt}). These resistances result in power losses in the solar cell, mainly characterised by a reduction in the fill factor. Indeed, high series and low shunt resistance have a detrimental effect on the FF, whilst leaving the J_{SC} and V_{OC} broadly unchanged. For example, as can be seen in **Figure 2.13**, high series resistance makes the JV curve less steep near V_{OC}, and has minimal influence near J_{SC}. The opposite is true for low R_{shunt}, which is also shown in **Figure 2.13**.

A high series resistance originates from the charge-carriers 'struggling' to move through the device. This could be caused by low charge-carrier mobilities within the

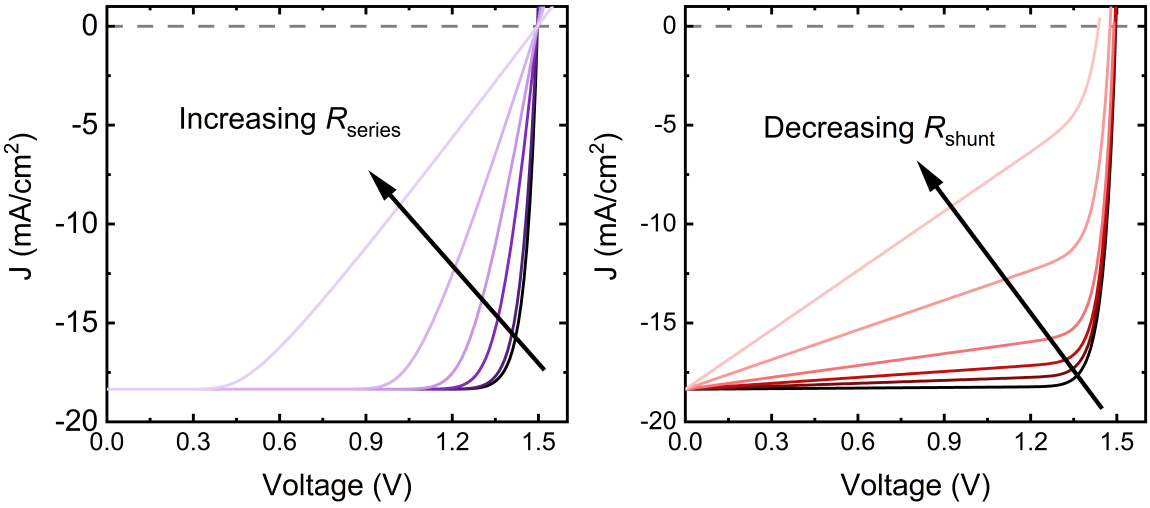


Figure 2.13: *Influence of R_{series} (left) and R_{shunt} (right) on solar cell device performance. High series and low shunt resistance have a detrimental effect on the fill factor (FF), whilst leaving the J_{SC} and V_{OC} broadly unchanged. High series resistance makes the JV curve less steep near V_{OC}, and has minimal influence near J_{SC}. Low shunt resistance has the opposite effect, mainly influencing the JV curve near J_{SC}.*

perovskite layer and/or the charge transport layers. I note that doping the organic transport layers allows one to by pass their low mobilities by increasing their conductivity through higher charge-carrier density. Low mobility within the bulk of the MHP would mean that electrons and holes were likely to recombine before reaching an electrode and being extracted. Therefore, this can be considered as a recombination loss owing to poor transport. This recombination between electrons and holes would reduce the number of charges being extracted to the external load, and therefore can reduce the short-circuit current density along with the FF substantially. Conversely, in the charge-transport layers, where only one charge-carrier density is much higher than the other, poor conductivity results in a loss of potential of the charge carriers but not a substantial decrease in the total concentration of charge-carriers. Therefore, if the transport layers are limiting, the J_{SC} is broadly unchanged, and a reduction in the FF is observed, consistent with the left panel in **Figure 2.13**. Another origin for high R_{series} is the contacts between layers in the solar cell device stack, which must be Ohmic for optimal performance. Since the charge carrier mobilities within metal halide perovskites is high ($\sim$ 30 cm^{2}V^{-1}s^{-1}[6]), transport throughout the bulk of the perovskite is unlikely to be the limiting factor, and the interfaces and transport within

the organic semiconductors (which have orders of magnitude lower mobilities) are likely to be the origin of the series resistance.

For optimal solar cell performance, a large shunt resistance (R_{shunt}) is required. A shunt is a pathway through which photogenerated charges can bypass the load, and so the energy of any charge passing through the shunt is not collected. The requirement for a high shunt resistance is even more critical under low light conditions, e.g. for indoor photovoltaics. In a low light regime, there are few photogenerated charge carriers, meaning that there is a smaller voltage driving charge extraction. In perovskite solar cells, the shunt resistance is likely to be heterogenious across a device area. The areas with the lowest shunt resistance are likely due to imperfections in the perovskite layr introduced during fabrication. These could include thickness variations, or even pinholes within the perovskite layer which can lead to 'shunts', or direct contact between the hole transport layer and electron transport layer, for example.

These factors can in fact be included in an updated version of the solar cell diode equation, where were presented the ideal version in **Equation 2.78**. An equivalent circuit for solar cell including R_{series} and R_{shunt} is shown in **Figure 2.14**.

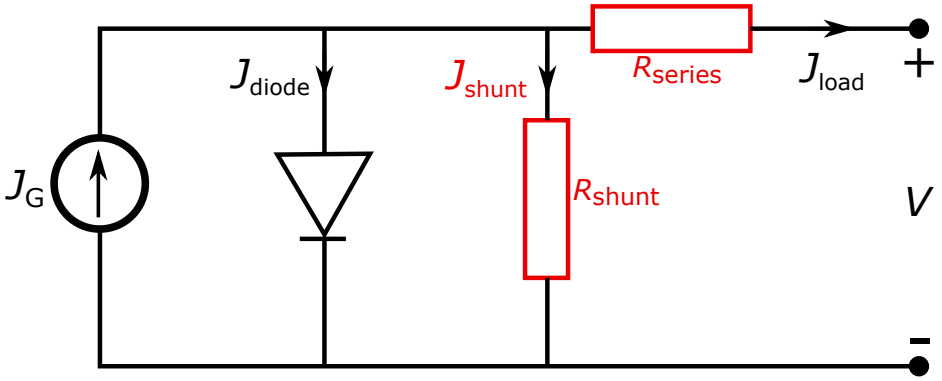


Figure 2.14: *Equivalent circuit of a solar cell including shunt and series resistance which are shown in red. The current source produces a current equivalent to J_{G}, and this is split between the diode, shunt and the load. At J_{SC}, no current passes through the diode, and so the shunt is the factor resulting in J_{SC} being less than the generated current J_{G}.*

Together, this results in an equation for the current through the load of

$$J(V) = J_{\text{G}} - J_0 \left[\exp\left(\frac{qV - JR_{\text{series}}}{k_{\text{B}}T} \right) - 1 \right] - \frac{(V + JR_{\text{series}})}{R_{\text{shunt}}}. \tag{2.103}$$

Consistent with our previous discussion, if $R_{\text{series}} \to 0$ and $R_{\text{shunt}} \to \infty$, **Equation 2.103** returns to the ideal solar cell equation. It is not possible to directly measure J_0, R_{series} or R_{shunt}, but it is possible to get an estimate for these parameters by fitting a measured JV curve to **Equation 2.103**. However, we have not yet accounted for the effect of non-radiative recombination on the device characteristics.

Ideality factor

The ideality factor n_{id} is a 'fitting parameter' that determines how close a solar cell is to ideal operation. For conventional pn junction solar cells, the ideality factor (n_{id}) is 1 for ideal operation and ranges to 2 for completely unideal solar cells. It is included in **Equation 2.103** in a straightforward manner, since it relates only to how 'ideal' the diode is, and so only factors into the exponential as

$$J(V) = J_{\text{G}} - J_0 \left[\exp\left(\frac{qV - JR_{\text{series}}}{n_{\text{id}} k_{\text{B}} T} \right) - 1 \right] - \frac{(V + JR_{\text{series}})}{R_{\text{shunt}}}. \tag{2.104}$$

While technically possible to extract n_{id} by fitting a JV curve as discussed previously, this not regularly done. More commonly, the n_{id} would be extracted from a dark JV curve, wherein $J_{\text{G}} = 0$, and then finding the slope when plotted on a log scale. However, the presence of R_{series} and R_{shunt} complicates the analysis significantly. For example, the influence of R_{shunt} at low voltages is often not negligible, particularly for perovskite solar cells, and so leads to an erroneous determination of n_{id}. Instead, let us consider **Equation 2.104** at open-circuit. In this case, $J = 0$, and this completely removes the influence of the series resistance, which then simplifies the analysis considerably. It is then possible to perform some straightforward mathematical manipulations, as follows

$$J_{\mathrm{G}} - J_0 \left[\exp\left(\frac{qV_{\mathrm{OC}}}{n_{\mathrm{id}}k_{\mathrm{B}}T}\right) - 1\right] - \frac{V_{\mathrm{OC}}}{R_{\mathrm{shunt}}} = 0, \tag{2.105}$$

$$\implies \frac{J_{\mathrm{G}} - V_{\mathrm{OC}}/R_{\mathrm{shunt}}}{J_0} = \exp\left(\frac{qV_{\mathrm{OC}}}{n_{\mathrm{id}}k_{\mathrm{B}}T}\right) - 1, \tag{2.106}$$

$$\implies \frac{qV_{\mathrm{OC}}}{n_{\mathrm{id}}k_{\mathrm{B}}T} = \ln\left[\frac{J_{\mathrm{G}} - V_{\mathrm{OC}}/R_{\mathrm{shunt}}}{J_0} + 1\right], \tag{2.107}$$

$$\implies V_{\mathrm{OC}} = \frac{k_{\mathrm{B}}T}{q}\, n_{\mathrm{id}} \ln\left[\frac{J_{\mathrm{G}} - V_{\mathrm{OC}}/R_{\mathrm{shunt}}}{J_0} + 1\right]. \tag{2.108}$$

If we make two (often well justified) assumptions that the effect of the shunt resistance is small, and that $J_{\mathrm{G}}/J_0 \gg 1$, then we arrive at

$$V_{\mathrm{OC}} = \frac{k_{\mathrm{B}}T}{q}\, n_{\mathrm{id}} \ln\left(\frac{J_{\mathrm{G}}}{J_0}\right). \tag{2.109}$$

Additionally with the knowledge that, for most cases, the generation current scales linearly with illumination intensity (i.e. $J_{\mathrm{G}}(nI) \approx nJ_{\mathrm{G}}(I)$, where n is factor by which the illumination intensity I is increased), we can then perform illumination dependent V_{OC} measurements, and the slope of V_{OC} against illumination intensity (or 'suns') will be proportional to the ideality factor. This measurement is often call a 'suns-V_{OC}' measurement for this reason [36].

Practically, when performing these experiments it is (often) straightforward to identify when shunts are playing a significant role. At the lowest illumination intensities (lowest J_{G}), the effect of the $V_{\mathrm{OC}}/R_{\mathrm{shunt}}$ term is no longer negligible, and instead causes the measured V_{OC} to deviate from the straight line observed at higher intensities. The region at low illumination intensities can, for most analyses, be safely neglected since it is far from charge-carrier densities of interest. However, this does highlight an interesting point – while often stated as simple one value, n_{id} is actually voltage-dependent! In conventional solar cells, at low bias, it is typical to find $n_{\mathrm{id}} \approx 2$ and $n_{\mathrm{id}} \approx 1$ at high bias.

In multi-layer device architectures such as those found with MHP solar cells, the ideality factor depends on several additional factors including energetic alignment be-

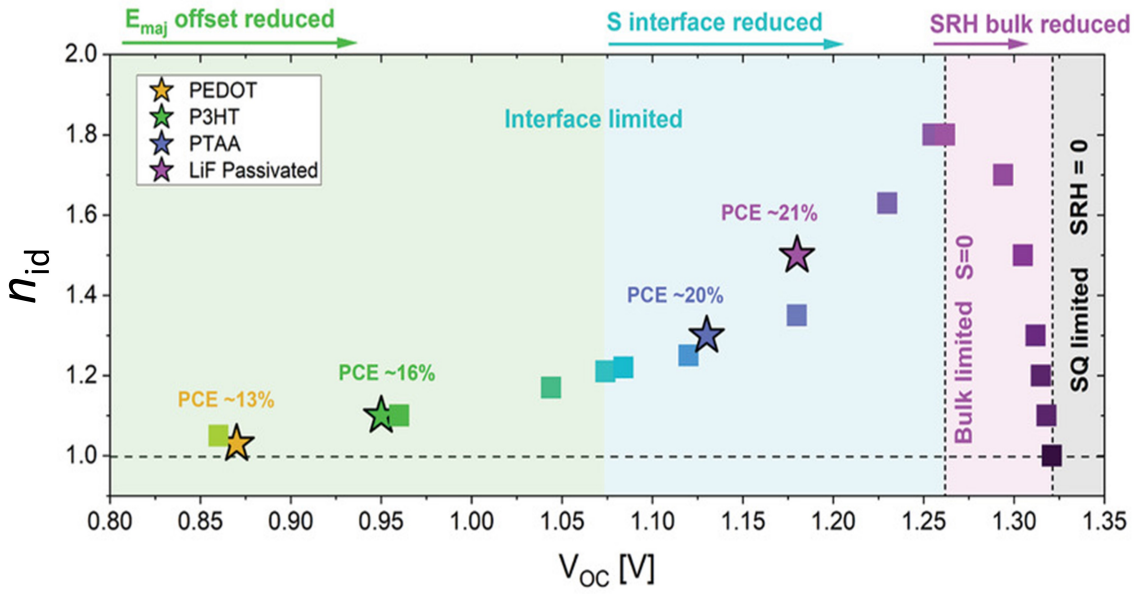


Figure 2.15: *Simulated ideality factor dependence on the open-circuit voltage (at AM1.5 illumination) for p-i-n MHP solar cells. First the energetic alignment at the HTL/MHP interface is reduced which delivers higher open-circuit voltage with only a small increase in the ideality factor. Then surface recombination velocity S, modelled to be identical at both interfaces, is varied from 1×10^5 to $0\,\mathrm{cms}^{-1}$. In this case, the increase in V_{OC} sees a corresponding rise in the ideality factor. Once the interface recombination has been minimised, the bulk non-radiative recombination was reduced by increasing the bulk carrier lifetime from 400 ns to 10 µs. The black region represents the detailed-balance (SQ) limit in the case of bimolecular recombination only. In this regime, the ideality factor is reduced for enhanced V_{OC}. The stars indicate experimental V_{OC}s and n_{id} values for cells characterised by different degree of interface recombination and E_{maj} offsets. Figure and caption adapted from [37].*

tween the MHP semiconductor and the adjacent charge transport layers, surface recombination velocities and the recombination within the bulk of the perovskite, which complicates the interpretation of the ideality factor. The influence of these factors is summarised in **Figure 2.15**. Counter-intuitively, when the interfaces are limiting the achievable V_{OC}, either through poor energetic alignment or high interfacial recombination, a higher ideality factor is actually indicative of a higher preforming solar cell. The trend is reversed when the quality of the bulk material is the limiting factor for efficient device performance. In this case, n_{id} is reduces from near 2 for high trap-mediated recombination rate (k_1) and trends to 1 as $k_1 \to 0$ and a corresponding increase in the V_{OC} is observed. This matches the trend expected from conventional semiconductors. However, since almost all MHP solar cells are limited by the interfaces with the charge

transport layers, one often discovers a higher ideality factor for the best performing devices.

2.3 Metal Halide Perovskites

Metal halide perovskite (MHP) semiconductors have caused a revolution in the field of photovoltaic research. This class of materials gets it name as it shares the same chemical formula, ABX_3, and crystal structure as the mineral $CaTiO_3$. $CaTiO_3$ is a naturally occurring mineral known as Perovskite, named after mineralogist Lev Perovski. However, there are a wealth of materials in the MHP family, many of which do not in fact adopt the perovskite crystal structure, nevertheless 'perovskite' is still used to describe them all.

In MHPs, A is a monovalent cation, typically methylammonium (MA^+, $CH_3NH_3^+$), formamidinium (FA^+, $HC(NH_2)_2^+$), caesium (Cs^+), or a mixture thereof; B is a divalent metal cation and is lead (Pb^{2+}) in this work; and the X-site is occupied by a monovalent halide, usually a mixture of iodide (I^-) or bromide (Br^-). The properties of the MHP semiconductor can be readily changed by tuning its chemical composition, which will be discussed in more detail later. The typical, cubic ABX_3 perovskite crystal structure is shown schematically in **Figure 2.16**. However, depending on factors including composition, temperature, pressure, or even synthesis route, the MHP unit cell can have orthorhombic or tetragonal symmetry [38–40].

The choice of A-, B- and X-site constituents can change the properties of the resulting semiconductor dramatically. However, due to the differing (average) ionic radii of the possible constituents of the perovskite lattice, not all combinations readily form the perovskite structure at room temperature and atmospheric pressure. To a first approximation, one can consider the Goldschmidt tolerance factor [41] which is given by

$$t = \frac{R_\mathrm{A} + R_\mathrm{B}}{\sqrt{2}(R_\mathrm{B} + R_\mathrm{X})}, \tag{2.110}$$

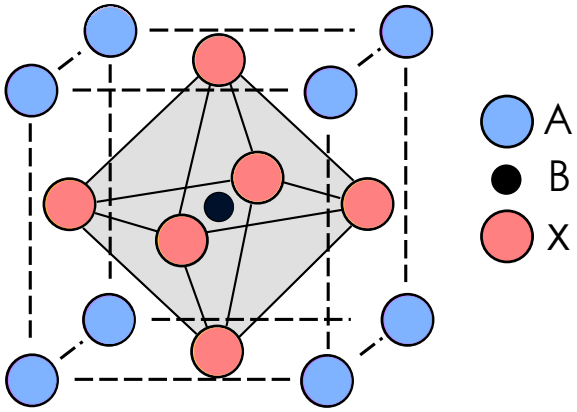


Figure 2.16: *Schematic of the cubic ABX_3 MHP crystal structure. The A-site is occupied by a monovalent cation, e.g. methylammonium, formamidinium, caesium (Cs^+), or a mixture thereof; B denotes a divalent metal cation and is lead (Pb^{2+}) in this thesis; and the X-site is a monovalent halide anion, typically a mixture of iodide (I^-) or bromide (Br^-).*

where R_A, R_B, R_X are the ionic radii of the A-, B- and X-sites respectively. A perovskite is likely to form for $0.8 < t < 1.0$, and outside of this range different structures will form. It is worth stressing that, in the case of organic-inorganic metal halide perovskite, the Goldschmidt tolerance factor should be treated only as a rough guide, and several studies have focused on extending its validity [42, 43]. This is because the Goldschmidt tolerance factor is geometrical in origin and assesses whether an atom (or molecule) with ionic radius R_A can fit within the BX_3 framework. However, in the case of MHPs, the A-site is often occupied by an organic molecule, which is not spherical and so has a poorly defined ionic radius.

Interestingly, studies concerning halide perovskites have been reported since the late 1800s – for example Wells investigated the crystal structure of Cs-based halide perovskites in 1893 [44]. Then, the first reports of organic-inorganic MHPs ($MAPbX_3$ and $MASnX_3$) were published in the late 1970s by Weber [45, 46]. Indeed, these reports even demonstrated alloying of the X-site [46], which is key research theme today and will be discussed in detail later in this thesis. The additional major developments were made in the mid-late 1990s by Mitzi and co-workers who measured charge-carrier

transport properties of MHPs [47, 48] and were the first to demonstrate room temperature electroluminsecene from MHPs [49]. The first report of using MHPs in a light-harvesting context came from the group of Miyasaka in 2009, who were able to fabricate a 3.8 % efficient dye-sensitised solar cell [50]. Following this development, Lee et al. made the major breakthrough by demonstrating that metal halide perovskites were not just a dye-molecule, but a semiconductor in their own right [51]. They did this by using an inert Al_2O_3 scaffold over which they deposited the perovskite. In this architecture, the perovskite would have to transport charge carriers over a substantial distances ($\sim$ 100 nm or more) in order for them to reach the electrodes. In this work, solar cells with PCEs exceeding 10 % were fabricated, providing strong evidence that charges were being efficiently transported in MHPs. Indeed, this was later quantified, first by Stranks et al. who observed significant photoluminescence (PL) lifetime shortening when the perovskite was coated in a charge extraction layer and, using basic drift-diffusion modelling, calculated diffusion lengths in excess of 1 μm for both electrons and holes [52]. This observation has been confirmed by many other researchers with a variety of techniques [7]. These long charge-carrier diffusion lengths are one of the properties that contributes to the immense success of solar cells based on MHP and has enabled the widespread used of the planar n-i-p or p-i-n device structures. Importantly, these planar heterojunction cells are not only more straightforward to fabricate on a laboratory scale, but they also lend themselves more directly towards large scale deposition, e.g. through thermal evaporation [53].

In addition to the long diffusion lengths discussed above, MHPs have several other properties that have enabled the PCEs of their solar cells to skyrocket over the past decade, as can be seen in **Figure 2.17**. Typically, metal halide perovskites have direct bandgaps and high absorption coefficients, which means that an absorber thickness of $\sim$ 500 nm is sufficient to efficiently harvest the solar spectrum [7, 39, 55]. In addition, high charge carrier mobilities in excess of 30 $cm^2V^{-1}s^{-1}$have been widely reported [7, 56, 57], as have long charge carrier lifetimes [6, 9, 56]. In fact, it is these two properties combined that enable the long charge carrier diffusion lengths discussed

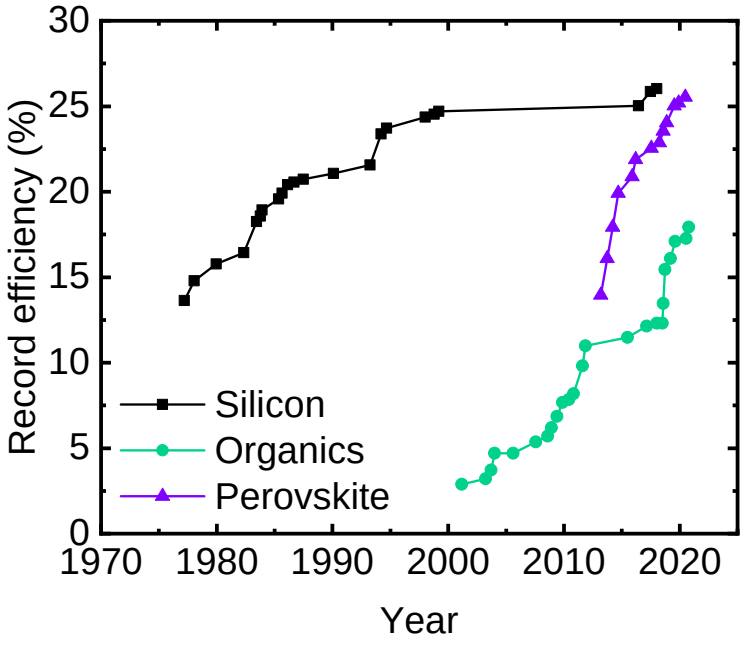


Figure 2.17: *Comparison of research solar cell record efficiency development. We show the incumbent technology crystalline silicon (black squares), bench marked against emerging technologies organic (green circles) and metal halide perovskite (purple triangles) solar cells. As is evident in the figure, PCEs of solar cells based on MHPs have skyrocketed at an unprecedented pace. Data taken from [54].*

earlier. Moreover, despite being processed from solution at low temperature, MHPs demonstrate low energetic disorder characterised through low Urbach energies [58, 59]. All these properties taken together are what have enabled the unprecedented rise in the performance of perovskite solar cells.

Arguably the most important and useful property of metal halide perovskites is their bandgap tunability. This class of semiconductors can tolerate a remarkable amount of disorder within its structure without severely hindering its optoelectronic performance – practically unique in the field of semiconductors. This means a large degree of alloying on the perovskite crystal structure (ABX_3) can be tolerated [60, 61]. The precise choice of the constituents of the perovskite crystal structure dramatically influence the optoelectronic properties of the MHP.

Primarily, the bandgap of metal halide perovskites is controlled by alloying on the B-site or X-site [62]. This is because the valence band and conduction band arise from orbitals of the B- and X-site consituents [62–64], and the A-site's influence on the bandgap is related mainly to the size of the unit cell, and so degree of overlap between

orbitals [64–66]. Pb is alloyed with Sn on the B-site of the perovskite, which results in 'bandgap bowing', with the minimum being ~ 1.25 eV for Sn quantities from $30-50\%$ [67, 68]. There is a rich literature on mixed Pb:Sn perovskites, a recent review can be found in Ref. [69], but they will not be discussed further hereafter.

The bandgap of the perovskite semiconductor can be increased by increasing the ratio of bromide:iodide on the X-site of the crystal lattice [61, 62, 70]. This increased bandgap makes MHPs ideal candidates for top cells in tandem photovoltaics. Efficient tandem solar cells require precisely paired bandgaps, such that each subcell generates the same current (called 'current-matching'). This can often be difficult to achieve for conventional semiconductors whose bandgaps are much more 'rigid'. However, MHP allow for precise fine-tuning of their bandgap, which makes them ideal candidates multijunction applications [71]. A comprehensive review of the properties of the most technologically relevant wide bandgap perovskites is given in **Section 2.3.1**.

Choice of the A-site has a relatively minor influence on the bandgap of the metal halide perovskite semiconductor. This has been rationalised by computational studies which have demonstrated that the orbitals which contribute to the band extrema originate primarily from metal and halide orbitals [62, 64], as discussed earlier. The A-site's orbitals contribute to states deeper within the bands. This is not to say that the A-site is without influence however. For example, the Cs-content on the A-site can introduce 'octahedral tilting', which alters the overlap between the orbitals in the crystal, and hence changes the bandgap [72]. In fact, despite not directly influencing the conduction or valence bands, the choice of the A-site composition is so critical that perovskites are usually referred to by the choice of the A-site, e.g. 'FAMA', 'FACs', 'triple cation' etc.. In fact, alloying of the A-site appears to be crucial for the best performing perovskite solar cells.

Single A-cation The archetypal perovskite is $MAPbI_3$, which has been extensively studied, though has many issues regarding its structural and thermal stability [73–75]. In principle, direct replacement of MA with formamidinium (FA) would be be

beneficial since the bandgap would be reduced towards the ideal for a single junction (owing to FA's larger size), and hence allow for more of the solar spectrum to be harvested. However, 'standard' $FAPbI_3$ is highly unstable in ambient conditions, readily transforming from the photoactive black (α) phase, into the non-perovskite yellow (δ) phase [61, 76, 77]. It is worth noting that the current world record efficiencies are, nominally, using $FAPbI_3$ as the photoactive material which has been stabilised in its α-phase by one strategy or another. However, many of these works on '$FAPbI_3$'contain MA or Cs, either explicitly [78–80], or only discovered through careful reading of their experimental methods, for example, one paper nominally investigating $FAPbI_3$ contained 35 mol% MACl within the precursor solution [81]. Therefore, in my opinion at least, one cannot truly consider these materials as comprising a single A-cation. This alloying is likely to induce a slight tilting of the lead-halide octahedra, which stabilises the structure [82].

While often neglected, the fully inorganic perovskites ($CsPb(I_xBr_{1-x})_3$) are also promising materials for optoelectronic applications [83], especially since they have outstanding thermal stability [84]. The bandgap of $CsPbBr_3$ is substantially too wide $\sim$ 2.4 eV for high performing solar cells, though it is the 'base' material in many light-emitting applications [85]. The bandgap of $CsPbI_3$ is $\sim$ 1.72 eV and so is much more promising for photovoltaic applications. Indeed, it is almost ideally suited as the top cell in perovskite-on-silicon tandems [86]. However, regrettably this material is thermodynamically stable in the photo-inactive δ-phase at room temperature, and the photoactive α-phase is only stable above 300 °C [83, 87]. Efforts have been made to stabilise $CsPbI_3$ at room temperature [88], but further work in this area is necessary.

Alloyed A-site As discussed above, the (truly) single A-site cation perovskites each have significant challenges. As such, alloyed A-site perovskites have proved to be be outstandingly successful. The highest efficiencies tend to be delivered for a mixed FAMA perovskite, first reported in Ref. [89]. For example, $FA_{0.83}MA_{0.17}PbI_3$, which delivered efficiencies above 18 % as early at 2015 [77, 90]. This FAMA family continues

to be successful, now routinely delivering efficiencies well in excess of 20 % [91, 92].

At a roughly the same time (2014), in a similar vein, binary alloys of either MA or FA with Cs were being investigated. Choi and coworkers investigated the addition of Cs into $MAPbI_3$ [93], achieving a PCE 8 %, modest even in 2014. These MACs based perovskites never 'took off', perhaps due to the addition of Cs in these compositions not overcoming the issues highlighted for pure $MAPbI_3$. In contrast, FACs based perovskites have proved to be hugely successful, and will be explored in detail over the course of this thesis. The first FACs alloy was reported by Jin-Wook Lee in group of Nam-Gyu Park in 2015, wherein they identified enhanced moisture stability and improved device performance when 10 % of the FA was replaced with Cs [94]. Following this work, Yi et al. proposed the enhanced stability is due to the miscibility of the α phases of $FAPbI_3$ and $CsPbI_3$, whereas there is a large energetic barrier to the mixing of their respective δ phases [95]. The vast potential of the FACs family of perovskites was further highlighted by McMeekin et al., wherein they demonstrated simultaneous alloying on the A- and X-sites [70]. This allowed for the identification of a perovskite composition that possessed good stability, and was well suited for use in a perovskite-on-silicon tandem. A key material identified within this work, namely $FA_{0.83}Cs_{0.17}Pb(I_{0.6}Br_{0.4})_3$, is investigated in detail in this thesis in **Chapters 5 & 6**.

The theme of alloyed A-sites goes yet further. Saliba and co-workers identified that the mixed FA/MA perovskties were delivering the highest efficiencies, but that the smaller Cs cation was beneficial for film formation and stability, and sought to combine these positive properties into one perovskite [96]. In this work, the authors showed that small Cs inclusion was sufficient to suppress δ phase impurities that are a perennial challenge in FAMA perovskites. In this work, stabilized PCEs exceeding 21 % were achieved, which was excellent in 2016. Moreover, the so-called 'triple cation' perovskite films are both more reproducible (less sensitive to processing conditions) and more thermally stable than FAMA perovskites [96]. These were all major advances, and triple cation perovskites are still widely implemented today [97, 98]. Indeed, they are the subject of **Chapter 4**.

A quadruple Rb/Cs/FA/MA perovskite was implemented, again first developed by Saliba and co-workers [99]. The incorporation of rubidium resulted in extremely high open-circuit voltages with respect to the bandgap investigated. While popular for some time, the quadruple cation has fallen out of favour, perhaps due to the additional preparation complexity required for such perovskites.

2.3.1 Methylammonium-free Wide Bandgap Perovskites

Manuscript related to this Section

The discussion presented in this Section is adapted from a manuscript due to be submitted, A. J. Ramadan, **R. D. J. Oliver**, M. B. Johnston, H. J. Snaith, *Progress and prospects in methylammonium-free wide bandgap metal halide perovskite photovoltaics*, *Manuscript in preparation.*

As previously discussed, metal halide perovskite (MHP) semiconductors have been the subject of intense research effort in the photovoltaic and broader optoelectronics research community over the past decade. This has led to soaring power conversion efficiencys (PCEs) of single junction perovskite solar cells, which now rival those achievable with crystalline silicon [54]. This is largely due to their ease of manufacture coupled with excellent optoelectronic properties which we have already discussed in detail earlier. Another key property of metal halide perovskites is their broadly tuneable optoelectronic properties achievable through careful choice of the constituents in the ABX_3 crystal structure. In such a way, a boundless choice of bandgaps between 1.2 – 3.2 eV are achievable [65]. Owing to this property, perovskites can be tailored toward a specific photovoltaic application. One particularly significant application is for use as the top cell in a tandem photovoltaic device, which requires a bandgap between 1.67 – 1.8 eV [71, 100–102]. Indeed, it is (widely) believed that perovskite semiconductors will first make an impact in the global photovoltaic market as the top cell component

of tandem technologies, first in conjunction with crystalline silicon (c-Si) and then in perovskite/perovskite tandems. The MA-free wide bandgap ($E_g \sim 1.8\,\text{eV}$) perovskite required all-perovskite tandems are investigated in **Chapters 5 & 6**.

The bottom cells in "hybrid" perovskite-based tandem solar cells perform excellently and are not the main limiting factor for future tandem developments. Crystalline silicon is well-established as a high efficiency photovoltaic technology and copper indium gallium selenide (CIGS) is a well-industrialised technology. For all-perovskite tandem photovoltaic devices, the bottom cells, fabricated from alloying Pb and Sn on the B-site, have recently enjoyed an outstanding improvement in their photovoltaic device performance, and are now approaching their thermodynamic limit for open-circuit voltage [103], and efficiencies approaching 24 % [104]. Overcoming reproducibility and long-term stability issues for the low bandgap Pb-Sn perovskites are key challenges, but is not the subject of this Section. The initial power conversion efficiency of wide bandgap perovskite top cells have not experienced the same successes and are therefore currently the subject of significant investigation.

Despite recent progress, devices based on high-bandgap perovskite semiconductors are still constrained far below their theoretical maximum performance. This is largely due to the open-circuit voltage (V_{OC}) of such cells not increasing with increasing bandgap as expected, instead plateauing at $\sim 1.2\,\text{V}$ [105]. This limited performance is particularly true for the most stable – and hence technologically relevant – materials choices. In this case we refer to perovskites that do not include methylammonium on the A-site, the instability of which is well documented [74, 106–108].

In this Section, we provide an overview of the developments within the field of methylammonium-free wide bandgap metal halide perovskite photovoltaics. This Section will focus on materials with bandgaps within the range of $1.6 - 1.9\,\text{eV}$ and with the composition $FA_{1-x}Cs_xPb(Br_yI_{1-y})_3$. In particular, studies which have focused on enhancing the interfaces within wide bandgap MHP solar cells are highlighted. The all-inorganic wide bandgap photovoltaics are not discussed here as there are already several excellent reviews on this area of research [109–111].

Metal Halide Perovskite Light Emitting Diodes (LEDs)

Alongside their implementation in photovoltaics, wide bandgap metal halide perovskites have proven highly successful as the emissive layer in light emitting diode (LED) devices [112–114]. This is an excellent indicator of their potential for success in photovoltaic applications. Within the perovskite LED community, photoluminescence quantum yield (PLQY) measurements are routinely used to screen perovskite compositions and determine their potential for producing high electroluminescence external quantum efficiency (EL-EQE) LED devices. There have been many reports within the LED literature of PLQY values exceeding 30 % for wide bandgap perovskite thin-films, however reported PLQY values for similar perovskites employed in solar cells are typically at least an order of magnitude lower [115–119]. It is well established that through applying quasi-Fermi level splitting (QFLS) analysis, PLQY measurements can predict the maximum open-circuit voltage (V_{OC}) achievable with a specific materials system or device stack [16]. As such, there is a direct correlation between higher PLQY and higher achievable V_{OC} values. We therefore believe that the successes of the perovskite LED community in developing perovskite thin-films with impressive PLQY values and LED devices with high EL-EQE efficiencies is an excellent indicator that the voltage losses plaguing the wide bandgap PV community are not inherent to the materials system. Instead, we posit that these losses are a direct result of the routes and methods through which we fabricate our perovskite materials and corresponding solar cell devices.

The work of the perovskite LED community indicates that there is considerable cause for optimism and highlights the need for more efforts on understanding both the fundamental properties of our MA-free wide bandgap perovskite materials and how our processing routes and device structures impact our corresponding device performances.

Crystal structure

Whilst considerable efforts have been made to understand the crystal structure of the wide bandgap $FA_{1-x}Cs_xPb(Br_yI_{1-y})_3$ materials we do not yet have a complete understanding of their structural properties and we are lacking crystal structures for many of

these perovskites. This is partly due to the vast number of potential perovskite compositions within the $FA_{1-x}Cs_xPb(Br_yI_{1-y})_3$ family and the fact that their structures are often informed by the processing environment and routes through which their corresponding thin films are fabricated. As such our understanding of the structure of these materials has been informed both by our understanding of the single cation, single halide perovskites systems and on a case-by-case basis. The recent work of An and co-workers offers an in-depth and broad overview of the structure of 49 different $FA_{1-x}Cs_xPb(Br_yI_{1-y})_3$ compositions, many of which have bandgaps > 1.6 eV, investigated using lab-based X-ray diffraction and grazing incidence wide angle X-ray scattering (GIWAXS) investigations [120]. This work presents a valuable library of structural information for a wide range of MA-free wide bandgap perovskites.

Halide segregation

Halide segregation is a process in which the different halide species physically separate in the perovskite material, usually driven by above bandgap illumination or current injection [121, 122]. The separation of different halide species leads to a heterogeneous energy landscape within the perovskite semiconductor which has numerous implications for both the fundamental physics and device applications of wide bandgap perovskites. For an in-depth review of halide segregation and its influence on material properties we recommend the perspective from Knight and Herz [121], herein we instead briefly discuss on the implications of halide segregation on device performance.

As the bromide-to-iodide ratio is increased on the X-site in the perovskite crystal structure, the bandgap is increased. However, the open-circuit voltage does not follow a similar trend, as would be expected, and instead plateaus after $\sim 20\,\%$ Br inclusion to a value of ~ 1.2 V [105]. At similar Br fractions, halide segregation becomes prevalent under illumination which results in the formation of iodide-rich regions which possess lower-than-desired bandgaps. Therefore, charges in the well-mixed wide bandgap phase funnel into these regions, losing energy in the process and hence reduce the achievable open-circuit voltage of high Br-content perovskites. This funnelling results in high

charge carrier densities in the I-rich phase, which in turn leads to extremely prevalent low energy photoluminescence [121, 123–126].However, the degree to which this process affected device performance was not fully understood.

Mahesh and co-workers quantified the extent to which halide segregation affects the open-circuit voltage in state-of-the-art metal halide perovskite solar cells [127]. In this study, we measured the band-edge of full photovoltaic devices using high sensitivity Fourier-transform photocurrent spectroscopy to determine the external quantum efficiency of devices before and after halide segregation. We then used detailed-balance calculations to fully quantify the effects of halide segregation on PV device performance. In this way, we were able to unambiguously determine the V_{OC} penalty due to halide segregation, discovering that halide segregation could only account for a small fraction of the lost voltage, and there were more significant losses elsewhere in the device architecture. This observation is true for the most commonly employed perovskite A-site compositions (e.g. FACs, FAMA, and FAMACs), and so demonstrates that careful optimisation of the device architecture of wide bandgap perovskite solar cells is of the utmost performance to unlock their full potential. Explicitly, halide segregation could account for an additional V_{OC} loss of ~ 100 mV, which is small compared to the non-radiative losses present in the device causing over 400 mV of lost voltage.

By reconciling the detailed-balance calculations with experimental observations, we discovered some remarkable properties about the halide segregation process and its influence on device performance. Firstly, only a remarkably small volume of the film, $\sim 1\,\%$, needs to have undergone halide segregation to have a significant impact on the device's V_{OC}. This observation of small, segregated domains has since been explicitly observed during cathodoluminescence measurements [128]. In addition, we were able to provide quantitative evidence the segregated, minority phase suffers from less non-radiative recombination than the majority, well-mixed phase, through a 19-fold enhanced electroluminescence quantum efficiency. These observations are not simply limited to $\mathrm{FA}_{1-x}\mathrm{Cs}_x\mathrm{Pb}(\mathrm{Br}_y\mathrm{I}_{1-y})_3$ perovskites and agree strongly with the observations made by Peña-Camargo et al. on the triple-cation FAMACs perovskite [129]. These

observations strongly indicate that a thorough understanding of the non-radiative loss mechanisms within wide bandgap perovskites is necessary, and an efficient mitigation strategy must be developed to unlock the potential of these materials for the eventual realisation of highly efficient tandem solar cells.

Progress in photovoltaic device performance

Whilst the optimum use of wide bandgap perovskite solar cells is through their implementation in tandem photovoltaics, the field has so far focused predominantly on their use in single junction solar cells. This has enabled great strides to be made in the understanding of wide bandgap perovskite device physics without the complicating factors of a recombination layer and second solar absorber material in connected series. Across the literature several approaches have been developed with the aims of enhancing the efficiency, stability and in some cases both. We summarise these approaches and highlight the areas we feel need more investigation by the community.

The current state of the art performance of p-i-n architecture $FA_{1-x}Cs_xPb(Br_yI_{1-y})_3$ solar cells was achieved by Chen and co-workers in their development of perovskite-organic monolithic tandem photovoltaics [130]. In their work they used a $FA_{0.75}Cs_{0.25}Pb(I_{0.6}Br_{0.4})_3$ perovskite (optical bandgap, E_g = 1.79 eV, determined by Tauc plot). The authors achieved outstanding device with a reported PCE of 17.8 % given by a fill factor (FF) of 78.9 %, J_{SC} of 17.90 mA cm^{-2}, and V_{OC} of 1.26 V. This was achieved by passivation of the interface between the HTL, in this work NiO_x, and the perovskite absorber with benzylphosphonic acid. Remarkably, this V_{OC} constitutes an increase of 80 mV to the control condition, implying a 20-fold enhancement of the radiative efficiency in full devices due to the HTL passivation alone.

Another impressive report of high-performance devices comes from Brinkmann and co-workers, also focussing on the optimisation of the HTL/perovskite interface for perovskite-organic tandem devices [131]. In this work a different self-assembled monolayer MeO-2PACz ([2-(3,6-Dimethoxy-9H-carbazol-9-yl)ethyl]phosphonic acid) is reported as the HTL, in addition to phenethylammonium iodide surface passivation of

the perovskite/electron transport layer (ETL) interface which produced devices with outstanding V_{OC} of 1.34 V for a $FA_{0.8}Cs_{0.2}Pb(I_{0.5}Br_{0.5})_3$ perovskite with an optical bandgap of 1.85 eV (determined through $d(EQE)/dE$). These studies are in strong agreement with our recent report highlighting that the HTL/perovskite interface is the most challenging in p-i-n devices and is deserving of the most attention [132].

Interestingly, the state-of-the-art n-i-p devices perform comparably to their p-i-n counterparts, in stark contrast to the $\sim$ 1.6 eV perovskites where n-i-p devices are substantially higher performing. This is highlighted by the work of Gharibzadeh and co-workers who achieved an outstanding V_{OC} of 1.31 V in a $FA_{0.83}Cs_{0.17}Pb(I_{0.6}Br_{0.4})_3$ (E_g = 1.72 eV, Tauc plot) n-i-p solar cell by using butylammonium bromide to form a thin two-dimensional Ruddlesden-Popper capping layer at the perovskite/HTL interface [133]. While this is an excellent result, the difference in performance of the wide bandgap perovskites in the two architectures is much smaller than for the narrower bandgap counterparts. The cause of this is not known. To some extent, the performance of p-i-n wide bandgap perovskites will be enhanced simply due to the additional effort dedicated to their optimisation. This is because p-i-n cells are more suitable for implementation in a two terminal (2T) tandem architecture: there are no high temperature annealing steps (i.e. to form the SnO_x ETL as in n-i-p cells) and there are reduced parasitic absorption optical losses within the tandem since the transport layers used in p-i-n solar cells are much thinner.

Interfacial passivation

Interfacial passivation has been critical to the rapid development of perovskite photovoltaics, and it has proven equally important in the $FA_{1-x}Cs_xPb(Br_yI_{1-y})_3$ perovskites [101, 134–137]. A range of approaches have been demonstrated for perovskites more suitable for single-junction photovoltaics ($E_g \sim 1.55$ eV) and those containing methylammonium. Fewer avenues have been explored for the MA-free wide-bandgap perovskites however there have still been significant efforts in this area.

One approach which has led to impressive efficiencies and stabilities is the imple-

mentation of ionic additives as both an interfacial passivation treatment and a bulk perovskite passivation treatment [101, 136, 138, 139]. Whilst this approach has predominantly been demonstrated on methylammonium containing perovskites [140], we have demonstrated that this approach can be incredibly successful in $FA_{1-x}Cs_xPb(Br_yI_{1-y})_3$ perovskites [101, 132, 136]. We utilised an organic ionic additive, 1-butyl-1-methylpiperidinium tetrafluoroborate ($[BMP]^+[BF_4]^-$), as a bulk perovskite additive and fabricated p-i-n-devices using a $FA_{0.83}Cs_{0.17}Pb(I_{0.77}Br_{0.23})_3$ perovskite (E_g = 1.67 eV, d(EQE)/dE). The champion devices achieved a PCE of 17.3 %, stabilised power output (SPO) of 16.5 % and a V_{OC} of 1.16 V. In addition to impressive device performances, ionic additive treatment results in a significant boost to the long-term stability of passivated devices. Unencapsulated devices aged under full-spectrum sunlight at 60 °C in ambient air demonstrated an average lifetime of degradation to 80 % of the peak PCE (T_{80}) of 975 hours, with the champion device achieving a T_{80} = 2630 hours. This is in stark comparison to our control devices which had dropped to a PCE < 5 % after 216 hours.

In their development of 4T perovskite/c-Si tandem photovoltaics, Jaysankar and co-workers implemented an ultra-thin layer of Al_2O_3 (thickness of 0.8 nm), through atomic layer deposition (ALD), in n-i-p photovoltaic devices based on a $FA_{0.85}Cs_{0.15}Pb(I_{0.71}Br_{0.29})_3$ perovskite (E_g = 1.72 eV, Tauc plot) [107]. This layer was introduced between the perovskite/spiro-OMeTAD interface in single junction devices and yielded an outstanding enhancement in the device's open-circuit voltage, from 1.11 V in the control devices to 1.22 V. This enhancement would be equivalent to an enhancement in radiative efficiency of more than a factor of 70, clearly highlighting just how critical the perovskite/HTL interface is in the n-i-p device structure. This substantial enhancement of the perovskite device enabled Jaysankar and co-workers to fabricate 4T tandem devices in conjunction with c-Si which delivered a PCE of 27.1 %.

One exciting area of perovskite research has been the foray into perovskite structures beyond the traditional three-dimensional (3D) ABX_3 crystal structure. Two-dimensional (2D) perovskite structures such as the Ruddlesden Popper (RP) and Dion Jacobson (DJ) phases can be formed by incorporating bulky monovalent (RP) or di-

valent cations (DJ) into the A-site of the perovskite structure resulting in the general structures $A_{n-1}B_nX_{3n+1}$ (RP) and $A'A_{n-1}B_nX_{3n+1}$ (DJ). Here, n refers to the number of lead halide plains between the organic spacer cations. The blending of these 2D phases with 3D perovskite to form 2D/3D heterostructures both as an interfacial modification or as a bulk passivation approach have been widely employed as a route to developing perovskite solar cells with long term stability and high efficiency [141–143]. In methylammonium-free wide bandgap perovskites 2D/3D heterostructures have been predominantly employed to modify the interface between the perovskite and adjacent charge transporting layers. This approach has been successful in both n-i-p and p-i-n architectures, and we summarise approaches and lessons learned below.

n-i-p device architecture Wang and co-workers demonstrated significant improvements to the operational device stability of $FA_{0.83}Cs_{0.17}Pb(I_{0.6}Br_{0.4})_3$ ($E_g = 1.72$ eV, $d(EQE)/dE$) photovoltaic devices with the incorporation of a 2D/3D perovskite heterostructure through the addition of butylammonium (BA) to the perovskite precursor solution [143]. Unlike many subsequent works the butylammonium cation was incorporated within the perovskite precursor solution as opposed to be used as a post-treatment to create an interface modification. The incorporation of the BA cation within the precursor solution was found to influence the perovskite thin film crystallinity and morphology with a composition of $BA_{0.09}(FA_{0.83}Cs_{0.17})_{0.91}Pb(I_{0.6}Br_{0.4})_3$ found to produce optimal photovoltaic devices. The champion device achieved a PCE $= 17.2\,\%$, $V_{OC} = 1.18\,V$ with a reduced hysteresis compared to the control device. Importantly unencapsulated devices held in ambient air ($\sim 45\%$ RH) under full-spectrum AM1.5, 75.6 $mWcm^{-2}$ irradiance were found to achieve a T_{80} of 1005 hours compared to a $T_{80} = 693$ hours for control devices demonstration a significant boost to the stability.

Gharibzadeh and co-workers have employed 2D/3D heterostructures to produce state-of the art n-i-p wide bandgap perovskite devices both as single junctions [133] (as discussed earlier) and for semi-transparent perovskite devices in four terminal (4T) tandems with both Si and CIGS (copper indium gallium selenide) [144]. The lat-

ter work builds on their impressive single junction devices using a butylammonium bromide surface post-treatment to form a 2D/3D perovskite heterostructure between the 3D perovskite $FA_{0.83}Cs_{0.17}Pb(I_{1-y}Br_y)_3$ and the spiro-MeOTAD (HTL) interface. This treatment induces changes to the structure of the perovskite with additional low angle peaks in measured X-ray diffraction patterns attributed to the presence of a Ruddlesden-Popper structure. This approach was expanded to a range of perovskite bandgaps from 1.65 eV - 1.86 eV and a boost in device performance was observed for all reported bandgaps. Interestingly, a difference was observed in the stability of the semi-transparent perovskite cells between the lower energy bandgaps $\leq$ 1.74 eV and those $>$ 1.74 eV. When measuring the PCE at a constant voltage under continuous 1 sun illumination, whilst no reduction in PCE was observed for the devices based on bandgaps of $\leq$ 1.74 eV, those based on bandgaps of 1.79 and 1.85 eV experienced a loss of PCE after $\sim$ 30 minutes. The authors offer a suggestion that this could be due to phase segregation for these compositions however it is clear more investigation would be required before this could be confirmed [144].

Zhou and co-workers report the use of a benzylamine post-treatment in a range of $FA_{0.85}Cs_{0.15}Pb(I_xBr_{1-x})_3$ perovskites as a route to boost the thermal photo-stability of the perovskite [145]. Thermal stability testing of a range of thin films was carried out in a N_2 atmosphere at 85 °C under a white light LED (no UV component). Without the benzylamine treatment, X-ray diffraction (XRD) and scanning electron microscopy (SEM) measurements demonstrated clear changes to the structure and morphology suggesting decomposition of the perovskite thin films after 8 hours however the benzylamine treatment was shown to inhibit these changes. The benzylamine treatment resulted in the presence of peaks in the diffraction patterns which were attributed to a $n = 1$ BA_2PbBr_4 structure. Additionally, treatment with benzylamine was found to boost the performance of photovoltaic devices based on $FA_{0.85}Cs_{0.15}Pb(I_{0.73}Br_{0.27})_3$ (E_g = 1.72 eV, Tauc plot). A significant boost in V_{OC} to 1.23 ± 0.01 V (compared to 1.14 ± 0.03 V for untreated devices) was observed, however in their champion JV significant hysteresis is present with the forward scan PCE = 15.7 % compared to a PCE

= 18.1 % for the reverse scan. The overall boost in performance afforded by the benzylamine treatment was maintained after ageing in air for 40 days at a RH = 65 ± 5 % with the PCE reducing by 20 % compared to untreated devices which showed a PCE reduction of 70 % after 21 days.

Bu and co-workers employed a phenylmethylamine bromide (PMABr) post–treatment to boost the efficiency and stability of photovoltaic devices based on an $FA_{0.8}Cs_{0.2}Pb(I_{0.7}Br_{0.3})_3$ perovskite (E_g = 1.74 eV, Tauc plot) [146]. Through X-ray scattering measurements the authors demonstrate that the concentration of the PMABr salt post-treatment is crucial in determining the nature of the 2D structure formed. At lower PMABr concentrations there is evidence of an $n = 1$ 2D perovskite forming whilst an additional $n = 2$ structure is seen at higher PMABr concentrations. Photovoltaic devices fabricated with a solely $n = 1$ 2D perovskite component, whilst more stable, were not as efficient as those fabricated with a mixture of $n = 1$ and $n = 2$ 2D perovskite structures present. For the latter case they report a champion device with a PCE of 18.5 % and a V_{OC} = 1.20 V under reverse scan (18.1 % and 1.19 V under forward scan). The steady-state power output of the champion devices are 15.8 % (0.96 V) for the control and 17.9 % (1.04 V) for the treated perovskite. This treatment was also found to enhance the moisture stability of the perovskite photovoltaic devices. After 2000 hours in dark storage with a RH = 20 ± 5 % the treated unencapsulated devices were demonstrated to show minimal performance losses when compared to the untreated devices. The authors also undertook near-edge X-ray absorption fine structure (NEXAFS) measurements to probe the molecular orientation of the PMABr molecules within the perovskite thin films. The results of these studies suggest that phenyl rings of the PMABr molecules adopt an edge-on orientation relative to the surface of the thin film which the authors suggest may help to impart a barrier against water molecules and boost the stability of the films in the presence of moisture.

p-i-n device architecture Chen and co-workers have demonstrated the use of $Pb(SCN)_2$ in combination with two organic cations phenethylammonium iodide (PEAI)

[147] and guanidinium bromide (GABr) [148] in boosting the efficiency and reducing voltage losses in $FA_{0.8}Cs_{0.2}Pb(I_{0.7}Br_{0.3})_3$ photovoltaic devices. Both works demonstrate that the addition of $Pb(SCN)_2$ can result in a boost to device performance which is then further enhanced by post-treatment of the perovskite thin film surface with PEAI or GABr. In their work investigating GABr the authors claim that post-treatment of the perovskite thin film with a GABr in isopropanol leads to the formation of a graded perovskite "homojunction" ($FA_{0.8}Cs_{0.2}Pb(I_{0.7}Br_{0.3})_3$:$GA_xFA_{0.8}Cs_{0.2}Pb(I_{0.7}Br_{0.3})_3$). They present the differences in surface potential observed in cross-sectional scanning kelvin probe force microscopy measurements between treated and untreated perovskite films as key evidence for this. Whilst they report a shift in the bandgap of the perovskite after treatment (from 1.74 eV to 1.75 eV determined from Tauc plots) and in the valence band maximum position measured using ultraviolet photoemission sprectroscopy (UPS) they do not offer any structural measurements to support these arguments. Nevertheless, with the GABr treatment they report a champion device PCE of 18.19 % and a V_{OC} of 1.24 V, compared to a PCE of 17.16 % and V_{OC} of 1.20 V.

In their work investigating PEAI Chen and co-workers report that post-treating their $FA_{0.8}Cs_{0.2}Pb(I_{0.7}Br_{0.3})_3$ films with a PEAI in isopropanol solution helps to suppress ion migration within the perovskite [147]. Using thermal admittance spectroscopy and molecular dynamics simulations they report that the presence of PEAI on the surface of the perovskite raises the energy barrier of diffusion for the iodide interstitial ions. For treated devices they report a champion PCE of 19.07 % and a V_{OC} of 1.25 V (E_g = 1.73 eV, Tauc plot). To achieve their champion PCE they employ a MgF_2 anti-reflection coating. Representative PCEs of 18.64 and 17.56 % are reported for treated and control devices respectively. The boost in device performance due to PEAI treatment is attributed to a reduction in the macroscopic J_0 as a result of the suppressed ion migration and therefore a reduction in defects at grain boundaries. The dual benefits of incorporating both $Pb(SCN)_2$ and PEAI have also been demonstrated in perovskite-Si tandem devices based on methylammonium containing wide bandgap perovskites [149].

Lewis bases such as thiophene have long been known to act as defect passivants through the propensity of S to bind with undercoordinated Pb^{2+} atoms [150]. Exploiting this interaction in combination with ammonium halide salts to produce quasi-2D thiophene based perovskite 2D/3D heterostructures has been demonstrated as an effective route to enhance photovoltaic device efficiency and stability in MA-containing perovskites [151]. Chen and co-workers demonstrate the efficacy of these heterostructures using, 2-thiophenethylammonium chloride (TEACl) as a post-treatment to the perovskite layer, in $FA_{0.8}Cs_{0.2}Pb(I_{0.8}Br_{0.2})_3$, ($E_g$ = 1.68 eV, Tauc plot) for both single junction (p-i-n) and 4T perovskite-CIGS tandem photovoltaic devices [152]. The champion single junction devices achieve a PCE of 20.31 % (SPO of 20.05 %) with a V_{OC} of 1.19 V, this is an impressive boost in performance compared to the control devices (PCE = 17.97 %, SPO = 17.56 %, $V_{OC} = 1.08\,V$). When combined with a CIGS bottom cell in a 4T tandem device, the authors report a PCE of 24 % for the optimal TEACl perovskite device. The TEACl treatment is demonstrated to enhance the stability of unencapsulated devices stored in air ($\sim$ 40 % RH) with a retention of 92.8 % of the initial efficiency compared to the control devices which only retained 53.7 % of their initial efficiency. It is unclear if these devices were stored in the dark or light. The treated devices also demonstrated enhanced stability when stored in the dark in N_2 and at 25 and 60 °C .

References

[1] Simon, S. H. *The Oxford solid state basics* (OUP Oxford, 2013).

[2] Nelson, J. A. *The Physics of Solar Cells* (Imperial College Press, 2003).

[3] Würfel, P. & Würfel, U. *Physics of solar cells: from basic principles to advanced concepts* (John Wiley & Sons, 2016).

[4] Binney, J. & Skinner, D. *The physics of quantum mechanics* (Oxford University Press, 2013).

[5] Noether, E. Invariante variationsprobleme. *Nachrichten von der Gesellschaft der Wissenschaften zu Göttingen, Mathematisch-Physikalische Klasse* **1918**, 235–257 (1918). URL `http://eudml.org/doc/59024`.

[6] Herz, L. M. Charge-carrier dynamics in organic-inorganic metal halide perovskites. *Annual Review of Physical Chemistry* **67**, 65–89 (2016).

[7] Johnston, M. B. & Herz, L. M. Hybrid perovskites for photovoltaics: charge-carrier recombination, diffusion, and radiative efficiencies. *Accounts of chemical research* **49**, 146–154 (2016).

[8] Baranowski, M. & Plochocka, P. Excitons in metal-halide perovskites. *Advanced Energy Materials* **10**, 1903659 (2020).

[9] Wehrenfennig, C., Eperon, G. E., Johnston, M. B., Snaith, H. J. & Herz, L. M. High charge carrier mobilities and lifetimes in organolead trihalide perovskites. *Advanced Materials* **26**, 1584–1589 (2014).

[10] Wehrenfennig, C., Liu, M., Snaith, H. J., Johnston, M. B. & Herz, L. M. Charge-carrier dynamics in vapour-deposited films of the organolead halide perovskite $CH_3NH_3PbI_{3-x}Cl_x$. *Energy & Environmental Science* **7**, 2269–2275 (2014).

[11] Boyer, E. J. Controversial Nobel Laureate Shockely dies. *LA Times* URL `http://articles.latimes.com/1989-08-14/news/mn-369_1_nobel-laureate-shockley`.

[12] Ehrler, B., Hutter, E. M. & Berry, J. J. The complicated morality of named inventions. *ACS Energy Letters* **6**, 565–567 (2021).

[13] Ball, J. M. & Petrozza, A. Defects in perovskite-halides and their effects in solar cells. *Nature Energy* **1**, 1–13 (2016).

[14] Byranvand, M. M. & Saliba, M. Defect passivation of perovskite films for highly efficient and stable solar cells. *Solar RRL* **5**, 2100295 (2021).

[15] Burhop, E. H. S. *The Auger effect and other radiationless transitions* (CUP Archive, 1952).

[16] Caprioglio, P. *et al.* On the relation between the open-circuit voltage and quasi-fermi level splitting in efficient perovskite solar cells. *Advanced Energy Materials* **9**, 1901631 (2019).

[17] Onno, A., Chen, C., Koswatta, P., Boccard, M. & Holman, Z. C. Passivation, conductivity, and selectivity in solar cell contacts: Concepts and simulations based on a unified partial-resistances framework. *Journal of Applied Physics* **126**, 183103 (2019).

[18] Green, M. A. Accurate expressions for solar cell fill factors including series and shunt resistances. *Applied Physics Letters* **108**, 081111 (2016).

[19] Rau, U., Paetzold, U. W. & Kirchartz, T. Thermodynamics of light management in photovoltaic devices. *Physical Review B* **90**, 035211 (2014).

[20] Guillemoles, J.-F., Kirchartz, T., Cahen, D. & Rau, U. Guide for the perplexed to the shockley–queisser model for solar cells. *Nature Photonics* **13**, 501–505 (2019).

[21] Kirchartz, T. & Rau, U. Detailed balance and reciprocity in solar cells. *physica status solidi (a)* **205**, 2737–2751 (2008).

[22] Rau, U., Blank, B., Müller, T. C. & Kirchartz, T. Efficiency potential of photovoltaic materials and devices unveiled by detailed-balance analysis. *Physical review applied* **7**, 044016 (2017).

[23] Rau, U. Reciprocity relation between photovoltaic quantum efficiency and electroluminescent emission of solar cells. *Physical Review B* **76**, 085303 (2007).

[24] Würfel, P. Thermodynamic limitations to solar energy conversion. *Physica E: Low-dimensional Systems and Nanostructures* **14**, 18–26 (2002).

[25] Kirchartz, T., Staub, F. & Rau, U. Impact of photon recycling on the open-circuit voltage of metal halide perovskite solar cells. *ACS Energy Letters* **1**, 731–739 (2016).

[26] Kirchartz, T. Photon management in perovskite solar cells. *The Journal of Physical Chemistry Letters* **10**, 5892–5896 (2019).

[27] Bracewell, R. The maximum of the planck energy spectrum. *Nature* **174**, 563–564 (1954).

[28] Rohde, R. A. Solar spectrum en.svg. *Wikipedia Foundation* (2013). URL `https://en.wikipedia.org/wiki/File:Solar_spectrum_en.svg`.

[29] Shockley, W. & Queisser, H. J. Detailed balance limit of efficiency of p-n junction solar cells. *Journal of Applied Physics* **32**, 510–519 (1961).

[30] Hirst, L. C. & Ekins-Daukes, N. J. Fundamental losses in solar cells. *Progress in Photovoltaics: Research and Applications* **19**, 286–293 (2011).

[31] Würfel, P. & Ruppel, W. Upper limit of thermophotovoltaic solar-energy conversion. *IEEE Transactions on Electron Devices* **27**, 745–750 (1980).

[32] Wurfel, P. The chemical potential of radiation. *Journal of Physics C: Solid State Physics* **15**, 3967 (1982).

[33] Landsberg, P. & Badescu, V. Carnot factor in solar cell efficiencies. *Journal of Physics D: Applied Physics* **33**, 3004 (2000).

[34] Markvart, T. The thermodynamics of optical étendue. *Journal of Optics A: Pure and Applied Optics* **10**, 015008 (2007).

[35] Green, M. A. Solar cell fill factors: General graph and empirical expressions. *Solid State Electronics* **24**, 788–789 (1981).

[36] Sinton, R. A., Cuevas, A. *et al.* A quasi-steady-state open-circuit voltage method for solar cell characterization. In *Proceedings of the 16th European photovoltaic solar energy conference*, vol. 1152, 4 (2000).

[37] Caprioglio, P. *et al.* On the origin of the ideality factor in perovskite solar cells. *Advanced Energy Materials* **10**, 2000502 (2020).

[38] Parrott, E. S. *et al.* Interplay of structural and optoelectronic properties in formamidinium mixed tin–lead triiodide perovskites. *Advanced Functional Materials* **28**, 1802803 (2018).

[39] Green, M. A., Ho-Baillie, A. & Snaith, H. J. The emergence of perovskite solar cells. *Nature Photonics* **8**, 506–514 (2014).

[40] Wright, A. D. *et al.* Electron–phonon coupling in hybrid lead halide perovskites. *Nature Communications* **7**, 1–9 (2016).

[41] Goldschmidt, V. M. Krystallbau und chemische Zusammensetzung. *Berichte der deutschen chemischen Gesellschaft (A and B Series)* **60**, 1263–1296 (1927).

[42] Li, C. *et al.* Formability of ABX_3 (X = F, Cl, Br, I) halide perovskites. *Acta Crystallographica Section B: Structural Science* **64**, 702–707 (2008).

[43] Sato, T., Takagi, S., Deledda, S., Hauback, B. C. & Orimo, S.-i. Extending the applicability of the Goldschmidt tolerance factor to arbitrary ionic compounds. *Scientific reports* **6**, 1–10 (2016).

[44] Wells, H. L. Über die cäsium-und kalium-bleihalogenide. *Zeitschrift für anorganische Chemie* **3**, 195–210 (1893).

[45] Weber, D. $CH_3NH_3PbX_3$, ein Pb (II)-system mit kubischer perowskitstruktur / $CH_3NH_3PbX_3$, a Pb (II)-system with cubic perovskite structure. *Zeitschrift für Naturforschung B* **33**, 1443–1445 (1978).

[46] Weber, D. $CH_3NH_3SnBr_xI_{3-x}$ ($x = 0 - 3$), ein Sn (II)-System mit kubischer Perowskitstruktur / $CH_3NH_3SnBr_xI_{3-x}$ ($x = 0 - 3$), a Sn (II)-system with cubic perovskite structure. *Zeitschrift für Naturforschung B* **33**, 862–865 (1978).

[47] Mitzi, D. B., Feild, C., Harrison, W. & Guloy, A. Conducting tin halides with a layered organic-based perovskite structure. *Nature* **369**, 467–469 (1994).

[48] Mitzi, D., Wang, S., Feild, C., Chess, C. & Guloy, A. Conducting layered organic-inorganic halides containing ⟨110⟩-oriented perovskite sheets. *Science* **267**, 1473–1476 (1995).

[49] Chondroudis, K. & Mitzi, D. B. Electroluminescence from an organic-inorganic perovskite incorporating a quaterthiophene dye within lead halide perovskite layers. *Chemistry of Materials* **11**, 3028–3030 (1999).

[50] Kojima, A., Teshima, K., Shirai, Y. & Miyasaka, T. Organometal halide perovskites as visible-light sensitizers for photovoltaic cells. *Journal of the american chemical society* **131**, 6050–6051 (2009).

[51] Lee, M. M., Teuscher, J., Miyasaka, T., Murakami, T. N. & Snaith, H. J. Efficient hybrid solar cells based on meso-superstructured organometal halide perovskites. *Science* **338**, 643–647 (2012).

[52] Stranks, S. D. *et al.* Electron-hole diffusion lengths exceeding 1 micrometer in an organometal trihalide perovskite absorber. *Science* **342**, 341–344 (2013).

[53] Liu, M., Johnston, M. B. & Snaith, H. J. Efficient planar heterojunction perovskite solar cells by vapour deposition. *Nature* **501**, 395–398 (2013).

[54] Laboratory, N. R. E. Best Research-Cell Efficiency Chart (Accessed: 2021-09-20). URL `https://www.nrel.gov/pv/cell-efficiency.html`.

[55] Nayak, P. K., Mahesh, S., Snaith, H. J. & Cahen, D. Photovoltaic solar cell technologies: analysing the state of the art. *Nature Reviews Materials* **4**, 269–285 (2019).

[56] Herz, L. M. Charge-carrier mobilities in metal halide perovskites: fundamental mechanisms and limits. *ACS Energy Letters* **2**, 1539–1548 (2017).

[57] Chen, Y. *et al.* Optoelectronic Properties of Mixed Iodide–Bromide Perovskites from First-Principles Computational Modeling and Experiment. *The Journal of Physical Chemistry Letters* **13**, 4184–4192 (2022).

[58] Ledinsky, M. *et al.* Temperature dependence of the urbach energy in lead iodide perovskites. *The Journal of Physical Chemistry Letters* **10**, 1368–1373 (2019).

[59] Sadhanala, A. *et al.* Preparation of single-phase films of $CH_3NH_3Pb(I_{1-x}Br_x)_3$ with sharp optical band edges. *The Journal of Physical Chemistry Letters* **5**, 2501–2505 (2014).

[60] Jacobsson, T. J. *et al.* Exploration of the compositional space for mixed lead halogen perovskites for high efficiency solar cells. *Energy & Environmental Science* **9**, 1706–1724 (2016).

[61] Eperon, G. E. *et al.* Formamidinium lead trihalide: a broadly tunable perovskite for efficient planar heterojunction solar cells. *Energy & Environmental Science* **7**, 982–988 (2014).

[62] Walsh, A. Principles of chemical bonding and band gap engineering in hybrid organic–inorganic halide perovskites. *The Journal of Physical Chemistry C* **119**, 5755–5760 (2015).

[63] Umebayashi, T., Asai, K., Kondo, T. & Nakao, A. Electronic structures of lead iodide based low-dimensional crystals. *Physical Review B* **67**, 155405 (2003).

[64] Brivio, F., Walker, A. B. & Walsh, A. Structural and electronic properties of hybrid perovskites for high-efficiency thin-film photovoltaics from first-principles. *APL Materials* **1**, 042111 (2013).

[65] Unger, E. *et al.* Roadmap and roadblocks for the band gap tunability of metal halide perovskites. *Journal of Materials Chemistry A* **5**, 11401–11409 (2017).

[66] Pazoki, M., Jacobsson, T. J., Hagfeldt, A., Boschloo, G. & Edvinsson, T. Effect of metal cation replacement on the electronic structure of metalorganic halide perovskites: Replacement of lead with alkaline-earth metals. *Physical Review B* **93**, 144105 (2016).

[67] Goyal, A. *et al.* Origin of pronounced nonlinear band gap behavior in lead–tin hybrid perovskite alloys. *Chemistry of Materials* **30**, 3920–3928 (2018).

[68] Klug, M. T. *et al.* Metal composition influences optoelectronic quality in mixed-metal lead–tin triiodide perovskite solar absorbers. *Energy & Environmental Science* **13**, 1776–1787 (2020).

[69] Gu, S. *et al.* Tin and mixed lead–tin halide perovskite solar cells: progress and their application in tandem solar cells. *Advanced Materials* **32**, 1907392 (2020).

[70] McMeekin, D. P. *et al.* A mixed-cation lead mixed-halide perovskite absorber for tandem solar cells. *Science* **351**, 151–155 (2016).

[71] Hörantner, M. T. *et al.* The potential of multijunction perovskite solar cells. *ACS Energy Letters* **2**, 2506–2513 (2017).

[72] Prasanna, R. *et al.* Band gap tuning via lattice contraction and octahedral tilting in perovskite materials for photovoltaics. *Journal of the American Chemical Society* **139**, 11117–11124 (2017).

[73] Stoumpos, C. C., Malliakas, C. D. & Kanatzidis, M. G. Semiconducting tin and lead iodide perovskites with organic cations: phase transitions, high mobilities, and near-infrared photoluminescent properties. *Inorganic Chemistry* **52**, 9019–9038 (2013).

[74] Conings, B. *et al.* Intrinsic thermal instability of methylammonium lead trihalide perovskite. *Advanced Energy Materials* **5**, 1500477 (2015).

[75] Misra, R. K. *et al.* Temperature-and component-dependent degradation of perovskite photovoltaic materials under concentrated sunlight. *The Journal of Physical Chemistry Letters* **6**, 326–330 (2015).

[76] Lee, J.-W., Seol, D.-J., Cho, A.-N. & Park, N.-G. High-efficiency perovskite solar cells based on the black polymorph of $HC(NH_2)_2PbI_3$. *Advanced Materials* **26**, 4991–4998 (2014).

[77] Jeon, N. J. *et al.* Compositional engineering of perovskite materials for high-performance solar cells. *Nature* **517**, 476–480 (2015).

[78] Kim, G. *et al.* Impact of strain relaxation on performance of α-formamidinium lead iodide perovskite solar cells. *Science* **370**, 108–112 (2020).

[79] Liu, Q. *et al.* Heterogeneous lead iodide obtains perovskite solar cells with efficiency of 24.27%. *Chemical Engineering Journal* 137676 (2022).

[80] Min, H. *et al.* Perovskite solar cells with atomically coherent interlayers on SnO_2 electrodes. *Nature* **598**, 444–450 (2021).

[81] Min, H. *et al.* Efficient, stable solar cells by using inherent bandgap of α-phase formamidinium lead iodide. *Science* **366**, 749–753 (2019).

[82] Doherty, T. A. *et al.* Stabilized tilted-octahedra halide perovskites inhibit local formation of performance-limiting phases. *Science* **374**, 1598–1605 (2021).

[83] Sutton, R. J. *et al.* Bandgap-tunable cesium lead halide perovskites with high thermal stability for efficient solar cells. *Advanced Energy Materials* **6**, 1502458 (2016).

[84] Kulbak, M., Cahen, D. & Hodes, G. How important is the organic part of lead halide perovskite photovoltaic cells? efficient cspbbr3 cells. *The Journal of Physical Chemistry Letters* **6**, 2452–2456 (2015).

[85] Veldhuis, S. A. *et al.* Perovskite materials for light-emitting diodes and lasers. *Advanced Materials* **28**, 6804–6834 (2016).

[86] Hörantner, M. T. & Snaith, H. J. Predicting and optimising the energy yield of perovskite-on-silicon tandem solar cells under real world conditions. *Energy & Environmental Science* **10**, 1983–1993 (2017).

[87] MØller, C. Crystal structure and photoconductivity of caesium plumbohalides. *Nature* **182**, 1436–1436 (1958).

[88] Marshall, A. R. *et al.* Dimethylammonium: An A-Site Cation for Modifying $CsPbI_3$. *Solar RRL* **5**, 2000599 (2021).

[89] Pellet, N. *et al.* Mixed-organic-cation perovskite photovoltaics for enhanced solar-light harvesting. *Angewandte chemie* **126**, 3215–3221 (2014).

[90] Baena, J. P. C. *et al.* Highly efficient planar perovskite solar cells through band alignment engineering. *Energy & Environmental Science* **8**, 2928–2934 (2015).

[91] Jiang, Q. *et al.* Surface passivation of perovskite film for efficient solar cells. *Nature Photonics* **13**, 460–466 (2019).

[92] Guo, Q. *et al.* Universal dynamic liquid interface for healing perovskite solar cells. *Advanced Materials* 2202301 (2022).

[93] Choi, H. *et al.* Cesium-doped methylammonium lead iodide perovskite light absorber for hybrid solar cells. *Nano Energy* **7**, 80–85 (2014).

[94] Lee, J.-W. *et al.* Formamidinium and cesium hybridization for photo-and moisture-stable perovskite solar cell. *Advanced Energy Materials* **5**, 1501310 (2015).

[95] Yi, C. *et al.* Entropic stabilization of mixed A-cation ABX_3 metal halide perovskites for high performance perovskite solar cells. *Energy & Environmental Science* **9**, 656–662 (2016).

[96] Saliba, M. *et al.* Cesium-containing triple cation perovskite solar cells: improved stability, reproducibility and high efficiency. *Energy & Environmental Science* **9**, 1989–1997 (2016).

[97] Zheng, X. *et al.* Managing grains and interfaces via ligand anchoring enables 22.3%-efficiency inverted perovskite solar cells. *Nature Energy* **5**, 131–140 (2020).

[98] Dong, C., Wang, Z.-K. & Liao, L.-S. Progress of triple cation organometal halide perovskite solar cells. *Energy Technology* **8**, 1900804 (2020).

[99] Saliba, M. *et al.* Incorporation of rubidium cations into perovskite solar cells improves photovoltaic performance. *Science* **354**, 206–209 (2016).

[100] Lal, N. N., White, T. P. & Catchpole, K. R. Optics and light trapping for tandem solar cells on silicon. *IEEE Journal of Photovoltaics* **4**, 1380–1386 (2014).

[101] Lin, Y.-H. *et al.* A piperidinium salt stabilizes efficient metal-halide perovskite solar cells. *Science* **369**, 96–102 (2020).

[102] Eperon, G. E. *et al.* Perovskite-perovskite tandem photovoltaics with optimized band gaps. *Science* **354**, 861–865 (2016).

[103] Tong, J. *et al.* Carrier lifetimes of $> 1\,\mu$s in Sn-Pb perovskites enable efficient all-perovskite tandem solar cells. *Science* **364**, 475–479 (2019).

[104] Hu, S. *et al.* Optimized carrier extraction at interfaces for 23.6% efficient tin–lead perovskite solar cells. *Energy & Environmental Science* **15**, 2096–2107 (2022).

[105] Slotcavage, D. J., Karunadasa, H. I. & McGehee, M. D. Light-induced phase segregation in halide-perovskite absorbers. *ACS Energy Letters* **1**, 1199–1205 (2016).

[106] Tan, H. *et al.* Dipolar cations confer defect tolerance in wide-bandgap metal halide perovskites. *Nature Communications* **9**, 1–10 (2018).

[107] Jaysankar, M. *et al.* Minimizing voltage loss in wide-bandgap perovskites for tandem solar cells. *ACS Energy Letters* **4**, 259–264 (2018).

[108] Tan, W., Bowring, A. R., Meng, A. C., McGehee, M. D. & McIntyre, P. C. Thermal stability of mixed cation metal halide perovskites in air. *ACS Applied Materials & Interfaces* **10**, 5485–5491 (2018).

[109] Chen, W., Li, X., Li, Y. & Li, Y. A review: crystal growth for high-performance all-inorganic perovskite solar cells. *Energy & Environmental Science* **13**, 1971–1996 (2020).

[110] He, R. *et al.* Wide-bandgap organic–inorganic hybrid and all-inorganic perovskite solar cells and their application in all-perovskite tandem solar cells. *Energy & Environmental Science* **14**, 5723–5759 (2021).

[111] Chen, J. & Choy, W. C. Efficient and stable all-inorganic perovskite solar cells. *Solar RRL* **4**, 2000408 (2020).

[112] Ji, K., Anaya, M., Abfalterer, A. & Stranks, S. D. Halide perovskite light-emitting diode technologies. *Advanced Optical Materials* **9**, 2002128 (2021).

[113] Ren, Z., Wang, K., Sun, X. W. & Choy, W. C. Strategies toward efficient blue perovskite light-emitting diodes. *Advanced Functional Materials* **31**, 2100516 (2021).

[114] Yang, D. *et al.* Toward stable and efficient perovskite light-emitting diodes. *Advanced Functional Materials* **32**, 2109495 (2022).

[115] Liu, Y. *et al.* Boosting the efficiency of quasi-2d perovskites light-emitting diodes by using encapsulation growth method. *Nano Energy* **80**, 105511 (2021).

[116] Warby, J. H. *et al.* Revealing factors influencing the operational stability of perovskite light-emitting diodes. *ACS Nano* **14**, 8855–8865 (2020).

[117] Hassan, Y. *et al.* Ligand-engineered bandgap stability in mixed-halide perovskite leds. *Nature* **591**, 72–77 (2021).

[118] Stranks, S. D., Hoye, R. L., Di, D., Friend, R. H. & Deschler, F. The physics of light emission in halide perovskite devices. *Advanced Materials* **31**, 1803336 (2019).

[119] Wang, Z. *et al.* Manipulating the trade-off between quantum yield and electrical conductivity for high-brightness quasi-2d perovskite light-emitting diodes. *Advanced Functional Materials* **28**, 1804187 (2018).

[120] An, Y. *et al.* Identifying high-performance and durable methylammonium-free lead halide perovskites via high-throughput synthesis and characterization. *Energy & Environmental Science* **14**, 6638–6654 (2021).

[121] Knight, A. J. & Herz, L. M. Preventing phase segregation in mixed-halide perovskites: a perspective. *Energy & Environmental Science* **13**, 2024–2046 (2020).

[122] Hoke, E. T. *et al.* Reversible photo-induced trap formation in mixed-halide hybrid perovskites for photovoltaics. *Chemical Science* **6**, 613–617 (2015).

[123] Knight, A. J. *et al.* Halide segregation in mixed-halide perovskites: influence of a-site cations. *ACS Energy Letters* **6**, 799–808 (2021).

[124] Barker, A. J. *et al.* Defect-assisted photoinduced halide segregation in mixed-halide perovskite thin films. *ACS Energy Letters* **2**, 1416–1424 (2017).

[125] Motti, S. G. *et al.* Phase segregation in mixed-halide perovskites affects charge-carrier dynamics while preserving mobility. *Nature Communications* **12**, 1–9 (2021).

[126] Yoon, S. J. *et al.* Tracking iodide and bromide ion segregation in mixed halide lead perovskites during photoirradiation. *ACS Energy Letters* **1**, 290–296 (2016).

[127] Mahesh, S. *et al.* Revealing the origin of voltage loss in mixed-halide perovskite solar cells. *Energy & Environmental Science* **13**, 258–267 (2020).

[128] Caprioglio, P. *et al.* Nano-emitting heterostructures violate optical reciprocity and enable efficient photoluminescence in halide-segregated methylammonium-free wide bandgap perovskites. *ACS Energy Letters* **6**, 419–428 (2021).

[129] Peña-Camargo, F. *et al.* Halide segregation versus interfacial recombination in bromide-rich wide-gap perovskite solar cells. *ACS Energy Letters* **5**, 2728–2736 (2020).

[130] Chen, W. *et al.* Monolithic perovskite/organic tandem solar cells with 23.6% efficiency enabled by reduced voltage losses and optimized interconnecting layer. *Nature Energy* **7**, 229–237 (2022).

[131] Brinkmann, K. *et al.* Perovskite–organic tandem solar cells with indium oxide interconnect. *Nature* **604**, 280–286 (2022).

[132] Oliver, R. D. *et al.* Understanding and suppressing non-radiative losses in methylammonium-free wide-bandgap perovskite solar cells. *Energy & Environmental Science* **15**, 714–726 (2022).

[133] Gharibzadeh, S. *et al.* Record open-circuit voltage wide-bandgap perovskite solar cells utilizing 2d/3d perovskite heterostructure. *Advanced Energy Materials* **9**, 1803699 (2019).

[134] Abdi-Jalebi, M. *et al.* Maximizing and stabilizing luminescence from halide perovskites with potassium passivation. *Nature* **555**, 497–501 (2018).

[135] Oliver, R. D. *et al.* Thermally stable passivation toward high efficiency inverted perovskite solar cells. *ACS Energy Letters* **5**, 3336–3343 (2020).

[136] Bai, S. *et al.* Planar perovskite solar cells with long-term stability using ionic liquid additives. *Nature* **571**, 245–250 (2019).

[137] Wolff, C. M., Caprioglio, P., Stolterfoht, M. & Neher, D. Nonradiative recombination in perovskite solar cells: the role of interfaces. *Advanced Materials* **31**, 1902762 (2019).

[138] Caprioglio, P. *et al.* Bi-functional interfaces by poly(ionic liquid) treatment in efficient pin and nip perovskite solar cells. *Energy & Environmental Science* **14**, 4508–4522 (2021).

[139] Noel, N. K. *et al.* Elucidating the role of a tetrafluoroborate-based ionic liquid at the n-type oxide/perovskite interface. *Advanced Energy Materials* **10**, 1903231 (2020).

[140] Niu, T. *et al.* Ionic liquids-enabled efficient and stable perovskite photovoltaics: progress and challenges. *ACS Energy Letters* **6**, 1453–1479 (2021).

[141] Grancini, G. *et al.* One-year stable perovskite solar cells by 2d/3d interface engineering. *Nature Communications* **8**, 1–8 (2017).

[142] Katan, C., Mercier, N. & Even, J. Quantum and dielectric confinement effects in lower-dimensional hybrid perovskite semiconductors. *Chemical Reviews* **119**, 3140–3192 (2019).

[143] Wang, Z. *et al.* Efficient ambient-air-stable solar cells with 2d–3d heterostructured butylammonium-caesium-formamidinium lead halide perovskites. *Nature Energy* **2**, 1–10 (2017).

[144] Gharibzadeh, S. *et al.* 2d/3d heterostructure for semitransparent perovskite solar cells with engineered bandgap enables efficiencies exceeding 25% in four-terminal tandems with silicon and cigs. *Advanced Functional Materials* **30**, 1909919 (2020).

[145] Zhou, Y. *et al.* Benzylamine-treated wide-bandgap perovskite with high thermal-photostability and photovoltaic performance. *Advanced Energy Materials* **7**, 1701048 (2017).

[146] Bu, T. *et al.* Structure engineering of hierarchical layered perovskite interface for efficient and stable wide bandgap photovoltaics. *Nano Energy* **75**, 104917 (2020).

[147] Chen, C. *et al.* Arylammonium-assisted reduction of the open-circuit voltage deficit in wide-bandgap perovskite solar cells: the role of suppressed ion migration. *ACS Energy Letters* **5**, 2560–2568 (2020).

[148] Chen, C. *et al.* Achieving a high open-circuit voltage in inverted wide-bandgap perovskite solar cells with a graded perovskite homojunction. *Nano Energy* **61**, 141–147 (2019).

[149] Kim, D. *et al.* Efficient, stable silicon tandem cells enabled by anion-engineered wide-bandgap perovskites. *Science* **368**, 155–160 (2020).

[150] Noel, N. K. *et al.* Enhanced photoluminescence and solar cell performance via lewis base passivation of organic–inorganic lead halide perovskites. *ACS Nano* **8**, 9815–9821 (2014).

[151] Sutanto, A. A. *et al.* Dynamical evolution of the 2d/3d interface: a hidden driver behind perovskite solar cell instability. *Journal of Materials Chemistry A* **8**, 2343–2348 (2020).

[152] Chen, C. *et al.* Interfacial engineering of a thiophene-based 2d/3d perovskite heterojunction for efficient and stable inverted wide-bandgap perovskite solar cells. *Nano Energy* **90**, 106608 (2021).

Chapter 3

Experimental Methods

In this chapter, I will describe all the experimental methods used in this thesis. I will describe the device fabrication steps and all spectroscopic, structural and morphological characterisation methods.

3.1 Device fabrication

3.1.1 Materials

Unless otherwise stated, all solvents used in work were purchased from Sigma Aldrich. All materials were used as received without additional purification.All material preparation steps were performed in an N_2 filled glovebox unless otherwise stated.

Substrates: Substrates were obtained from a range of suppliers during the course of this thesis.

In **Chapter 4**, FTO (flurine-doped tin oxide) substrates were purchased from Pilkington with a sheet resisitivity of 7 $\Omega\,\square^{-1}$. The substrates were etched with Zn powder and 2 M HCl acid to achieve the desired electrode pattern.

In **Chapter 5**, devices were fabricated in Potsdam with pre-patterned 25 mm x 25 mm indium tin oxide (ITO) substrates were purchased from Lumtec with a sheet

resisitivity of 15 $\Omega\,\square^{-1}$.

In **Chapter 6**, a variety of indium tin oxide (ITO) suppliers were used due to supply issues during the course of the project. Predominantly, 30 mm × 30 mm pre-patterned ITO substrates were purchased from AMG or Biotain crystal. The sheet resistance as approximately 10 $\Omega\,\square^{-1}$.

Throughout this thesis THz spectroscopy measurements were performed on z-cut quartz substrates (area 1.3 cm^2), as were the time-correlated single photon counting measurements presented in **Chapter 5 & Chapter 6**.

Ionic additive: The ionic additive 1-butyl-1-methylpiperidinium tetrafluoroborate ($[BMP]^+\,[BF_4]^-$, purity 99 %) was purchased from Sigma Aldrich. The ionic additive was dissolved in a 4:1 volume ratio of dimethylformamide (DMF) and dimethylsulfoxide (DMSO) and shaken overnight.

Benzylammonium bromide synthesis: 5 mL of benzylamine and 30 mL of ethanol were mixed and stirred in a 250 mL 2-neck flask in an ice-water bath. Then 7 mL of HBr acid (48 wt% in water) was slowly added into the mixture. The mixture was stirred for 2 h at 0 °C in an ice water bath. The solvent was removed by a rotary evaporator at 50 °C and a white precipitate was formed. The white precipitate was then washed with diethyl ether and filtered using a Buchner filtration system. After filtration, the white powder was dissolved into hot ethanol to obtain a supersaturated solution. The solution was put into a freezer overnight. The white precipitate was then washed with diethyl ether and collected by vacuum filtration. After filtration, the large white crystallites (benzylammonium bromide, BenABr) were collected and dried in a vacuum oven at 60 °C overnight. It was then transferred to an N_2 glovebox where it was weighed ahead of device fabrication.

Benzylammonium bromide solution: The benzylammonium bromide powder was weighed in a N_2 filled glovebox and dissolved in chlorobenzene to the desired

concentration, as described in **Chapter 4**. The solution was stirred overnight at a temperature of 50 °C.

Perovskite precursor: In **Chapter 4**, the triple cation perovskite $Cs_{0.05}\left(FA_{0.83}MA_{0.17}\right)_{0.95}Pb\left(I_{0.9}Br_{0.1}\right)_3$, first developed by Saliba et al. [1] was utilised. To form the perovskite precursor, lead iodide (99.99 %, PbI_2, Alfa Aesar), lead bromide (> 98 %, $PbBr_2$, Alfa Aesar), cesium iodide (99.999 %, CsI, Alfa Aesar), formamidinium iodide (FAI, GreatCell Solar) and methylammonium iodide (MAI, GreatCell Solar) were weighed to the appropriate stoichiometry and dissolved in 4:1 ratio (by volume) of N,N-dimethylformamide (DMF) and dimethyl sulfoxide (DMSO) to achieve a concentration of 1.4 M.

In **Chapters 5 & 6**, the $FA_{0.83}Cs_{0.17}Pb\left(I_{0.6}Br_{0.4}\right)_3$ perovskite, first developed by McMeekin et al. [2] was utlisied. The precursor solution was obtained by stoichiometrically weighing formamidinium iodide (FAI, GreatCell Solar), caesium iodide (CsI, AlfaAesar), lead iodide (PbI_2, TCI) and lead bromide ($PbBr_2$, AlfaAesar) in an N_2 filled glovebox. For devices made in Potsdam in **Chapter 5**, the materials were instead weighed in ambient air before being transferred into an N_2 filled glovebox. The precursor salts were dissolved in a mixture (4:1 ratio by volume) of dimethylformamide (DMF) and dimethylsulfoxide (DMSO). The precursors solution was stirred at room temperature overnight. To mix the ionic additive into the precursor solution, an appropriate volume of the ionic additive solution was added to the perovskite precursor solution to obtain a perovskite concentration of 1.3 M for the precursor and 0.5 $mg\,mL^{-1}$ of the ionic additive. For control devices, the same volume of neat DMF:DMSO was added to the perovskite precursor to achieve a concentration of 1.3 M. Both the control and ionic additive-containing precursor solutions were shaken on an orbital-shaker for at least 30 minutes prior to deposition. Explicitly, the desired perovskite solutions was achieved by performing the following steps. Firstly, the precursor salts were weighed to within 1 mg according to values presented in **Table 3.1**. To make the precursor solution, 2 mL of solvent (4:1 DMF:DMSO) was added to achieve a nominal concentra-

tion of 1.56 M. This solution was stirred overnight at room temperature to ensure the precursors had fully dissolved. This solution was then decanted into separated vials, 1 mL in each. We note there was residual precursor solution left due to volume expansion whilst the precursors dissolved. To one vial, 0.2 mL of neat DMF:DMSO was added to achieve a target concentration of 1.3 M and hence form the control solution. To the other vial, 0.2 mL of ionic additive solution (3 $\mathrm{mg\,mL^{-1}}$) was added to achieve a nominal 1.3 M perovskite containing 0.5 $\mathrm{mg\,mL^{-1}}$ of ionic additive.

Table 3.1: *The masses of the precursor salts required to achieve a solution of a nominal concentration of 1.56 M when adding 2 mL of solvent (4:1 DMF:DMSO).*

Precursor salt	Mass (mg)
FAI	445.3
CsI	137.8
PbI_2	575.3
$PbBr_2$	687.0

Hole transport layer: In **Chapter 4**, the hole transport layer (HTL) solution was made by dissolving poly(4-butyl-N,N-diphenylaniline) (polyTPD) (purchased from 1-Material) in toluene at a concentration of 1 $\mathrm{mg\,mL^{-1}}$ with 20 wt% 2,3,5,6-Tetrafluoro-7,7,8,8-tetracyanoquinodimethane (F_4-TCNQ, Lumtec) to dope the solution and resulting thin film after deposition.

In **Chapter 5**, poly[bis(4-phenyl)(2,4,6-trimethylphenyl)amine] (PTAA) (purchased from Sigma Aldrich) was used as the hole transport layer. To form the solution, PTAA was weighed in ambient air before being transferred into an N_2 filled glovebox, where it was dissolved in toluene at a concentration of 1.5 $\mathrm{mg\,mL^{-1}}$.

In **Chapter 6**, a range of hole transport layers were used. PTAA ($M_\mathrm{W} = 12,000$) was purchased from Flexink and dissolved in CB at a concentration of 2.0 $\mathrm{mg\,mL^{-1}}$. poly(9,9-dioctylfluorene-alt-N-(4-sec-butylphenyl)-diphenylamine) (TFB) ($M_\mathrm{W} = 45,000$) was purchased from Osilla and dissolved in CB at a concentration of 2.0 $\mathrm{mg\,mL^{-1}}$. poly(9,9-dioctylfluorene-alt-benzothiadiazole) (F8BT) was purchased from Osilla and dissolved in CB at a concentration of 2.0 $\mathrm{mg\,mL^{-1}}$.

F6-TCNNQ (1,3,4,5,7,8-hexafluorotetracyanonaphthoquinodimethane) was purchased from Lumtec and used to dope the HTL solutions, typically at 1 wt%.

Electron transport layer (ETL): In **Chapters 4 & 6**, the ETL solution was formed by dissolving PCBM ([6,6]-phenyl-C61-butyric acid methyl ester, Solenne) in 3:1 (by volume) cholorbenzene (CB):dichlorobenene (DCB) at a concentration of 20 $\mathrm{mg\,mL^{-1}}$.

Hole blocking layer: In **Chapters 4 & 6** the 'hole blocking layer' was prepared by dissolving bathocuproine (98 %, BCP, Alpha Aesar) at 0.5 $\mathrm{mg\,mL^{-1}}$ in isopropanol (IPA). This solution was stirred overnight at 70 °C before deposition.

3.1.2 Deposition protocols

Triple cation perovskite

In **Chapter 4**, the triple cation perovskite $\mathrm{Cs_{0.05}\,(FA_{0.83}MA_{0.17})_{0.95}\,Pb\,(I_{0.9}Br_{0.1})_3}$ was deposited according to the following procedure. 170 μL of precursor solution was deposited dynamically onto the substrate at 1000 rpm. After remaining at this speed for 9 s, the speed was increased to 5000 rpm over 4 s, where it remained for 45 s. A solvent quench with 400 μL of toluene 5 s before the end of the program was performed and the films were annealed at 100 °C for 1 hour. The films were left to cool before any additional layer was applied.

Wide bandgap perovskite

For devices fabricated at the University of Potsdam, 120 μL of perovskite precursor solution was deposited onto a static substrate. The substrate accelerated to 3500 rpm over 3 s where it remained for 35 s. After 10 s, 200 μL of ethylacetate was dropped onto the substrate. At the end of the spincoating procedure, the films were annealed at 100 °C for 1 hour.

For all other wide bandgap samples, 175 μL of the precursor solution was dynamically deposited onto the substrate spinning at 1000 rpm. The substrate then accelerated at rate of 800 rpm/s to a top speed of 5000 rpm, at which speed it remained for 30 s. An antisolvent quench was performed by depositing 350 μL of anisole onto the substrate 5 s before the end of the program. The films were annealed for 45 minutes at 100 °C .

If processing on z-cut quartz substrates, 50 μL of the precursor solution was dynamically deposited onto the substrate spinning at 1000 rpm. After 5 s, the spin speed increased to 5000 rpm over 5 s, where it remained for 30 s. An antisolvent quench was performed by depositing 50 μL of anisole onto the substrate 5 s before the end of the program. The films were annealed for 30 minutes at 100 °C .

BenABr

If present, the benzylammonium bromide surface passivation was applied onto the perovskite surface which had been allowed to return to room temperature following its annealing step. 40 μL of the BenABr solution was deposited dynamically onto the substrate spinning at 2000 rpm for 20 s. After this step, the films were annealed at 100 °C for 60 s.

polyTPD

70 μL of F_4-TCNQ doped polyTPD solution was deposited using the dynamic spin-coating method in air (relative humidity $\sim$ 40 %) at 2000 rpm. After spinning for 20 s, the films were annealed at 130 °C for 15 minutes. The substrates were then transferred to a N_2 filled glovebox in which all other layers were deposited.

PTAA

70 μL of the PTAA solution was deposited onto a stationary substrate which accelerated to 6000 rpm over 3 s where it remained for 30 s. Immediately after the program had

finished, the substrate was annealed at 100 °C for 10 minutes. The substrates were allowed to return to room temperature following this procedure.

TFB & polymer blends

TFB & the polymer blends were deposited in the same manner as PTAA and were also annealed at 100 °C for 10 minutes.

PFN-Br

The poly(9,9-bis(3'-(N,N-dimethyl)-N-ethylammoinium-propyl-2,7-fluorene)-alt-2,7-(9,9-dioctylfluorene))dibromide (PFN-Br) layer was formed by dynamically depositing 60 μL of the PFN-Br solution onto the substrate spinning at 5000 rpm for 20 s. No anneal was performed following this step.

[6,6]-phenyl-C61-butyric acid methyl ester ($PC_{61}BM$)

In **Chapters 4 & 6** $PC_{61}BM$ was dynamically spin coated on top of the perovskite layer at 2000 rpm using 40 muL of solution and annealed for 3 minutes at 100 °C .

Bathocuproine (BCP)

In **Chapters 4 & 6** BCP was dynamically spin coated on top of the $PC_{61}BM$ layer at 5000 rpm using 100 μL of solution with a 1 minute anneal at 100 °C .

In **Chapter 5**, BCP was deposited by thermal evaporation at rate of 0.1 $\text{Å}\,\text{s}^{-1}$until a thickness of 8 nm was achieved. The deposition took place under high vacuum ($\sim 10^{-7}$ mbar).

C60

In **Chapter 5**, C60 was used as the ETL. The perovskite samples were allowed to cool following their anneal before being transferred to a custom evaporation chamber. C60 was deposited at 0.2 Å/s to achieve a thickness of 30 nm. Following this deposition,

8 nm of bathocuproine at a rate of 0.1 Å/s. The deposition took place under high vacuum ($\sim 10^{-7}$ mbar).

LiF

If present, LiF was deposited at a rate of 0.2 Å/s until a thickness of 1 nm was achieved. The deposition took place under high vacuum ($\sim 10^{-7}$ mbar).

Metal electrodes

The solar cell devices were finished with metal electrodes which were deposited by thermal evaporation. In **Chapters 4 & 6** a Kurt J. Lesker Nano 36 evaporator was used to deposit 100 nm silver electrodes by thermal evaporation under high vacuum ($\sim 10^{-6}$ mbar) at a rate of approximately 0.05 nms^{-1}. For the stability measurements, 3 nm of Cr was first deposited at a rate of 0.01 nms^{-1}, before 100 nm of Au at 0.02 nms^{-1}. The electrodes had an active area of 0.0919 cm^2 in **Chapter 4**, and 0.25 and 1 cm^2 in **Chapter 6**.

In **Chapter 5**, copper was used as the top electrode for devices made in Potsdam. 100 nm of Cu was deposited under high vacuum ($\sim 10^{-7}$ mbar) at a rate of $0.3 - 0.7$ Å/s to achieve a thickness of 100 nm. The active area of the solar cells is 6 mm^2 and is defined by the overlap of the ITO and Cu electrodes.

3.2 Photophysical characterisation

3.2.1 Optical-pump terahertz-probe spectroscopy (OPTPS)

OPTPS measurements were performed by Dr. Leonardo R. V. Buizza.

An amplified laser system (Spectra Physics, MaiTai - Empower - Spitfire) with a central wavelength 800 nm, 35 fs pulse duration and 5 kHz repetition rate was used to generate THz radiation via the inverse spin hall effect [3] and was detected using free-space electro-optic sampling with a 1 mm-thick ZnTe (110) crystal, a Wollaston prism

and a pair of balanced photodiodes. The THz pulse was measured in transmission geometry. The pump beam was frequency-doubled to 400 nm by a β-barium- borate (BBO) crystal.

OPTP Fitting

We follow the same process outlined by Wehrenfennig et al.[4]. As discussed in **Chapter 2**, charge-carrier recombination in metal-halide perovskites can generally be well-described by the following differential equation (**Equation 2.40**) [5]:

$$\frac{\mathrm{d}n}{\mathrm{d}t} = -k_1 n - k_2 n^2 - k_3 n^3, \tag{3.1}$$

where the terms have their usual meanings as explained previously.

The change in transmitted THz radiation $(\Delta T/T)\,(t) \equiv x$, with $\Delta T = T_{\mathrm{excited}} - T_{\mathrm{dark}}$, is proportional to the photoexcited charge carrier density in the thin film via

$$n(t) = \phi C x(t). \tag{3.2}$$

Here ϕ indicates the number of free charge-carriers generated per photon, and $C = \tilde{n_0}/x(0)$ is the proportionality factor between the initial THz response $x(0)$ and the absorbed photon density $\tilde{n_0}$, which is given by

$$\tilde{n_0} = \frac{E\,\lambda\,\alpha(\lambda)}{h\,c\,A_{\mathrm{eff}}}\,(1 - R_{\mathrm{pump}}(\lambda))\,. \tag{3.3}$$

The effective overlap area A_{eff} is the effective overlap area of the optical pump and THz probe beams and can be calculated from the pump and probe beam parameters, whilst the absorption ($\alpha(\lambda)$) and reflection ($R_{\mathrm{pump}}(\lambda)$) coefficients are measured for each sample, h is Planck's constant, c is the speed of light, E is the energy contained in an optical excitation pulse of wavelength λ(= 400 nm in this thesis), and λ is the wavelength. Although for very high excitation fluences ($> 50\,\mu\mathrm{Jcm}^{-2}$) the proportionality in **Equation 3.2** no longer holds, the fluences employed here were all below this threshold (at most $34\,\mu\mathrm{Jcm}^{-2}$), meaning that we calculate C as the average value

across all fluences.

Substituting **Equation 3.2** into **Equation 3.1** gives

$$\frac{\mathrm{d}x}{\mathrm{d}t} = -C^2\phi^2 k_3 x^3 - C\phi k_2 x^2 - k_1 x \tag{3.4}$$

$$= -A_3 x^3 - A_2 x^2 - A_1 x. \tag{3.5}$$

In this case, given that fluences were kept below $34\,\mu\mathrm{Jcm}^{-2}$ (equivalent to a photoexcited charge-carrier density of $n \approx 5 \times 10^{18}\,\mathrm{cm}^{-3}$), Auger recombination was found to contribute negligibly. Thus, setting $k_3 = A_3 = 0$, an analytical solution can be found to the ordinary different equation (ODE) using standard techniques, yielding

$$x(t) = \frac{A_1}{\kappa \mathrm{e}^{A_1 t} - A_2}, \text{where } \kappa = \frac{A_1}{x(0)} + A_2. \tag{3.6}$$

These solutions are fitted globally to the decays across all fluences in order to extract the rate constants A_i. The value of k_1, and thus A_1, is fixed using the value obtained from TCSPC measurements. The values of k_2 is then calculated as $k_2 = A_2/\phi C$ and we further assume $\phi = 1$ i.e. that all photons are converted to free charges, as is typical in most bulk 3D perovskites [6].

Finally, in order to account for an initial spatially varying charge-carrier density (due to absorption following the Beer-Lambert law), the fitting algorithm takes into account an exponentially decaying charge-carrier density. This is done by dividing the sample into 30 equally thick slices and computing the decay function for each of these individually.

Calculation of Charge-Carrier Mobilities

Charge-carrier mobility (μ) is linked to the photoconductivity of a thin film by

$$\mu = \frac{\Delta S\, A_{\mathrm{eff}}}{Ne} \tag{3.7}$$

Here ΔS is the sheet conductivity of the film, N is the number of photoexcited free charge carriers, and e is the elementary charge.

Given that THz wavelengths are both much longer than the perovskite film thickness ($\lambda_{\mathrm{THz}} \gg d_{\mathrm{perovskite}}$) and shorter than the quartz substrate thickness ($\lambda_{\mathrm{THz}} < d_{\mathrm{substrate}}$), we can use the following approximation for the sheet photoconductivity of a thin film between two media (A and B) with refractive indeces n_{A} and n_{B}

$$\Delta S = -\epsilon_0 c(n_{\mathrm{A}} + n_{\mathrm{B}}) \left(\frac{\Delta T}{T} \right). \tag{3.8}$$

Here $\Delta T = T_{\mathrm{excited}} - T_{\mathrm{dark}}$ is the photoinduced change in the THz electric field, and in our case, medium A is vacuum ($n_{\mathrm{A}} = 1$) and medium B is z-cut quartz ($n_{\mathrm{B}} = 2.13$).

We determine the number of photoexcited charge-carriers using

$$N = \phi \frac{E\,\lambda}{h\,c} \left(1 - R_{\mathrm{pump}}(\lambda)\right) \left(1 - T_{\mathrm{pump}}(\lambda)\right) \tag{3.9}$$

where E is the energy contained in an optical excitation pulse of wavelength λ (= 400 nm), $R_{\mathrm{pump}}(\lambda)$ and $T_{\mathrm{pump}}(\lambda)$ are the sample reflectivity and transmittance at $\lambda =$ 400 nm, and ϕ is the branching ratio of photons to free charges.

We can substitute **Equations 3.8 & 3.9** into **Equation 3.7**, in order to obtain

$$\phi\mu = -\epsilon_0 c(n_{\mathrm{A}} + n_{\mathrm{B}}) \frac{A_{\mathrm{eff}} hc}{Ee\lambda \left(1 - R_{\mathrm{pump}}(\lambda)\right) \left(1 - T_{\mathrm{pump}}(\lambda)\right)} \left(\frac{\Delta T}{T} \right) \tag{3.10}$$

Given that the branching ratio $0 \leq \phi \leq 1$, the calculated effective charge-carrier mobility is always an underestimate; it is only identical to the true free-carrier mobility when there is full conversion of photons to free charges, although this is typically the case for bulk 3D perovskites [6]. Further, the determined charge-carrier mobility arises from contributions to the conductivity from both free electrons and free holes, and these cannot be separated. Thus, the effective mobility values shown throughout this thesis are in fact the sum of electron and hole mobilities.

3.2.2 Time-correlated single photon counting (TCSPC)

TCSPC measurements were carried out using a 398 nm laser (PicoHarp, LDH-D-C-405M) to photoexcite the thin films, in pulsed excitation mode with the repetition rate stated alongside the data. Photoluminescence was collected and coupled into a grating spectrometer (Princeton Instruments SP-2558), with a photon-counting detector (PDM series from MPD). Timing is controlled electronically using a PicoHarp300 event timer. PL transients were measured at the peak wavelengths of the steady-state PL spectra unless otherwise stated.

TCSPC fitting

For the isolated films in **Chapters 4 & 5**, a least-squares fit was carried out in Python script on the lowest-fluence PL decays using a stretched exponential of the form

$$I(t) = I_0 \mathrm{e}^{\left(\frac{t}{\tau}\right)^{\beta}}, \tag{3.11}$$

where I_0 is the initial intensity, τ is an analogue to the lifetime and β is the stretching factor which must be between 0 and 1. A characteristic decay time can then be extracted as

$$\langle\tau\rangle = \int_0^{\infty} \mathrm{e}^{\left(\frac{t}{\tau}\right)^{\beta}} \mathrm{d}t = \frac{\tau}{\beta}\Gamma\left(\frac{1}{\beta}\right), \tag{3.12}$$

where Γ is the Gamma function. The justification for the use of stretched exponentials is as follows. A stretched exponential arises from the continuous sum of exponential decays [7], and the volumetric recombination rate constant *may* depend on the charge-carrier density, but this is, to my knowledge, just an assumption. Pragmatically, this function represents the TCSPC transients of isolated perovskite thin films (no transport layers) well, and so is popular in the field. However, care must be taken when using this approach to extract a characteristic decay time. Firstly, this form is not explicitly related to any recombination order, and so characteristic lifetimes extracted from the use of stretched exponentials are not strictly the first-order lifetime. However, this

characteristic lifetime can be used a good approximation, provided one is explicit about this. Secondly, the characteristic lifetimes that arise from stretched exponential fitting of different TCSPC transients should only be compared if the stretching factor β is comparable.

For the films with transport layers attached in **Chapter 5**, a least squares fit was carried out using a double exponential $I = A_1 e^{-t/T_1} + A_2 e^{-t/T_2}$. No direct physical basis is claimed for this fitting. It was used to ensure an accurate reproduction of the TCSPC transient and, importantly, ensures a smooth numerical derivative, which is necessary for the calculation of the differential lifetime.

3.2.3 Photoluminescence quantum yield (PLQY)

In **Chapter 5**, photoluminescence quantum yield (PLQY) mesurements were performed as follows. A continuous wave 520 nm laser diode (Insaneware) was coupled into an optical fibre which entered an integrating sphere to photoexcite the sample. The intensity of the laser was equivalent to the 1 sun AM1.5 illumination. To confirm this calibration, a solar cell of the appropriate bandgap was illuminated in the integrating sphere and its short-circuit current density (J_{SC}) was measured to be in good agreement with the value determined from a solar simulator. The light from the sphere was coupled into a second optical fibre which was measured using an Andor SR393i-B spectrometer.

The integrating sphere and fibre were calibrated by shining a halogen lamp of known spectrum into the sphere. A spectral correction factor was determined to ensure the detected spectrum of the lamp matched its known spectral irradiance.

To determine the absolute photon number, the corrected spectral irradiance was first divided by the photon energy (to give spectral photon density) and then numerical integration was performed to obtain the absolute photon count for both excitation and photoluminescence. To verify the accuracy of these measurements, three test samples (purchased from Hamamatsu Photonics) of known PLQY ($\sim 70\%$) were measured. We determined the PLQY of the test samples to within a small ($< 5\%$) relative error.

In **Chapters 4 & 6**, PLQY measurements were performed in broadly the same manner. The differences are the samples were photoexcited with a 405 nm continuous wave laser, and the spectrometer used was a QEPro (OceanOptics). In these Chapter, the intergrating sphere, optical fibre and spectrometer system was calibrated using a OceanInsight HL-3P-INT-CAL halogen lamp of known spectrum. In additon, PLQY was determined using the 'De Mello method', first described in Ref [8].

3.2.4 UV-Vis absorption

Absorption spectra were taken using a Bruker Vertex 80v Fourier-Transform Infrared (FTIR) spectrometer, with a tungsten halogen source and a silicon diode detector. Measurements were carried out under vacuum (< 5 mbar).

3.2.5 Ellipsometry

The optical constants were measured using a Woollam RC2 Ellipsometer. The ellipsometer was calibrated using a reference silicon wafer with 20 nm SiO_2 on top. Ellipsometric data $(\Psi - \delta)$was acquired at four angles: 45°, 55°, 65°, 75°. The software CompleteEASE was used to model the data. The data was first fitted to the Cauchy relation in a small region of the sub-bandgap region. A B-spline was used to fit the remainder of the spectrum. The extinction co-efficient was set to zero below the bandgap. Kramers-Kronig consistency was maintained. The ellipsometry measurements and analysis were performed by Dr. Suhas Mahesh.

3.2.6 Time-resolved emission spectroscopy (TRES)

Time-resolved emission spectroscopy (TRES) measurements were performed in **Chapter 6**. The samples were photoexcited in vacuum ($\sim 5 \times 10^{-3}$ mbar) with a pulsed 398 nm centre wavelength laser with a repition rate of 5 MHz. Time-correlated single photon counting transients were recorded for detection wavelengths between $425 - 700$ nm with 5 nm steps. Data was collected at each wavelength for 60 s. The temporal

resolution was 4 ps.

3.3 Structural Characterisation

3.3.1 X-ray diffraction

X-ray diffraction patterns were measured using a Panalytical X'pert powder diffractometer with a copper K_α X-ray source, $\lambda = 0.1541$ nm.

3.4 Electronic characterisation

3.4.1 Ultraviolet photoemission sprectroscopy (UPS)

Ultraviolet photoemission sprectroscopy (UPS) was conducted using a monochromated helium discharge lamp (HIS 13 FOCUS GmbH, photon energy of 21.22 eV) in an ultrahigh vacuum system (base pressure of 1×10^{-9} mbar). All spectra were recorded at room temperature and normal emission using a hemispherical electron analyser (SPECSPhoibos 100). Secondary electrons cut-off (SECO) spectra were conducted at a negative bias of 10 V. Thickness of the C60 layer was monitored using a quartz crystal microbalance, thus corresponding a mass-thickness. All samples were transferred directly from the N_2 filled gloveboxinto the vacuum chamber without exposing to ambient air. These measurements were performed and analysed by Dr. Fengshuo Zu, at Humboldt Univerity, Berlin.

3.4.2 X-ray photoemission spectroscopy (XPS)

A Thermo Scientific Kα X-Ray photoelectron spectrometer was used to perform XPS measurements. A monochromatic Al Kα at a take-off angle of 90 degrees was used an X-ray source. The core level XPS spectra were recorded using a pass energy of 20 eV (resolution approximately 0.4 eV) from an analysis area of 300 μm $\times$ 300 μm. The spec-

trometer work function and binding energy scale were calibrated using the Fermi edge and 3*d* peak recorded from a polycrystalline silver (Ag) sample prior to the commencement of the experiments. Fitting procedures to extract peak positions from the XPS data were carried out using the Casa XPS software suite. A Shirley background was used and the spectra were fit with a mixture of Gaussian/Lorentzian (Lorentzian = 30 %) line shapes. These measurements were performed by Dr. Alexandra J. Ramadan.

3.5 PV Device Characterisation

3.5.1 *JV* characteristics

In **Chapter 4**, Current-voltage (*JV*) characteristics were recorded in ambient air under simulated AM1.5 solar light (1 sun, 100 mWcm^{-2}) generated by an ABET Class AAB sun 2000 simulator. Each device was measured with a 20 mV voltage step and a 100 ms time step (scan rate of 0.2 Vs^{-1}). All devices were masked with a 0.0919 cm^2 metal aperture to define the active area and eliminate edge effects. Stabilized power output (SPO) measurements were performed by holding the device at the voltage of the maximum power point, as determined by the *JV* characteristic, and monitoring the current density over the course of 60 s, the power density then being given as the $J \times V$ product as always.

In **Chapter 5**, solar cells were measured at the University of Potsdam according to the following protocol. Current density - voltage (*JV*) curves were obtained in a 2-wire source-sense configuration with a Keithley 2400. The samples were illuminated using an Oriel class AAA Xenon lamp-based sun simulator at an intensity of approximately 100 mWcm^{-2} of AM1.5G irradiation. The illumination intensity was monitored simultaneously with a Si photodiode. The exact illumination intensity was used for efficiency calculations, and the simulator was calibrated with a KG5 filtered silicon solar cell (certified by Fraunhofer ISE). The obtained short-circuit current density is checked by integrating the product of the external quantum efficiency (EQE) and the

solar spectrum which matches the obtained J_{SC} within less than 3 %. The temperature of the cell was fixed to 25 °C and a voltage ramp (scan rate) of 0.2 V/s was used, unless otherwise stated.

In **Chapter 6**, current-density voltage characteristics were measured in ambient air ($\sim 25\,°C, 45 \pm 10\%$ relative humidity) using a Keithley 2401 in a 4-wire configuration. To illuminate the perovskite solar cells, a Wavelabs SINUS-220 LED light-source was used which accurately reproduces the AM1.5 solar spectrum at an intensity of $100\,mWcm^{-2}$. The intensity was calibrated using a Fraunhofer silicon reference solar cell. The reference cell is a $2\,cm \times 2\,cm$ KG3-filtered Si photodiode. The lamp intensity was set to produce the same short-circuit current from the photodiode as its certified 1 sun value.

The device active area of the perovskite solar cells was $0.25\,cm^2$ or $1\,cm^2$ defined by an opaque metal mask. The measurement protocol was: 1. The open-circuit voltage was measured was 20 s; 2. a dark JV curve was measured performing the reverse scan, from $-1.35\,V$ to $0.1\,V$ and then immediately the forward scan, from $0.1\,V$ to $-1.35\,V$; 3. The illuminated JV was measured by performing the reverse scan, from $-1.35\,V$ to $0.1\,V$ and then immediately the forward scan, from $0.1\,V$ to $-1.35\,V$. The scan rate was $\sim 100\,mVs^{-1}$; 4. A JV curve (scan rate 0.3 V/s) in both forward and reverse directions was performed. The current density through the cell was limited to $25\,mAcm^{-2}$, and the JV sweep was halted if this value was exceeded. 4. The maximum power point of the device under test was tracked for at least 30 s using a gradient decent algorithm; 5. The short-circuit current density was monitored for 5 s.

3.5.2 Ageing experiments

Encapsulation was performed by affixing a glass cover slip to the complete devices using a UV-activated epoxy (LT-U001, Lumtec) in a N_2 filled glovebox. The devices were then placed in an ATLAS Suntest XLS+ aging box where they were held at 85 °C and light soaked. The light source was a Xe arc lamp, filtered to closely match the AM1.5 solar spectrum. The light pulsed rapidly ($\sim$ 100 Hz), which resulted in a time-average

irradiance equivalent to 0.76 suns. Devices were removed 30 minutes prior to testing to allow them to return to room temperature.

3.5.3 External quantum efficiency (EQE)

The external quantum efficiency of our devices was determined using Fourier transform photocurrent spectroscopy. Our custom-built set up is based on a Bruker Vertex 80v Fourier transform interferometer. The solar cells were masked with a metal aperture such that the whole active area was illuminated by a tungsten halogen lamp. A CaF_2 beamsplitter was used. To determine the EQE, the photocurrent spectrum of the device under test was divided by that of a calibrated Si reference cell (Newport) of a known EQE. The acquisition time for each photocurrent spectrum was approximately 60 seconds.

To determine the short-circuit current from the EQE measurements, the overlap integral of the AM1.5 photon flux ($\varphi_{\mathrm{AM1.5}}$) with the EQE was calculated. Explicitly, this is given by

$$J_{\mathrm{SC}} = q \int_0^{\infty} EQE(\lambda)\, \varphi_{\mathrm{AM1.5}}(\lambda)\, \mathrm{d}\lambda \tag{3.13}$$

where q is the elementary charge and λ is the wavelength.

3.5.4 Intensity dependent open-circuit voltage measurements

Intensity dependent V_{OC} measurements were performed using a continuous wave laser of central wavelength 445 nm (Insaneware). A continuously variable neutral density filterwheel (ThorLabs) was used to attenuate the laser power (up to OD 6).

The light intensity was simultaneously measured with a silicon photodetector and a Keithley 485 to ensure the accuracy of the measurement. The measurement was performed by first measuring the open-circuit voltage at a given intensity and a variable exposure time to ensure steady-state was achieved. Then the device was taken to short circuit for 1 second whilst the filter wheel rotated to the next position. A custom-built

Labview program was written to automate the measurement. To check whether the V_{OC} reached steady-state conditions, the temporal evolution of the open-circuit voltage and the J_{SC} was recorded with a resolution of 200 ms. Moreover, the exposure time was varied before the V_{OC} value was taken at each intensity step which did not lead to significant changes in the open-circuit voltage as previously reported [9]. These measurements were performed by Dr. Pietro Caprioglio at the University of Potsdam.

3.5.5 Pseudo JV-curve (pJV) determination

The pJV curves were determined as follows, in line with a recent publication [9]. Firstly, illumination intensity-dependent PLQY or V_{OC} measurements were performed. The PLQY measurements were converted into QFLS values as described above. Then the intensity axis was converted to current density, by setting the current density value at 1-sun to be 95 % of the radiative potential (in this case 19.0 mA cm^{-2}). The axes were then inverted so the horizontal axis was voltage (from V_{OC} or QFLS/q measurements) and the vertical axis a current. Then, we subtract each value of the current by the generation current which ensures 0 V corresponds to J_{SC} conditions and 0 mA cm^{-2} to the open-circuit voltage equivalent.

3.5.6 Photoluminescence imaging

Photoluminescence imaging on full devices was performed according to our recent study [10]. In brief, the devices were excited using a ThorLabs M450LP1 LED. The intensity of the LED illumination was controlled using a Multicomp PRO MP710086 bench power supply, to ensure one-sun equivalent photon flux (i.e. $J_{SC}^{\text{solar sim}} = J_{SC}^{\text{LED}}$).

The PL was collected using an ANDOR Zyla 4.2 sCMOS sensor, which was cooled to 0°C . A Kowa LM50XC lens was used. The aperture was set to F5.6 to increase the depth of field such that the entire device stack was in focus. To remove the effect of stray light, the entire set-up was placed in a 'light-tight' enclosure. In all the experiments undertaken, 10 reference images in the dark were taken before and

after the experiment. To perform an accurate background subtraction, the average background was calculated by averaging the values at each pixel for all the reference images taken. The values per pixel of the background image were subtracted from the data.

The code used for data acquisition and data analysis are provided free and open source under the lesser GPL licence:

Equipment control: `https://gitlab.com/pod-group/pl-imaging-control`, and,

Data analysis: `https://gitlab.com/pod-group/PL_imaging_analysis`.

These measurements and the analysis were performed by Akash Dasgupta.

3.6 Drift-diffusion simulations

The simulations were performed using SCAPS (Solar Cell Capacitance Simulator), which is an open-source software package that can be obtained from `https://users.elis.ugent.be/ELISgroups/solar/projects/scaps` upon the conditions requested by the developers Marc Burgelman *et al.* [11]. The simulation parameters used in **Chapter 5** are presented below.

Parameter	**Value (control)**	**Value (ionic additive)**	**Comment**
Bandgap	1.8 eV	1.8 eV	From the optical data presented in **Figure 5.1**
Electron affinity	3.8 eV	3.8 eV	This leads to band misalignments of 0.1 eV at each interface, consistent with the V_{OC}-QFLS mismatch we observe [12].
Dielectric permittivity (ϵ_r)	22	22	

Conduction band effective density of states (N_c)	1.5×10^{18} cm^{-3}	1.5×10^{18} cm^{-3}	
Valence band effective density of states (N_v)	1.5×10^{18} cm^{-3}	1.5×10^{18} cm^{-3}	
Electron thermal velocity	1×10^{7} cms^{-1}	1×10^{7} cms^{-1}	
Hole thermal velocity	1×10^{7} cms^{-1}	1×10^{7} cms^{-1}	
Electron mobility	1 $cm^2V^{-1}s^{-1}$	1 $cm^2V^{-1}s^{-1}$	The THz mobilities measured in this study were higher than this input. However, a better fit to the JV curves was obtained with a mobility of 1 $cm^2V^{-1}s^{-1}$, which might be related to the THz mobility being consider short-range and so is insensitive to the influence of, for example, grain boundaries [13]. This value is consistent with simulation values used in the literature [14, 15].
Hole mobility	1 $cm^2V^{-1}s^{-1}$	1 $cm^2V^{-1}s^{-1}$	See above
Shallow uniform donor density	1×10^{10} cm^{-3}	1×10^{10} cm^{-3}	

Shallow uniform acceptor density	1×10^{10} cm^{-3}	1×10^{10} cm^{-3}	
Radiative recombination rate (k_2)	5×10^{-11} $cm^{-3}s^{-1}$	5×10^{-11} $cm^{-3}s^{-1}$	Determined from experiment, data shown in **Figure 5.2**
Parameter (perovskite defect)	**Value (Control)**	**Value (ionic additive)**	**Comment**
Defect type	Neutral	Neutral	
Electron capture cross section	1×10^{-15} cm^2	1×10^{-15} cm^2	
Hole capture cross section	1×10^{-15} cm^2	1×10^{-15} cm^2	
Trap profile	Uniform	Uniform	
Trap density	2.2×10^{14} cm^{-3}	1.1×10^{14} cm^{-3}	These values set the bulk lifetimes to be 450 ns, and 900 ns as determined from TCSPC measurements on the bulk perovskite
Parameter (HTL)	**Value (control)**	**Value (IA)**	**Comment**
Bandgap	3.0 eV	3.0 eV	
Electron affinity	2.5 eV	2.5 eV	This leads to band misalignments of 0.1 eV at each interface, consistent with the V_{OC}-QFLS mismatch we observe [12].
Dielectric permittivity (ϵ_r)	3.5	3.5	

Conduction band effective density of states	1×10^{20} cm^{-3}	1×10^{20} cm^{-3}	
Valence band effective density of states	1×10^{20} cm^{-3}	1×10^{20} cm^{-3}	
Electron thermal velocity	1×10^{7} cms^{-1}	1×10^{7} cms^{-1}	
Hole thermal velocity	1×10^{7} cms^{-1}	1×10^{7} cms^{-1}	
Electron mobility	1×10^{-5} $cm^2V^{-1}s^{-1}$	1×10^{-5} $cm^2V^{-1}s^{-1}$	
Hole mobility	1×10^{-4} $cm^2V^{-1}s^{-1}$	1×10^{-4} $cm^2V^{-1}s^{-1}$	
Shallow uniform donor density	1×10^{5} cm^{-3}	1×10^{5} cm^{-3}	
Shallow uniform acceptor density	1×10^{5} cm^{-3}	1×10^{5} cm^{-3}	

Parameter (HTL defect)	**Value (Control)**	**Value (ionic additive)**	**Comment**
Defect type	Neutral	Neutral	
Electron capture cross section	1×10^{-15} cm^2	1×10^{-15} cm^2	
Hole capture cross section	1×10^{-15} cm^2	1×10^{-15} cm^2	
Trap profile	Uniform	Uniform	

Trap density	1×10^{17} cm^{-3}	1×10^{17} cm^{-3}	
Parameter (HTL interface)	**Value (Control)**	**Value (ionic additive)**	**Comment**
Defect type	Acceptor	Acceptor	
Electron capture cross section	1×10^{-16} cm^2	1×10^{-16} cm^2	
Hole capture cross section	1×10^{-16} cm^2	1×10^{-16} cm^2	
Total density	1.3×10^{12} cm^{-2}	0.45×10^{12} cm^{-2}	This sets the surface recombination velocity (SRV) at each HTL interface to be those that were determined in **Table 5.1**.
Parameter (ETL)	**Value (control)**	**Value (IA)**	**Comment**
Bandgap	2.0 eV	2.0 eV	
Electron affinity	3.9 eV	3.9 eV	This leads to band misalignments of 0.1 eV at each interface, consistent with the V_{OC}-QFLS mismatch we observe [12].
Dielectric permittivity (ϵ_r)	5.0	5.0	
Conduction band effective density of states	1×10^{20} cm^{-3}	1×10^{20} cm^{-3}	
Valence band effective density of states	1×10^{20} cm^{-3}	1×10^{20} cm^{-3}	

Electron thermal velocity	1×10^7 cms^{-1}	1×10^7 cms^{-1}	
Hole thermal velocity	1×10^7 cms^{-1}	1×10^7 cms^{-1}	
Electron mobility	1×10^{-2} $cm^2V^{-1}s^{-1}$	1×10^{-2} $cm^2V^{-1}s^{-1}$	
Hole mobility	1×10^{-2} $cm^2V^{-1}s^{-1}$	1×10^{-2} $cm^2V^{-1}s^{-1}$	
Shallow uniform donor density	1×10^5 cm^{-3}	1×10^5 cm^{-3}	
Shallow uniform acceptor density	1×10^5 cm^{-3}	1×10^5 cm^{-3}	
Parameter (ETL defect)	**Value (Control)**	**Value (ionic additive)**	**Comment**
Defect type	Neutral	Neutral	
Electron capture cross section	1×10^{-15} cm^2	1×10^{-15} cm^2	
Hole capture cross section	1×10^{-15} cm^2	1×10^{-15} cm^2	
Trap profile	Uniform	Uniform	
Trap density	1×10^{17} cm^{-3}	1×10^{17} cm^{-3}	
Parameter (ETL interface)	**Value (Control)**	**Value (ionic additive)**	**Comment**
Defect type	Donor	Donor	
Electron capture cross section	1×10^{-16} cm^2	1×10^{-16} cm^2	

Hole capture cross section	1×10^{-16} cm^2	1×10^{-16} cm^2	
Total density	5.6×10^{12} cm^{-2}	0.64×10^{12} cm^{-2}	This sets the surface recombination velocity (SRV) at each ETL interface to be those that were determined in **Table 5.1**.

Table 3.2: *Input parameters for the drift-diffusion simulations presented in* ***Chapter 5****. If no explanation for a value is provided, the values used are consistent with SCAPS simulations presented in the literature [14, 15]. In particular, ref [14] provides detailed information from each parameter is determined.*

References

[1] Saliba, M. *et al.* Cesium-containing triple cation perovskite solar cells: improved stability, reproducibility and high efficiency. *Energy & Environmental Science* **9**, 1989–1997 (2016).

[2] McMeekin, D. P. *et al.* A mixed-cation lead mixed-halide perovskite absorber for tandem solar cells. *Science* **351**, 151–155 (2016).

[3] Seifert, T. *et al.* Efficient metallic spintronic emitters of ultrabroadband terahertz radiation. *Nature Photonics* **10**, 483–488 (2016).

[4] Wehrenfennig, C., Liu, M., Snaith, H. J., Johnston, M. B. & Herz, L. M. Charge-carrier dynamics in vapour-deposited films of the organolead halide perovskite $CH_3NH_3PbI_{3-x}Cl_x$. *Energy & Environmental Science* **7**, 2269–2275 (2014).

[5] Johnston, M. B. & Herz, L. M. Hybrid perovskites for photovoltaics: charge-carrier recombination, diffusion, and radiative efficiencies. *Accounts of chemical research* **49**, 146–154 (2016).

[6] Herz, L. M. Charge-carrier dynamics in organic-inorganic metal halide perovskites. *Annual Review of Physical Chemistry* **67**, 65–89 (2016).

[7] Johnston, D. Stretched exponential relaxation arising from a continuous sum of exponential decays. *Physical Review B* **74**, 184430 (2006).

[8] de Mello, J. C., Wittmann, H. F. & Friend, R. H. An improved experimental determination of external photoluminescence quantum efficiency. *Advanced Materials* **9**, 230–232 (1997).

[9] Stolterfoht, M. *et al.* How to quantify the efficiency potential of neat perovskite films: Perovskite semiconductors with an implied efficiency exceeding 28%. *Advanced Materials* **32**, 2000080 (2020).

[10] Dasgupta, A. *et al.* Visualizing macroscopic inhomogeneities in perovskite solar cells. *ACS Energy Letters* **7**, 2311–2322 (2022).

[11] Burgelman, M., Nollet, P. & Degrave, S. Modelling polycrystalline semiconductor solar cells. *Thin Solid Films* **361**, 527–532 (2000).

[12] Caprioglio, P. *et al.* On the relation between the open-circuit voltage and quasi-fermi level splitting in efficient perovskite solar cells. *Advanced Energy Materials* **9**, 1901631 (2019).

[13] Lim, J. *et al.* Elucidating the long-range charge carrier mobility in metal halide perovskite thin films. *Energy & Environmental Science* **12**, 169–176 (2019).

[14] Diekmann, J. *et al.* Pathways toward 30% efficient single-junction perovskite solar cells and the role of mobile ions. *Solar RRL* **5**, 2100219 (2021).

[15] Caprioglio, P. *et al.* On the origin of the ideality factor in perovskite solar cells. *Advanced Energy Materials* **10**, 2000502 (2020).

Chapter 4

Thermally Stable Passivation towards High Efficiency Inverted Perovskite Solar Cells

Publication related to this chapter

The results in this chapter have been published in **R. D. J. Oliver**, Yen-Hung Lin, Alexander J. Horn, Chelsea Q. Xia, Jonathan H. Warby, Michael B. Johnston, Alexandra J. Ramadan, Henry J. Snaith, *Thermally Stable Passivation toward High Efficiency Inverted Perovskite Solar Cells*, *ACS Energy Lett.*, 2020, **5**, 11, pages 3336–3343.

4.1 Summary of results

Although metal halide perovskite photovoltaics have shown an unprecedented rise in power conversion efficiency (PCE) they remain far from their theoretical PCE limit. The highest efficiencies to-date are delivered when polycrystalline films are enhanced via "molecular passivation", but this can introduce new instabilities, in particular under severe accelerated ageing conditions (e.g. at 85 °C in the dark or under full spectrum simulated sunlight). Here, we utilise a benzylammonium bromide passivation treatment to improve device performance, achieving a champion stabilised power output

(SPO) of 19.5 % in a p-i-n device architecture. We correlate the improved device performance with a significant increase in charge carrier diffusion lengths, mobilities and lifetimes. Furthermore, treated devices maintain an increased performance during 120 hours combined stressing under simulated full-spectrum sunlight at 85 °C , indicating that enhancement from this passivation treatment is sustained under harsh accelerated ageing conditions. This is a crucial step towards real-world-operation relevant passivation treatments.

4.2 Introduction

As discussed in **Section 2.3**, metal halide PSCs are attracting immense interest in the photovoltaic research community due to their remarkable optoelectronic properties including long carrier diffusion lengths, direct tunable bandgap and high absorption coefficients [1–4]. This has pushed the power conversion efficiencies (PCEs) of laboratory scale single junction PSCs to $>$ 25 %, comparable with established technologies such as crystalline silicon [5]. However, many of the fabrication routes which have been reported in the literature to result in high-efficiency PSCs, negatively impact the long-term operational stability of the devices. Notably, the highest efficiency devices still use a substantial amount of methylammonium (MA) as the A-cation, the instability of which is well documented [6–10]. Furthermore, these PSCs employ a n-i-p architecture, using 2,2',7,7'-Tetrakis[N,N-di(4-methoxyphenyl)amino]-9,9'-spirobifluorene (Spiro-OMeTAD) as the hole transporting material. Not only is Spiro-OMeTAD itself unstable, but the additives required for optimal device performance (lithium-TFSi (Lithium bis(trifluoromethanesulphonyl)imide) and tBP (4-tert-Butylpyridine)) further limit the lifetime of the devices substantially [11, 12]. As such there has been a significant move within the field towards using the "inverted" p-i-n device architecture, which removes the need for spiro-OMeTAD, reduces the hysteresis of PSCs and is more directly applicable to perovskite-on-silicon tandem technologies [13]. However, inverted PSCs have thus far delivered reduced efficiency as compared to

their n-i-p counterparts, due to lower open-circuit voltages (V_{OC}s) originating from increased non-radiative recombination which is particularly severe at the interfaces with the charge-transporting layers [14–16].

Recent work by Jiang *et al.* highlights the limitations of contemporary passivation methods [17]. They report the use of phenethylammonium iodide (PEAI) as a surface passivation treatment in n-i-p PSCs and achieve an impressive champion PCE of 23.6 %. However, for thermal ageing at 85 °C in the dark, the authors find that they need to replace Spiro-OMeTAD with the more thermally stable PTAA, reducing the maximum PCE to 19.1 %. Moreover, the comparative improvement due to the PEAI surface passivation treatment vanishes after less than 50 hours of 85 °C ageing in the dark. The evidence is that at higher annealing temperatures the PEAI forms a layered 2D phase with PbI_2 from the perovskite, which is assumed to diminish the availability of PEAI to act as a surface passivation molecule [17]. Despite achieving impressive PCEs, this work highlights the need for thermally stable passivation treatments combined with thermally stable device architectures, so that the improvements would last over the lifetime of modules should they be implemented in the field.

Benzylamine rather than the ammonium salt, has been previously used to modify the surface of metal halide perovskites [18, 19]. Here we report the use of benzylammonium bromide as a passivation treatment in inverted perovskite solar cells. We achieve devices with high champion stabilized power output (SPO) efficiencies of 19.5 % and we show that upon severe accelerated aging at 85 °C , at 0.76 solar irradiance, we observe a sustained improvement from the passivation treatment. This indicates that the passivation treatment does not noticeably deteriorate even under these harsh conditions.

4.3 Results and Discussion

4.3.1 Optoelectronic properties

Our study focuses on the effect of BenABr on the triple cation perovskite $Cs_{0.05}(FA_{0.83}MA_{0.17})_{0.95}Pb(I_{0.9}Br_{0.1})_3$ (FA is formamidinium), first reported by Saliba et al., with and without our passivation [20]. The treatment was applied by depositing BenABr dissolved in chlorobenzene by spincoating, fuller details can be found in **Section 3.1.2**. To determine the efficacy of BenABr as a passivation treatment we studied its influence on the photoluminescence (PL) of the perovskite films, as well as the charge carrier dynamics. We measured the photoluminescence quantum yield (PLQY) of the perovskite films on glass substrates and on device relevant substrates with isolated CTLs following the procedure of De Mello *et al.* [21]. For the HTL, we use fluorine-doped tin oxide (FTO) / polyTPD substrates, whereas to investigate the PL quenching induced by the ETL, perovskite films were first prepared on glass and subsequently coated with $PC_{61}BM$. As discussed in detail **Section 2.1.3**, PLQY is a powerful technique when assessing the quality of the perovskite semiconductor to be used in a solar cell since an increase in PLQY indicates that less non-radiative recombination is occurring within the film or at the interfaces. A higher PLQY results in an increase in the quasi-Fermi level splitting (QFLS), and should lead to improved device performance through an increase in open-circuit voltage [22–25]. For a standard PV material, we can calculate the change in QFLS following passivation (ΔQFLS = $QFLS_{passivated}$ - $QFLS_{pristine}$). To do this, we make use of **Equation 2.75** for both the passivated and pristine cases. The change in QFLS can then be calculated according to

$$\begin{aligned}\Delta\text{QFLS} &= \text{QFLS}_{\text{passivated}} - \text{QFLS}_{\text{pristine}} \\ &= \text{QFLS}_{\text{rad}}^{\text{passivated}} + k_{\text{B}}T\,\ln\left(\text{PLQY}_{\text{passivated}}\right) \\ &\qquad - \left[\text{QFLS}_{\text{rad}}^{\text{pristine}} + k_{\text{B}}T\,\ln\left(\text{PLQY}_{\text{pristine}}\right)\right] \\ &= k_{\text{B}}T\left[\ln\left(\text{PLQY}_{\text{passivated}}\right) - \ln\left(\text{PLQY}_{\text{pristine}}\right)\right] \\ &= k_{\text{B}}T\ln\left(\frac{\text{PLQY}_{\text{passivated}}}{\text{PLQY}_{\text{pristine}}}\right),\end{aligned} \tag{4.1}$$

where we have assumed the passivation has not changed the bandgap, and so the QFLS in the radiative limit is unchanged for each case, or $\text{QFLS}_{\text{rad}}^{\text{passivated}} - \text{QFLS}_{\text{rad}}^{\text{pristine}} = 0$. Now we can substitute $T = 298$ K into the above equation to arrive at

$$\Delta\text{QFLS} = 25.7\,\text{meV} \times \ln\left(\frac{\text{PLQY}_{\text{passivated}}}{\text{PLQY}_{\text{pristine}}}\right). \tag{4.2}$$

Equation 4.2 is a straightforward way to calculate the expected increase in open-circuit voltage for a given PLQY ratio. Therefore we expect in the region of 60 mV increase in open-circuit voltage, for every order of magnitude increase in radiative efficiency in the complete device [26]. Indeed, **Equation 4.2** can be modified to calculate the bandgap independent loss from the radiative limit. By setting $\text{PLQY}_{\text{passivated}}$ to be unity, i.e. in the ideal case, and then inputting the measured PLQY ($\text{PLQY}_{\text{measured}}$), we obtain

$$\Delta\text{QFLS}_{\text{rad}} = -25.7\text{meV} \times \ln\left(\text{PLQY}_{\text{measured}}\right) \tag{4.3}$$

where $\text{PLQY}_{\text{measured}}$ is expressed in absolute terms (i.e. not as a percentage).

We present the PLQY values in **Figure 4.1a** and summarise them in **Table 4.1**. We determine that the PLQY for the treated films increases in all cases, with the most substantial increase present for the perovskite films coated with $PC_{61}BM$. This $PC_{61}BM$/perovskite interface is known to induce the most non-radiative recombination in p-i-n devices, thus the main factor that limiting the open-circuit voltage [16, 24],

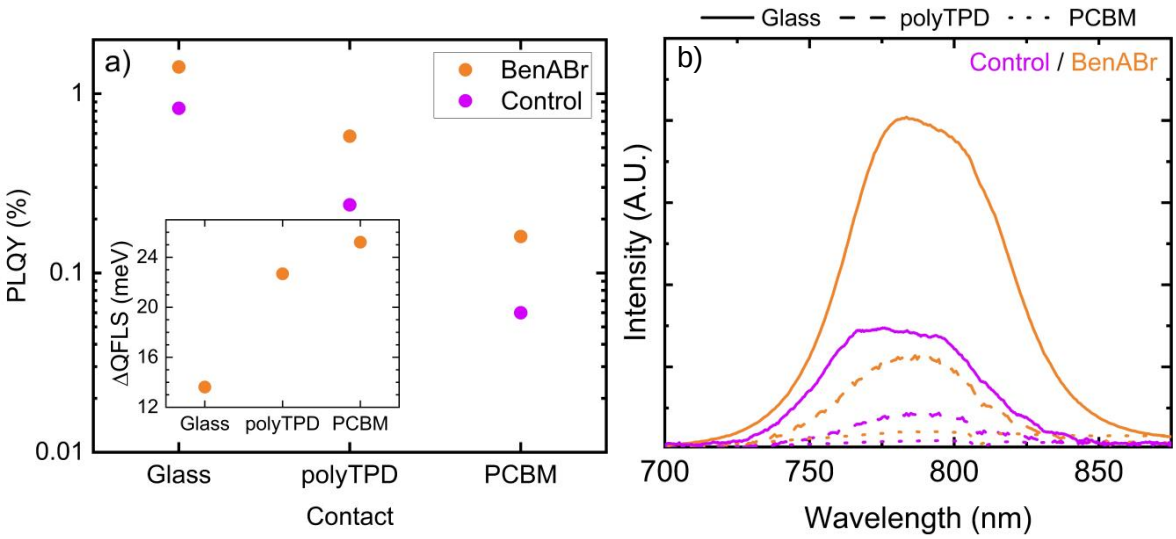


Figure 4.1: *a) PLQY values for treated (orange) and pristine (purple) samples with no charge transport layer (glass), and with isolated p-type (polyTPD) and n-type ($PC_{61}BM$) contacts. Inset: The boost in QFLS as determined by* ***Equation 4.2*** *for the same samples. b) Photoluminescence spectra for treated (orange) and control (purple) samples on glass substrates (solid lines), isolated hole-selective contact (polyTPD, dashed lines) and electron-selective contact ($PC_{61}BM$, dotted lines). Adapted with permission from ACS Energy Lett. 2020,* ***5****, 11, 3336–3343. [27] Copyright 2020, American Chemical Society.*

corroborated by the lower absolute photoluminescence quantum yield which we determine here. The PL spectra are presented in **Figure 4.1b**, which demonstrates that the BenABr does not have a significant effect on the shape of the PL, but results in a significant enhancement in intensity (which is quantified via the PLQY measurements discussed earlier). The films coated on glass have a slight asymmetrical character, which we attribute to the perovskite thin film growth being hindered by this choice of substrate.

The photoluminescence quantum yield is nearly 3 times larger for treated films at the $PC_{61}BM$ (electron selective) interface, which corresponds to an expected gain of ΔQFLS = 25 meV, as we show in the inset in **Figure 4.1a** and in **Table 4.1**. Since this interface is the dominant source of non-radiative recombination in p-i-n cells, we expect this to translate into a similar boost in V_{OC} in complete devices [24].

We measured the charge carrier lifetimes of the treated and pristine perovskite thin films on quartz substrates using TCSPC. As can be seen in **Figure 4.2a**, the PL decay for the treated film is much slower than that of the pristine one. This suggests extended

Contact	$PLQY_{pristine}$ (%)	$\Delta QFLS_{rad}^{pristine}$ (meV)	$PLQY_{passivated}$ (%)	$\Delta QFLS_{rad}^{passivated}$ (meV)	$\Delta QFLS$ (meV)
Glass	0.83	123	1.41	109	13.6
polyTPD	0.24	155	0.58	132	22.7
$PC_{61}BM$	0.06	191	0.16	165	25.2

Table 4.1: *PLQY values for pristine and passivated samples processed on glass (glass), with the additional coating of PCBM (PCBM) and processed on polyTPD coated FTO (polyTPD). Also shown are the $\Delta QFLS$ from the radiative limit $\Delta QFLS_{rad}$ and the $\Delta QFLS$ between the passivated and non-passivated films.*

charge-carrier lifetimes in the passivated films. From fitting these decays to a stretched exponential [28]

$$I(t) = A\mathrm{e}^{\left(\frac{t-t_0}{\tau}\right)^{\beta}} + C \tag{4.4}$$

where $I(t)$ is the PL intensity at time t, A is a normalizing constant, t is the time after the excitation pulse, t_0 an initial time offset, C is a constant offset in intensity, τ is an analogue to lifetime and β is the stretching factor. The mean relaxation time, which we define as the lifetime, is the area under the decay curves and hence is calculated as

$$\langle\tau\rangle = \int_0^{\infty} A\mathrm{e}^{\left(\frac{t}{\tau}\right)^{\beta}}\mathrm{d}t = A\frac{\tau}{\beta}\Gamma\left(\frac{1}{\beta}\right), \tag{4.5}$$

where $\Gamma(x)$ is the gamma function. (In the analysis for the lifetime, the maximum value of the TCSPC transient was was to time 0, which means that $t_0 = 0$, so does not appear in the above equation). A least-squares regression was implemented between 5 and 2500 ns to achieve the fits shown in **Figure 4.2a**, which yields the parameters presented in **Table 4.2**.

From fitting the decays, we use **Equation 4.5** we extract a lifetime of 390 ns and 85 ns for the treated and pristine films respectively. This indicates a reduced level of non-radiative recombination in the treated perovskite, which is typical of reduced trap-state density.

To delve into the short-range charge-carrier dynamics, we performed optical-pump

Parameter	Control	BenABr treated
A	0.74	0.93
τ (ns)	95	315
β	0.73	0.67
t_0 (ns)	20	6.4
C	3.9×10^{-3}	1.7×10^{-2}
$\langle\tau\rangle$ (ns)	85	394

Table 4.2: *Fitted parameters for a stretched exponential (**Equation 4.4**) to the time-correlated single photon counting (TCSPC) transients presented in **Figure 4.2a**.*

terahertz-probe spectroscopy (OPTPS) and terahertz time-domain spectroscopy (THz-TDS) on these isolated perovskite films. These measurements and analysis were performed by Dr. Chelsea Q. Xia. This non-contact technique enables us to investigate the electro-optic properties, such as photoconductivity and charge-carrier mobility, on a much faster time scale than the PL dynamics, which can be less than 100 fs, and in addition removes the effect of metallic contact incurred on solar cell devices [2, 29, 30]. **Figure 4.3a** shows the dark conductivity spectra for pristine and treated films, which indicates two prominent phonon modes around 1 THz and 2 THz featured as Lorentzian oscillators. From these data we can calculate the absorption coefficient at THz frequencies. From THz spectroscopy measurements, we obtain the complex conductivity as a function of frequency (ω),

$$\sigma(\omega) = \sigma_{\text{real}}(\omega) + i\sigma_{\text{imag}}(\omega), \tag{4.6}$$

where i is the square root of -1, σ_{real} and σ_{imag} refers to the real imaginary part of the dark conductivity respectively, which we show in **Figure 4.3a**. From these data, we calculate the dielectric function according to

$$\varepsilon_{\text{r}}(\omega) = \varepsilon_{\infty} + \frac{i}{\varepsilon_0\omega}\sigma(\omega) \tag{4.7}$$

where ε_{∞} is the dielectic function at high frequency and is assumed to be 30 Fm^{-1}, ε_0 is the vacuum permittivity. The real and imaginary parts, n and κ respectively, of the

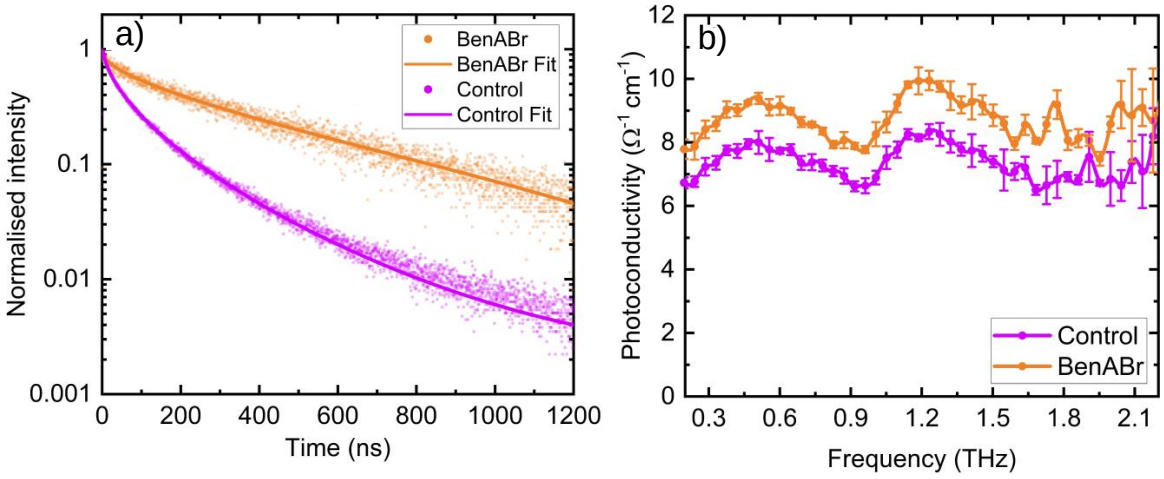


Figure 4.2: *a) Time-resolved photoluminescence (TRPL) transients for pristine (purple) and benzylammonium bromide treated (orange) films. The decays were fitted with a stretched exponential (**Equation 4.4**) from which lifetimes of 85 ns and 390 ns were extracted for the pristine and treated films respectively. b) Real part of THz photoconductivity spectra induced by photoexcitation. The spectra without photoexcitation are shown later. Adapted with permission from ACS Energy Lett. 2020, **5**, 11, 3336–3343. [27] Copyright 2020, American Chemical Society.*

refractive index can be obtained by taking the square root of the dielectric function. Then the absorption coefficient is calculated using

$$\alpha(\omega) = \frac{2\omega}{c}\kappa \tag{4.8}$$

where c is the speed of light. The calculated absorption coefficient is shown in **Figure 4.3b**, and is on the order of 10^3 cm^{-1}, indicating an absorption depth of a few micrometers, indicating the THz beam is sensitive to the entire perovskite thin film. The absorption coefficient for the treated film is slightly higher and the two phonon modes are prominent throughout.

We define the photoconductivity as the change of conductivity between a sample under photoexcitation and in the dark. The photoexcitation was applied by an ultrafast laser pulse of 400 nm center wavelength and 5.2 μJcm^{-2} fluence. **Figure 4.2b** displays the real part of the photoconductivity of the benzylammonium bromide-treated and untreated films. For both films, the spectrum is relatively flat over the frequency range of the experiment, and agrees with a Drude picture of band-like transport [31]. Small replica of the two phonon modes observed in **Figure 4.3a** can also be seen

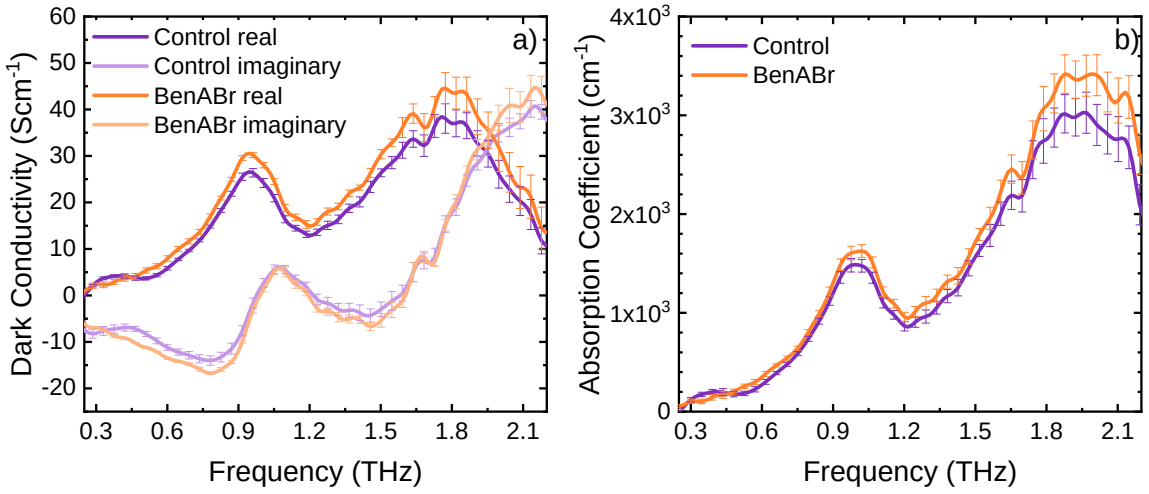


Figure 4.3: *a) Dark conductivity spectra measured using THz spectroscopy without photoexcitation. Data corresponding to the control sample is shown in purple, and data for the benzylammonium bromide treated sample is presented in orange. The real part of the conductivity is shown in dark lines, and the imaginary part in faint lines. b) the absorption coefficient for control (purple) and BenABr-treated (orange) perovskite films at THz frequencies. These measurements and analysis were performed by Dr. Chelsea Q. Xia. Adapted with permission from ACS Energy Lett. 2020, **5**, 11, 3336–3343. [27] Copyright 2020, American Chemical Society.*

superimposed on the spectra, indicating an electron-phonon coupling effect, which may suppress the charge-carrier transport [32]. Significantly, the BenABr treated film exhibited a 20 % higher photoconductivity than the pristine film. This additional boost from $\sim 7\,\mathrm{Scm}^{-1}$ to $\sim 9\,\mathrm{Scm}^{-1}$ indicates improved charge carrier mobility in the treated films.

We fit the photoconductivity data presented in **Figure 4.2b** with a Drude model, as follows. Using OPTPS, we measured the photoconductivity spectrum ($\Delta\sigma$) of the samples under a photoexcitation fluence of 2 $\mu\mathrm{Jcm}^{-2}$. According to the following equation, the photoconductivity can be expressed in terms of THz transitivity:

$$\Delta\sigma(\omega) = \frac{\varepsilon_0 c(1+n_{\mathrm{sub}})}{d}\frac{\Delta T(\omega)}{T(\omega)} \tag{4.9}$$

where ε_0 is the permittivity of free space, n_{sub} is the refractive index of the quartz substrate and d is the thickness of the thin film and ΔT is the difference in THz transmission between photoexcitation and non-photoexcitation. As shown in **Figure 4.2b**, the photoconductivity spectrum shows a Drude response with a relatively flat real

part and the imaginary part was approximately 0, on top of which phonon modulation occurs at 1 THz and 2 THz, due to electron-phonon coupling. The Drude model is expressed analytically by the following equation:

$$\Delta\sigma(\omega) = \frac{Ne^2}{m^*}\frac{i}{\omega + i\gamma}, \tag{4.10}$$

where e is the electron charge, N is the electron density and m^* is the electron effective mass and γ is the momentum scattering rate, from which the electron mobility can be extracted according to

$$\mu = \frac{e}{m^*\gamma}. \tag{4.11}$$

Therefore, by fitting the above Drude model to the measured photoconductivity spectrum, we can extract the charge carrier mobilities of the films. The mobilities of the pristine and treated films were $\mu = (51.2 \pm 3.7)\,\mathrm{cm^2V^{-1}s^{-1}}$ and $\mu = (62.5 \pm 4.2)\,\mathrm{cm^2V^{-1}s^{-1}}$ respectively. As far as we are aware, these mobilities determined from THz spectroscopy are the highest yet reported for polycrystalline metal halide perovskite films, even those reported thus far for the neat iodide perovskites, with typical values ranging from $8 - 35\,\mathrm{cm^2V^{-1}s^{-1}}$ [33]. This is therefore indicative of extremely high quality of perovskite absorber layers, with much reduced short-range charge carrier scattering [2, 29, 33]. Furthermore, as discussed earlier, the THz beam is sensitive to the entirety of the perovskite thin-film. Therefore, the observation of a significantly enhanced charge-carrier mobility upon surface passivation demonstrates the dramatic influence surface quality has on the optoelectronic properties of these metal halide perovskite (MHP) semiconductors.

From the mobility and TCSPC data, we can extract the diffusion length of charge carriers in the perovskite bulk according to the procedure outline in **Section 2.1.3**. We obtain k_1 from fitting the photoluminescence decays in **Figure 4.2a**, yielding values of $k_1 = 3.1 \times 10^7\,\mathrm{s^{-1}}$ and $k_1 = 4.1 \times 10^6\,\mathrm{s^{-1}}$ for pristine and BenABr treated films respectively. Using **Equation 2.42**, we calculate diffusion lengths of $L_\mathrm{d} = (2.1 \pm$

0.2) μm and $L_d = (6.1 \pm 0.4)\mu$m for reference and treated films respectively. These diffusion lengths are extremely high and thus are promising for high device performance.

This is because the short-circuit current density can be increased by improving the generation efficiency, the collection efficiency of charge-carriers, or both. The measurements discussed thus far probe the charge-carrier transport properties which will impact the collection efficiency. A consensus is emerging in the field that it is the diffusion current that dominates charge transport in perovskite solar cells (given sufficiently selective charge transport layers), however recent work has shown that a built-in potential is still required for optimal device performance [34, 35]. This built-in potential results in a drift current which helps to extract carriers at 0 V (J_{SC} conditions).

In our work, the improvements in charge carrier lifetimes, mobilities and diffusion lengths indicate a higher quality charge-carrier transport within the perovskite film in the presence of the benzylammonium bromide passivation treatment. The electric field from the THz probe during the OPTPS measurements, induces and probes drift current to determine charge-carrier mobility. As such, combining these measurements with the recombination parameters from OPTPS and time-resolved photoluminescence (TRPL) gives an accurate indication of the charge carrier transport within the perovskite semiconductor [30]. Therefore, given that we see improved charge-carrier transport in the treated films, we can have confidence that the charge collection efficiency will be increased. However, we note that this is unlikely to be the full picture. Gaining precise understanding about improvements to the short-circuit current density following passivation requires significant further studies which are beyond the scope of this chapter.

4.3.2 Structural and chemical characterisation

These improvements in PLQY and charge-carrier lifetimes suggest passivation of trap states. Previous reports on benzylamine suggested that the molecule acts as a passivation agent by anchoring to the to the lead-halide octahedra [36]. To investigate the nature of the chemical binding of the benzylammonium bromide salt with the

perovskite we used XPS. These measurements and analysis were performed by Dr. Alexandra J. Ramadan. In **Figure 4.4a** we show high-resolution XPS spectra for the Br $3d$, Pb $4f$, Cs $3d$, I $3d$ core levels in a pristine film and one treated with 5 mg mL^{-1} of BenABr. We choose this concentration since it resulted in the best device performance, which will be discussed later (**Figure 4.6**). Full details of peak positions and fittings can be found in **Figures 4.5a&b**. We observe no significant shifts in binding energy of the Br $3d$, Pb $4f$, Cs $3d$ and I $3d$ core levels and the peak shape remains unchanged between the pristine samples and those with BenABr present. The binding energies of these peaks show no significant shifts from those reported for similar perovskites [37, 38]. Therefore, this lack of difference in the electronic structure of Pb $4f$ between the pristine and treated films does not present evidence that BenABr is binding to the Pb-octahedra within the perovskite, in contrast to what has been suggested with similar molecules [17, 39]. It may be the case that the differences in electronic structure of the Pb $4f$ probed within the first $\sim$ 10 nm of the film, are too small to detect when only a surface layer of benzylammonium ions are present on the film. However, we also note that although it is regularly assumed, clear irrefutable evidence is yet to be presented that the post treatment of a 3D perovskite with larger ammonium cations will automatically result in binding of those larger cations within the lead-halide octahedral frameworks.

In contrast to the Pb $4f$ spectra, we do observe significant differences in the C $1s$ spectra, which we show in **Figure 4.4b**. Of particular note is the peak at 284.1 eV which is present only in the spectra of samples treated with benzylammonium bromide. We attribute this to the presence of C in an aryl environment [40]. Additionally using the XPS measurements, we calculated the relative atomic composition of the surface of the perovskite for the pristine and treated films. Our XPS measurements were carried out using a lab-based Al Kα X-ray source which has a penetration depth of up to 10 nm and therefore we can use them to approximate the surface chemistry of the thin film samples. As can be seen in **Figure 4.4c**, we observe an increase in the relative quantities of C, N and Br on the treated film as compared to the control.

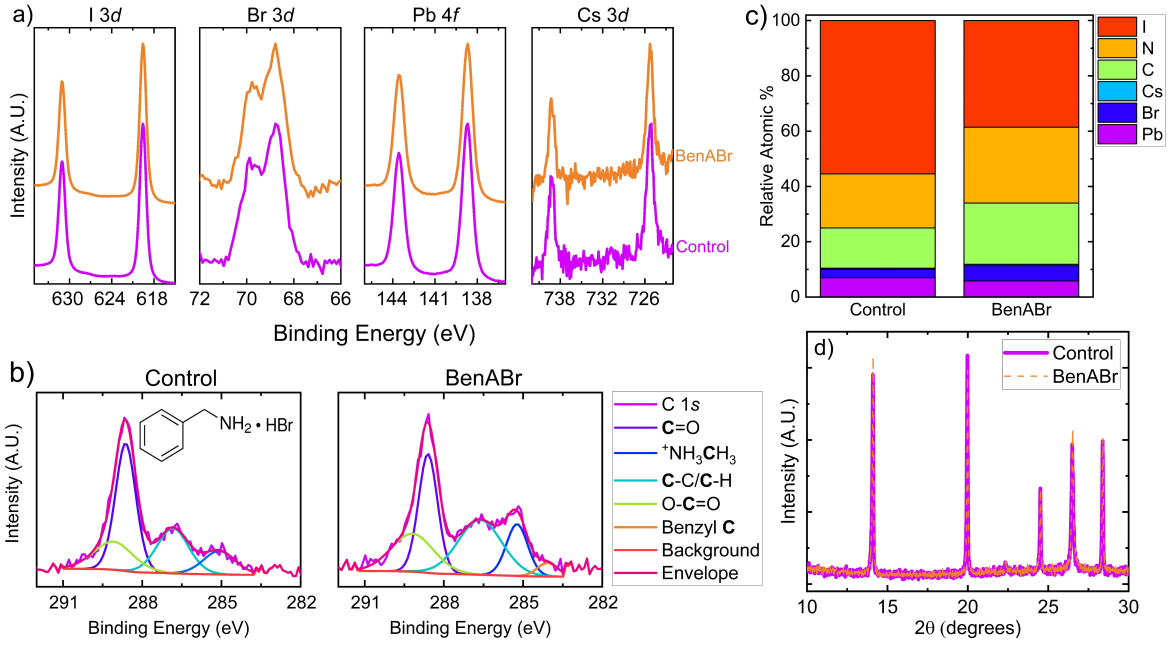


Figure 4.4: *a) High resolution XPS spectra of the Br 3d, Pb 4f, Cs 3d, I 3d core levels for pristine (purple) and BenABr treated (orange) films. Full details of the fittings can be found in* ***Figure 4.5****. b) High resolution XPS of the C 1s core level for pristine (left) and BenABr treated (right) films with fittings displayed. Inset shows the molecular structure of the BenABr molecule. c) Relative atomic composition of the surface for pristine (left) and BenABr treated (right) films. The measurements and analysis in a)-c)were performed by Dr. Alexandra J. Ramadan. d) XRD patterns for pristine (purple) and BenABr treated (orange) films. Adapted with permission from ACS Energy Lett. 2020,* ***5****, 11, 3336–3343. [27] Copyright 2020, American Chemical Society.*

This strongly suggests that the BenABr is present predominantly on the surface of the perovskite thin film, but we cannot conclude if there is strong chemical bonding of the benzylammonium to the perovskite structure.

To examine if the treatment with BenABr has a significant influence upon the crystal structure of the underlying perovskite films, we carried out X-ray diffraction (XRD) measurements. The diffraction pattern for treated perovskite films, which we display in **Figure 4.4d**, exhibits no significant differences when compared to that of pristine perovskite films. Unlike previous reports on similar molecules [17, 19, 39], we see no evidence for the formation of a two dimensional $BenA_2PbX_4$ phase, where peaks at approximately $2\theta = 12°, 18°$ and $25°$ would be expected [41]. Therefore, we conclude that BenABr does not influence the crystal structure of the perovskite films. For completeness, we carried out scanning electron microscopy (SEM) to examine the

morphology of the respective systems. The BenABr treated films exhibit morphologies akin to the pristine films, which we present in **Figure 4.5c**. We note that an undetectably small 2D phase could have formed on the surface of the perovskite, but our structural, chemical, and electronic characterization has demonstrated no evidence for this. Therefore, our materials characterization suggests that whilst BenABr improves the optoelectronic properties of the perovskite film, it does this without influencing the chemical or structural properties of the material suggesting that it is acting as a defect/trap passivation agent. We suggest that the passivation mechanism may be due to the filling of halide vacancies on the surface of the perovskite, as evidenced by a greater fraction of bromide in the elemental composition shown in **Figure 4.4c**. Detailed discussion pertaining to the defect chemistry of MHP semiconductors is beyond the scope of this current Chapter. However, several excellent reviews on the subject can be found in Refs. [42–44]. I note, however, that much of this work has focused nearly exclusively on pure MA-based perovskites, and it is not clear whether the mixed cation MHPs would possess the same defect chemistry. Nevertheless, halide vacancies have been found to be among the most thermodynamically stable [45], and iodide vacancies assist the diffusion iodide ions within the MHP semiconductor which can screen the built-in field in devices [46]. Therefore, while not definitely proven in this work, halide vacancy filling owing to the BenABr treatment could contribute towards the enhanced device performance we observe.

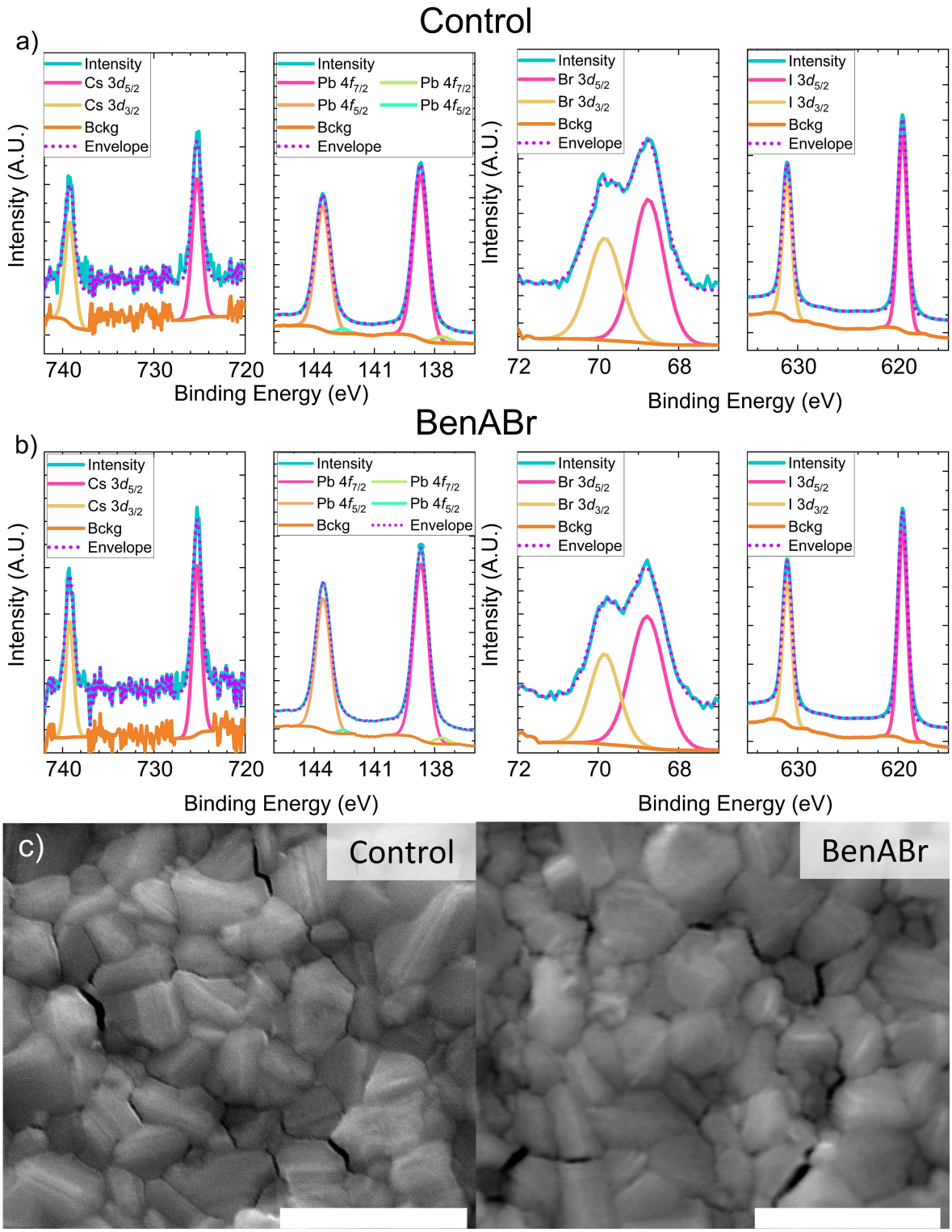


Figure 4.5: *XPS fittings for the Cs 3d, Pb 4f, Br 3d and I 3d core levels for a) pristine and b) BenABr treated samples. The intensity and envelope have been offset to make the fittings clearer. c) Scanning electron micrographs for a) control (left) and b) BenABr treated (right) samples. Scales bars are 1 µm. The SEM images were taken by Jonathan H. Warby. Adapted with permission from ACS Energy Lett. 2020,* ***5****, 11, 3336–3343. [27] Copyright 2020, American Chemical Society.*

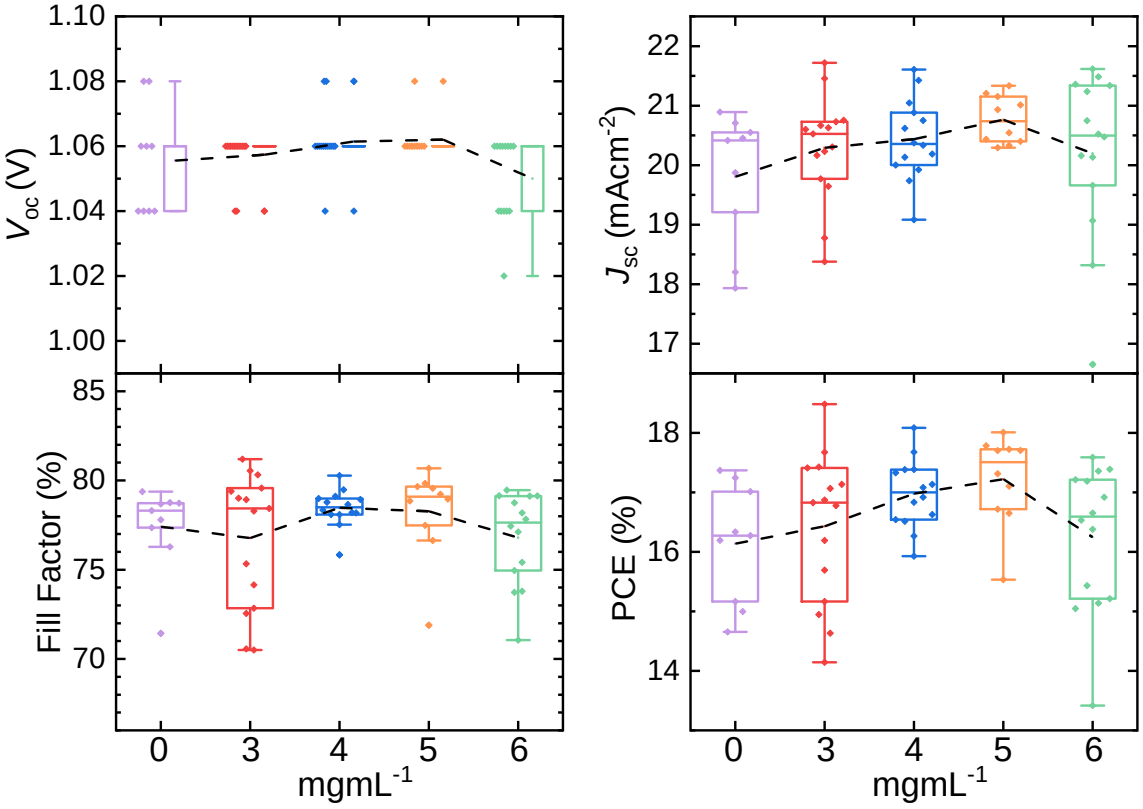


Figure 4.6: *PV device statistics for the optimisation of the benzylammonium bromide treatment for concentrations of 0 (untreated) and* $3-6$ mg mL^{-1} *of BenABr dissolved in CB. The data points are overlapped onto the boxplots which show the median (central line), the mean (squares, connected with dashed lines as a guide to the eye), and the median of the upper and lower halves of the data (top and bottom lines of the box, respectively). The top and bottom whiskers are drawn to the highest/lowest data point within 1.5 times the interquartile range from the top and bottom of the box, respectively. Adapted with permission from ACS Energy Lett. 2020,* ***5****, 11, 3336–3343. [27] Copyright 2020, American Chemical Society.*

4.3.3 Photovoltaic device performance

In order to assess the impact of BenABr passivation in complete solar cells, we fabricated a series of perovskite solar cells (PSCs) with the concentrations of BenABr ranging from 3 – 6 mg mL^{-1} in the following device architecture: FTO / polyTPD / perovskite / $PC_{61}BM$ / BCP / Ag. We observed a significant increase in performance for the BenABr-treated devices, as compared to the untreated devices. We found an optimum concentration of BenABr at 5 mg mL^{-1} , and show the full range of BenABr concentrations investigated and their relevant device parameters in **Figure 4.6**.

Following the optimisation process, as shown in **Figure 4.6**, the performance of

Table 4.3: *Average (champion) device parameters for the BenABr concentrations investigated.*

Condition	PCE (%)	V_{OC} (V)	J_{SC} (mA cm^{-2})	Fill factor (%)
Control	15.09 (18.17)	1.038 (1.06)	20.38 (22.72)	72.0 (76.7)
3 mg mL^{-1}	15.86 (18.57)	1.042 (1.06)	21.39 (22.66)	71.9 (78.6)
4 mg mL^{-1}	16.42 (18.48)	1.055 (1.06)	20.82 (21.72)	75.3 (80.5)
5 mg mL^{-1}	16.75 (19.28)	1.061 (1.08)	21.02 (22.77)	75.9 (79.9)
6 mg mL^{-1}	15.84 (17.59)	1.046 (1.06)	20.43 (21.35)	74.6 (77.8)

the devices continued to improve. This observation is quite common in the field of perovskite photovoltaics [19, 47–50], and the exact mechanism for the improvement is still unknown despite recent studies [51]. We present champion and average device parameters in **Table 4.3** for devices that were stored in an N_2 filled glovebox for one week after which the performance had stopped changing. The box plots for the 'steady state' PCEs is shown in the inset of **Figure 4.7a**.

In **Figure 4.7a** we show the champion stabilised power output (SPO) for control and 5 mg mL^{-1} treated devices. We observe a significant improvement, achieving an impressive SPO of 19.5 % in the treated devices, as compared to 18.4 % for control devices. The BenABr treatment also reduced the hysteresis in the JV scans. We note that the BenABr treatment ameliorates all of the main device parameters. For the optimal concentration of 5 mg mL^{-1} , the fill factor increases by 3.8 % absolute, and there is an increase in the open-circuit voltage of 22 mV, consistent with reduced non-radiative recombination. Further, this improvement in V_{OC} is entirely consistent with the increased luminescence efficiency of the perovskite films with the charge selective contacts (**Figure 4.1a**), from which we predict an increase in quasi-Fermi level splitting of $\sim$ 25 mV.

Another route in which the BenABr treatment leads to improved device performance is through an increased short-circuit current density. To verify this, we measured the external quantum efficiency (EQE) of our devices. As can be seen in **Figure**

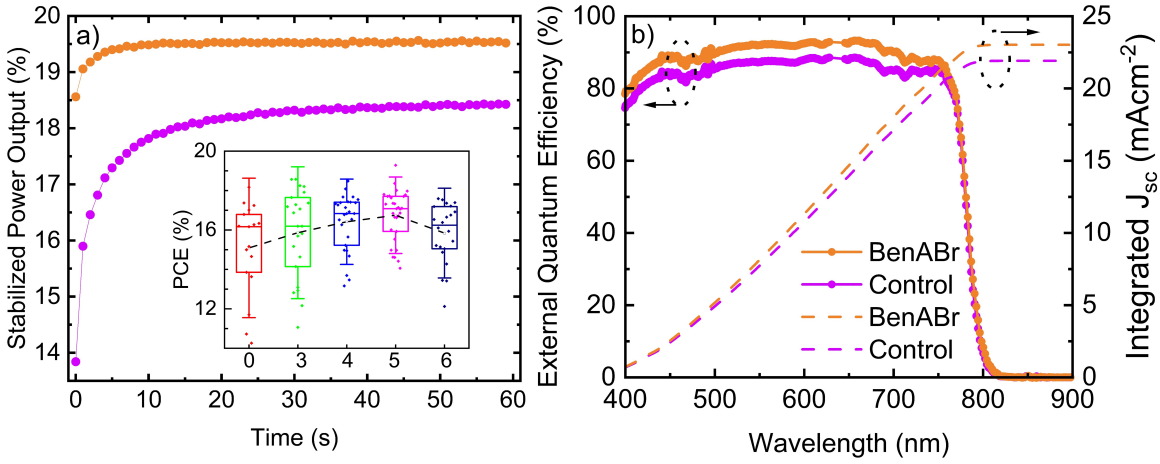


Figure 4.7: *a) Stabilised power output (SPO) traces for the champion control (purple) and treated (orange) devices. Inset: Box plots showing the PCE for the range of BenABr concentrations investigated (x-axis unit is in* mg mL^{-1} *) The dotted line is a guide for the eye and connects the mean value of the distributions. b) external quantum efficiency (EQE) spectra for champion control (purple) treated (orange) devices. Integrating the EQE over the AM 1.5 spectrum gives* J_{SC} *values of 21.9* mA cm^{-2} *and 23.0* mA cm^{-2} *for control and treated devices respectively. Adapted with permission from ACS Energy Lett. 2020,* ***5****, 11, 3336–3343. [27] Copyright 2020, American Chemical Society.*

4.7b, there is a panchromatic increase of the EQE with the BenABr treatment. These data suggest improved charge extraction to the external circuit across the entire range of our absorption, which leads to higher short-circuit current densities. Integrating the EQE for control and treated devices over the AM 1.5 solar spectrum gives short-circuit current density values of 21.9 mA cm^{-2} and 23.0 mA cm^{-2} respectively (an error of $<$ 3 % compared with the *JV* scans).

This enhancement of the short circuit current density following the BenABr treatment is unexpected. The diffusion lengths of charge carriers, as judged from our mobility and carrier lifetime measurements discussed in **Section 4.3.1**, is substantial for both control and treated films, at 2.1 and 6.1 μm respectively. While these values are upper bounds, as they do not account for reduced lifetimes due to interfacial recombination induced by the charge transport layers, the high fill factors which we observe for both cases are also consistent with diffusion current (as opposed to drift) being sufficient for charge transport out of the absorber layer, demonstrating that a strong electric field (as is present under short-circuit conditions) is not required to extract charge car-

riers. We therefore postulate that the improvement in J_{SC} with BenABr treatment may be due to increased homogeneity following BenABr treatment. In the reference cells, there may be complete polycrystalline domains which are not contributing to photocurrent generation and collection, which would reduce the J_{SC} while leaving the FF largely unaffected, if these domains are not in communication with the rest of the film. Heterogeneity is well known to be present in PSCs [52, 53], but its influence on the J_{SC} is not yet fully understood. Understanding the precise origin of this increased photocurrent density is beyond the scope of the present work.

Thermal Stability

Thermal stability is an essential requirement for surface passivation treatments, otherwise any improvement due to the passivation would be lost over time. Therefore, we investigated the stability of PSCs with the BenABr treatment by stressing encapsulated devices at elevated (85 °C) temperatures under simulated solar irradiance concomitantly, in an open-circuit condition. This is condition ISOS-L-2 as set out by the stability consensus, and we choose the higher temperature (85 °C instead of 65 °C) and open-circuit conditions [54]. We employed the relatively harsh 85 °C light soaking (AM 1.5) aging conditions since we are interested in understanding if the improvement owing to the BenABr treatment itself is maintained under these conditions, rather than assessing the overall stability of the underlying perovskite. We present the evolution of the PV performance parameters in **Figure 4.8**. Both treated and reference devices decay relatively rapidly under these severe ageing conditions. However, this is consistent with what we have recently reported for similar control devices, without any further improvement from stabilizing ionic additives [55].

Importantly, we find here that the devices treated with BenABr maintain an increased performance over their pristine counterparts, most evident in the inset on **Figure 4.8a**. This suggests that the improvement from the passivation treatment is maintained under light and high temperature thermal stressing. On further investigation, we see that the BenABr treatment maintains a substantial improvement in the

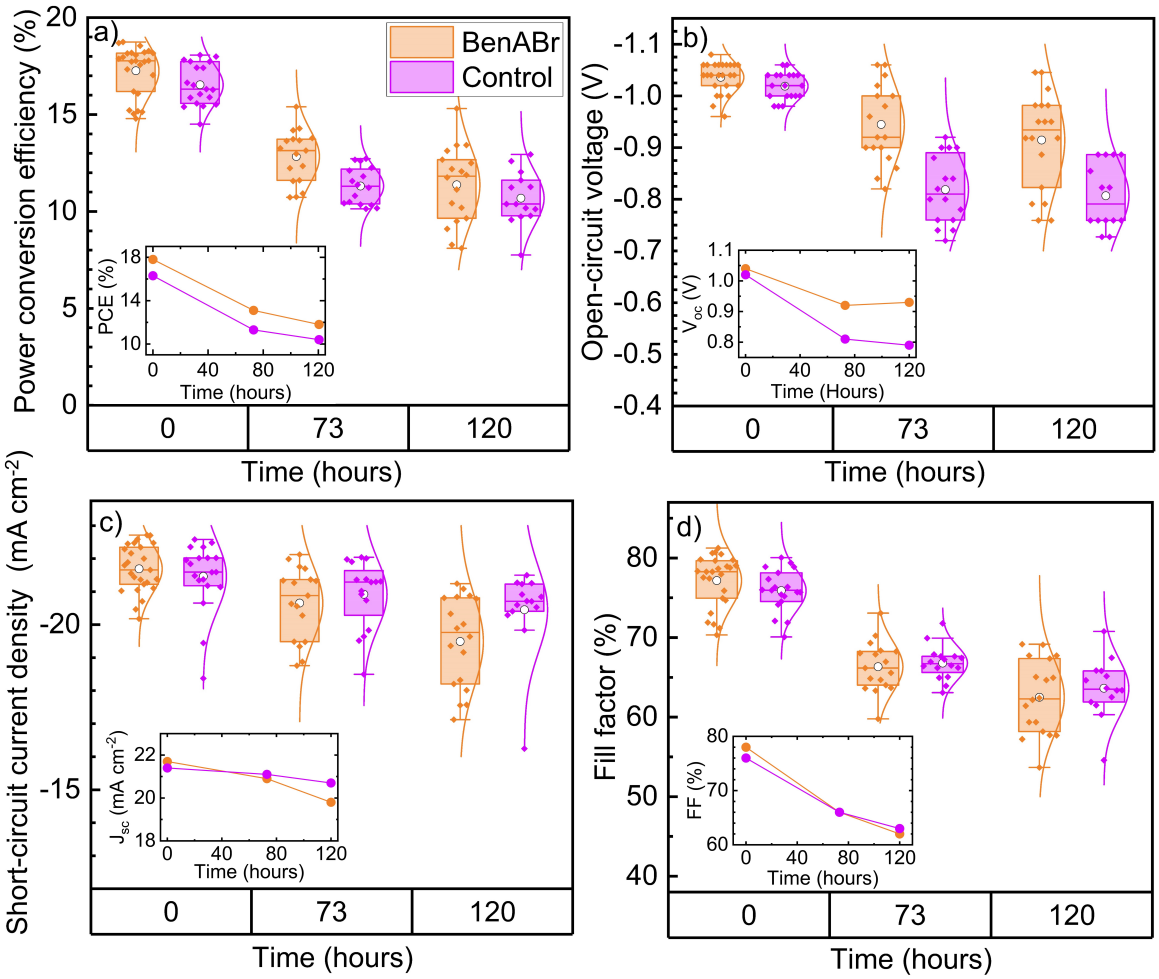


Figure 4.8: *Evolution of the a) PCE, b) V_{OC}, c) J_{SC} and d) FF for encapsulated treated (orange) and control (purple) devices aged at 85 °C under simulated AM 1.5 irradiance in an open-circuit condition (as per ISOS-L-2)[54]. The data points are overlapped onto the boxplots which show the median (central line), the mean (white circle), the median of the upper and lower halves of the data (top and bottom lines of the box respectively). The top and bottom whiskers are drawn to the highest/lowest datapoint within 1.5 times the interquartile range from the top and bottom of the box respectively. Normal distributions to the data are shown on the right of each box plot. The insets show the evolution of the median values of each device parameter over time. Adapted with permission from ACS Energy Lett. 2020, **5**, 11, 3336–3343. [27] Copyright 2020, American Chemical Society.*

open circuit voltage, from a boost of $\sim$ 20mV to $\sim$ 140mV. This indicates a significantly reduced level of non-radiative recombination in the treated devices during the ageing experiment suggesting that BenABr is continuing to act as a passivation treatment during the aging and has not degraded and lost functionality. Indeed, it seems that its effect is becoming yet more pronounced during this aging experiement. This is notably in contrast to other contemporary passivation routes, such as phenethylam-

monium iodide [17].

4.4 Conclusion

In this work we have demonstrated a thermally stable passivation treatment, which is an essential requirement if any treatment is to have a prospect of being implemented in modules intended for use in the field. The treatment, benzylammonium bromide, increases the optoelectronic quality of the perovskite semiconductor layer as assessed through photoluminescence and time domain THz spectroscopic studies. This improvement occurs despite there being no evidence for the BenABr treatment chemically binding to the perovskite, or changing its crystallinity or surface morphology. The work we have presented here is an important step forward on the road to the commercialization of PSCs, since we highlight the potential for thermally stable passivation treatments resulting in high efficiency devices.

Contributions

R. D. J. Oliver, Alexandra J. Ramadan and Yen-Hung Lin initiated the project. Yen-Hung Lin provided insightful feedback throughout the project. R. D. J. Oliver and Alexander J. Horn made the perovskite solar cells in this work. Chelsea Q. Xia performed the optical-pump terahertz-probe spectroscopy measurements and analysis. Jonathan H. Warby took the SEM images and synthesised the benzylammonium bromide. Michael B. Johnston supervised the project, particularly the OPTPS experiments and analysis. Alexandra J. Ramadan performed the XPS measurements and analysis, and was the main supervisor for this work. Henry J. Snaith provided overall supervision of the project. Everything else presented within this chapter was done by R. D. J. Oliver.

References

[1] Stranks, S. D. *et al.* Electron-hole diffusion lengths exceeding 1 micrometer in an organometal trihalide perovskite absorber. *Science* **342**, 341–344 (2013).

[2] Wehrenfennig, C., Eperon, G. E., Johnston, M. B., Snaith, H. J. & Herz, L. M. High charge carrier mobilities and lifetimes in organolead trihalide perovskites. *Advanced Materials* **26**, 1584–1589 (2014).

[3] McMeekin, D. P. *et al.* A mixed-cation lead mixed-halide perovskite absorber for tandem solar cells. *Science* **351**, 151–155 (2016).

[4] Huang, J., Yuan, Y., Shao, Y. & Yan, Y. Understanding the physical properties of hybrid perovskites for photovoltaic applications. *Nature Reviews Materials* **2**, 1–19 (2017).

[5] Laboratory, N. R. E. Best Research-Cell Efficiency Chart (Accessed: 2021-09-20). URL `https://www.nrel.gov/pv/cell-efficiency.html`.

[6] Conings, B. *et al.* Intrinsic thermal instability of methylammonium lead trihalide perovskite. *Advanced Energy Materials* **5**, 1500477 (2015).

[7] Habisreutinger, S. N., McMeekin, D. P., Snaith, H. J. & Nicholas, R. J. Research update: Strategies for improving the stability of perovskite solar cells. *APL Materials* **4**, 091503 (2016).

[8] Wang, D., Wright, M., Elumalai, N. K. & Uddin, A. Stability of perovskite solar cells. *Solar Energy Materials and Solar Cells* **147**, 255–275 (2016).

[9] Nenon, D. P. *et al.* Structural and chemical evolution of methylammonium lead halide perovskites during thermal processing from solution. *Energy & Environmental Science* **9**, 2072–2082 (2016).

[10] Dualeh, A., Gao, P., Seok, S. I., Nazeeruddin, M. K. & Grätzel, M. Thermal behavior of methylammonium lead-trihalide perovskite photovoltaic light harvesters. *Chemistry of Materials* **26**, 6160–6164 (2014).

[11] Christians, J. A. *et al.* Tailored interfaces of unencapsulated perovskite solar cells for¿ 1,000 hour operational stability. *Nature Energy* **3**, 68–74 (2018).

[12] Hou, Y. *et al.* A generic interface to reduce the efficiency-stability-cost gap of perovskite solar cells. *Science* **358**, 1192–1197 (2017).

[13] Snaith, H. J. *et al.* Anomalous hysteresis in perovskite solar cells. *The Journal of Physical Chemistry Letters* **5**, 1511–1515 (2014).

[14] Stolterfoht, M. *et al.* Visualization and suppression of interfacial recombination for high-efficiency large-area pin perovskite solar cells. *Nature Energy* **3**, 847–854 (2018).

[15] Momblona, C. *et al.* Efficient vacuum deposited pin and nip perovskite solar cells employing doped charge transport layers. *Energy & Environmental Science* **9**, 3456–3463 (2016).

[16] Wolff, C. M., Caprioglio, P., Stolterfoht, M. & Neher, D. Nonradiative recombination in perovskite solar cells: the role of interfaces. *Advanced Materials* **31**, 1902762 (2019).

[17] Jiang, Q. *et al.* Surface passivation of perovskite film for efficient solar cells. *Nature Photonics* **13**, 460–466 (2019).

[18] Wang, F. *et al.* Phenylalkylamine passivation of organolead halide perovskites enabling high-efficiency and air-stable photovoltaic cells. *Advanced Materials* **28**, 9986–9992 (2016).

[19] Zhou, Y. *et al.* Benzylamine-treated wide-bandgap perovskite with high thermal-photostability and photovoltaic performance. *Advanced Energy Materials* **7**, 1701048 (2017).

[20] Saliba, M. *et al.* Cesium-containing triple cation perovskite solar cells: improved stability, reproducibility and high efficiency. *Energy & Environmental Science* **9**, 1989–1997 (2016).

[21] de Mello, J. C., Wittmann, H. F. & Friend, R. H. An improved experimental determination of external photoluminescence quantum efficiency. *Advanced Materials* **9**, 230–232 (1997).

[22] Ross, R. T. Some thermodynamics of photochemical systems. *The Journal of Chemical Physics* **46**, 4590–4593 (1967).

[23] Miller, O. D., Yablonovitch, E. & Kurtz, S. R. Strong internal and external luminescence as solar cells approach the shockley–queisser limit. *IEEE Journal of Photovoltaics* **2**, 303–311 (2012).

[24] Stolterfoht, M. *et al.* The impact of energy alignment and interfacial recombination on the internal and external open-circuit voltage of perovskite solar cells. *Energy & Environmental Science* **12**, 2778–2788 (2019).

[25] Caprioglio, P. *et al.* On the relation between the open-circuit voltage and quasi-fermi level splitting in efficient perovskite solar cells. *Advanced Energy Materials* **9**, 1901631 (2019).

[26] Nayak, P. K., Mahesh, S., Snaith, H. J. & Cahen, D. Photovoltaic solar cell technologies: analysing the state of the art. *Nature Reviews Materials* **4**, 269–285 (2019).

[27] Oliver, R. D. *et al.* Thermally stable passivation toward high efficiency inverted perovskite solar cells. *ACS Energy Letters* **5**, 3336–3343 (2020).

[28] Johnston, D. Stretched exponential relaxation arising from a continuous sum of exponential decays. *Physical Review B* **74**, 184430 (2006).

[29] Milot, R. L., Eperon, G. E., Snaith, H. J., Johnston, M. B. & Herz, L. M. Temperature-dependent charge-carrier dynamics in ch3nh3pbi3 perovskite thin films. *Advanced Functional Materials* **25**, 6218–6227 (2015).

[30] Johnston, M. B. & Herz, L. M. Hybrid perovskites for photovoltaics: charge-carrier recombination, diffusion, and radiative efficiencies. *Accounts of chemical research* **49**, 146–154 (2016).

[31] Milot, R. L. *et al.* The effects of doping density and temperature on the optoelectronic properties of formamidinium tin triiodide thin films. *Advanced Materials* **30**, 1804506 (2018).

[32] Wright, A. D. *et al.* Electron–phonon coupling in hybrid lead halide perovskites. *Nature Communications* **7**, 1–9 (2016).

[33] Herz, L. M. Charge-carrier mobilities in metal halide perovskites: fundamental mechanisms and limits. *ACS Energy Letters* **2**, 1539–1548 (2017).

[34] Sandberg, O. J. *et al.* On the question of the need for a built-in potential in perovskite solar cells. *Advanced Materials Interfaces* **7**, 2000041 (2020).

[35] Kirchartz, T., Bisquert, J., Mora-Sero, I. & Garcia-Belmonte, G. Classification of solar cells according to mechanisms of charge separation and charge collection. *Physical Chemistry Chemical Physics* **17**, 4007–4014 (2015).

[36] Yang, S. *et al.* Functionalization of perovskite thin films with moisture-tolerant molecules. *Nature Energy* **1**, 1–7 (2016).

[37] Ramadan, A. J. *et al.* Unravelling the improved electronic and structural properties of methylammonium lead iodide deposited from acetonitrile. *Chemistry of Materials* **30**, 7737–7743 (2018).

[38] Ramadan, A. J. *et al.* Revealing the stoichiometric tolerance of lead trihalide perovskite thin films. *Chemistry of Materials* **32**, 114–120 (2019).

[39] Gharibzadeh, S. *et al.* Record open-circuit voltage wide-bandgap perovskite solar cells utilizing 2d/3d perovskite heterostructure. *Advanced Energy Materials* **9**, 1803699 (2019).

[40] Liu, Z. *et al.* A hydrophilic covalent organic framework for photocatalytic oxidation of benzylamine in water. *Chemical Communications* **56**, 766–769 (2020).

[41] Mao, L. *et al.* Role of organic counterion in lead-and tin-based two-dimensional semiconducting iodide perovskites and application in planar solar cells. *Chemistry of Materials* **28**, 7781–7792 (2016).

[42] Ball, J. M. & Petrozza, A. Defects in perovskite-halides and their effects in solar cells. *Nature Energy* **1**, 1–13 (2016).

[43] Zhou, Y., Poli, I., Meggiolaro, D., De Angelis, F. & Petrozza, A. Defect activity in metal halide perovskites with wide and narrow bandgap. *Nature Reviews Materials* **6**, 986–1002 (2021).

[44] Moia, D. & Maier, J. Ion transport, defect chemistry, and the device physics of hybrid perovskite solar cells. *ACS Energy Letters* **6**, 1566–1576 (2021).

[45] Motti, S. G. *et al.* Defect activity in lead halide perovskites. *Advanced Materials* **31**, 1901183 (2019).

[46] Eames, C. *et al.* Ionic transport in hybrid lead iodide perovskite solar cells. *Nature Communications* **6**, 1–8 (2015).

[47] Deng, Y., Dong, Q., Bi, C., Yuan, Y. & Huang, J. Air-stable, efficient mixed-cation perovskite solar cells with cu electrode by scalable fabrication of active layer. *Advanced Energy Materials* **6**, 1600372 (2016).

[48] Lee, D. S. *et al.* Passivation of grain boundaries by phenethylammonium in formamidinium-methylammonium lead halide perovskite solar cells. *ACS Energy Letters* **3**, 647–654 (2018).

[49] You, J. *et al.* Improved air stability of perovskite solar cells via solution-processed metal oxide transport layers. *Nature Nanotechnology* **11**, 75–81 (2016).

[50] Li, N. *et al.* Mixed cation $FA_xPEA_{1-x}PbI_3$ with enhanced phase and ambient stability toward high-performance perovskite solar cells. *Advanced Energy Materials* **7**, 1601307 (2017).

[51] Cho, Y. *et al.* Elucidating mechanisms behind ambient storage-induced efficiency improvements in perovskite solar cells. *ACS Energy Letters* **6**, 925–933 (2021).

[52] de Quilettes, D. W. *et al.* Impact of microstructure on local carrier lifetime in perovskite solar cells. *Science* **348**, 683–686 (2015).

[53] Tennyson, E. M., Doherty, T. A. & Stranks, S. D. Heterogeneity at multiple length scales in halide perovskite semiconductors. *Nature Reviews Materials* **4**, 573–587 (2019).

[54] Khenkin, M. V. *et al.* Consensus statement for stability assessment and reporting for perovskite photovoltaics based on isos procedures. *Nature Energy* **5**, 35–49 (2020).

[55] Lin, Y.-H. *et al.* A piperidinium salt stabilizes efficient metal-halide perovskite solar cells. *Science* **369**, 96–102 (2020).

Chapter 5

Understanding and suppressing non-radiative losses in methylammonium-free wide-bandgap perovskite solar cells

Publication related to this chapter

The results in this chapter have been published in **R. D. J. Oliver**, P. Caprioglio, F. Peña-Camargo, L. R. V. Buizza, F. Zu, A. J. Ramadan, S. G. Motti, S. Mahesh, M. M. McCarthy, J. H. Warby, Y.-H. Lin, N. Koch, S. Albrecht, L. M. Herz, M. B. Johnston, D. Neher, M. Stolterfoht, H. J. Snaith, *Understanding and Suppressing Non-Radiative Losses in Methylammonium-Free Wide-Bandgap Perovskite Solar Cells*, *Energy Environ. Sci.*, 2022, **15**, pages 714-726.

5.1 Summary of results

With power conversion efficiencies of perovskite-on-silicon and all-perovskite tandem solar cells increasing at rapid pace, wide bandgap (> 1.7 eV) metal halide perovskite (MHP) semiconductors are becoming a major focus of academic and industrial photovoltaic research. Compared to their lower bandgap (≤ 1.6 eV) counterparts, these types of perovskites suffer from higher levels of non-radiative losses in both the bulk material and in device configurations, constraining their efficiencies far below their thermodynamic potential. In this work, we investigate the energy losses in MA free high-Br-content wide bandgap perovskites by using a combination of THz spectroscopy, steady-state and time-resolved photoluminescence, coupled with drift-diffusion simulations. The investigation of this system allows us to study charge-carrier recombination in these materials and devices in the absence of halide segregation due to the photostabilty of formamidinium-cesium based lead halide perovskites. We find that these perovskites are characterised by large non-radiative recombination losses in the bulk material and that the interfaces with transport layers in solar cell devices strongly limit their open-circuit voltage. In particular, we discover that the interface with the hole transport layer performs particularly poorly, in contrast to 1.6 eV bandgap MHPs which are generally limited by the interface with the electron-transport layer. To overcome these losses, we incorporate and investigate the recombination mechanisms present with perovskites treated with the ionic additive (IA) 1-butyl-1-methylpiperidinium tetrafluoroborate ($[BMP]^+[BF_4]^-$). We find that this additive not only improves the radiative efficiency of the bulk perovskite, but also reduces the non-radiative recombination at both the hole and electron transport layer interfaces of full photovoltaic devices. In addition to unravelling the beneficial effect of this specific treatment, we further optimise our solar cells by introducing an additional LiF interface treatment at the electron transport layer interface. Together these treatments enable MA-free 1.79 eV bandgap perovskite solar cells with open-circuit voltages of 1.22 V and power conversion efficiencies approaching 17 %, which is among the highest reported for this material system.

5.2 Introduction

During the last decade, metal halide perovskite solar cells have experienced an unprecedented rise in power conversion efficiency (PCE) which now exceeds 25 % in single-junction cells, approaching the record efficiency of crystalline silicon [1]. This remarkable development can be explained by the impressive optoelectronic properties of these perovskites, including long charge-carrier diffusion lengths, high absorption coefficients and low levels of electronic disorder, quantified via low Urbach energies [2–6]. These properties, along with the relative ease of manufacturing perovskite thin films and widely tuneable bandgap, make metal halide perovskite solar cells a highly attractive prospect for commercialisation [4, 7, 8]. Importantly, the bandgap energies practically achievable make this technology suitable for multijunction architectures, either in combination with Si or low-bandgap perovskite sub cells [9, 10]. However, despite over 29.5 % efficiency having already been demonstrated for perovskite-on-silicon tandems, the wider bandgap perovskite top cells still contain many more fundamental losses, than their lower bandgap single junction counterparts. For example, wide bandgap (WBG) perovskites ($E_g > 1.7$ eV), essential for tandem applications, suffer from severe open-circuit voltage (V_{OC}) losses [11]. Despite recent progress, the mechanisms that cause the wide bandgap materials to underperform as compared to the lower bandgap materials are still not fully understood [11].

As discussed in **Section 2.3**, high-efficiency wide-bandgap perovskites are prepared by tuning the halide ratio from I to Br on the X site of the perovskite crystal lattice, ABX_3 [4, 7]. As such, a wide range of bandgaps from $\sim$ 1.5 to $\sim$ 2.3 eV can be achieved, while the X-site is varied from triiodide to tribromide for the lead-based perovskites [7]. Importantly, in multijunction tandem devices, either in perovskite-on-Si or perovskite-on-perovskite device configurations, bandgaps of $\sim$ 1.7 eV and $\sim$ 1.8 eV respectively, are required to ensure that the sub-cells are current-matched while still producing the highest voltage and hence maximising efficiency [9, 12]. However, to reach such bandgaps, a certain critical Br content ($\sim$ 20%) is surpassed after which the perovskite material can exhibit phase instability under illumination, undergoing

segregation of the halide species [13–16]. This segregation is particularly severe for perovskites containing methylammonium on the A-site [16]. Importantly, after a certain ratio of Br is surpassed, the V_{OC} of these devices saturates at a value of ca. 1.2 V [17]. In early studies, this led to the conclusion that the formation of low bandgap I-rich domains is the main factor limiting the V_{OC} in solar cells featuring a higher concentration of Br [13, 17–19]. However, it has been recently clarified that the low V_{OC}s observed in wide bandgap perovskites are predominantly caused by a low radiative efficiency of the initial wide bandgap phase and strong non-radiative recombination at the interfaces with the charge transport layers [11, 20, 21]. As such, it is important to understand how the conduction and valence bands of the wide bandgap perovskite align with the energy levels of transport layers which are commonly used for perovskites with a narrower bandgap. It has been shown that good energetic alignment between the perovskite and the transport layers is crucial to achieving high V_{OC} and exploiting the radiative potential of the neat semiconductor [22, 23].

Another key issue for perovskite photovoltaics is their long-term stability. It has been shown that the longevity of perovskite solar cells (PSCs) can be ameliorated by eliminating MA from the crystal lattice [24–26]. In addition to that, it has recently been reported that incorporating IAs into the perovskite precursor solution can substantially enhance the lifetime of PSCs [10, 27]. One such additive, 1-butyl-1-methylpiperidinium tetrafluoroborate ($[BMP]^+[BF_4]^-$) was shown to effectively act as defect passivating agent concomitantly enhancing the device stability, contrary to many common surface passivation techniques which are not suitable for long-term operational stability [10, 27–29]. However, despite these impressive improvements, the effects of this approach on the recombination mechanisms are yet to be understood.

In this work, we focus on MA-free, $FA_{0.83}Cs_{0.17}Pb(I_{0.6}Br_{0.4})_3$, wide bandgap perovskite solar cells, both with and without IA modification, to investigate the radiative losses in state-of-the-art wide bandgap systems that are unaffected by halide phase segregation. Through photoluminescence quantum yield (PLQY) measurements and quasi-Fermi level splitting (QFLS) analysis on complete cells, partial device stacks and

neat materials, we quantify and pinpoint the origin of the non-radiative losses in devices based on wide bandgap perovskites. Interestingly, compared to 1.6 eV bandgap perovskites, despite the absence of phase segregation, wide bandgap perovskites are generally characterised by larger non-radiative recombination in the neat material, setting their QFLS far below their thermodynamic limit. Additionally, both the hole and electron transport layers (HTL and ETL respectively), induce severe interface non-radiative recombination, resulting in rather limited V_{OC}. Using time-resolved photoluminescence (TRPL) studies, we calculate that that the IA reduces the surface recombination velocity (SRV) at each interface by approximately one order of magnitude. We find the SRV at the perovskite/C60 interface can be further reduced by the incorporation of a 1 nm thick LiF interlayer. Lastly, combining photoemission spectroscopy measurements and drift-diffusion simulations, we rationalise the crucial role of the energetic alignment between the perovskite absorber and the charge-transport layers in wide bandgap systems. With this understanding, we fabricate high efficiency 1.79 eV PSCs exhibiting PCEs approaching 17 % with a V_{OC} of 1.22 V, which is among the highest reported for MA-free wide bandgap PSCs [30–34]. Furthermore, we identify that new transport layers are crucial to harness the full performance potential of these MA-free wide bandgap perovskite.

5.3 Results and discussion

5.3.1 Bulk optoelectronic properties

In this work, we use the methylammonium-free formamidinium-caesium ($FA_{0.83}Cs_{0.17}Pb(I_{0.6}Br_{0.4})_3$) based perovskite first developed by McMeekin *et al.* [4], which has a wide bandgap of $\sim$ 1.8 eV when processed via the anti-solvent quenching method. We chose this material due to its high stability and suitability for implementation in perovskite-on-perovskite tandem photovoltaic devices. To establish the impact of the ionic additive on the optoelectronic properties of $FA_{0.83}Cs_{0.17}Pb(I_{0.6}Br_{0.4})_3$, a

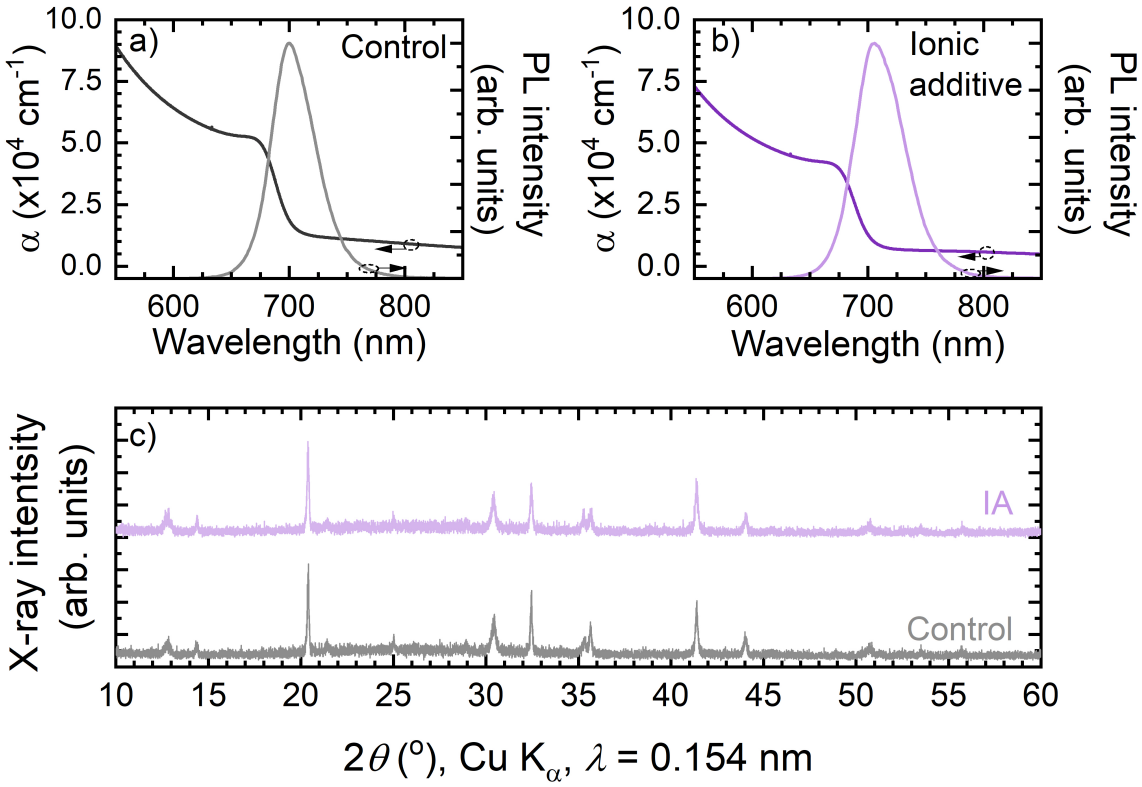


Figure 5.1: *a) Absorption coefficient (dark grey) and steady-state photoluminescence spectra (light grey) for control $FA_{0.83}Cs_{0.17}Pb(I_{0.6}Br_{0.4})_3$ perovskite thin films b) Absorption coefficient (dark purple) and steady-state photoluminescence spectra (light purple) for 1-butyl-1-methylpiperidinium tetrafluoroborate ($[BMP]^+[BF_4]^-$) modified $FA_{0.83}Cs_{0.17}Pb(I_{0.6}Br_{0.4})_3$ perovskite thin films. The optical measurements were performed on z-cut quartz substrates. c) X-ray diffraction patterns for control (grey) and IA-modified perovskite thin films on ITO substrates. Reproduced from [35] with permission from the Royal Society of Chemistry.*

thorough spectroscopic characterisation of control and IA-modified thin films was carried out. 'IA-modification' is explained in more detail in **Chapter 3**, however, in brief, it entails the addition of a small (0.5 mg mL^{-1}) of $[BMP]^+[BF_4]^-$ into the perovskite precursor solution before spincoating. The absorption coefficient, α, of control and IA-modified thin films is very similar for both samples as shown in **Figures 5.1a & b**. In line with this, the similarity of the X-ray diffraction (XRD) patterns (**Figure 5.1c**) of both samples demonstrates the negligible effect of the IA on the average crystallinity of the perovskite thin films. Further, as can be seen in **Figures 5.1a & b**, the shape and position of photoluminescence spectra are unchanged following IA-modification.

To delve into the effect of the ionic additive on the charge-carrier dynamics within

the bulk of the perovskite semiconductor, time-resolved photophysical spectroscopic studies were performed. In such measurements, perovskite thin films are photoexcited by laser pulses. Following an excitation pulse, the charge carrier concentration, n, within the perovskite semiconductor can be accurately described by the differential equation [3]

$$\frac{\mathrm{d}n}{\mathrm{d}t} = -k_1 n - k_2 n^2. \tag{5.1}$$

t is the time following the excitation pulse, k_1 is the monomolecular recombination rate related to first-order non-radiative trap-mediated recombination, k_2 is the bimolecular recombination rate describing radiative second-order band-to-band recombination within the perovskite semiconductor, and we have neglected higher-order (Auger) recombination and assumed equal concentrations of electrons and holes. **Equation 5.1** is simply the simplified version of **Equation 2.40**, wherein it is explained in much more detail.

To investigate the intrinsic properties of the perovskite thin films, optical-pump terahertz-probe spectroscopy (OPTPS) studies were performed. These measurements and analysis were performed by Dr. Leonardo R. V. Buizza. This technique does not require metallic electrodes and allows for investigation of the optoelectronic properties of the thin films, such as charge-carrier mobility and bimolecular (radiative) recombination, on picosecond timescales. This allows us to assess the charge-carrier dynamics of isolated perovskite thin films without the influence of any transport layers. The THz photoconductivity transients for control and IA-modified thin films are shown in **Figure 5.2a & Figure 5.2b**, respectively. Numerical fits to the measured transient photoconductivity decays allow for the extraction of the bimolecular charge-carrier recombination constant k_2 (Auger recombination was neglected, as it was found to contribute negligibly at the charge-carrier densities investigated here, full details are provided in **Chapter 3**). The extracted value k_2 is found to be unchanged with the addition of the ionic additive (values of 0.50 ± 0.06 and $0.52 \pm 0.05 \times 10^{-10}\,\mathrm{cm^3 s^{-1}}$ for control and IA modified samples respectively), implying little change in the fundamen-

tal electronic structure of the material with the addition of the IA [36]. These values are in line with values previously measured for mixed-cation lead mixed-halide perovskites [37, 38]. However, we note that they are underestimates of the actual intrinsic values of k_2 owing to the large thickness of the thin films measured here (> 500 nm), which leads to a substantial role for charge-carrier diffusion and photon reabsorption which masks the intrinsic value of the bimolecular recombination rate constant [39]. Concomitantly, we find that the charge-carrier mobilities are high in both control and treated films, in excess of $32\,\mathrm{cm^2V^{-1}s^{-1}}$. These values are substantially higher than values reported in the literature for similar Br contents, approaching values measured for triiodide perovskites, demonstrating the high quality of our control and IA treated thin-films [38, 40–43]. Nevertheless, considering that these measurements are short-range mobilities, it should be noted that these values represent upper limits of the effective mobility (or short-range intra-grain mobilities) [43]. Overall, the absorption and OPTPS measurements thus show us that the optical absorption, charge-carrier mobility and bimolecular (radiative) recombination rates are unaffected by the inclusion of 1-butyl-1-methylpiperidinium tetrafluoroborate into the perovskite precursor solution.

We now turn our attention to the extrinsic properties of these methylammonium-free wide bandgap perovskites. Time-resolved photoluminescence measurements were carried out to study the trap-assisted recombination regime in these materials. Transient decays of the PL measured using time-correlated single photon counting (TCSPC) are shown in **Figure 5.2c and Figure 5.2d** for control and IA-modified thin-film samples respectively. We fit the low excitation fluence transients ($16\,\mathrm{nJcm^{-2}}$) with a stretched exponential [44, 45], from which we extract the monomolecular recombination rate constant (k_1) (details provided in **Chapter 3**). We observe more than a two-fold reduction (from $k_1 = 1.0 \pm 0.1 \times 10^7\,\mathrm{s^{-1}}$ to $k_1 = 0.39 \pm 0.04 \times 10^7\,\mathrm{s^{-1}}$) with the inclusion of the IA, indicating reduced trap-mediated recombination. Due to the lower value of k_1 in the IA treated film, using the optical-pump terahertz-probe mobilites, we estimate that the diffusion length is enhanced from 2.8 μm to 4.8 μm. Details of

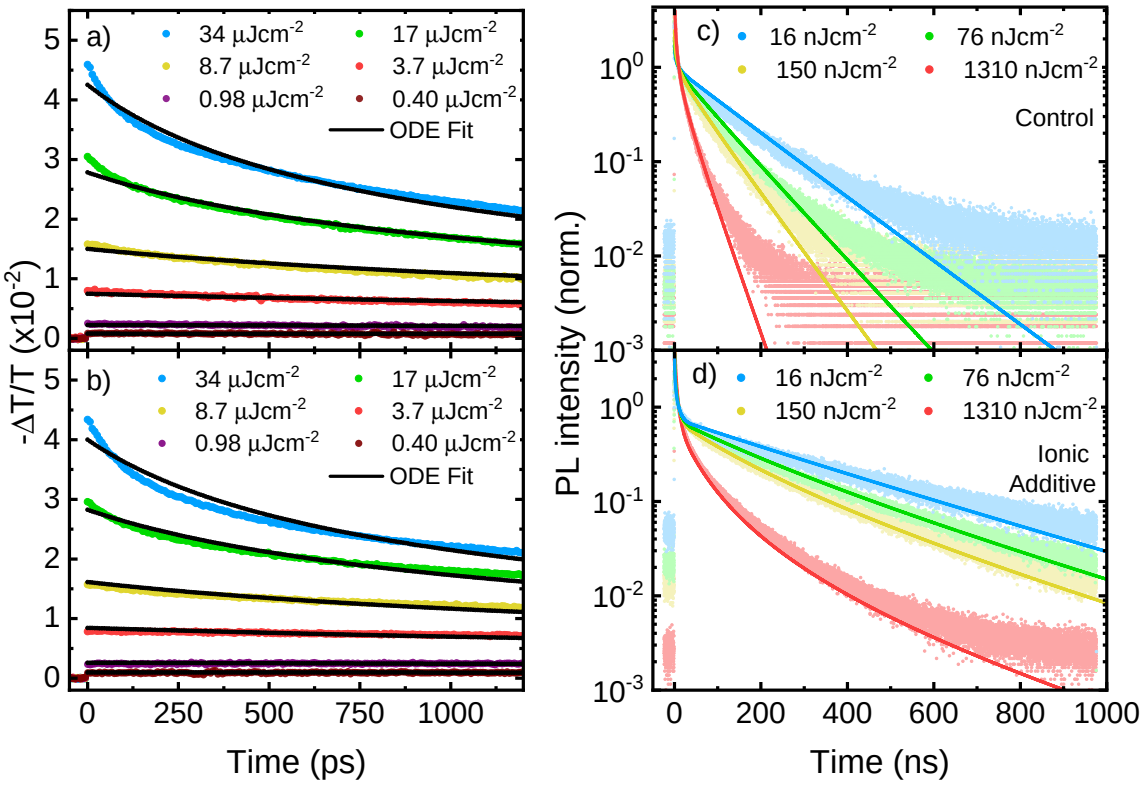


Figure 5.2: *Photophysical data for control (top row) and ionic additive (bottom row) samples on quartz substrates. (a, b) Optical-pump terahertz-probe spectroscopy (OPTPS) transient photoconductivity decays at fluences of* 34, 17, 8.7, 3.7, 0.98, 0.40 μJcm^{-2} *(blue, green, yellow, red, purple, brown dots respectively) for control and IA modified samples respectively. Fitted numerical solutions to an ODE are shown as black lines (see* ***Chapter 3*** *for details). OPTPS measurements were performed by Dr. Leonardo R. V. Buizza. (c and d) Time-resolved photoluminescence transients measured using time-correlated single photon counting at fluences of* 16, 76, 155 *and* 1310 nJcm^{-2} *(blue, green, yellow and red dots respectively) measured using pulsed (*1 MHz *repetition rate) excitation at* 398 nm *on the same samples as for the THz measurements. The data is normalised to the value at* 10 ns *following the laser pulse to allow for better visualisation. The solid lines are fits to the decays using the model described in detail later. Diffusion was modelled for the first 20 ns (the charge-carrier profile was uniform throughout following this time). Reproduced from [35] with permission from the Royal Society of Chemistry.*

this calculation are presented in **Chapters 2 & 4**. Both these values are substantial (much thicker than the perovskite active layer thickness of $\sim$ 500 nm and, as such, the devices based on this material are unlikely to be limited by the diffusion lengths of the charge carriers.

To better understand the impact of the ionic additive upon the charge-carrier dynamics, we investigated the fluence dependence of the TCSPC PL transients. As

observed in **Figures 5.2c & 5.2d**, the PL decays recorded for the control sample are characterised by stretched dynamics and a more substantial shortening of lifetimes with increasing excitation fluence, in comparison to the ionic additive modified sample. We are able to explain this behaviour using a basic recombination model, discussed below, which reveals that the IA preferentially passivates traps for one charged species, greatly reducing trap-mediated recombination in the bulk perovskite. The fitting discussed below was performed by Dr. Silvia G. Motti.

If the dynamics were to be described by a simple recombination model, as in **Equation 5.1**, the control sample would require an order of magnitude higher value of k_2, and, importantly, can not be explained from changing k_1 alone. As discussed in **Section 2.1.3**, k_2 is an intrinsic property of the semiconductor and so we would not expect it to be influenced by passivation of traps by the incorporation of 1-butyl-1-methylpiperidinium tetrafluoroborate. Diffusion and/or reabsorption effects, which can influence the measured ('extrinsic') k_2 [39], cannot explain the difference in the TCSPC transients, as these effects would also be prevalent in the OPTPS measurements, contrary to our measurements presented in **Figures 5.2a & 5.2b** which show very similar behaviour for control and IA-modified samples. Instead, we propose that the lower excitation density and higher repetition rate in the TCSPC measurements (1 MHz as opposed to 5 kHz in the OPTPS experiment) influence the charge-carrier dynamics significantly, notably by altering the amount of trapped charge carriers that 'carry over' from one excitation pulse to the next, as detailed below.

In more detail, the PL dynamics are recorded at lower excitation densities, and therefore experience more significant impact of trap states (i.e. $k_1 > k_2 n$ and so is the dominant factor in **Equation 5.1**). And secondly, the PL is acquired with a higher repetition rate of the pulsed photoexcitation (1MHz, as opposed to 5 kHz in the OPTPS experiment). Given the long lifetimes of trapped carriers in these lead halide perovskite semiconductors [46], the shorter time period between photoexcitation pulses can result in trap-filling and population build-up. The effect of the repetition rate on the photoexcited state dynamics depends on trapping and the balance of electron/hole

lifetimes. To investigate the impact of higher repetition rate, we consider a model (similarly previously reported in ref. [47]) that describes the decay of electron and hole populations (n and p, respectively) as

$$\frac{\mathrm{d}n}{\mathrm{d}t} = -k_1^{\mathrm{e}} n - k_2 np \tag{5.2}$$

$$\frac{\mathrm{d}p}{\mathrm{d}t} = -k_1^{\mathrm{h}} p - k_2 np \tag{5.3}$$

where k_1^{e} and k_1^{h} are the trap-mediated recombination rates for electrons and holes respectively. The photoluminescence intensity is, as always, proportional to the np product, and so $PL = k_2 np$.

To account for charge-carrier build-up, the remaining populations at the time of arrival of the next pulse are used as initial conditions for the next iteration. The process is repeated for 50 pulses, when steady-state conditions are reached. The rates, k_1^{e} and k_1^{h}, were adjusted to reproduce the fluence-dependent dynamics, and the value for k_2 was kept fixed for both samples (in agreement with the observation of unchanged higher order recombination in the OPTPS dynamics).

The PL dynamics shows a sharp decay at early-time that is likely associated with surface effects and/or the diffusion of charge carriers away from the initial photogeneration profile [45, 48]. According to the high charge-carrier mobilities in these semiconductors, diffusion is expected to result in a uniform distribution across the thickness of the film within a few nanoseconds [49]. As a first step in the implementation of our model, we neglect the early-time dynamics and consider the initial condition to be a uniform distribution of charge-carriers across the thickness of the film.

Figure 5.3 shows that the PL dynamics of the perovskite films fabricated with the ionic additive can be very accurately described by equal decay rates for electrons and holes, while the fluence-dependence observed for the control sample can be reproduced by unbalanced rates. We note that although we present k_1^{h} to be higher than k_1^{e}, these two parameters are interchangeable and the choice of the higher rate is arbitrary.

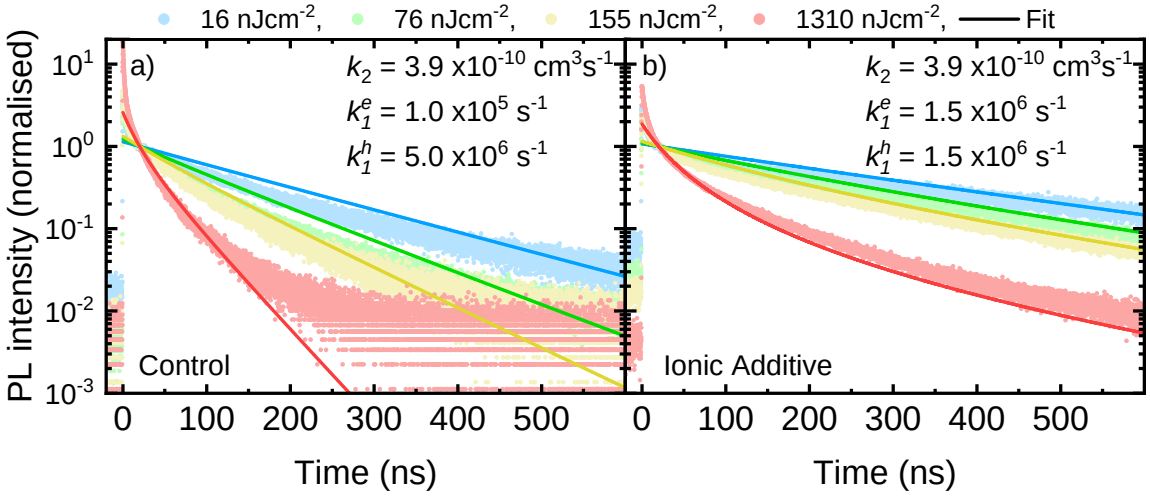


Figure 5.3: *Experimental (dots) and modelled (lines) PL dynamics using* ***Equations 5.2 & 5.3****, for the perovskite film without (a) and with (b) ionic additive modification. Initial distribution of charge-carriers was considered to be uniform across the film thickness in this case. Data and model were normalised at* $t = 20\,\text{ns}$ *to better visualise the dynamics without the early-time components associated with surface and diffusion effects [39, 48]. Reproduced from [35] with permission from the Royal Society of Chemistry.*

To better account for the early-time recombination, we have then implemented the simulation of diffusion effects. For such, we first calculate the photogeneration profile across 100 slices of the film thickness, resulting from the absorption of the 400 nm light (according to the absorption coefficients shown in **Figure 5.1a & 5.1b**). Diffusion is calculated using a forward Euler method similar to previous reports [39]. The limited temporal resolution of the TCSPC experiment for acquiring the photoluminescence dynamics does not allow for a precise analysis of the early-time components of the decay. However, any significant differences in the diffusion dynamics would have an impact on the recombination observed in the OPTPS experiment. As no differences had been observed, the diffusion coefficients were kept fixed for both films with and without ionic additive modification.

The dark solid lines in **Figures 5.2c & 5.2d** show the modelled PL dynamics, implementing diffusion effects, for the control and $[BMP]^+[BF_4]^-$ modified samples respectively, which accurately describes the fluence-dependence of the experimental data. Importantly, such an agreement is reached without changes to the effective bimolecular recombination rate. The difference between the control and ionic additive films results

from the unbalanced electron-hole trapping dynamics in the control sample and the consequent build-up of a charge carrier population owing to the 1 MHz repetition rate of the photoexcitation. We note that other effects could play a role in the stretching of the decays, such as variations in the ambipolar diffusion upon trap state filling, lateral diffusion, photon reabsorption and the efficiency of photoluminescence outcoupling and collection. Nonetheless, we observe a very good agreement between the model and the fluence-dependence of the experimentally acquired PL dynamics.

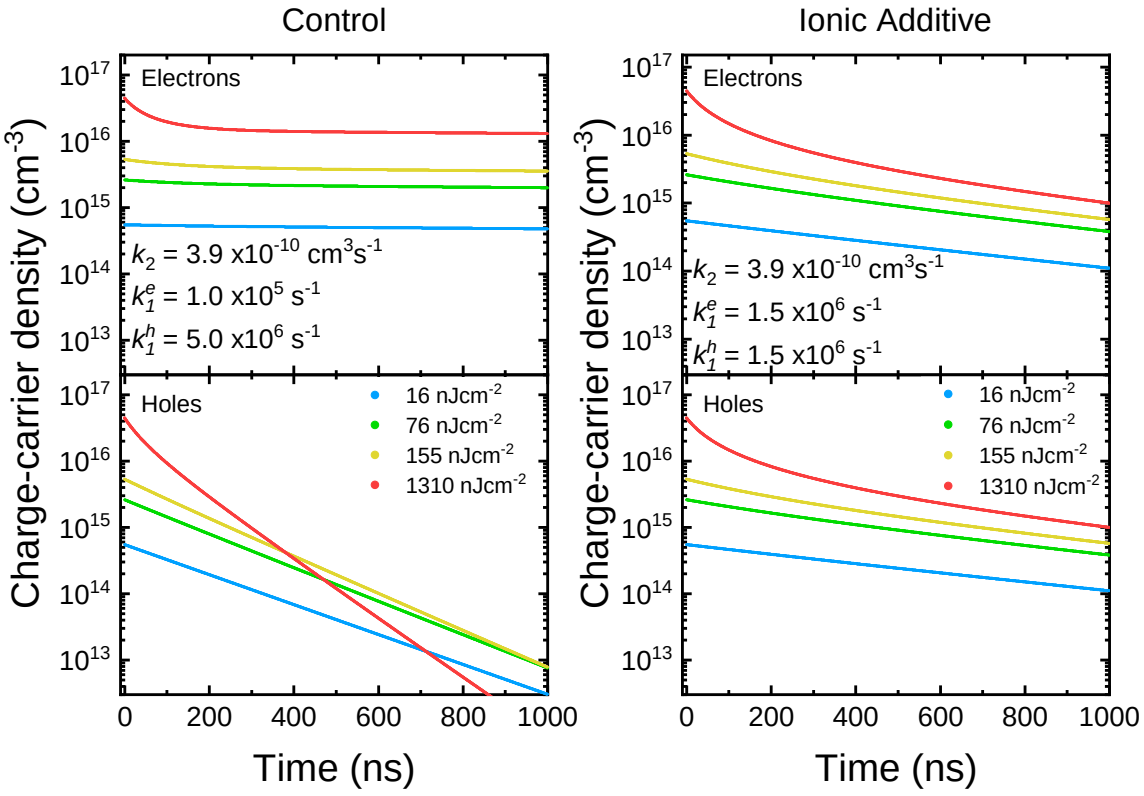


Figure 5.4: *Modelled electron and hole populations for control and $[BMP]^+[BF_4]^-$ modified perovskite thin films obtained using* ***Equations 5.2 & 5.3****. The left column shows the electron (top) and hole (bottom) populations for unbalanced trapping rates, representing the control perovskite. The right column shows the electron (top) and hole (bottom) populations for balanced trapping rates, representing the IA-modified perovskite. The values of k_1^h and k_1^e required to reproduce the transients in* ***Figure 5.3*** *were used in this plot. Reproduced from [35] with permission from the Royal Society of Chemistry.*

To better understand this effect, we show in **Figure 5.4** the individual electron and hole populations obtained from **Equations 5.2 & 5.3** for the case of balanced and unbalanced rates. When one type of carrier (electrons/holes) decays with a higher

rate, the remaining population of the opposite carrier cannot recombine radiatively. If the non-radiative decay of these remaining carriers is slow enough, a significant population of free carriers will be present when the next photoexcitation pulse arrives. A sequence of pulses will then create a steady-state population that will affect the observed radiative recombination. This 'photodoping' effect will depend on the photoexcitation intensity and can therefore explain the shortening of lifetimes observed with increasing fluence in the control perovskite film, even though the bimolecular radiative rates are unchanged. **Figure 5.5a & 5.5b** shows the population build-up over a sequence of 50 pulses of 1MHz photoexcitation for unbalanced and balanced trapping rates respectively. Over the course of 50 excitation pulses, a substantial population of one carrier species builds up in for the case of unbalanced trapping, which would in turn affect the PL dynamics. For comparison, we observe in **Figure 5.5c & 5.5d** that 5 kHz photoexcitation (as used in the OPTPS experiment) results in a population build-up many orders of magnitude lower, which would result in negligible effects on the recorded recombination dynamics.

We confirmed the role of trap-filling by conducting repetition rate dependent TCSPC measurements and found shorter lifetimes in the control sample for less frequent excitation pulses which can be see in **Figure 5.6**. In contrast, the lifetime for the IA modified sample was found to be independent of the repetition rate.

We support the model used to fit the PL transients in **Figure 5.2** by performing fluence-dependent TCSPC measurements with a slower repetition rate, which allows more time between excitation pulses for traps to depopulate. Crucially, the PL transients of the control perovskite are best reproduced with unbalanced trap-mediated recombination rates for electrons and holes, whereas the PL transients of the IA sample can be very accurately reproduced with balanced trapping rates. Therefore, even when the role of trap-filling and population build up is reduced due to the extended time between pulses, our model appears to be appropriate.

We cannot identify the specific nature of the trap species which is passivated by the IA from our studies here. However, the role of this same passivation molecule

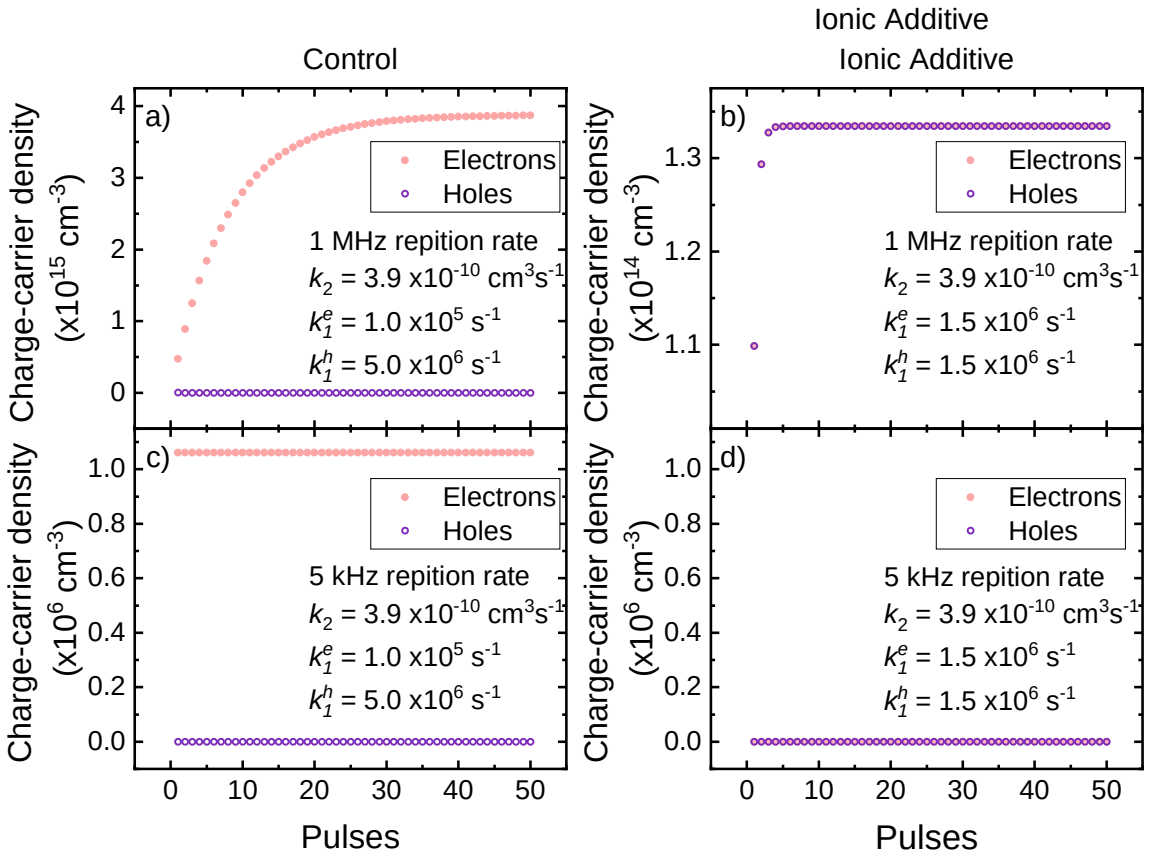


Figure 5.5: *Remaining electron and hole populations at the time of arrival of the next photoexcitation pulse obtained from* ***Equations 5.2 & 5.3****, at fluence* 16 nJcm^{-2} *with* 1 MHz *(a,b) and* 5 kHz *(c,d) repetition rate, for balanced (b,d) (IA-modified sample) and unbalanced (a,c) (control sample) electron and hole monomolecular rate constants* k_1^e *and* k_1^h*. Reproduced from [35] with permission from the Royal Society of Chemistry.*

upon inhibiting photochemical degradation, which is considered to proceed via hole-trapping on Iodide interstitials [10], and recent studies showing that hole-traps are prevalent at non-radiative recombination sites [50], is consistent with hole-traps being predominantly passivated by this IA.

Our spectroscopic analysis of the optoelectronic properties of the bulk material demonstrates that IA incorporation reduces the non-radiative recombination losses within the bulk material without altering any of the fundamental structural, optical and electronic properties of the perovskite semiconductor.

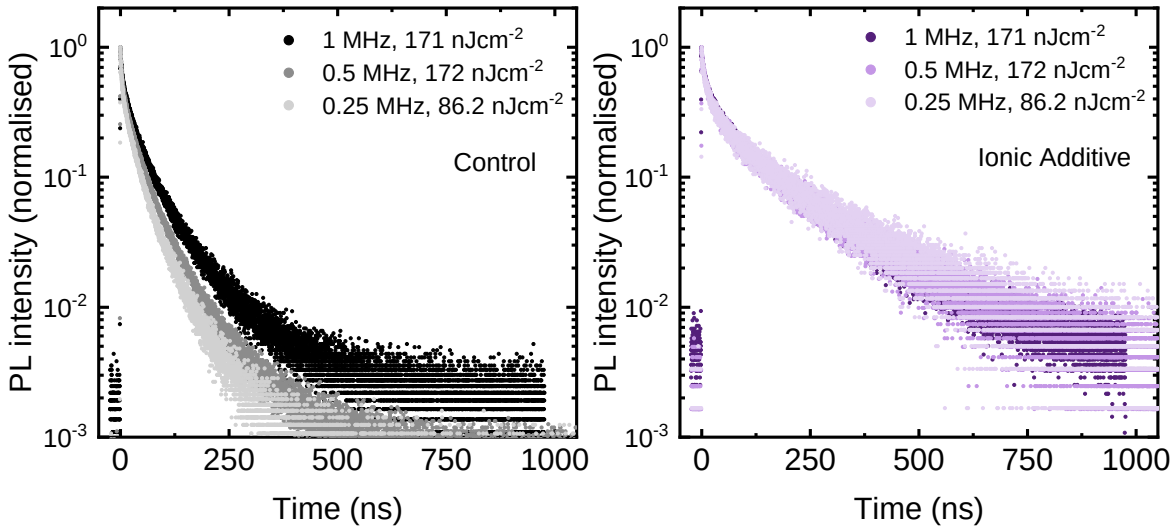


Figure 5.6: *Time-correlated single photon counting measurements for control (left panel, grey points) and IA modified (right panel, purple points) perovskite thin films deposited on quartz. The films were excited using a 398 nm centre wavelength laser at a range of repetition rates,* 1 MHz *(dark),* 500 kHz *(medium) and* 250 kHz *(light). The fluences were kept as constant as possible between each fluence and are shown in the legend. Importantly, the lifetimes are shorter for less frequent excitation pulses in the control sample, whereas the lifetimes are repetition rate independent for the* $[BMP]^+[BF_4]^-$ *modified sample. This supports the assumption of trap-filling and population build-up being substantial in the control sample, and less significant in the IA modified perovskite thin film. Reproduced from [35] with permission from the Royal Society of Chemistry.*

5.3.2 Interface recombination

To quantify the effect of $[BMP]^+[BF_4]^-$ addition on the interfacial recombination in partial device stacks we carried out photoluminescence quantum yield (PLQY) measurements. We performed these measurements on both glass substrates, to assess recombination in the bulk material, as well as on partial device stacks to determine to degree of interfacial recombination at each CTL/perovskite interface. As can be seen in **Figure 5.7**, the isolated control perovskite on glass (grey symbols) suffers from significant non-radiative losses achieving a PLQY of only 0.2 %. This is consistent with previous studies and below values usually achievable in MA-free 1.6 eV-bandgap materials [11, 20, 21, 51–53]. Given that our samples do not show phase segregation (discussed later), this indicates that perovskites comprising a higher Br content exhibit a large degree of non-radiative losses, possibly as the result of a higher density of traps in the initial mixed phase [11, 20, 21, 51–53]. When either the hole transport layer

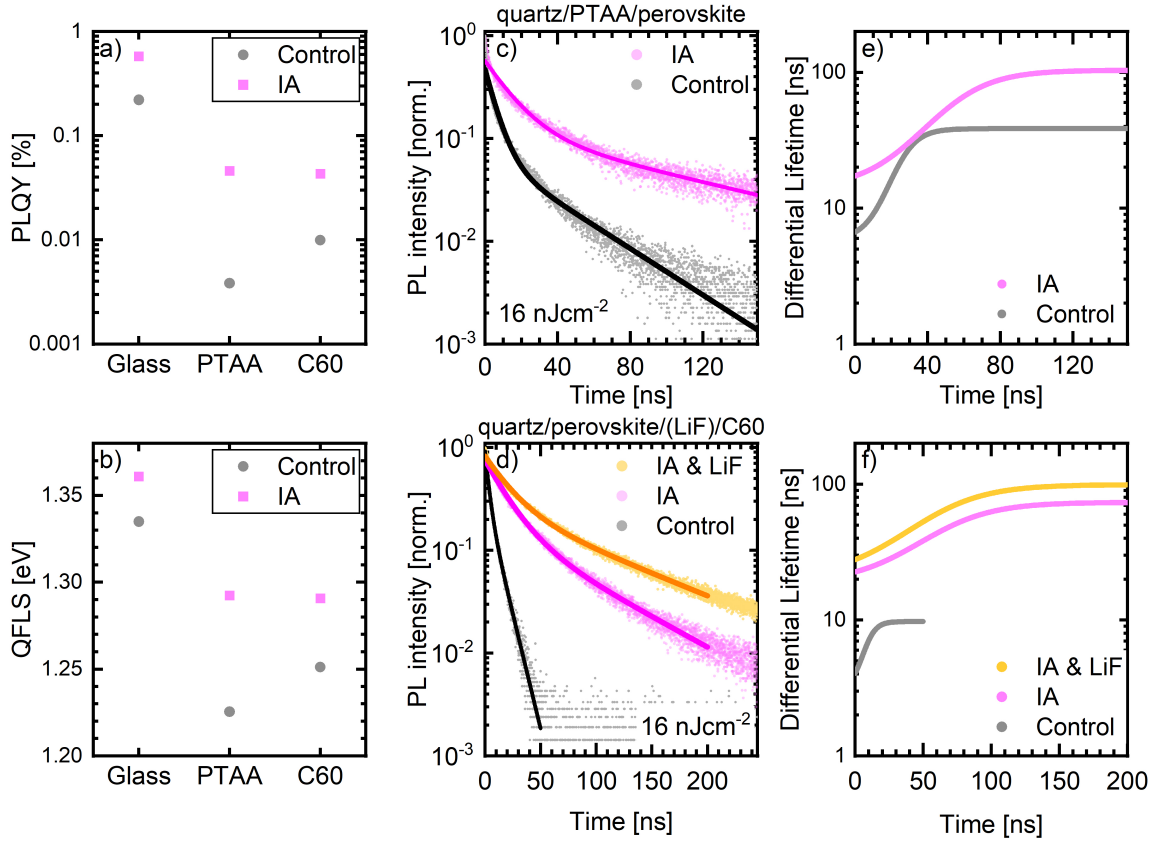


Figure 5.7: *Photoluminescence quantum yield (PLQY) for isolated perovskite thin films on glass (labelled glass), a half device stack ITO/PTAA/PFN-Br/perovskite (labelled PTAA) and glass/perovskite/C60 (labelled C60) for control (grey symbols) and IA modified (pink symbols). (b) The quasi-Fermi level splitting (QFLS) of the same samples calculated from the PLQY presented in (a), calculated as described in* ***Chapter 2****. (c) Time-correlated single photon counting (TCSPC) decays for quartz/PTAA/perovskite samples with control (grey symbols) and acia modified (pink symbols) perovskites. The samples were illuminated from the perovskite side with a 398 nm laser at a fluence of 16* $\mathrm{nJcm^{-2}}$*. The dark curves are double-exponential fits to the photoluminescence transients. (d) TCSPC decays for quartz/perovskite/(LiF)/C60 samples with control (no LiF, grey symbols) and IA modified (pink symbols) perovskite and IA modified perovskite with a LiF interlayer before the C60 (orange symbols). The samples were illuminated from the quartz side with a 398 nm centre wavelength laser at a fluence of 16* $\mathrm{nJcm^{-2}}$*. The dark curves are double-exponential fits to the PL transient. (e and f) The differential lifetime* $\tau_{\mathrm{diff}}(t)$ *calculated using* ***Equation 5.4*** *for the PL transients presented in (c and d) respectively. Reproduced from [35] with permission from the Royal Society of Chemistry.*

(HTL) or the ETL are attached, the PLQY is significantly reduced owing to strong interfacial recombination. Interestingly, here the losses at the HTL interface are larger compared with the ETL interface, contrary to 1.6 eV bandgap perovskites using the same transport layers where the majority of the non-radiative recombination originates at the ETL interface [20, 21, 48]. Such a scenario might originate from the substantially different energetics that these perovskites may present in conjunction with the transport layers [22, 23]. Importantly, when the ionic additive $[BMP]^+[BF_4]^-$ is incorporated in the perovskite, the PLQY is enhanced not only in the neat material, denoting a reduction of trap-assisted recombination in the bulk, as discussed earlier, but also at both the HTL and the ETL interfaces, **Figure 5.7**. This key finding highlights how despite the IA being added to the precursor solution, its effects are strongly visible at the perovskite/transport layer interfaces. Accordingly, the QFLS of the IA treated samples is also enhanced, demonstrating the possibility of high open-circuit voltages (V_{OC}s) in full photovoltaic devices [22, 54, 55]. The improvement of the bulk perovskite observed following IA incorporation can originate from an effective reduction of trap densities, either by passivation of defects or by influencing the crystallisation process. On the other hand, the increase in QFLS when either transport layer is attached denotes that, even though the IA is incorporated directly in the bulk material, this additive may help to form a more ideal interface between the perovskite and each transport layer, either providing a better energetic alignment or by reducing the trap density at the interface.

To understand the influence of IA incorporation on the interfacial recombination kinetics, we measured the transient decay of the photoluminescence of partial device stacks using time-correlated single photon counting (TCSPC). We investigated quartz/PTAA/perovskite (HTL stack) and quartz/perovskite/(LiF)/C60 (ETL stack) samples. Fluence-dependent photoluminescence transients were measured but are not discussed further in this thesis. In our investigation, we illuminated the HTL stack from the perovskite side, and the ETL stack from the quartz side. This ensures there is no parasitic absorption in the transport layer which would make further analysis chal-

lenging. The PL transients corresponding to the lowest excitation fluence (16 nJcm^{-2}) for HTL and ETL stacks are shown in **Figure 5.7c & Figure 5.7d** respectively. We fit the decays using a double exponential and show them with dark lines. The double exponential is used primarily to accurate reproduce the transient and no physical basis is claimed. The transient PL of the half stacks is influenced by several factors. In addition to charge-carrier recombination within the perovskite itself, charge transfer to the CTL becomes important, as does interfacial recombination between the majority carrier in the CTL with the minority carrier in the perovskite [45, 56]. To disentangle these processes we define a differential lifetime which is given by

$$\tau_{\text{diff}}(t) = -\left(\frac{\mathrm{d}\ln\varphi(t)}{\mathrm{d}t}\right)^{-1} \tag{5.4}$$

where $\varphi(t)$ is the photon flux. To perform this analysis, we fit the PL transients with a double exponential, since it accurately reproduces the transient, and take the numerical derivative of this fit, to determine τ_{diff}. As can be seen in **Figures 5.7e & 5.7f**, the lifetimes reach a plateau at large delay time. The initial rise at short delay times is attributed to charge transfer into the transport layers, whereas the longer lifetime is dominated by interface recombination [45, 56]. As is evident in **Figures 5.7e & 5.7f**, the incorporation of the IA significantly enhances the differential lifetime at large delay times, indicative of reduced interface recombination. This agrees with our PLQY measurements where we demonstrated reduced non-radiative recombination at each charge transport layer with the IA present under steady-state conditions. Moreover, to investigate the possibility of reducing the interface recombination further, we implemented an ultra-thin ($\sim$ 1 nm) LiF interlayer between the perovskite and ETL as previously reported [48, 57, 58]. As expected, when LiF is included between the IA-modified perovskite thin film and the C60, the differential lifetime is further enhanced. To quantify the influence of LiF alone, we compared the PL transients of a control perovskite/LiF/C60 sample and an IA/C60 sample. While the LiF interlayer does reduce the interfacial recombination, the IA treatment alone is more effective.

The lifetimes extracted from PL transients above (τ_{eff}) will be governed by both

Table 5.1: *Lifetimes extracted from time-correlated single photon counting (TCSPC) measurements of at 16* $\mathrm{nJcm^{-2}}$ *for the HTL and ETL stack. The surface recombination velocity (SRV) was calculated according to* ***Equation 5.6****. The bulk lifetimes used were 450 ns and 900 ns for control and IA modified samples respectively, taken from the fittings in* ***Figure 5.2c & 5.2d****.*

Condition	Sample	Illumination side	τ_{eff} (ns)	SRV ($\mathrm{cms^{-1}}$)
Control	HTL stack	perovskite	38	1300
IA	HTL Stack	perovskite	100	450
Control	ETL Stack	quartz	10	5600
IA	ETL Stack	quartz	73	640
IA & LiF	ETL Stack	quartz	99	450

bulk and surface recombination according to the relation [59]

$$\frac{1}{\tau_{\mathrm{eff}}} = \frac{1}{\tau_{\mathrm{bulk}}} + \frac{1}{\tau_{\mathrm{surface}}}. \tag{5.5}$$

We have determined the effective lifetime with the transport layers present in **Figures 5.7e & 5.7f**, and the "bulk lifetime" when the transport layers are absent, from the fitting in **Figure 5.2c & 5.2d**. Combining these values allows us to calculate the lifetime associated with recombination at the perovskite/CTL heterojunctions. If we assume that the recombination at the perovskite/CTL interface is far greater than at the perovskite/quartz or perovskite/air interfaces, we can express the surface lifetime as [48, 59, 60]

$$\tau_{\mathrm{surface}} = \frac{d}{SRV} + \frac{4}{D}\left(\frac{d}{\pi}\right)^2 \tag{5.6}$$

where d is the sample thickness, D is the diffusion coefficient and SRV is the surface recombination velocity. We determine D using the Einstein relation $D = \mu k_{\mathrm{B}} T/q$, where k_{B} is Boltzmann's constant, T the absolute temperature and μ the mobility obtained in the THz spectroscopy measurements. It is therefore possible for us to estimate the surface recombination velocity at each interface, which we display in **Table 5.1**.

For the control sample, the value of the surface recombination velocity at the fullerene interface is comparable to values reported in the literature for narrower bandgaps [60], but the SRV at the PTAA interface is substantially higher compared to literature values usually reported for $\sim$ 1.6 eV bandgap perovskites [48, 60]. This correlates with our PLQY data and shows again that the PTAA interface performs relatively poorly in the control samples for these wide bandgap materials, as we show in **Figures 5.7a & 5.7b**. Accordingly, we see that IA modification results in substantially reduced SRVs as compared to the control system in the same stack configuration. A large beneficial effect from the IA is observed at the C60 interface, where the SRV is reduced by close to one order of magnitude. As expected, the addition of LiF helps to reduce the surface recombination velocity value even further to as low as 450 cms^{-1}. This value is among the lowest reported for MA-free perovskites [61]. This is particularly impressive since our measurements were performed on perovskite films in contact with a CTL – known to induce significant non-radiative recombination as discussed earlier [62]. This reduction of surface recombination velocitys and enhanced radiative efficiency is extremely promising for corresponding photovoltaic device performance.

5.3.3 Photovoltaic device performance

To corroborate our study on the recombination mechanisms in wide bandgap perovskites thin films, we implement these materials in a p-i-n device architecture. Inverted p-i-n device architectures have numerous advantages over their n-i-p counterparts including reduced hysteresis, low temperature processability, and consequent suitability for silicon tandem technologies [63, 64]. The device architecture, shown in **Figure5.8a**, comprises PTAA as the hole transport layer which is coated with an 'ultra-thin' layer of PFN-Br onto which the perovskite layer is deposited. The solar cell is then finished by evaporating thin LiF interlayer (depending on the device type), C60 as the electron transport layer, bathocuproine (BCP) and Cu as top electrode. The perovskite absorber is optionally modified by adding an optimised amount (0.5 $\mathrm{mg\,mL}^{-1}$) of the ionic additive $[\mathrm{BMP}]^{+}[\mathrm{BF}_4]^{-}$ to the precursor solution.

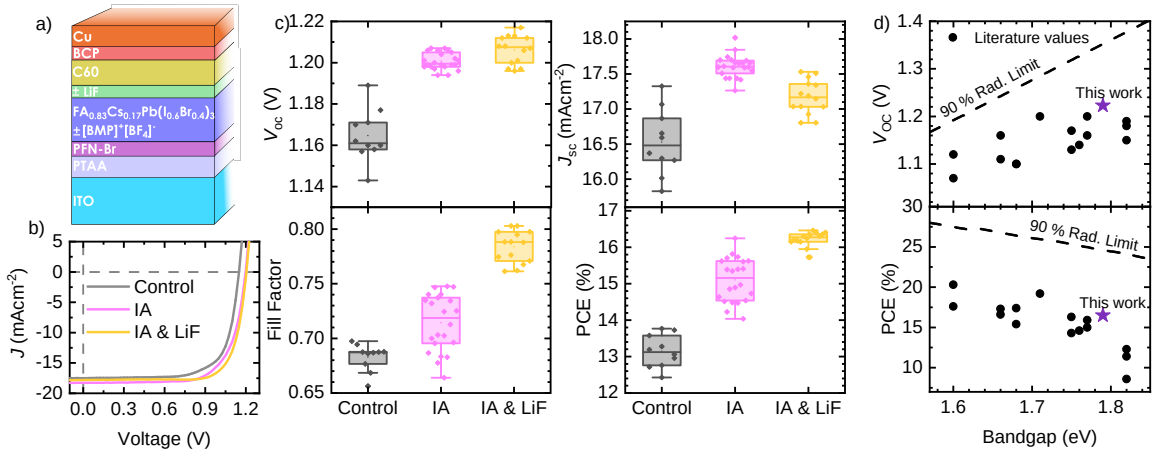


Figure 5.8: *Photovoltaic device performance. (a) Schematic of the device architecture utilised in this study. The '±' indicates elements which depend on the device type. The device active area was 0.06 cm^2. (b) Exemplary JV curves for the three types of devices investigated. (c) Statistical summary of reference FACs based perovskite solar cells (grey), IA modified devices (pink) and IA modified devices implementing a LiF interlayer (orange). The data points are overlapped onto the boxplots which show the median (central line), and the median of the upper and lower halves of the data (top and bottom lines of the box, respectively). The top and bottom whiskers are drawn to the highest/lowest data point within 1.5 times the interquartile range from the top and bottom of the box, respectively. (d) Literature comparison between our work (denoted with a star) and pin-type devices with methylammonium-free perovskite solar cells. The dashed lines represent 90 % of the radiative limit with respect to the bandgap energy. The data and references for the literature search can be found in* ***Table 5.2****. Reproduced from [35] with permission from the Royal Society of Chemistry.*

The beneficial effects of the IA addition in devices are clearly visible in the exemplary JV-curves represented in **Figure5.8b**, where the V_{OC}, J_{SC} and FF are improved upon the incorporation of the ionic additive. To corroborate the J_{SC} values measured on the solar simulator, we measured the external quantum efficiency (EQE) of the devices, and then calculated the integrated J_{SC}, which is presented in **Figure 5.10a**. We find the integrated current is in good agreement with the J_{SC} determined from the current-voltage characteristics. Furthermore, with the addition of a LiF interlayer the FF is greatly enhanced and the V_{OC} also increases. The statistical summary of the three types of devices investigated in this work are presented in **Figure 5.8c**. Here, the combination of the IA with a LiF interlayer allows us to reach V_{OC} of 1.22 V, FF above 80 % and PCEs approaching 17 %.

We present the forward and reverse scans for each device type investigated, and

Table 5.2: *Reported values of the open-circuit voltage and power conversion efficiency for methylammonium-free p-i-n perovskite solar cells. These data are compared against those achieved in this Chapter in* ***Figure 5.8****.*

Perovskite	Bandgap (eV)	V_{OC} (V)	PCE (%)	Ref.
$FA_{0.83}Cs_{0.17}Pb(I_{0.75}Br_{0.25})_3$	1.68	1.10	15.4	[30]
$FA_{0.75}Cs_{0.25}Pb(I_{0.8}Br_{0.2})_3$	1.68	1.10	17.4	[30]
$FA_{0.83}Cs_{0.17}Pb(I_{0.6}Br_{0.4})_3$	1.75	1.13	14.3	[30]
$FA_{0.6}Cs_{0.4}Pb(I_{0.7}Br_{0.3})_3$	1.75	1.17	16.3	[30]
$FA_{0.6}Cs_{0.4}Pb(I_{0.7}Br_{0.3})_3$	1.76	1.14	14.6	[31]
$FA_{0.6}Cs_{0.3}DMA_{0.1}Pb(I_{0.7}Br_{0.3})_3$ (DMA is dimethylammonium)	1.71	1.20	19.2	[34]
$FA_{0.8}Cs_{0.2}Pb(I_{0.5}Br_{0.5})_3$	1.82	1.15	8.6	[32]
$FA_{0.8}Cs_{0.2}Pb(I_{0.5}Br_{0.5})_3$	1.82	1.18	11.4	[32]
$FA_{0.8}Cs_{0.2}Pb(I_{0.5}Br_{0.5})_3$	1.82	1.19	12.3	[32]
$FA_{0.83}Cs_{0.17}Pb(I_{0.9}Br_{0.1})_3$	1.6	1.07	17.6	[10]
$FA_{0.83}Cs_{0.17}Pb(I_{0.9}Br_{0.1})_3$ with $[BMP]^+[BF_4]^-$	1.6	1.12	20.3	[10]
$FA_{0.83}Cs_{0.17}Pb(I_{0.77}Br_{0.23})_3$	1.66	1.11	16.6	[10]
$FA_{0.83}Cs_{0.17}Pb(I_{0.77}Br_{0.23})_3$ with $[BMP]^+[BF_4]^-$	1.66	1.16	17.3	[10]
$FA_{0.8}Cs_{0.2}Pb(I_{0.6}Br_{0.4})_3$	1.77	1.16	15.0	[33]
$FA_{0.8}Cs_{0.2}Pb(I_{0.6}Br_{0.4})_3$	1.77	1.20	15.9	[33]

the stabilised power output of these devices in **Figure 5.9**. While the forward and reverse scans do not perfectly overlap in each case, the hysteresis is not too severe for each condition investigated, and over a wide range of scan speeds. The addition of the IA does seem to increase the hysteresis as compared to the control, but this can be ameliorated to a large degree by the inclusion of the LiF interlayer. The maximum power point of each of these devices is tracked over a 5 minute period, the results of which are shown in **Figure 5.9d**. This shows that the power output of these device is stable over this time window. However, the light source for this measurement could not be properly calibrated, and so the precise values should be taken mainly as a guide. However, the relative improvement is indeed trustworthy, and clearly demonstrates the

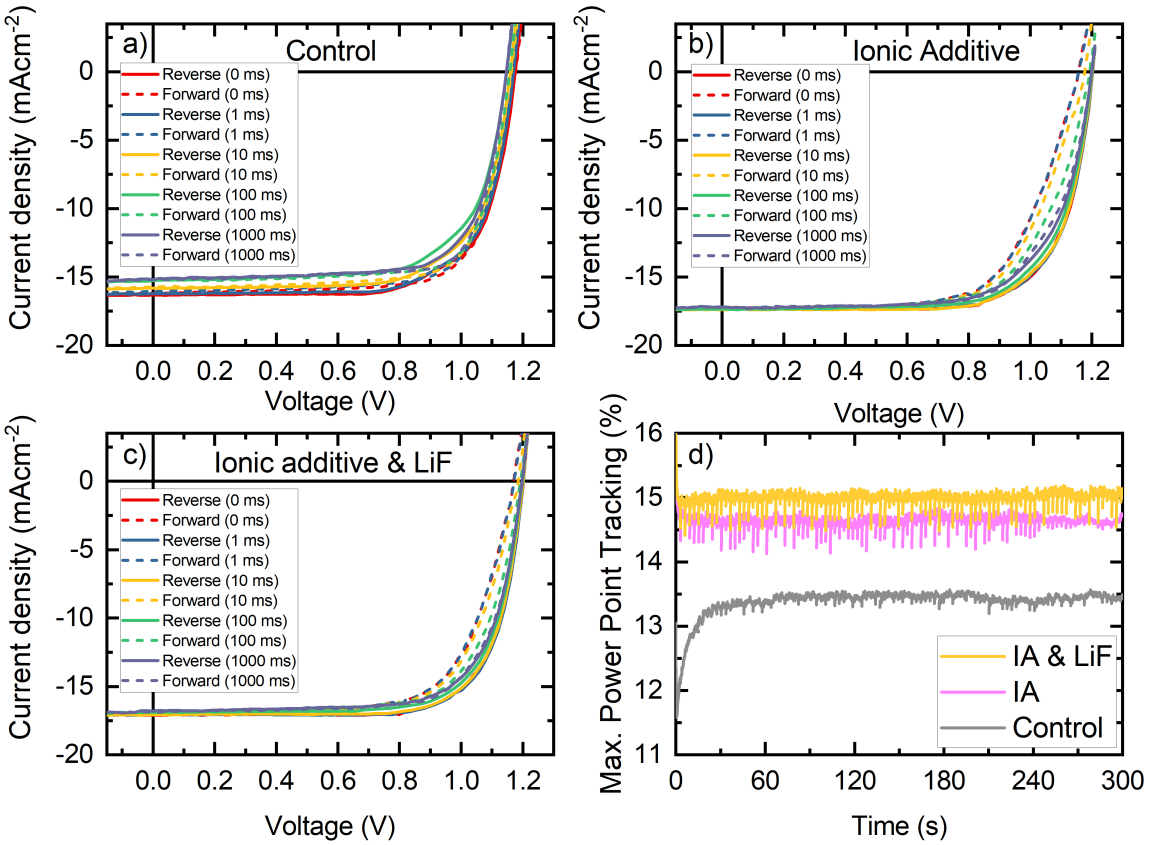


Figure 5.9: *Forward and reverse scans at a wide range of settling times* $(0-1000\,\mathrm{ms})$ *for representative a) control, b) IA modified and c) IA modified with a LiF interlayer devices. The settling time refers to how long a certain bias is applied before the corresponding current-density measurement is taken. d) Maximum power point tracking for the same devices recorded over 5 minutes. These measurements were performed by Francisco Peña-Camargo at the University of Potsdam. Reproduced from [35] with permission from the Royal Society of Chemistry.*

substantial improvement afforded by IA modification.

To compare our results with those published in the literature literature, in **Figure 5.8d** we show that wide bandgap MA-free perovskites, especially in p-i-n architectures, are prone to modest power conversion efficiency (PCE), due to larger V_{OC} losses compared to the radiative potential at the respective bandgap. The work presented here goes a significant way to overcoming many of these losses.

While the V_{OC} and FF improvements are expected from devices showing increased radiative efficiency, as discussed previously, the enhancement of the short-circuit current density, evident in **Figure 5.8c**, following IA modification is unexpected. Such an effect would imply either increased charge-carrier generation, extraction, or both.

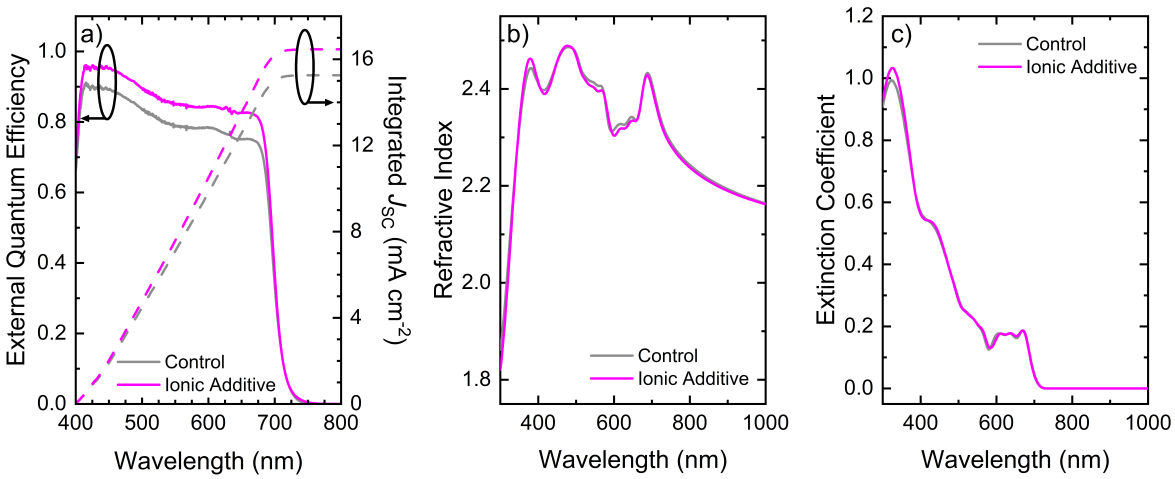


Figure 5.10: *a) External quantum efficiency (EQE) and integrated short-circuit current density for representative control (grey) and $[BMP]^+[BF_4]^-$-modified (purple) devices. The integrated current shows good agreement with the J_{SC} determined from the JV curves. Explicitly, the J_{SC} determined from the JV curves was 15.0 mA cm^{-2} and 16.8 mA cm^{-2} which compares to 15.2 mA cm^{-2} and 16.5 mA cm^{-2} integrated current densities for control and IA modified devices respectively. b) refractive index and c) extinction coefficient of the control (grey) and $[BMP]^+[BF_4]^-$-treated (purple) thin films deposited on z-cut quartz substrates as determined by ellipsometry. These measurements and analysis were performed by Dr. Suhas Mahesh. All samples have similar optical constants, and so the increased J_{SC} cannot be explained by a different electric-field profile within the bulk of the perovskite semiconductor. Therefore, the enhancement in J_{SC} is unlikely to be due increased charge carrier generation following IA incorporation. Reproduced from [35] with permission from the Royal Society of Chemistry.*

To rule out the possibility of increased charge-carrier generation, the optical constants of the perovskite, with and without the IA, were measured by ellipsometry. As can be seen from **Figures 5.10b & 5.10c**, the optical constants of the control and IA-modified perovskite are extremely similar. As such we do not expect that there will be increased charge-carrier generation upon IA modification. Due to the similar optical constants and film thicknesses, we can rule out any optical effect increasing the J_{SC}. It has recently been reported that mobile ions are the origin of short-circuit current density losses in perovskite solar cells [65]. Whilst determining the precise origin of the current density increase is beyond the scope of the current work, we suggest the increased J_{SC} may be due to reduced ionic mobility following $[BMP]^+[BF_4]^-$ modification. Such an effect would reduce the severity of current losses in these types of devices, manifesting as an increased J_{SC} as compared to the control devices.

To corroborate the combination of our findings and to better correlate this im-

Table 5.3: *Comparing the device performance parameters of actual devices without (control) and with IA modification (IA) with those determined using drift-diffusion simulations, taking the mobility, bulk lifetimes and SRVs values that were determined in the main text. A full list of the device simulation inputs can be found in* ***Table 3.2****.*

Condition	J_{SC} (mA cm^{-2})	FF (%)	V_{OC} (V)	PCE (%)
Control	17.0 ± 0.5	68 ± 2	1.16 ± 0.01	13.7 ± 0.5
Control Simulated	16.8	70.0	1.18	14.0
IA	17.5 ± 0.5	72 ± 3	1.20 ± 0.01	15.2 ± 0.5
IA Simulated	16.9	75.9	1.21	15.6

proved device performance with the spectroscopic characterisation performed earlier, drift-diffusion simulations were performed using SCAPS [66]. Importantly, we use values determined experimentally in our earlier analysis as input simulation parameters, including the bulk lifetimes and surface recombination velocities at each interface. Moreover, the energy alignment between the layers is informed by the photoemission spectroscopy results, which are discussed in detail later. A table of the input parameters can be found in **Table 3.2**. Our simulations were able to reproduce the photovoltaic device performance parameters well in all aspects apart from the enhanced short-circuit current density following IA modification. As discussed earlier, this enhacement to the J_{SC} is unexpected, and so it is perhaps unsurprising that this effect would not be reproduced by the drift-diffusion simulations. A comparison between the drift-diffusion simulations and the real photovoltaic device parameters is presented in **Table 5.3**. The close agreement strongly supports our spectroscopic investigations into the energy loss pathways in these materials and partial device stacks. This demonstrates the validity of our earlier analysis, but highlights that understanding current losses in these p-i-n devices requires further investigation. We now investigate the recombination occuring within full devices.

5.3.4 Recombination analysis in full devices

To assess the effects of the $[BMP]^+[BF_4]^-$ and LiF on the recombination mechanisms in complete devices, we carried out two sets of illumination intensity dependent measure-

ments: illumination intensity dependent PLQY and illumination intensity dependent V_{OC} ($V_{OC}(I)$, I is the excitation intensity). The PLQY measurements were carried out on isolated thin films on glass substrates and the V_{OC} measurements on full devices. The PLQY measurements are used to determine the quasi-Fermi level splitting. As proposed in a recent publication, QFLS intensity dependent measurements (QFLS(I)) can be used to reconstruct a pseudo JV-curve (pJV) for isolated perovskite thin films in the absence of the influence of charge transport layers (more detail is given in **Chapter 3**) [67]. Due to the absence of CTLs, which induce significant additional non-radiative recombination as discussed in **Setion 5.3.2**, such pJV curves therefore represent the maximum efficiency achievable with a particular absorber in the absence of interfacial recombination. In addition, it is possible to reconstruct a pJV curve using $V_{OC}(I)$ measurements on full devices. Thereby, such pJV curves are influenced exclusively by the recombination processes taking place in the device, at the interfaces or within the perovskite semiconductor, and, crucially, not during charge-carrier transport. This is because no charges are extracted during open-circuit voltage measurements. The advantage of this analysis approach is that through PLQY (and V_{OC}) measurements over a wide range of illumination intensities, we can estimate the effect of charge-carrier recombination on both the V_{OC} and the FF at the same time. This technique allows for the untangling of transport and recombination loss mechanisms within the devices, and ultimately facilitates estimating a potential efficiency of the single absorber or the device in absence of interfacial and transport losses. Notably, the intensity dependent photoluminescence spectra, showed no evidence of PL shift upon constant illumination and high illumination intensities (up to $\sim$ 5 suns equivalent), denoting the absence of phase segregation that is usually observed in methylammonium-containing high Br content perovskites [13, 15, 16, 20].

In **Figures 5.11a-c**, we compare the 'normal' JV measured on the solar simulator with the pJV of the same device (from $V_{OC}(I)$ measurements) and that of the bare absorber (from QFLS(I) measurements). From these data, it is possible to quantify and visualise the significance of non-radiative and transport losses of our different

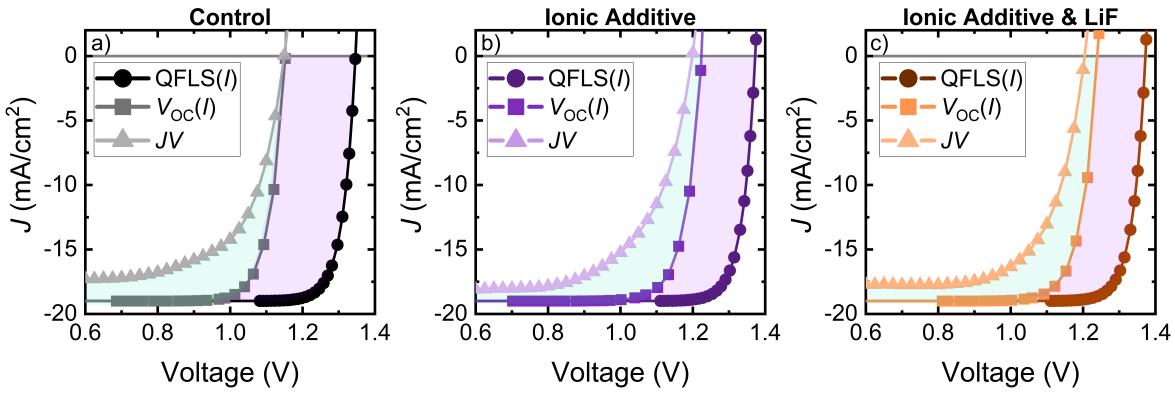


Figure 5.11: *The results are shown in (a) for the reference perovskite, in (b) for the perovskite including IA, and in (c) with the additional addition of a LiF interlayer. In (a,b,c) the right-most curve is determined from PLQY(I) measurements which are converted into QFLS(I) of thin films on glass, and so represents a pseudo JV-curve with minimal interface recombination. The centre curve is derived from $V_{OC}(I)$ measurements on full devices, and represents a pseudo JV-curve with interfacial recombination, but in the absence of transport losses. The left-most curve is the JV curve of the same device measured on the solar simulator. As such, the purple shaded area represents the interfacial losses at each point along a the JV curve, and the green region denotes the transport losses. These measurements were performed by Dr. Pietro Caprioglio at the University of Potsdam. Reproduced from [35] with permission from the Royal Society of Chemistry.*

cells and materials. The losses are highlighted as the shaded purple and turquoise areas, respectively, between the different *JV* and p*JV* in **Figures 5.11a–c**. These plots graphically demonstrate that the incorporation of the IA is effective at both reducing the recombination and transport losses in complete devices, and both losses are further reduced by the addition of LiF. This finding is in excellent agreement with our TCSPC analysis on the IA's effect on the bulk material and each interface between the perovskite and the CTLs. Additionally, in the case of an isolated thin film, this estimates the ideal case of a solar cell with zero interfacial losses. This highlights how this 1.79 eV (determined from the inflection point of the EQE) bandgap IA modified perovskite could potentially achieve a PCE of 23.17 % if implemented in a fully optimised device, where all recombination and transport losses at interfaces and in the device are eliminated. We present the estimated device characteristics in **Table 5.4**.

In **Figure 5.12a**, the ideality factor from the V_{OC} intensity dependence study is calculated and shows that the devices treated with $[BMP]^+[BF_4]^-$ and LiF exhibit

Sample	Method	pJ_{SC} (mA cm^{-2})	V_{OC} (V)	pFF (%)	pPCE (%)
Control	QFLS(I)	19	1.345	88.5	22.61
Control	V_{OC}(I)	19	1.156	88.2	19.37
IA	QFLS(I)	19	1.375	88.7	23.17
IA	V_{OC}(I)	19	1.22	85.5	19.81
IA & LiF	QFLS(I)	19	1.375	88.7	23.17
IA & LiF	V_{OC}(I)	19	1.23	87.7	20.5

Table 5.4: *Estimated PCE (in the absence of interfacial and/or transport losses) obtained from the pJV of cells and isolated thin films for the materials investigated in the study. The J_{SC} used here to estimate the efficiency potentials are calculated by assuming 95 % of the thermodynamic limit corresponding to the bandgap.*

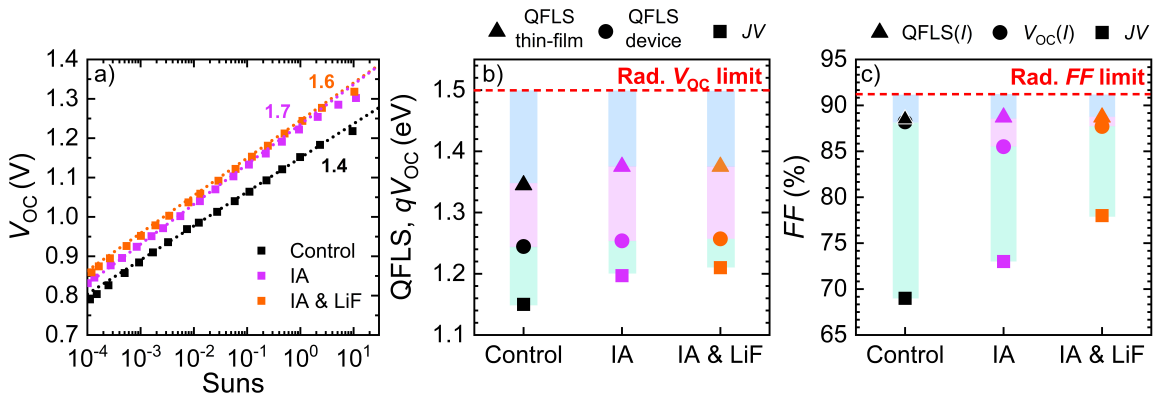


Figure 5.12: *a) V_{OC} intensity-dependent measurements and ideality factors for solar cell devices implementing control, IA-modified, and IA-modified with additional LiF interlayer before the C60. b) V_{OC} energy losses summary calculated from the samples and data presented in* ***Figure 5.11****. c) A summary of fill factor energy losses calculated from the samples and data presented in* ***Figure 5.11****.These measurements were performed by Dr. Pietro Caprioglio at the University of Potsdam. Reproduced from [35] with permission from the Royal Society of Chemistry.*

larger ideality factors compared to the reference cell. These results are in line with a recent study and demonstrate the effective reduction of interface recombination upon optimisation, in agreement with the enhanced V_{OC} evident in **Figure 5.8c** [68]. The LiF has a negligible effect on the QFLS in the absence of a transport layer, which implies that it has no direct passivation effect, and may be viewed as a 'buffer layer' between the perovskite and the C60. The absence of a passivation effect would suggest LiF alone does not change the recombination properties within the perovskite semiconductor, which explains the similarity of the pJV curves derived from QFLS(I) for the IA and IA & LiF cases summarised in **Table 5.4**.

We summarise the impact of non-radiative losses on the radiative potential of our devices in **Figure 5.12b**. Generally, this MA-free wide bandgap perovskite is characterised by a large degree of non-radiative losses (indicated in blue) compared to the radiative open-circuit voltage limit of 1.50 V present for a solar absorber with the optical properties of the 'isolated' (no electronic contacts) MHP thin-films. This denotes strong non-radiative losses taking place in the perovskite semiconductor, possibly due to high density of traps even in the absence of transport layers, which are reduced by $[BMP]^+[BF_4]^-$ implementation. As discussed earlier, the contacting with the transport layers results in significant interfacial non-radiative losses (purple region) and therefore a further reduction in the V_{OC} and QFLS. Importantly, the QFLS of the full devices represents the maximum realistically achievable open-circuit voltage which originates internally from the device's photoactive layer. Interestingly, however, the externally measured V_{OC} of these exact same devices lies substantially below these values, as indicated by the shaded turquoise region. We find here that IA and LiF treatments improve the QFLS of the full devices (including the metallic electrodes). Critically, they also improve the V_{OC} of the very same devices, but to a more significant degree than the improvement in QFLS. As a result, although not entirely eliminated, the mismatch between the QFLS and the V_{OC} is reduced with these treatments (shaded turquoise region in **Figure 5.12b**). We proceed to investigate the origin of the remaining mismatch.

A mismatch between QFLS and V_{OC} has been previously attributed to an energetic

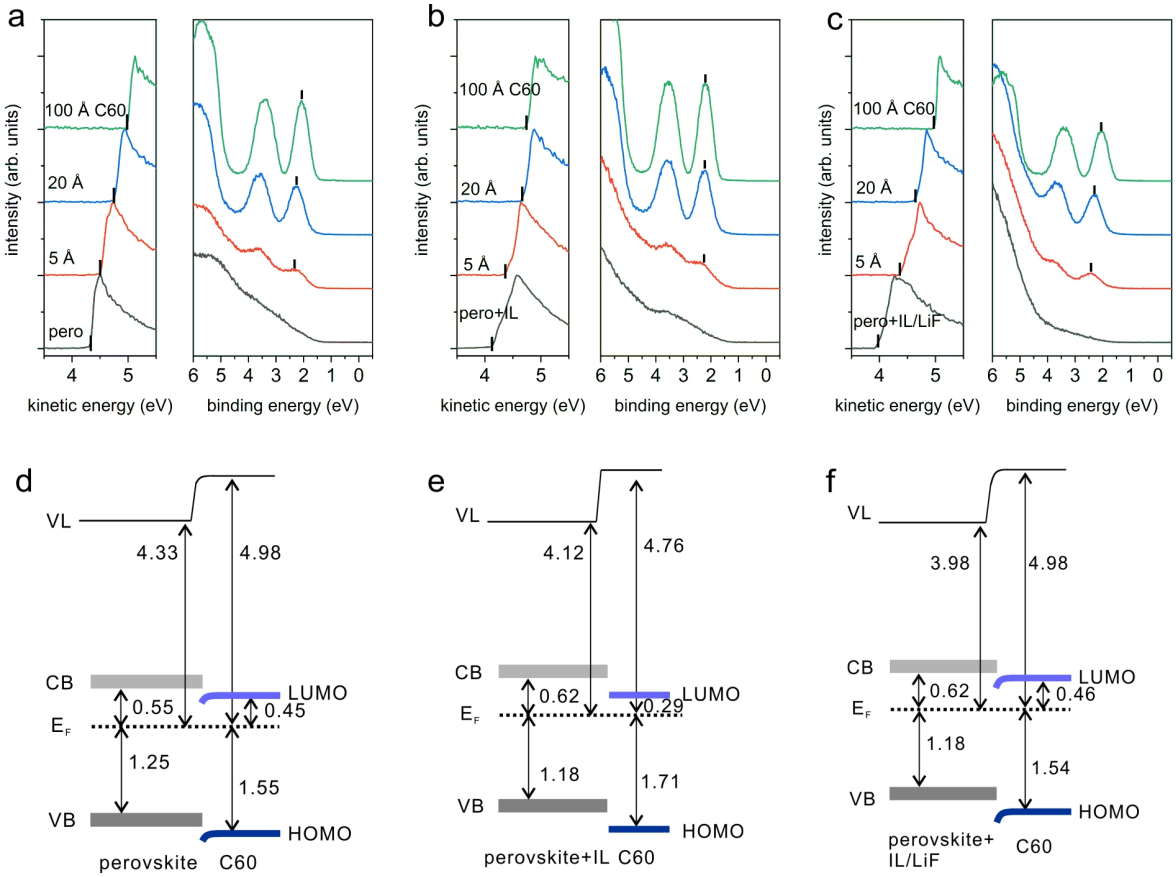


Figure 5.13: *a), b) and c) show the ultraviolet photoemission sprectroscopy (UPS) measurements for control, IA-modified and IA-modified & LiF perovskite thin films on ITO/PTAA substrates respectively. Sequential deposition of C60 was performed and UPS measurements were repeated at C60 thicknesses of 5, 20 and 100 Å, allowing the reconstruction of the energetics at this interface. In a), b) and c), the left panel shows the secondary electron cut-off which gives the work function, and the right panel shows the valence band region, from which the valence band onset is extracted. d), e) and f) show the flat-band diagrams of this interface which are inferred using the measurements from a), b) and c) respectively. These measurements and analysis were performed by Dr. Fengshuo Zu at Humboldt University of Berlin. Reproduced from [35] with permission from the Royal Society of Chemistry.*

misalignment between the perovskite and the charge transport layers in combination with interface recombination [22, 23]. To investigate the origin of this loss in our devices, we conducted ultraviolet photoemission sprectroscopy (UPS) measurements specifically probing the perovskite / C60 interfaces by performing multistep sequential deposition of C60 molecules, which are presented in **Figure 5.13**. As such, we are able to reconstruct the energetics at these specific interfaces accurately, and the band diagrams derived from these measurements are also presented. Our UPS measurements highlight a misalignment between the conduction band of the perovskite and the low-

est unoccupied molecular orbital (LUMO) of the C60 in all conditions investigated, despite the implementation of IA or LiF. Therefore, we conclude that the reduction of the QFLS-V_{OC} mismatch in these devices is unlikely to be due to a better energetic alignment of the perovskite with the ETL. Such a reduction in the mismatch could be related to the partial specific resistances for electrons and holes at the CTL interfaces [69, 70]. However, we observe that the Fermi level is shifted towards mid-gap upon IA modification, which may be due to a reduction in surface defects in line with previous analysis within the literature [71, 72]. The finding of the energetic misalignment between the perovskite and the C60 is significant and sufficient to give rise to a QFLS-V_{OC} mismatch. However, we do not exclude the possibility of an additional energetic misalignment between the highest occupied molecular orbital (HOMO) of the PTAA and the perovskite valence band. Since the PTAA HOMO is well-aligned with the valence band of 1.6 eV perovskites, the shifting of the perovskite valence band away from vacuum as the Br content is increased is likely to induce an energetic misalignment in these wide bandgap perovskites [23, 73].

As shown in **Figure 5.12b**, even for optimised devices utilising the combination IA and LiF, the V_{OC} measured in the device still lies more than 60 meV below the potentially achievable internal QFLS. Therefore, developing transport layers with better energetic alignment, or another approach to reduce the mismatch between internal and external voltage, would enable full exploitation of the radiative potential of the optimised perovskite and interfaces.

Moreover, this need for a new device architecture for MA-free wide bandgap perovskites is further highlighted in **Figure 5.12c**. Therein, we find the pseudo-fill factors (pFFs) determined from the isolated materials on glass for each condition lie extremely close to the radiative limit, indicating that recombination losses have a minimal impact on the FF of these materials. On the other hand, we see a significant difference between the pFF determined from the intensity dependent V_{OC} measurements (presented in **Figure 5.12a**) and the FF determined from the JV-curves, indicating the carrier transport losses out of the device, are the main cause for FF loss in these devices. We

find that, firstly the IA and then the LiF addition, successfully reduce the difference between the ideal "transport-free" FF and the FF measured in JV scans. However, this finding again highlights the need for improved charge transport layers for wide bandgap perovskite semiconductors.

5.4 Conclusions

In this work, we have unravelled the origin of performance limitations in methylammonium-free p-i-n wide bandgap perovskite solar cells. We have demonstrated that these solar cells are limited by significant non-radiative recombination in the bulk material which is exacerbated by the attachment of both electron and hole transport layers. We further show that there is a large energetic misalignment between the perovskite and the charge transport layers. To overcome these limitations, we incorporated the ionic additive 1-butyl-1-methylpiperidinium tetrafluoroborate into the perovskite precursor solution which is known to substantially enhance the stability of perovskite solar cells but its influence on device performance was unclear. We found that the incorporation of this additive reduces non-radiative recombination within the bulk of the perovskite, as well as at each interface with the charge transporting layers. This passivation effect results in substantially reduced surface recombination velocities at these interfaces. In addition, we showed that a thin LiF interlayer between the perovskite and the C60 further reduces the surface recombination velocity. We implement this knowledge to fabricate high performance 1.79 eV bandgap perovskite solar cells, which approach 17 % PCE with a V_{OC} of 1.22 V. This is among the highest reported for methylammonium-free wide bandgap perovskite solar cells. We then performed a thorough recombination analysis in the full devices. We found that the combination of the ionic additive and LiF interlayer significantly reduce the transport losses in full devices, likely due to the substantially lower SRVs present at the interfaces in these devices. In addition, the V_{OC} sits below the QFLS of the full devices, which we attribute to energetic misalignment between the perovskite and the charge transporting layers. To recover this lost

voltage, better alignment of transport layers is essential. Therefore, we suggest that new transport layers better suited for wide bandgap materials need to be implemented in addition to the IA treatment we report here. This is the subject of **Chapter 6**.

Contributions

R. D. J. Oliver and P. Caprioglio devised the project with input from A. J. Ramadan, M. Stolterfoht, D. Neher, and H. J. Snaith. R. D. J. Oliver, P. Caprioglio, F. Peña-Camargo, made the perovskite solar cells. R. D. J. Oliver made the samples for optical measurements. R. D. J. Oliver, P. Caprioglio performed the photoluminescence quantum yield measurements and analysis. L. R. V. Buizza performed the optical-pump terahertz-probe spectroscopy measurements and analysis. R. D. J. Oliver performed the TCSPC measurements with guidance from L. R. V. Buizza. F. Zu conducted the UPS measurements and analysis. A. J. Ramadan assisted with structural measurements, assisted with the manuscript and provided detailed supervision throughout. S. G. Motti performed the TCSPC data modelling. S. Mahesh performed the ellipsometry measurements and analysis. M. M. McCarthy helped with materials development. J. H. Warby assisted with PLQY measurements. A. J. Ramadan Y.-H. Lin, N. Koch, S. Albrecht, L. M. Herz, M. B. Johnston, D. Neher, M. Stolterfoht, H. J. Snaith all provided supervision to the project.

References

[1] Laboratory, N. R. E. Best Research-Cell Efficiency Chart (Accessed: 2021-09-20). URL `https://www.nrel.gov/pv/cell-efficiency.html`.

[2] Stranks, S. D. *et al.* Electron-hole diffusion lengths exceeding 1 micrometer in an organometal trihalide perovskite absorber. *Science* **342**, 341–344 (2013).

[3] Wehrenfennig, C., Liu, M., Snaith, H. J., Johnston, M. B. & Herz, L. M. Charge-carrier dynamics in vapour-deposited films of the organolead halide perovskite $CH_3NH_3PbI_{3-x}Cl_x$. *Energy & Environmental Science* **7**, 2269–2275 (2014).

[4] McMeekin, D. P. *et al.* A mixed-cation lead mixed-halide perovskite absorber for tandem solar cells. *Science* **351**, 151–155 (2016).

[5] Green, M. A., Ho-Baillie, A. & Snaith, H. J. The emergence of perovskite solar cells. *Nature Photonics* **8**, 506–514 (2014).

[6] Sadhanala, A. *et al.* Preparation of single-phase films of $CH_3NH_3Pb(I_{1-x}Br_x)_3$ with sharp optical band edges. *The Journal of Physical Chemistry Letters* **5**, 2501–2505 (2014).

[7] Eperon, G. E. *et al.* Formamidinium lead trihalide: a broadly tunable perovskite for efficient planar heterojunction solar cells. *Energy & Environmental Science* **7**, 982–988 (2014).

[8] Snaith, H. J. Present status and future prospects of perovskite photovoltaics. *Nature Materials* **17**, 372–376 (2018).

[9] Eperon, G. E. *et al.* Perovskite-perovskite tandem photovoltaics with optimized band gaps. *Science* **354**, 861–865 (2016).

[10] Lin, Y.-H. *et al.* A piperidinium salt stabilizes efficient metal-halide perovskite solar cells. *Science* **369**, 96–102 (2020).

[11] Mahesh, S. *et al.* Revealing the origin of voltage loss in mixed-halide perovskite solar cells. *Energy & Environmental Science* **13**, 258–267 (2020).

[12] Hörantner, M. T. & Snaith, H. J. Predicting and optimising the energy yield of perovskite-on-silicon tandem solar cells under real world conditions. *Energy & Environmental Science* **10**, 1983–1993 (2017).

[13] Hoke, E. T. *et al.* Reversible photo-induced trap formation in mixed-halide hybrid perovskites for photovoltaics. *Chemical Science* **6**, 613–617 (2015).

[14] Barker, A. J. *et al.* Defect-assisted photoinduced halide segregation in mixed-halide perovskite thin films. *ACS Energy Letters* **2**, 1416–1424 (2017).

[15] Knight, A. J. & Herz, L. M. Preventing phase segregation in mixed-halide perovskites: a perspective. *Energy & Environmental Science* **13**, 2024–2046 (2020).

[16] Knight, A. J. *et al.* Halide segregation in mixed-halide perovskites: influence of a-site cations. *ACS Energy Letters* **6**, 799–808 (2021).

[17] Unger, E. *et al.* Roadmap and roadblocks for the band gap tunability of metal halide perovskites. *Journal of Materials Chemistry A* **5**, 11401–11409 (2017).

[18] Slotcavage, D. J., Karunadasa, H. I. & McGehee, M. D. Light-induced phase segregation in halide-perovskite absorbers. *ACS Energy Letters* **1**, 1199–1205 (2016).

[19] Suchan, K., Merdasa, A., Rehermann, C., Unger, E. L. & Scheblykin, I. G. Complex evolution of photoluminescence during phase segregation of $MAPb(I_{1-x}Br_x)_3$ mixed halide perovskite. *Journal of Luminescence* **221**, 117073 (2020).

[20] Peña-Camargo, F. *et al.* Halide segregation versus interfacial recombination in bromide-rich wide-gap perovskite solar cells. *ACS Energy Letters* **5**, 2728–2736 (2020).

[21] Caprioglio, P. *et al.* Nano-emitting heterostructures violate optical reciprocity and enable efficient photoluminescence in halide-segregated methylammonium-free wide bandgap perovskites. *ACS Energy Letters* **6**, 419–428 (2021).

[22] Caprioglio, P. *et al.* On the relation between the open-circuit voltage and quasi-fermi level splitting in efficient perovskite solar cells. *Advanced Energy Materials* **9**, 1901631 (2019).

[23] Stolterfoht, M. *et al.* The impact of energy alignment and interfacial recombination on the internal and external open-circuit voltage of perovskite solar cells. *Energy & Environmental Science* **12**, 2778–2788 (2019).

[24] Conings, B. *et al.* Intrinsic thermal instability of methylammonium lead trihalide perovskite. *Advanced Energy Materials* **5**, 1500477 (2015).

[25] Habisreutinger, S. N., McMeekin, D. P., Snaith, H. J. & Nicholas, R. J. Research update: Strategies for improving the stability of perovskite solar cells. *APL Materials* **4**, 091503 (2016).

[26] Nenon, D. P. *et al.* Structural and chemical evolution of methylammonium lead halide perovskites during thermal processing from solution. *Energy & Environmental Science* **9**, 2072–2082 (2016).

[27] Bai, S. *et al.* Planar perovskite solar cells with long-term stability using ionic liquid additives. *Nature* **571**, 245–250 (2019).

[28] Jiang, Q. *et al.* Surface passivation of perovskite film for efficient solar cells. *Nature Photonics* **13**, 460–466 (2019).

[29] Oliver, R. D. *et al.* Thermally stable passivation toward high efficiency inverted perovskite solar cells. *ACS Energy Letters* **5**, 3336–3343 (2020).

[30] Bush, K. A. *et al.* Compositional engineering for efficient wide band gap perovskites with improved stability to photoinduced phase segregation. *ACS Energy Letters* **3**, 428–435 (2018).

[31] Leijtens, T. *et al.* Tin–lead halide perovskites with improved thermal and air stability for efficient all-perovskite tandem solar cells. *Sustainable Energy & Fuels* **2**, 2450–2459 (2018).

[32] Li, Z. *et al.* Wide-bandgap perovskite/gallium arsenide tandem solar cells. *Advanced Energy Materials* **10**, 1903085 (2020).

[33] Wang, Y. *et al.* Cross-linked hole transport layers for high-efficiency perovskite tandem solar cells. *Science China Chemistry* **64**, 2025–2034 (2021).

[34] Palmstrom, A. F. *et al.* Enabling flexible all-perovskite tandem solar cells. *Joule* **3**, 2193–2204 (2019).

[35] Oliver, R. D. *et al.* Understanding and suppressing non-radiative losses in methylammonium-free wide-bandgap perovskite solar cells. *Energy & Environmental Science* **15**, 714–726 (2022).

[36] Davies, C. L. *et al.* Bimolecular recombination in methylammonium lead triiodide perovskite is an inverse absorption process. *Nature Communications* **9**, 1–9 (2018).

[37] Rehman, W. *et al.* Charge-carrier dynamics and mobilities in formamidinium lead mixed-halide perovskites. *Advanced Materials* **27**, 7938–7944 (2015).

[38] Rehman, W. *et al.* Photovoltaic mixed-cation lead mixed-halide perovskites: links between crystallinity, photo-stability and electronic properties. *Energy & Environmental Science* **10**, 361–369 (2017).

[39] Crothers, T. W. *et al.* Photon reabsorption masks intrinsic bimolecular charge-carrier recombination in $CH_3NH_3PbI_3$ perovskite. *Nano letters* **17**, 5782–5789 (2017).

[40] Buizza, L. R. *et al.* Charge-carrier dynamics, mobilities, and diffusion lengths of 2d–3d hybrid butylammonium–cesium–formamidinium lead halide perovskites. *Advanced Functional Materials* **29**, 1902656 (2019).

[41] McMeekin, D. P. *et al.* Crystallization kinetics and morphology control of formamidinium–cesium mixed-cation lead mixed-halide perovskite via tunability of the colloidal precursor solution. *Advanced Materials* **29**, 1607039 (2017).

[42] Herz, L. M. Charge-carrier mobilities in metal halide perovskites: fundamental mechanisms and limits. *ACS Energy Letters* **2**, 1539–1548 (2017).

[43] Lim, J. *et al.* Elucidating the long-range charge carrier mobility in metal halide perovskite thin films. *Energy & Environmental Science* **12**, 169–176 (2019).

[44] Johnston, D. Stretched exponential relaxation arising from a continuous sum of exponential decays. *Physical Review B* **74**, 184430 (2006).

[45] Kirchartz, T., Márquez, J. A., Stolterfoht, M. & Unold, T. Photoluminescence-based characterization of halide perovskites for photovoltaics. *Advanced Energy Materials* **10**, 1904134 (2020).

[46] Motti, S. G. *et al.* Defect activity in lead halide perovskites. *Advanced Materials* **31**, 1901183 (2019).

[47] Ulatowski, A. M. *et al.* Charge-carrier trapping dynamics in bismuth-doped thin films of $MAPbBr_3$ perovskite. *The Journal of Physical Chemistry Letters* **11**, 3681–3688 (2020).

[48] Stolterfoht, M. *et al.* Visualization and suppression of interfacial recombination for high-efficiency large-area pin perovskite solar cells. *Nature Energy* **3**, 847–854 (2018).

[49] Motti, S. G. *et al.* Phase segregation in mixed-halide perovskites affects charge-carrier dynamics while preserving mobility. *Nature Communications* **12**, 1–9 (2021).

[50] Doherty, T. A. *et al.* Performance-limiting nanoscale trap clusters at grain junctions in halide perovskites. *Nature* **580**, 360–366 (2020).

[51] Schutt, K. *et al.* Overcoming zinc oxide interface instability with a methylammonium-free perovskite for high-performance solar cells. *Advanced Functional Materials* **29**, 1900466 (2019).

[52] Trimpl, M. J. *et al.* Charge-carrier trapping and radiative recombination in metal halide perovskite semiconductors. *Advanced Functional Materials* **30**, 2004312 (2020).

[53] Godding, J. S. *et al.* Oxidative passivation of metal halide perovskites. *Joule* **3**, 2716–2731 (2019).

[54] Ross, R. T. Some thermodynamics of photochemical systems. *The Journal of Chemical Physics* **46**, 4590–4593 (1967).

[55] Miller, O. D., Yablonovitch, E. & Kurtz, S. R. Strong internal and external luminescence as solar cells approach the shockley–queisser limit. *IEEE Journal of Photovoltaics* **2**, 303–311 (2012).

[56] Krogmeier, B., Staub, F., Grabowski, D., Rau, U. & Kirchartz, T. Quantitative analysis of the transient photoluminescence of $CH_3NH_3PbI_3/PC_{61}$ BM heterojunctions by numerical simulations. *Sustainable Energy & Fuels* **2**, 1027–1034 (2018).

[57] Seo, J. *et al.* Benefits of very thin PCBM and LiF layers for solution-processed p–i–n perovskite solar cells. *Energy & Environmental Science* **7**, 2642–2646 (2014).

[58] Al-Ashouri, A. *et al.* Monolithic perovskite/silicon tandem solar cell with $> 29\%$ efficiency by enhanced hole extraction. *Science* **370**, 1300–1309 (2020).

[59] Sproul, A. Dimensionless solution of the equation describing the effect of surface recombination on carrier decay in semiconductors. *Journal of Applied Physics* **76**, 2851–2854 (1994).

[60] Wang, J. *et al.* Reducing surface recombination velocities at the electrical contacts will improve perovskite photovoltaics. *ACS Energy Letters* **4**, 222–227 (2018).

[61] Jariwala, S. *et al.* Reducing surface recombination velocity of methylammonium-free mixed-cation mixed-halide perovskites via surface passivation. *Chemistry of Materials* **33**, 5035–5044 (2021).

[62] Wolff, C. M., Caprioglio, P., Stolterfoht, M. & Neher, D. Nonradiative recombination in perovskite solar cells: the role of interfaces. *Advanced Materials* **31**, 1902762 (2019).

[63] Snaith, H. J. *et al.* Anomalous hysteresis in perovskite solar cells. *The Journal of Physical Chemistry Letters* **5**, 1511–1515 (2014).

[64] Nayak, P. K., Mahesh, S., Snaith, H. J. & Cahen, D. Photovoltaic solar cell technologies: analysing the state of the art. *Nature Reviews Materials* **4**, 269–285 (2019).

[65] Thiesbrummel, J. *et al.* Universal current losses in perovskite solar cells due to mobile ions. *Advanced Energy Materials* **11**, 2101447 (2021).

[66] Burgelman, M., Nollet, P. & Degrave, S. Modelling polycrystalline semiconductor solar cells. *Thin Solid Films* **361**, 527–532 (2000).

[67] Stolterfoht, M. *et al.* How to quantify the efficiency potential of neat perovskite films: Perovskite semiconductors with an implied efficiency exceeding 28%. *Advanced Materials* **32**, 2000080 (2020).

[68] Caprioglio, P. *et al.* On the origin of the ideality factor in perovskite solar cells. *Advanced Energy Materials* **10**, 2000502 (2020).

[69] Onno, A., Chen, C. & Holman, Z. C. Electron and hole partial specific resistances: a framework to understand contacts to solar cells. In *2019 IEEE 46th Photovoltaic Specialists Conference (PVSC)*, 2329–2333 (IEEE, 2019).

[70] Onno, A., Chen, C., Koswatta, P., Boccard, M. & Holman, Z. C. Passivation, conductivity, and selectivity in solar cell contacts: Concepts and simulations based on a unified partial-resistances framework. *Journal of Applied Physics* **126**, 183103 (2019).

[71] Zu, F. *et al.* Surface state density determines the energy level alignment at hybrid perovskite/electron acceptors interfaces. *ACS Applied Materials & Interfaces* **9**, 41546–41552 (2017).

[72] Shin, D. *et al.* Mechanism and timescales of reversible p-doping of methylammonium lead triiodide by oxygen. *Advanced Materials* **33**, 2100211 (2021).

[73] Tao, S. *et al.* Absolute energy level positions in tin- and lead-based halide perovskites. *Nature Communications* **10**, 1–10 (2019).

Chapter 6

Optimised Hole Transport Layer Through Blended Polymers

6.1 Summary of results

The interfacial recombination between the wide bandgap ($\sim 1.8\,\mathrm{eV}$) metal halide perovskite and the hole transport layer has recently been discovered as a major bottleneck for solar cells based on these materials. This interface induces rapid nonradiative recombination pathways, and there is poor energetic alignment between the VB of the MHP semiconductor and HOMO of the HTL, which both constrain the V_{OC} of solar cells well below its thermodynamic potential.

In this Chapter, a novel hole transport layer strategy is developed based on blending the polymers PTAA and TFB. The influence of the blend ratio on photovoltaic device performance is investigated in detail, with a best performing blend being a 2:1 PTAA:TFB blend. The basic optoelectronic and structural properties of the MHP semiconductor grown on the different polymer blends were found to markedly similar. The optoelectronic properties of the polymer blends themselves were investigated through absorption, PL and time-resolved emission spectroscopy measurements. The absorption of the polymer blends can be described accurately as an appropriately weighted linear combination of the individual polymer absorption. In contrast, the

PL from the blends seems to entirely originate from the TFB. Actres measurements revealed that the HOMO-LUMO transition is accelerated upon increasing TFB addition. However, there is no consistent trend in these photophysical data that would suggest that the blended polymers ought to perform better when incorporated as the HTL in PV devices. Therefore, while providing large ($\sim 50\,\mathrm{mV}$) enhancements to the open-circuit voltage, the precise working mechanism(s) of the blended polymer system remain unclear. Current work to unravel the physics underpinning this system include ultraviolet photoemission spectroscopy, and synchrotron-based X-ray scattering studies to elucidate energetic and structural properties of the polymer blends respectively.

6.2 Introduction

So far in this thesis, the necessity for multijunction solar cells was outlined in **Chapters 1 & 2**. We have discussed in detail why MHP semiconductors have immense potential in this area, and provided a thorough review of the literature pertaining to MA-free wide bandgap perovskites in **Section 2.3.1**. From the literature and my own work, it was clear that these wide bandgap materials perform poorly compared to their lower bandgap (~ 1.6 eV) metal halide perovskites. In **Chapter 5**, we explored the recombination processes occurring within this material class in detail, and unravelled their major loss pathways.

We discovered that the interface between the perovskite and the hole transport layer (HTL) was particularly detrimental to the device performance due to severe interfacial recombination. Moreover, we discovered that, within the very same device, a substantial mismatch between the achieved open-circuit voltage (V_{OC}), and the calculated quasi-Fermi level splitting (QFLS) from photoluminescence quantum yield (PLQY) measurements. The QFLS originates from the MHP semiconductor itself and indicates the realistic upper bound for the device V_{OC} [1]. This mismatch is often attributed to an energetic misalignment at the interface(s) between the perovskite and the adjacent charge transport layers (CTLs) [2]. Therefore, it is clear that a new charge transport

layer strategy for this p-i-n wide bandgap perovskite solar cells is required, and simply utilising the structure optimised for $\sim$ 1.6 eV perovskites is a major bottleneck that must be overcome [3]. Therefore, the development of new strategies for the CTLs within wide bandgap MHPs is a priority.

In fact, optimisation of the HTL has resulted in significant enhancements to the efficiency of both 'medium' [4] and wide bandgap perovskites [5], as well as tandem solar cells [4, 5]. The works highlighted here are perhaps the ones that 'kickstarted' the self-assembled monolayer (SAM) excitement in the field since they have enabled high V_{OC}s and exceptional FF values (routinely $> 80\,\%$). Both of these factors can be understood in the context of **Chapter 5**. Devices based on these SAMs regularly deliver devices with efficiencies exceeding 20 % [4–6], or similarly impressive values for the wider bandgap perovskites [7, 8].

There are, however, some issues for perovskite solar cells (PSCs) based on these SAMs. Firstly, the SAMs-based devices are often hailed as highly reproducible [4], but anyone who has worked with these materials knows that is far from the case. While within a substrate, devices will have very similar performance, the whole batch can, and often will, fail for an unknowable reason. Therefore, despite their impressive performance in solar cells, there is a strong question mark over their suitability for industrial activities. Furthermore, owing to their functionality relying on their binding to the ITO, they are not suitable for every application (e.g. in a tandem application where a different interlayer might be used).

The use of semiconducting polymers overcome these issues. They are readily processed from solution and would be more than suitable for large-scale industrial processing through, for example, printing techniques [9–11]. Herein, we report the development of a new strategy for the hole transport layer suitable for high efficiency wide bandgap perovskite photovoltaics wherein two commercially available polymers are blended. The blending of these polymers is a straightforward way to optimise the PV device performance of this family of MHP semiconductors, yielding significant enhancements to the open-circuit voltage and power conversion efficiency.

6.3 Results and discussion

In the first instance, we sought to investigate a range of different hole transport layers to assess their suitability for implementation in conjunction with the wide bandgap perovskite $FA_{0.83}Cs_{0.17}Pb(I_{0.6}Br_{0.4})_3$, which was the focus of **Chapter 5**. The first step taken was to assess the quality of the interface between the different hole transport layers and the perovskite semiconductor. Processing on a new HTL can have a large influence on the resulting perovskite solar cell [12]. There are many reasons for this, but a major factor is that it is not guaranteed that the perovskite will form in the same manner, and so it is possible that additional non-radiative recombination pathways could have been induced. Therefore, we used photoluminescence quantum yield (PLQY) measurements to benchmark the radiative efficiency of the different HTL/metal halide perovskite systems investigated, and show the results in **Figure 6.1**.

The systems investigated were perovskite processed directly on ITO (the worst case scenario), PTAA/PFN-Br, TFB/PFN-Br, V1148 (a novel hole transporting layer synthesised by the group of Tadas Malinauskas at Kaunas University of Technology), V1148/PFN-Br and F8BT/PFN-Br substrates. We attempted to coat the perovskite on each hole transport layer without a PFN-Br layer, however severe wetting issues resulted in extremely poor coverage. These conditions were discarded as they were unsuitable for device applications. Therefore, a wetting layer of PFN-Br on top of these systems (with the exception of V1148) was necessary. The highest occupied molecular orbital (HOMO) postion, predominantly informed from literature values, is shifted further from vacuum as one progresses through the list. Explicitly, the HOMO positions (or work function for ITO) are approximately $\sim -4.4\,\text{eV}$ for ITO (UPS measurements) [15], $\sim -5.2\,\text{eV}$ for PTAA (UPS measurements) [16], $\sim -5.5\,\text{eV}$ for TFB [17] (UPS measurements), V1148's HOMO was measured to be $\sim -5.4\,\text{eV}$ at KTU using cyclic voltammetry, and $\sim -5.9\,\text{eV}$ F8BT (UPS measurement) [18]. Several caveats are required for these values. Firstly, not all values were measured using the same technique and cyclic voltammetry is known to significantly underestimate the bandgap compared to the 'true' value determined from photoelectron spectroscopy in small molecule semi-

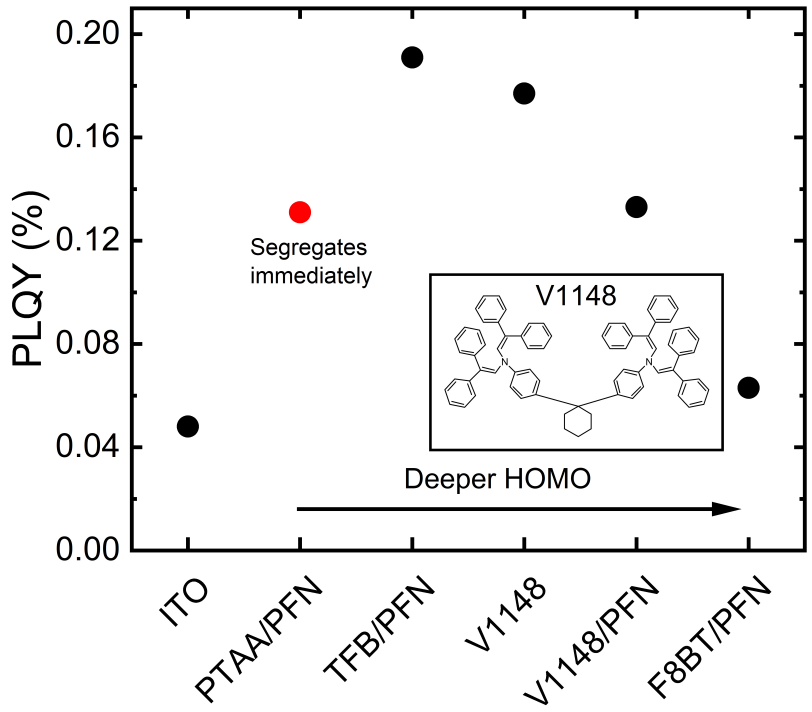


Figure 6.1: *Photoluminescence quantum yield (PLQY) measurements of a wide bandgap perovskite ($FA_{0.83}Cs_{0.17}Pb(I_{0.6}Br_{0.4})_3$) processed on a range of hole conductors. The HOMO positions, informed from literature values, are shifted away from vacuum from left to right on the plot. The samples were photoexcited with a continuous wave 405 nm centre wavelength laser at an intensity of $\sim 60\,\mathrm{mWcm^{-2}}$, which is the equivalent above-bandgap photon flux from AM1.5 illumination. Therefore the same number of electron-hole pairs ought to be formed from this illumination. The point corresponding to PTAA/PFN-Br is marked in red as the photoluminescence showed evidence of halide segregation, which gives an increased radiative efficiency which would not result in enhanced open-circuit voltage (V_{OC})[13, 14]. V1148, molecule structure shown in the inset, is a novel hole conductor synthesised at the Kaunas University of Technology in the group of Tadas Malinauskas.*

conductors [19]. As such, comparison between HOMO positions determined through UPS measurements on polymeric semiconductors and cyclic voltammetry on a small molecule semiconductor should be done cautiously. Moreover, the values determined for the polymer semiconductors should be treated as a guide only since the exact values vary substantially across the literature (though it is apparent that many cited values disagree with the HOMO position that was actually reported in the referenced paper). Therefore, I am using these HOMO positions as a guide only. Notwithstanding the uncertainty in the absolute values, an interesting trend with HOMO position is observed, as can be seen in **Figure 6.1**.

At first the PLQY is quite low which is expected when processing directly on ITO [2]. The PLQY increases towards a maximum for intermediate HOMO positions, before falling again for deeper HOMOs. The point corresponding to PTAA/PFN-Br is marked in red as the photoluminescence showed evidence of halide segregation, which gives an increased radiative efficiency which would not result in enhanced open-circuit voltage (V_{OC}) [13, 14, 20]. Despite this artificially enhanced radiative efficiency of the perovskite in contact with PTAA, the perovskite coated on TFB is able to achieve a higher PLQY, which ought to lead to enhanced V_{OC}s in full photovoltaic devices [1, 21, 22]. We note that there may be additional co-factors that influence the radiative efficiency of the samples presented in **Figure 6.1**, (e.g. interface quality), and the HOMO position may not be the dominant factor determining the PLQY of these samples. Nevertheless, the observation that utilising TFB (a molecule with a slightly deeper HOMO level compared to PTAA) as the HTL leads to a higher PLQY is encouraging for photovoltaic device applications.

In the following, we choose to investigate poly(9,9-dioctylfluorene-alt-N-(4-sec-butylphenyl)-diphenylamine) (TFB). The rationale being that it possesses a deeper HOMO compared to PTAA, but is still a commercially available polymer and so might be a suitable direct replacement. Furthermore, TFB is reported to have high hole mobility of $\sim 5 \times 10^{-3}\,\mathrm{cm^2V^{-1}s^{-1}}$ [23], comparable to values reported for PTAA [24]. In addition, it was hoped that the deeper HOMO would deliver better energetic alignment with the valence band (VB) of the perovskite [3, 25], and so reduce the QFLS-V_{OC} mismatch identified in **Chapter 5**.

Despite this enhancement to the absolute photoluminescence, TFB as a direct replacement performed poorly compared to PTAA. The devices fabricated with TFB as the hole transport layer were characterised by a deterioration in all of the key device parameters, especially the short-circuit current density (J_{SC}) and fill factor (FF) as can be seen in **Figure 6.2a**. This was the case independent of TFB solution concentration, or the solvent from which this layer was processed, I show chlorobenzene and toluene in the figure as examples. This suggests that, despite forming an interface with fewer

non-radiative recombination losses as judged by PLQY measurements, the TFB layer was performing poorly at extracting holes from the device. This is perhaps surprising given that TFB ought to have similar hole conductivity as PTAA. The thickness of the TFB layer was investigated and had only a minor effect on the device performance. Given these observations, I suggest that the HOMO level of TFB in fact lies deeper than the valence band maximum of the perovskite, and so forms an energetic barrier to hole extraction. This suggestion is investigated in more detail later in the chapter.

Following this work, I decided to investigate the possibility of using TFB as an interfacial modification layer on top of PTAA. I investigated this strategy because of the more ideal interface TFB forms with the perovskite, but its implementation as a direct replacement HTL was unsuccessful. Therefore, I was seeking the enhanced interface quality from the TFB, while keeping the charge transport properties of the PTAA. In fact, such a 'stacked' HTL strategy has been reported in the adjacent field of halide perovskite light emitting diodes [26]. This strategy requires 'orthogonal' solvents to avoid dissolving the underlying layer(s) when processing the next. In an attempt to achieve this, p-xylene was utilised as the solvent for TFB since TFB was found to dissolve well in this solvent, whereas PTAA was more sparingly soluble.

The stabilised open-circuit voltages from such a strategy a presented in **Figure 6.2b**. This strategy is benchmarked against the case of just PTAA with a standard perovskite (control), and against PTAA with an 1-butyl-1-methylpiperidinium tetrafluoroborate ($[BMP]^+[BF_4]^-$)-modified perovskite as reported in detail in **Chapter 5**. As can be seen in **Figure 6.2b**, the enhancement to the open-circuit voltages achievable with this bilayer HTL outstrips those provided by the ionic additive-modification presented previously. This is strong evidence that the one of the major findings of the previous Chapter, the HTL interface limiting devices based on this material, was accurate and that enhancing this interface alone can result in outstanding enhancements to the V_{OC}. Indeed, the enhancement of $\sim$ 60 mV from this bilayer strategy would imply a 10-fold enhanced radiative efficiency of compared to the control case. There are unfortunate drawbacks to this strategy however. Firstly, the J_{SC} of these bilayer

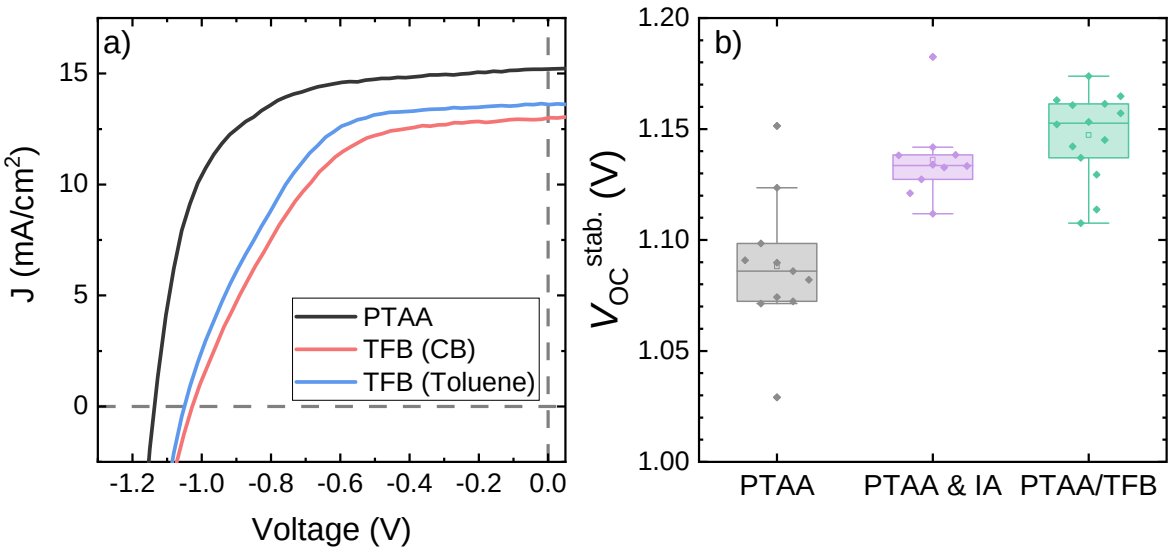


Figure 6.2: *a) Comparison of representative JV curves comparing devices with PTAA as the hole transport layer and TFB as the direct replacement for PTAA. The TFB was processed from CB (red) and toluene (blue). TFB performs poorly as a direct replacement for PTAA, with a reduction in all key device parameters. b) Comparison of the stabilised open-circuit voltage (V_{OC}) for control (PTAA), $[BMP]^+[BF_4]^-$-passivated (as in* ***Chapter 5****) and devices with a bilayer PTAA/TFB HTL. The bilayer HTL strategy provides a greater enhancement to the stabilised V_{OC} than the passivation strategy, demonstrating the importance of enhancing the quality of this interface.*

devices is still rather modest, highlighting that hole-extraction might still be an issue. Secondly, while I found that p-xylene is a poor solvent for PTAA, it is not completely insoluble. Therefore, I found that this device structure was quite unreliable, with swathes of devices failing for an unknowable reason. I believe this is not an issue for bilayer hole injection layers in LED devices since the transport layers in these devices are typically substantially thicker [26, 27], and so partial dissolution of the underlying layer is not detrimental. This was one of the limitations of the SAM-based transport layer that I was aiming to overcome. Therefore, I decided to rethink the strategy used in this work.

Instead of the bilayer strategy, I decided to investigate blending the polymers. In all of the blends, equal concentrations of TFB and PTAA (typically 2 mg mL^{-1}) were prepared in different vials, and then the solutions were mixed by volume – e.g. the 2:1 PTAA:TFB blend is prepared by mixing 200 μL of PTAA solution with 100 μL of TFB solution. By using this strategy, I had hoped to form an 'effective' HTL, whereby I could tune the energetics by simply altering the ratio of one polymer to the other

in the blend. In this way I could develop a strategy which required only the most straightforward optimisation to be tailored to different perovskite compositions. For the majority of this work, I continue the focus on $FA_{0.83}Cs_{0.17}Pb(I_{0.6}Br_{0.4})_3$, which has a bandgap of ~ 1.8 eV. Over the course of this work, an in-depth device optimisation process was undertaken. I investigated many factors which may influence device performance and/or the physics of the blended polymer (citations indicate related studies where these factors were investgiated), including the hole transport layer thickness [28–30], blend ratio, the solvent from which the polymer was cast [31, 32], and doping the HTL [33, 34]. In addition, I also investigated the possibility of including a layer of PEDOT:PSS (poly(3,4-ethylenedioxythiophene):polystyrene sulfonate) beneath the blend as this strategy has shown great benefit in LED materials [26]. Herein, I do not discuss the device optimisation process in detail. Instead, I present a comparison of representative *JV* curves of the control and 'starting point' blended polymers, alongside the final, optimised condition in **Figure 6.3**. The optimised blend enhances all key device parameters and reduces the hysteresis significantly. I note the reverse scan for the 'early blend' exhibits unusual behaviour with the current density being higher near the maximum power point than at short-circuit conditions. This peculiar behaviour is eliminated with a fully optimised HTL, and so was not investigated further.

In the optimised condition, the polymer blend is cast from chlorobenzene, with 2:1 PTAA:TFB. The device performance is further enhanced by doping the polymer blend with 1 wt% F6-TCNNQ (1,3,4,5,7,8-hexafluorotetracyanonaphthoquinodimethane) which most likely increases the conductivity and selectivity of the HTL. Following this optimisation, I sought to understand why this particular blend was was optimal in PV devices. In the following, I discuss the physics of the blended polymers themselves, and blended polymer/metal halide perovskite heterostructures that results in such enhancements in the PV device performance. Unless otherwise stated, all polymers (including PTAA and TFB) will have been doped with 1 wt% F6-TCNNQ.

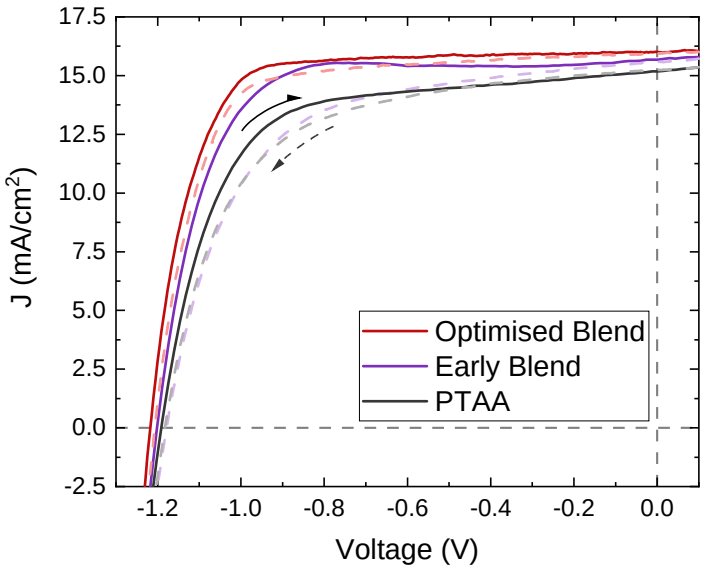


Figure 6.3: *JV curves for representative control (PTAA as the hole transport layer, grey), the initial polymer blend (purple) and the final, fully optimised polymer blend (red) as the HTL. Reverse (solid line) and forward (dashed line) are shown for each condition. The optimised blend enhances all key device parameters and reduces the hysteresis significantly. I note the reverse scan for the 'early blend' exhibits unusual behaviour with the current density being higher near the maximum power point than at short-circuit conditions. This peculiar behaviour is eliminated with a fully optimised HTL however.*

6.3.1 Photovoltaic device performance

Having optimised the processing conditions for the polymer-blend based photovoltaic devices, I investigated the effect of the blending ratio on the photovoltaic device performance. This was done to assess why certain polymer blends perform better in photovoltaic devices by understanding the way(s) the blend composition affects the device physics. As such, a range of devices with different polymer hole transport layers were fabricated. The device architecture was ITO coated glass / polymers / $FA_{0.83}Cs_{0.17}Pb(I_{0.6}Br_{0.4})_3$ / $PC_{61}BM$ / BCP / Cr / Au. The polymers investigated were pure PTAA and TFB, and 3:1, 2:1, 1:1, and 1:2 PTAA:TFB blends. Each of these polymers was at a concentration of 2.0 mg mL^{-1} and is processed from chlorobenzene. As stated earlier, each polymer was doped with 1 wt% F6-TCNNQ. In **Figure 6.4**, a statistical summary of the key device characteristics is presented. It is evident that the blended polymers significantly outperform either of the pure polymers in all device parameters, apart from the short-circuit current density. The J_{SC} is slightly enhanced

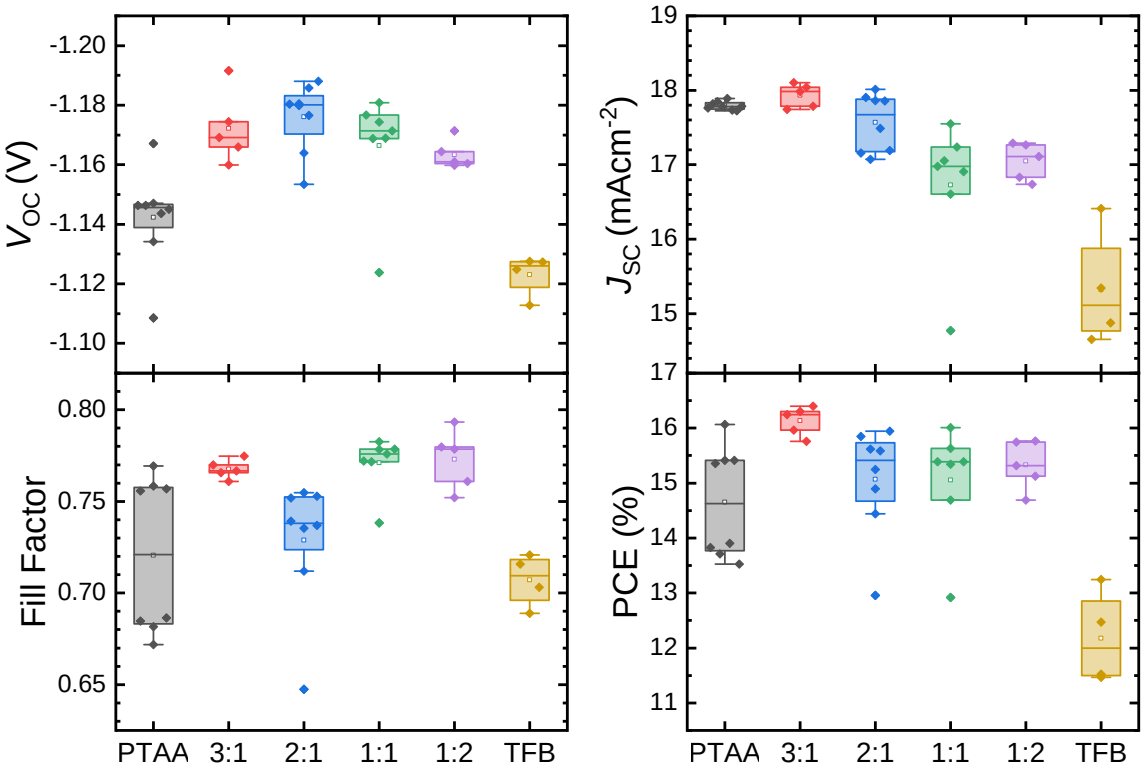


Figure 6.4: *The photovoltaic device parameters are presented for devices based on $FA_{0.83}Cs_{0.17}Pb(I_{0.6}Br_{0.4})_3$ processed on different polymer hole transport layers. The polymer blends deliver a substantial enhancement to the open-circuit voltage, however there is a penalty to the short-circuit current density for more TFB-rich blends. An enhancement to the fill factor is also observed for blended polymers. I note the exception for the 2:1 blend, but this was most likely caused by extrinsic factors (I had to pause fabrication during this batch due to my disability), and other batches show an enhanced fill factor for the 2:1 blend. These factors combine to deliver an enhanced PCE for devices based on the polymer blends. The data points are overlapped onto the boxplots which show the median (central line), the mean (white square), the median of the upper and lower halves of the data (top and bottom lines of the box respectively). The top and bottom whiskers are drawn to the highest/lowest datapoint within 1.5 times the interquartile range from the top and bottom of the box respectively.*

for the modest blend ratios before falling rapidly for the materials with greater TFB content. There is a clear trend in the open-circuit voltage as more TFB is included in the blend until a maximum for the 2:1 blend ratio. Following this maximum, the V_{OC} falls again. If we benchmark these results against the devices in **Chapter 5**, we see that from adapting the HTL alone, we can exceed the power conversion efficiency obtained from $[BMP]^+[BF_4]^-$ incorporation, which reached a PCE of $\sim$ 15.5%. In addition, it is worth noting that the device active area used in this Chapter is over four times larger than in **Chapter 5** (0.25 cm^2 Vs 0.06 cm^2). This highlights just how critical

this interface is for these methylammonium-free wide bandgap perovskite solar cells. Moreover, we had identified a $\sim 50\,\mathrm{mV}$ offset between the QFLS and the V_{OC} achieved on the very same device. Informed by our ultraviolet photoemission sprectroscopy measurements (**Figure 5.13**), we suggested that this mismatch might be due to poor energetic alignment between the charge transport layers and the perovskite semiconductor. Interesting, the enhancement to the open-circuit voltage observed from the polymer blend strategy is of a very similar magnitude to the QFLS-V_{OC} offset in the PTAA-based devices.

To compare the maximum attainable PV device performance, the solar-to-electrical power conversion efficiencies derived from maximum power point tracking (MPPT) for 30 s under continuous AM1.5 illumination for devices utilising PTAA (grey), and the polymer blend (purple and blue) as the hole transport layer are presented in **Figure 6.5a**. The polymer blend devices significantly outperform the device utilising PTAA as the hole transport layer. The champion polymer blend solar cell (blue trace) performs outstandingly, though I note it is an outlier. For this reason I include a more 'standard' high performance polymer blend (purple trace) to allow for a fairer comparison. Nevertheless, whilst the outright champion is an outlier, I believe it is still valuable to consider as it demonstrates the upper bound potential of this strategy. The inset in **Figure 6.5a** shows the efficiency of the champion polymer blend device tracked over 30 minutes of continuous AM1.5 illumination. The device achieves an outstanding PCE (from MPPT) of 17.5 % after 30 minutes, demonstrating the stability of its impressive efficiency.

With blended-polymer systems, there is the possibility of spontaneous de-mixing of the polymers [35, 36]. If this were to happen, we might expect that the device performance of the polymer-blend based device might deteriorate over time. However, after storage in an N_2 filled glovebox for over 6 months, we instead observed an slight enhancement to the photovoltaic device performance was observed which can be seen in **Figure 6.5b**. This enhancement is observed predominantly in the FF of these devices, which is quite common in the field [37] as briefly discussed in **Chapter 4**. It

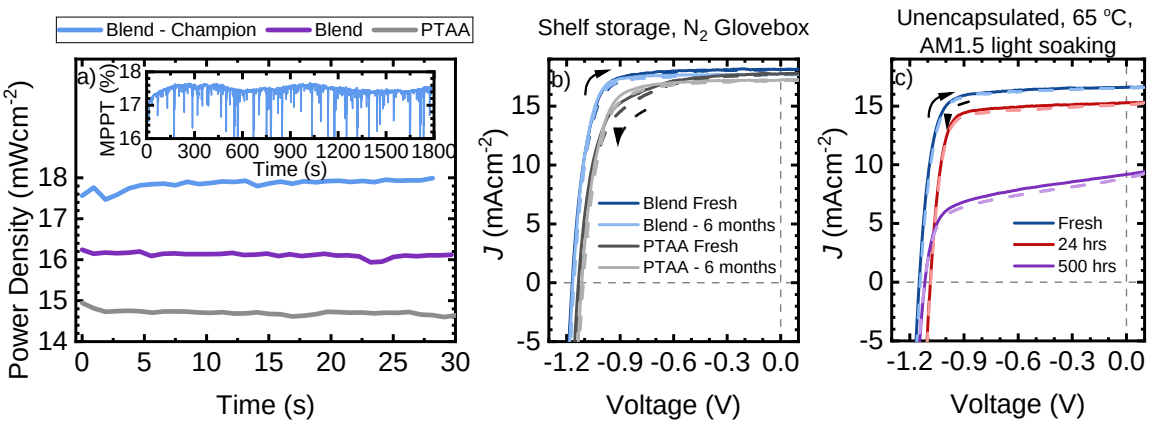


Figure 6.5: *a) Power conversion efficiencies derived from maximum power point tracking (MPPT) for* 30 s *under continuous AM1.5 illumination for wide bandgap perovskite solar cells utilising PTAA (grey), and the polymer blend (purple and blue) as the hole transport layer. The blue trace is the champion efficiency delivered by the polymer blend, but is significantly higher than the average, therefore the purple curve is included as a 'fairer' comparison between PTAA and the polymer blends. Inset: MPPT efficiency for the same champion polymer blend device over 30 minutes. The drops in the performance are a 'quirk' of the tracking algorithm and not an intrinsic property of the solar cell. b) Comparison of forward (dashed lines) and reverse (solid lines) JV curves for freshly made devices (dark curves) and the same devices stored for 6 months in a nitrogen filled glovebox (light curves) for PTAA-based (grey) and polymer blend-based (blue) devices. c) Comparison of forward (dashed lines) and reverse (solid lines) JV curves for polymer blend-based device that is freshly made device (blue), aged for 24 hours (red) and 500 hours (purple) unencapsulated in an open-circuit condition at* 65 °C *and under continuous AM1.5 illumination.*

is very promising for the long term applicability of utilising the polymer blend strategy for enhancing the performance of these wide bandgap perovskite photovoltaic devices.

To test further the suitability of the polymer blend devices for long-term operation, devices incorporating the polymer blend as the hole transport layer were subjected to harsh accelerated ageing. Explicitly, the devices were stressed at open-circuit at 65 °C under full spectrum AM1.5 simulated sunlight with no encapsulation. The forward and backward *JV* scans for a device aged for 0, 24 and 500 hours under these harsh conditions are presented in **Figure 6.5c**. The deterioration observed in the PV device performance is dominated by a reduction in the short-circuit current density, most likely driven by a physical loss of perovskite material within the device. Remarkably, the open-circuit voltage is mostly maintained for these unpassivated wide bandgap perovskite devices. This demonstrates that there has not been a significant

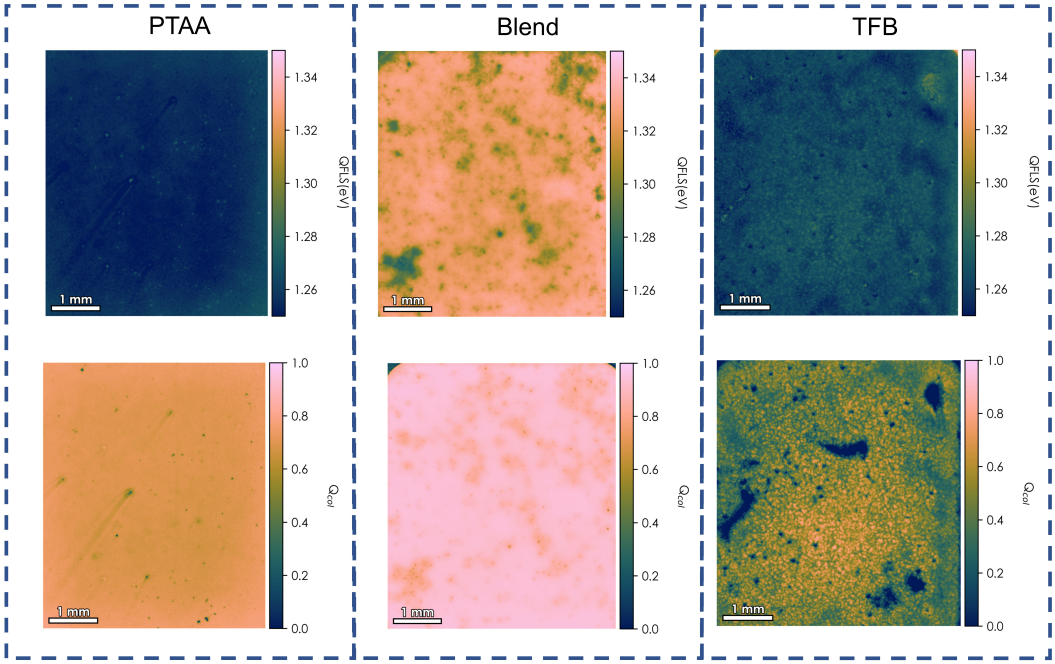


Figure 6.6: *Spatial distribution of the QFLS (top row) across an entire device active area (0.25 cm^2) for devices employing PTAA (left), polymer blend (centre) and TFB as the hole transport layer. These maps were derived from photoluminescence imaging of devices at open-circuit. Charge-collection quality (Q_{col}, bottow row) of the same devices. Q_{col} is defined in our recent study [40], and is a measure of the difference in the luminescence between open- and short-circuit. The scale bar is* 1 mm. *These measurements were performed by Akash Dasgupta.*

enhancement to the severity of the non-radiative recombination present within this device. The stability observed within these polymer blend based devices outstrips the state of the art in a similar ageing condition (polyTPD was used as the HTL in this study) [38]. Furthermore, there was no substantial increase to the hysteresis present within these devices, unlike similar studies [38, 39]. Therefore, I believe there should be no concerns regarding the suitability of the polymer blend for implementation in real-world applications.

To further assess the influence of heterogeneity within these devices, photoluminescence imagining was performed across entire device areas ($\sim$ 0.25 cm^2). These measurements were performed on devices comprising PTAA, the optimised polymer blend or TFB as the HTL. An estimate for the quasi-Fermi level splitting (QFLS) can be obtained from the raw PL data and is shown in the top row of **Figure 6.6**. The assumptions made to arrive at this estimate are discussed in more detail in our recent

publication [40]. Notwithstanding the uncertainty present within the absolute values, the relative differences between the samples can be readily compared. As can be seen in **Figure 6.6**, the device incorporating the polymer blend as the HTL is clearly much brighter than either the PTAA- or TFB-based devices. This is to be expected given the trend in the open-circuit voltage evident in **Figure 6.4**. Interestingly, we observe a far greater degree of inhomogeneity in the device based on the polymer blend. However, even the most poorly performing areas of the polymer blend outstrip the highest performing regions in the PTAA and are comparable to the best regions of the TFB-based device. This provides an exciting additional avenue for further enhancements to devices based on the polymer blends. If the uniformity can be enhanced to the value that most of the device achieves, an additional boost to the device open-circuit voltage is to be expected.

Additionally, we calculate the 'charge collection quality', Q_{col} which is derived in detail in Ref. [40]. The essence of Q_{col} is in quantifying the difference between the intensity of the PL at open- ($\mathrm{PL}^{\mathrm{OC}}$) and short-circuit ($\mathrm{PL}^{\mathrm{SC}}$) conditions. In this work, we use the definition

$$Q_{\mathrm{col}} \approx 1 - \frac{\mathrm{PL}^{\mathrm{SC}}}{\mathrm{PL}^{\mathrm{OC}}}, \tag{6.1}$$

where the ideality factor is modelled to be unity for simplicity. At short-circuit, all charges ought to be extracted, and therefore $\mathrm{PL}^{\mathrm{SC}} = 0$, which would give a charge-collection quality of unity. In such a scenario, any charges generated at open-circuit are being efficiently extracted from the cell, yielding a collection quality of 1. However, there is one important, and rarely discussed, caveat to **Equation 6.1**. Implicitly, it assumes that the PLQY is unchanged under different external biases, which is unlikely to be fully justified. For example, it is not uncommon to find metal halide perovskite solar cells delivering higher PL intensity at short-circuit, despite substantial current being extracted to the external load. This would imply that the remaining charge-carriers in the device are recombining more efficiently at short-circuit than open-circuit (i.e. $\mathrm{PLQY}^{\mathrm{SC}} > \mathrm{PLQY}^{\mathrm{OC}}$), and so despite fewer carriers being present at J_{SC}, a greater

fraction are recombining radiatively which originates the greater PL intensity. This is a surprising finding and requires further investigation, but is beyond the scope of the current chapter.

Nevertheless, the maps of Q_{col} yield insights into the devices studied here. Most strikingly, the Q_{col} map of the TFB-based sample (bottom right **Figure 6.6**) is extremely more heterogeneous than its corresponding QFLS map. Overall it is much 'dimmer', indicating lower Q_{col}, than the PTAA- or polymer blend-based devices. Moreover, only the TFB-based device possesses 'dead spots' where $Q_{\mathrm{col}} \approx 0$ on the mm length scale. In such regions, the PL is unchanged at open- and short-circuit which is indicative of extremely poor charge-extraction from the solar cell. This agrees with the poor J_{SC} observed for the TFB devices presented in **Figure 6.2 & 6.4**. Moreover, this is strong evidence for my earlier suggestion that TFB-only devices were constrained by their ability to extract holes from the device. I suggest that this is most likely to be induced by improper energetic alignment of its HOMO with the perovskite valence band.

In the following, I investigate why the different blend ratios perform differently.

6.3.2 Polymer blend / metal halide perovskite heterostructures

I investigated to what extent changing the underlying polymer influenced the properties of the metal halide perovskite (MHP) semiconductor deposited on top. The absorption coefficient of the perovskite for each condition was measured and are shown as pale curves in **Figure 6.7a**. There are negligible changes to the value of the absorption coefficient for each condition investigated. In line with this, the X-ray diffraction patterns for MHP semiconductors grown on these different polymers are similar, as can be seen in **Figure 6.7b**. The similarity of the XRD patterns is strong evidence that blending the polymers is not having a significant effect on the underlying crystallinity of the MHP semiconductor. Moreover, since the absorption coefficients of each of the conditions investigated shows the same character (i.e. steepness and onset position),

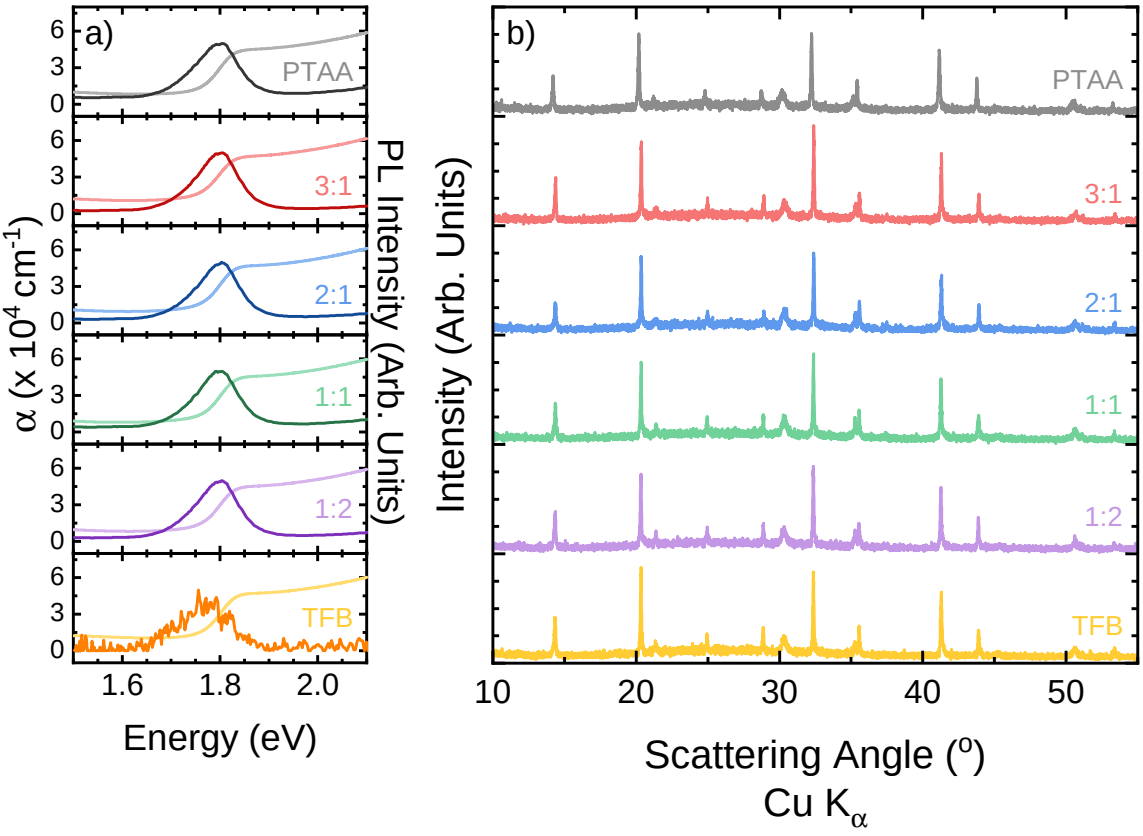


Figure 6.7: *a) Absorption coefficient, α, (pale curves) and steady state photoluminescence (bold curves) of $FA_{0.83}Cs_{0.17}Pb(I_{0.6}Br_{0.4})_3$ processed on each polymer hole transport layer investigated in detail on this chapter. No significant changes to the absorption coefficient or the steady state photoluminescence was observed (expect the PL for TFB, but this is likely an experimental error and should be retested). b) X-ray diffraction (XRD) patterns of the perovskite semiconductors processed on the polymer HTLs. No significant changes to the perovskite crystallinity were observed. The X-ray source was Cu Kα, $\lambda = 0.154$ nm.*

we can be confident that there is a negligible influence on the energetic disorder at the bandedge of the perovskite semiconductor. The photoluminescence spectra for these perovskite thin films was also measured, and is presented in **Figure 6.7a**. No changes to the PL peak position or peak shape was observed for the perovskite on different polymers. I note that the PL peak for TFB is noisier due to lower intensity, but this is due to an experimental error and should be retested.

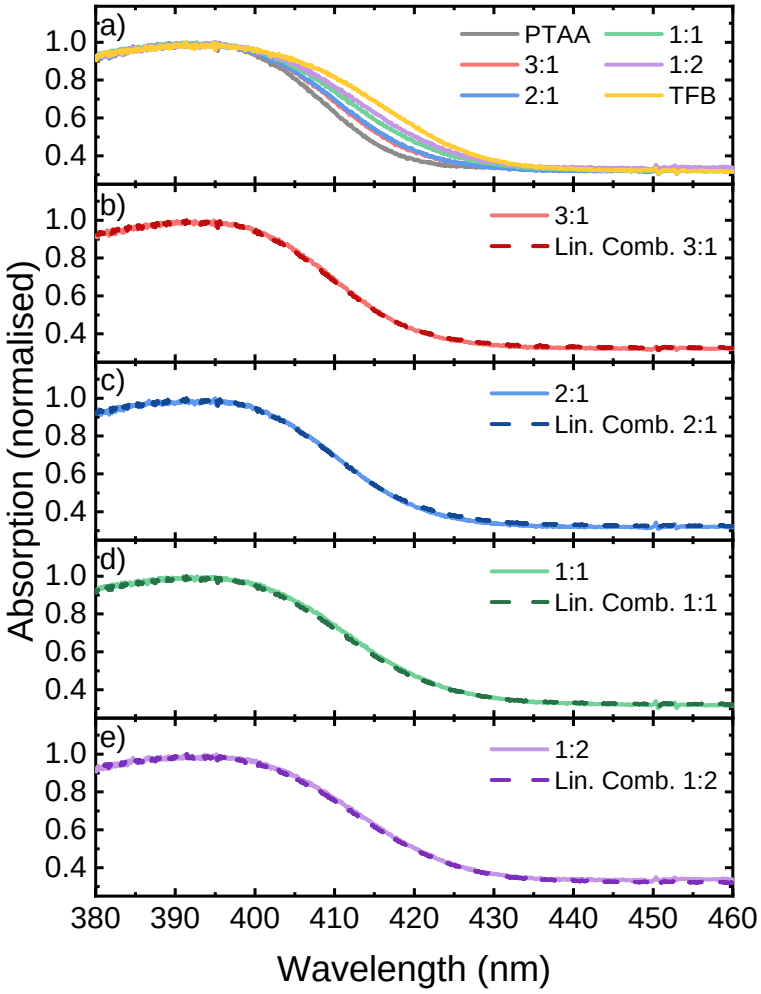


Figure 6.8: *a) Normalised absorption of the PTAA (grey), TFB (yellow) and 3:1 (red), 2:1 (blue), 1:1 (green) and 1:2 (purple) PTAA:TFB blends. As the blend is tuned from PTAA to TFB, the absorption onset is red-shifted. b)-e) Comparison between the measured absorption (solid lines) and a 'linear combination' (dark, dashed lines) of the PTAA and TFB absorption for 3:1, 2:1, 1:1. and 1:2 blend ratios respectively. Explicitly, the linear combination means, in the 3:1 case, the dashed line was calculated as ((3×PTAA absorption) + TFB absorption)/4.*

6.3.3 Physics of the blended polymer system

Since this is a novel hole conducting strategy, I sought to investigate the physics of the blended polymer system itself. I investigated the photophysical properties of the individual polymers. All systems investigated in this section are undoped. By uncovering the physics of the polymer blends, I seek insights into why this strategy reveals such enhancements to the photovoltaic device performance, as is seen in **Figure 6.3**. As before, I investigate the system as a function of the blend ratio, to see how the differing compositions affect the physics within the layer itself. From these insights, I hope to

understand why certain blend ratios significantly outperform others when incorporated as the HTL in full photovoltaic devices.

In **Figure 6.8**, the normalised absorption for PTAA (grey), TFB (yellow) and 3:1 (red), 2:1 (blue), 1:1 (green) and 1:2 (purple) PTAA:TFB blends are shown. As the blend is tuned from PTAA to TFB, the absorption onset is red-shifted, which is to be expected since TFB has a narrower bandgap than PTAA [16, 17]. To investigate whether the absorption of the blended polymers could be described in terms of its constituent polymers, I compared the measured absorption against a 'linear combination' of the constituent polymers' absorption. Explicitly, taking the 3:1 blend as an example, the linear combination is described as

$$\frac{(3 \times \text{PTAA absorption}) + \text{TFB absorption}}{4}.$$

As is evident from the overlap between the solid and dashed line in **Figures 6.8b-e**, the absorption predicted from the linear of PTAA and TFB absorption closely matches that measured on the polymer blends themselves for all blending ratios investigated. This is strong evidence that, firstly, the ratio of the polymers in solution is being realised in the final thin film. Secondly, it shows that, in the absorption, the polymer blend is behaving as a super position of the individual polymers themselves. This is evidence that no new electronic states are being formed in the blends which can then contribute to the absorption. However, to fully quantify this, significantly more sensitive absorption measurements should be performed, perhaps using photothermal deflection spectroscopy. This would enable the identification of potential new features many orders of magnitude weaker than were detectable here. Since the spot size for the absorption measurements is quite large ($\sim$ mm scale), it cannot distinguish between a closely blended polymer thin film, and one with large 'domains' of one or the other polymer. Therefore, it is important to quantify the intermixing of the blend using morphological measurements.

As can be seen in **Figure 6.9**, the morphology of the pure PTAA (left), TFB (right) and the 2:1 PTAA:TFB blend (centre) are very similar, and there is no evidence of

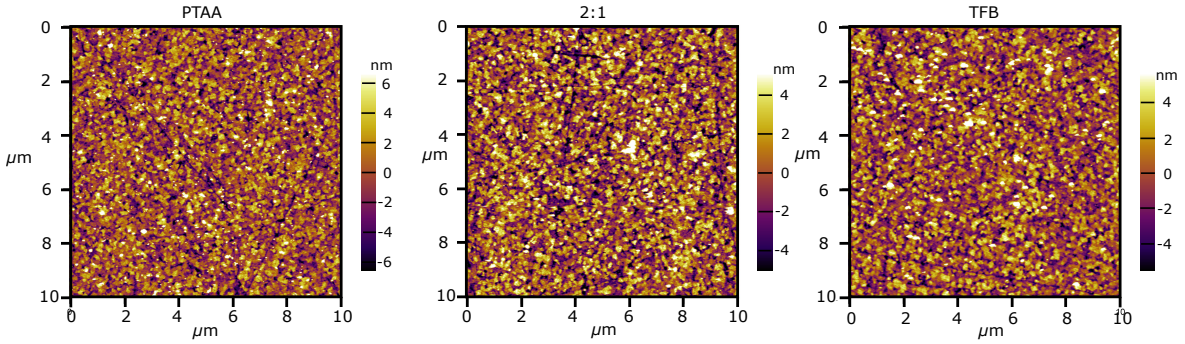


Figure 6.9: *Atomic force microscopy (AFM) images for pure PTAA (left), TFB (right) and the 2:1 PTAA:TFB blend (centre). The micrographs were taken on a 10 μm by 10 μm area of the polymer thin films on ITO (device relevant) substrates. The root-mean-square roughness was 3.25 nm, 2.56 nm, 2.86 nm for PTAA, the 2:1 blend and TFB respectively. These measurements were performed by Dr. Alexandra J. Ramadan Ramadan.*

phase segregation between the two polymers. Phase separation is a phenomenon that can be encountered in polymer-polymer blend systems and assessed using atomic force microscopy (AFM) measurements [35, 41–43]. Phase segregation can be driven by the choice of solvent – its volatility and the solubility of each polymer [35, 36, 44]. For example, if one polymer is more soluble than the other, it will stay in solution longer during the spin coating process, which can drive the formation of large domains [35, 45]. Highly volatility solvents, such as chlorobenzene used here, promote small domain sizes (well intermixed polymers), which are kinetically trapped in this morphology [35, 36, 45]. These measurements show that the PV device driven optimisation process promoted a finely mixed blend, whose morphology is akin to that of the individual polymers. Moreover, it demonstrates that the absorption measurements presented in **Figure 6.8** are representative of a blended material, and is not simply that large, poorly mixed domains of the individual polymers were being detected.

The photophysical properties of the blended polymer system were then investigated. I note that this is a different scenario to that present within a device. During photoluminescence measurements, electron-hole pairs are generated directly in the blended polymer, whereas in a device, they would be generated within the bulk of the perovskite, and ideally only the hole would transferred to the blended polymers. However, by investigating the photophysical properties of the polymer blend, I was investigating

if there was any evidence for charge transfer between the polymers, and to gain insights into how the different blend ratios would work in a full photovoltaic device.

The steady-state photoluminescence (PL) were measured by exciting the polymer samples in vacuum ($\sim 5\times10^{-3}$ mbar) by a 398 nm laser at two intensities, 510 mWcm^{-2} and 180 mWcm^{-2} the spectra are shown in the top and bottom rows in **Figure 6.10** respectively. The samples were measured in vacuum to reduce the influence of atmospheric effects as far as possible. In performing these steady-state measurements, I wanted to assess if the PL peak would shift in a continuous way in a similar manner to the absorption onset shown in **Figure 6.8**. In **Figure 6.10**, the unnormalised PL spectra (left column) show that for 3:1, 2:1 and 1:1 PTAA:TFB ratios, the PL is much brighter than either of the individual polymers. The increased PL intensity in the blended polymers could originate from an enhancement to the radiative efficiency of the material resulting in a greater fraction of the electron-hole pairs recombine radiatively. It is not simply that more carriers are excited in the blended polymer system, indeed from the blue-shift evident in **Figure 6.8a**, fewer electron-hole pairs ought to be generated in the blends than in neat TFB. Therefore, through the blending process a 'passivation-style' effect is being induced which is surprising. From the HOMO and LUMO positions reported in the literature, we might in fact expect to 'split' the exciton in these blends, since TFB ought to have a deeper HOMO level, and PTAA a shallower LUMO [16, 17]. Therefore, we might expect holes to be transferred to the PTAA and electrons to the TFB. This would manifest itself in a decreased PL intensity in the blended polymer systems. The fact that this is not observed is good evidence that the 'exciton splitting' mechanism is not occurring within the polymer blend thin films. Indeed, the offset is predicted to be $\sim 0.1 - 0.2\,\text{eV}$, which is below the 'rule of thumb' of $\sim 0.3\,\text{eV}$ normally present within bulk heterojunction solar cells which drives exciton splitting [46]. In contrast, the 1:2 blend ratio has an extremely similar, though slightly dimmer, PL response to TFB. This suggests that, despite the blend being 1/3 PTAA, the 1:2 blend's PL response is entirely dominated by TFB.

To gain insights into the origin of the increased photoluminescence intensity of the

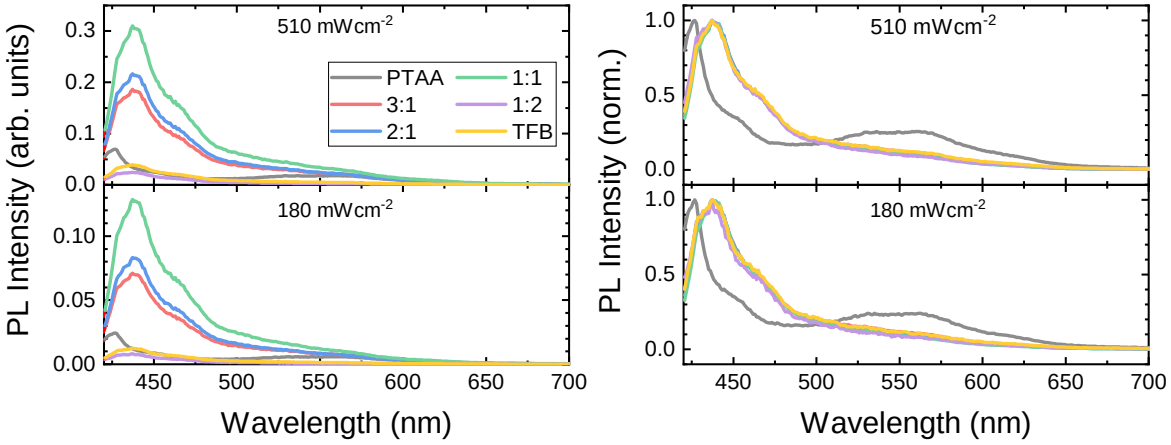


Figure 6.10: *Photoluminescence spectra for polymer and blended polymer thin films on quartz. The samples were excited in vacuum ($\sim 5 \times 10^{-3}$ mbar) by a 398 nm laser at two intensities, 510 $mWcm^{-2}$ (top row) and 180 $mWcm^{-2}$ (bottom row). The first column shows the raw spectra, and the second column the spectra have been normalised.*

3:1, 2:1 and 1:1 polymer blends, the normalised PL spectra are shown in the second column in **Figure 6.10**. As is clear in these plots, the PL spectra of each of the polymer blends very closely resembles that of TFB, and a continuous shifting of the PL peak position is not observed as may have been expected from the absorption measurements presented in **Figure 6.8**. Therefore, these data may suggest that the excitons generated on TFB recombine on TFB, but those generated on PTAA are being transferred onto the TFB, where electron-hole pairs can radiatively recombine. Therefore, the photoluminescence shape is being entirely determined by the TFB. The transfer of the exciton to the TFB means that the offset in the highest occupied molecular orbital (HOMO) positions between the TFB and PTAA is quite modest, as expected from literature values. Despite this modest offset, **Figure 6.4** demonstrates just how significant this can be for PV device performance.

To investigate whether the time-scale for exciton transfer between PTAA and TFB could be resolved, time-resolved emission spectroscopy (TRES) was performed. This technique maps the evolution of the luminescence spectra over time. TRES measurements were performed on all polymer blends investigated and are presented in **Figure 6.11**, wherein the left-hand column shows the 'raw data' to show the spectral shape's evolution, and the right-hand column has been normalised at each wavelength to more clearly visualise the dynamics. In each case investigated, the dominant HOMO-LUMO

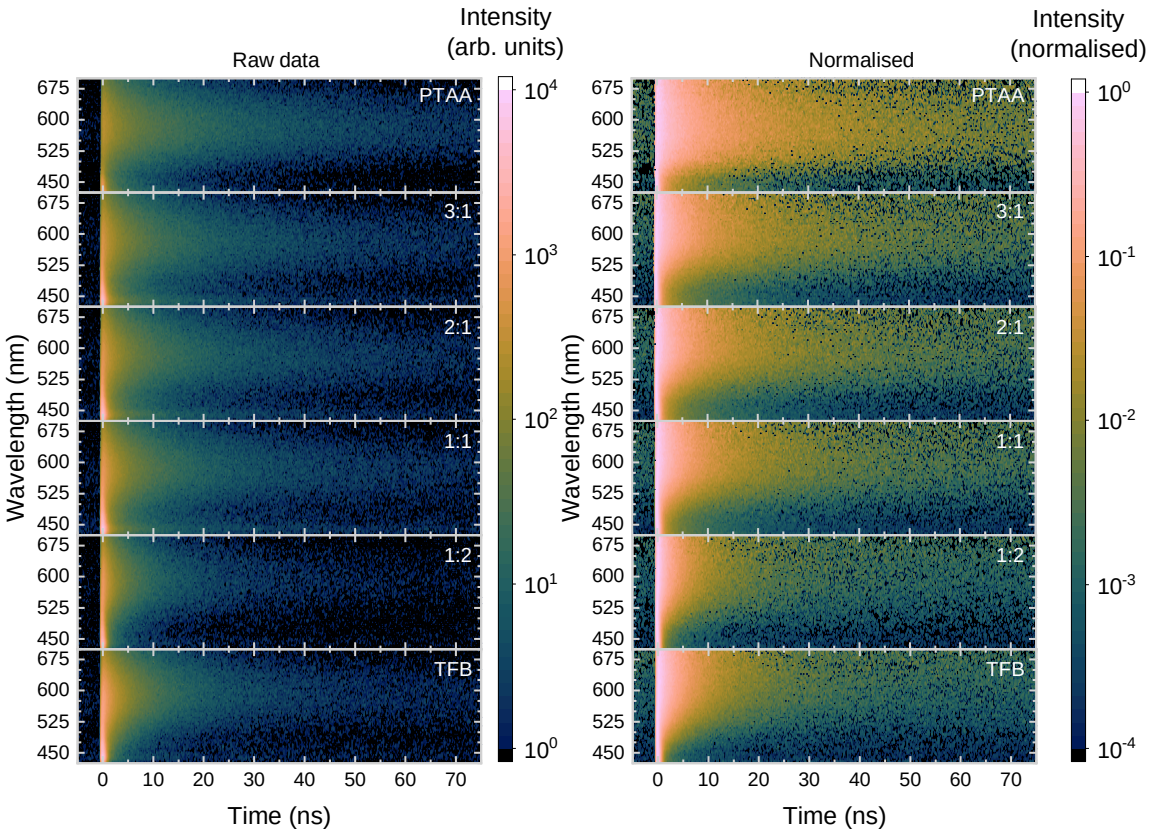


Figure 6.11: *Time-resolved emission spectroscopy of the blended polymer systems investigated. The left column shows the raw data and so allows one to compare how the spectrum of each polymer evolves over time after illumination pulse. The right column shows the same data, but each transient has been normalised a time = 0. This was done to allow one to see which regions of the emission were longest lived for each polymer system. The Scientific colour map "batlow" [47] is used in this figure to prevent visual distortion of the data and to ensure its suitability for readers with colour-vision deficiencies [48].*

transition decays rapidly over time, which is shown most clearly in **Figure 6.12** where the signal from **Figure 6.11** was integrated between $425-455$ nm. This recombination timescale of ~ 10 ns is typical for polymeric semiconductors. The lifetime of this exciton recombination is longest for the pure PTAA film, and is substantially shortened for increasing quantities of TFB. However, in each of the conditions investigated, there is a significant red-shifted PL that persists for much longer. The emission integrated between $555-605$ nm is presented in **Figure 6.12**. Similarly to the high-energy emission, the emission is longest lived for PTAA and a substantial shortening is observed for increased TFB content. The 1:2 blend has a slightly shorter lifetime than the neat TFB. The origin of this red-shifted emission is not clear. A possible explanation is that

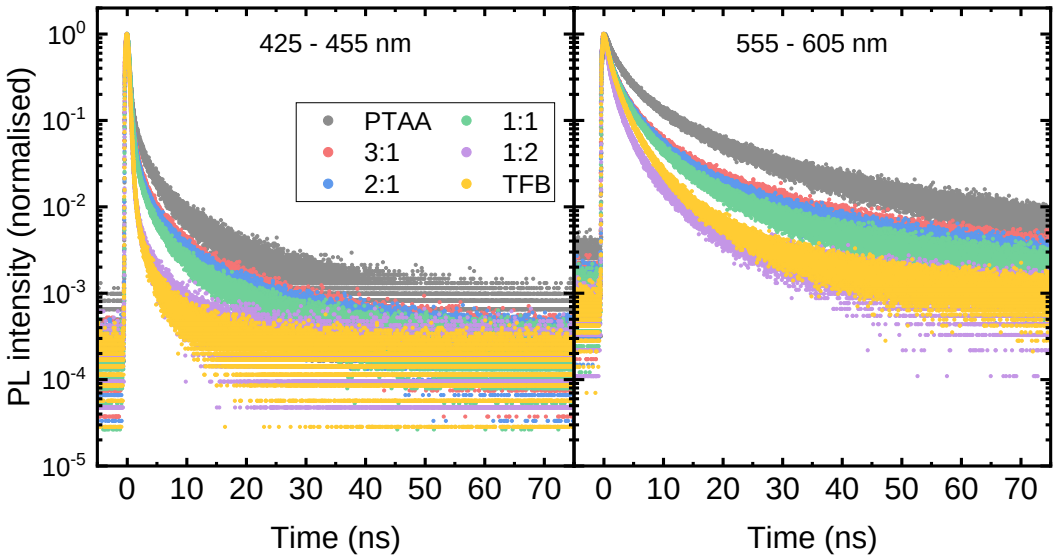


Figure 6.12: *The photoluminescence spectra in* ***Figure 6.11*** *is integrated between* $425-455\,\text{nm}$ *(left) and* $555-605\,\text{nm}$ *(right) and then normalised for each of the polymer conditions investigated. The left plot corresponds to the HOMO-LUMO transition, and the right investigates the dynamics of the red-shifted emission. In each case, the lifetime is the longest for pure PTAA and is reduced on increasing TFB content.*

it could originate from the lowest triplet state and so the observed emission is phosphorescence. Radiative recombination from the triplet state ought to be spin-forbidden, and so is substantially slower than the fluorescence observed between $425-455\,\text{nm}$. Indeed, the scale of the energy difference between the rapid, higher energy and the red-shifted emission ($\sim 0.7\,\text{eV}$) is consistent with the expected difference between lowest singlet and triplet [49]. However, it is not clear how this would affect the hole transporting property of these layers when used as a HTL in full PV devices.

6.4 Conclusion and Future Work

I plan to complete this study during my postdoctoral work, however, I think it is possible to draw some intermediary conclusions and describe the future work planned to answer the major outstanding questions.

In this Chapter, I investigated strategies to improve the hole transport layer / wide bandgap metal halide perovskite interface, taking $FA_{0.83}Cs_{0.17}Pb(I_{0.6}Br_{0.4})_3$ ($E_g = 1.8\,\text{eV}$) as the model system. This interface was found to perform particularly poorly,

for the first time, in **Chapter 5**, and poor energetic alignment between the perovskite and charge transport layers was identified as a major limiting factor. Therefore, I sought to implement a novel HTL which possessed a deeper HOMO compared to the conventionally implemented PTAA. I decided to use TFB since it meets this requirement, but is still a commercially available polymer and so should not offer a major bottle neck. However, implementing TFB alone was found to perform poorly, most likely due to poor hole extraction which could be explained by its HOMO lying deeper than the valence band maximum of the perovskite. Motivated by the desire to form a 'tunable' HTL, I decided to blend the two polymers in a hope to form an 'effective material' with a tunable energetics and so can be tailored to a specific perovskite.

The blended polymer system was found to be an extremely promising new HTL candidate, delivering high performance devices with greater reliability than those processed on self-assembled monolayers. There is a clear trend in terms of device open-circuit voltage, with the 2:1 PTAA:TFB blend delivering the highest V_{OC}s and the champion device whose stabilised PCE exceeded 17.5 % after 30 minutes of maximum power point tracking. The basic structure and optoelectronic properties of the perovskite were found to be insensitive of PTAA:TFB ratio of the HTL on which they were deposited.

The photophysical properties of the polymers themselves were then investigated through absorption, PL and time-resolved emission spectroscopy measurements. The absorption of the polymer blends can be described accurately as an appropriately weighted linear combination of the individual polymer absorption. In contrast, the PL from the blends seems to entirely originate from the TFB. TRES measurements revealed that the HOMO-LUMO transition is accelerated upon increasing TFB addition. However, there is no consistent trend in these photophysical data that would suggest a that the blended polymers ought to perform better when incorporated as the HTL in PV devices.

Currently ongoing investigations are seeking greater insight into the structure of the polymer blend systems through synchrotron based X-ray scattering studies. The

HOMO position of the blends is being measured through photoemission spectroscopy to see if we detect a continuous shifting as we did in the absorption. Moreover, preliminary investigations have shown that this strategy is adaptable to different bandgap perovskites, and only the ratio of PTAA:TFB needs to be adapted to achieve the benefit to the performance.

Future investigations will involve transient absorption measurements. These will be undertaken to understand the charge transfer properties between the perovskite semiconductor and the polymer(s). In addition, these investigations should be able to detect charge transfer between the polymers themselves. As such, this will help us to understand why the PL of the polymer blend system is dominated by the TFB, and how charges are transferred from the perovskite into this novel HTL before being extracted from the device.

References

[1] Caprioglio, P. *et al.* On the relation between the open-circuit voltage and quasi-fermi level splitting in efficient perovskite solar cells. *Advanced Energy Materials* **9**, 1901631 (2019).

[2] Stolterfoht, M. *et al.* The impact of energy alignment and interfacial recombination on the internal and external open-circuit voltage of perovskite solar cells. *Energy & Environmental Science* **12**, 2778–2788 (2019).

[3] Oliver, R. D. *et al.* Understanding and suppressing non-radiative losses in methylammonium-free wide-bandgap perovskite solar cells. *Energy & Environmental Science* **15**, 714–726 (2022).

[4] Al-Ashouri, A. *et al.* Conformal monolayer contacts with lossless interfaces for perovskite single junction and monolithic tandem solar cells. *Energy & Environmental Science* **12**, 3356–3369 (2019).

[5] Al-Ashouri, A. *et al.* Monolithic perovskite/silicon tandem solar cell with $> 29\%$ efficiency by enhanced hole extraction. *Science* **370**, 1300–1309 (2020).

[6] Sun, J. *et al.* Niox-seeded self-assembled monolayers as highly hole-selective passivating contacts for efficient inverted perovskite solar cells. *Solar RRL* **5**, 2100663 (2021).

[7] Chen, W. *et al.* Monolithic perovskite/organic tandem solar cells with 23.6% efficiency enabled by reduced voltage losses and optimized interconnecting layer. *Nature Energy* **7**, 229–237 (2022).

[8] Brinkmann, K. *et al.* Perovskite–organic tandem solar cells with indium oxide interconnect. *Nature* **604**, 280–286 (2022).

[9] Yan, H. *et al.* A high-mobility electron-transporting polymer for printed transistors. *Nature* **457**, 679–686 (2009).

[10] Muccini, M. A bright future for organic field-effect transistors. *Nature Materials* **5**, 605–613 (2006).

[11] Heeger, A. J. Semiconducting polymers: the third generation. *Chemical Society Reviews* **39**, 2354–2371 (2010).

[12] Yao, Y. *et al.* Organic hole transport layers for efficient, stable and scalable inverted perovskite solar cells. *Advanced Materials* 2203794 (2022).

[13] Caprioglio, P. *et al.* Nano-emitting heterostructures violate optical reciprocity and enable efficient photoluminescence in halide-segregated methylammonium-free wide bandgap perovskites. *ACS Energy Letters* **6**, 419–428 (2021).

[14] Knight, A. J. & Herz, L. M. Preventing phase segregation in mixed-halide perovskites: a perspective. *Energy & Environmental Science* **13**, 2024–2046 (2020).

[15] Park, Y., Choong, V., Gao, Y., Hsieh, B. R. & Tang, C. W. Work function of indium tin oxide transparent conductor measured by photoelectron spectroscopy. *Applied Physics Letters* **68**, 2699–2701 (1996).

[16] Endres, J. *et al.* Electronic structure of the $CsPbBr_3$/polytriarylamine (PTAA) system. *Journal of Applied Physics* **121**, 035304 (2017).

[17] Hwang, J. *et al.* Photoelectron spectroscopic study of the electronic band structure of polyfluorene and fluorene-arylamine copolymers at interfaces. *The Journal of Physical Chemistry C* **111**, 1378–1384 (2007).

[18] Vaynzof, Y., Kabra, D., Chua, L. L. & Friend, R. H. Improved electron injection in poly(9,9'-dioctylfluorene)-co-benzothiodiazole via cesium carbonate by means of coannealing. *Applied Physics Letters* **98**, 62 (2011).

[19] Sworakowski, J. How accurate are energies of HOMO and LUMO levels in small-molecule organic semiconductors determined from cyclic voltammetry or optical spectroscopy? *Synthetic Metals* **235**, 125–130 (2018).

[20] Mahesh, S. *et al.* Revealing the origin of voltage loss in mixed-halide perovskite solar cells. *Energy & Environmental Science* **13**, 258–267 (2020).

[21] Ross, R. T. Some thermodynamics of photochemical systems. *The Journal of Chemical Physics* **46**, 4590–4593 (1967).

[22] Stolterfoht, M. *et al.* Visualization and suppression of interfacial recombination for high-efficiency large-area pin perovskite solar cells. *Nature Energy* **3**, 847–854 (2018).

[23] Khan, R., Poplavskyy, D., Kreouzis, T. & Bradley, D. Hole mobility within arylamine-containing polyfluorene copolymers: a time-of-flight transient-photocurrent study. *Physical Review B* **75**, 035215 (2007).

[24] Zhang, W. *et al.* Systematic improvement in charge carrier mobility of air stable triarylamine copolymers. *Journal of the American Chemical Society* **131**, 10814–10815 (2009).

[25] Tao, S. *et al.* Absolute energy level positions in tin- and lead-based halide perovskites. *Nature Communications* **10**, 1–10 (2019).

[26] Hassan, Y. *et al.* Ligand-engineered bandgap stability in mixed-halide perovskite leds. *Nature* **591**, 72–77 (2021).

[27] Warby, J. H. *et al.* Revealing factors influencing the operational stability of perovskite light-emitting diodes. *ACS Nano* **14**, 8855–8865 (2020).

[28] Stolterfoht, M. *et al.* Approaching the fill factor shockley–queisser limit in stable, dopant-free triple cation perovskite solar cells. *Energy & Environmental Science* **10**, 1530–1539 (2017).

[29] Le Corre, V. M. *et al.* Charge transport layers limiting the efficiency of perovskite solar cells: how to optimize conductivity, doping, and thickness. *ACS Applied Energy Materials* **2**, 6280–6287 (2019).

[30] Saliba, M. *et al.* How to make over 20% efficient perovskite solar cells in regular (n–i–p) and inverted (p–i–n) architectures. *Chemistry of Materials* **30**, 4193–4201 (2018).

[31] Shaheen, S. E. *et al.* 2.5% efficient organic plastic solar cells. *Applied Physics Letters* **78**, 841–843 (2001).

[32] Li, G., Zhu, R. & Yang, Y. Polymer solar cells. *Nature Photonics* **6**, 153–161 (2012).

[33] Tremblay, M.-H. *et al.* A photo-crosslinkable bis-triarylamine side-chain polymer as a hole-transport material for stable perovskite solar cells. *Sustainable Energy & Fuels* **4**, 190–198 (2020).

[34] Liu, D. *et al.* Improved performance of inverted planar perovskite solar cells with F4-TCNQ doped PEDOT:PSS hole transport layers. *Journal of Materials Chemistry A* **5**, 5701–5708 (2017).

[35] Lee, C., Lee, S., Kim, G.-U., Lee, W. & Kim, B. J. Recent advances, design guidelines, and prospects of all-polymer solar cells. *Chemical Reviews* **119**, 8028–8086 (2019).

[36] Zhang, Z.-G. & Li, Y. Polymerized small-molecule acceptors for high-performance all-polymer solar cells. *Angewandte Chemie International Edition* **60**, 4422–4433 (2021).

[37] Cho, Y. *et al.* Elucidating mechanisms behind ambient storage-induced efficiency improvements in perovskite solar cells. *ACS Energy Letters* **6**, 925–933 (2021).

[38] Lin, Y.-H. *et al.* A piperidinium salt stabilizes efficient metal-halide perovskite solar cells. *Science* **369**, 96–102 (2020).

[39] Bai, S. *et al.* Planar perovskite solar cells with long-term stability using ionic liquid additives. *Nature* **571**, 245–250 (2019).

[40] Dasgupta, A. *et al.* Visualizing macroscopic inhomogeneities in perovskite solar cells. *ACS Energy Letters* **7**, 2311–2322 (2022).

[41] Murari, N. M., Crane, M. J., Earmme, T., Hwang, Y.-J. & Jenekhe, S. A. Annealing temperature dependence of the efficiency and vertical phase segregation of polymer/polymer bulk heterojunction photovoltaic cells. *Applied Physics Letters* **104**, 223906 (2014).

[42] Mori, D. *et al.* Polymer/polymer blend solar cells with 2.0% efficiency developed by thermal purification of nanoscale-phase-separated morphology. *ACS Applied Materials & Interfaces* **3**, 2924–2927 (2011).

[43] Ade, H. *et al.* Phase segregation in polymer thin films: Elucidations by x-ray and scanning force microscopy. *EPL (Europhysics Letters)* **45**, 526 (1999).

[44] Fan, B. *et al.* Optimisation of processing solvent and molecular weight for the production of green-solvent-processed all-polymer solar cells with a power conversion efficiency over 9%. *Energy & Environmental Science* **10**, 1243–1251 (2017).

[45] Lee, C. *et al.* Correlation between phase-separated domain sizes of active layer and photovoltaic performances in all-polymer solar cells. *Macromolecules* **49**, 5051–5058 (2016).

[46] Chen, X.-K. *et al.* A unified description of non-radiative voltage losses in organic solar cells. *Nature Energy* **6**, 799–806 (2021).

[47] Crameri, F. Scientific colour maps. *Zenodo* (2018).

[48] Crameri, F., Shephard, G. & Heron, P. The misuse of colour in science communication. *Nature Communications* **11**, 5444 (2020).

[49] Köhler, A. & Beljonne, D. The singlet–triplet exchange energy in conjugated polymers. *Advanced Functional Materials* **14**, 11–18 (2004).

Chapter 7

Conclusions and Future Work

The work presented in this thesis has focused on understanding and improving the quality of the interfaces within MHP solar cells. The interfaces within these devices have emerged as the key limiting factor constraining their performance.

For most of the development of solar cells based on MHP semiconductors, high efficiency single junction devices were sought. The highest performance solar cells are delivered via molecular passivation, but this can often introduce new instabilities into the device structure. As the efficiencies of MHP solar cells are edging ever closer to their thermodynamic limit, there is an increasing focus on wide bandgap (> 1.7 eV) metal halide perovskite (MHP) semiconductors which enable tandem solar cells which dramatically increase the maximum attainable efficiency, and so can reduce the cost of power produced from solar. However, the physics of these wide bandgap MHP semiconductors was relatively unexplored, particularly in full device configurations and so their performance lagged significantly behind their single junction counterparts.

In **Chapter 4**, the interfaces in solar cells based on $Cs_{0.05}(FA_{0.83}MA_{0.17})_{0.95}Pb(I_{0.9}Br_{0.1})_3$ ($E_g = 1.6\,eV$) were investigated. Consistent with other reports in the literature, we discovered that the interface between this perovskite and the electron transport layer ($PC_{61}BM$) is the limiting factor in these devices. Passivation of this interface had been attempted in the literature previously, but the benefit of these treatments was lost after only a short amount of time under accelerated ageing conditions. In this Chap-

ter, I developed an thermally stable passivation strategy based on benzylammonium bromide which delivers stabilised power outputs up to 19.5 %. This treatment reduces the non-radiative losses at the perovskite/$PC_{61}BM$ interface whilst not affecting the perovskite crystallinity or morphology. Importantly, the benefit from this treatment is maintained over the course of ageing at (85 °C, full spectrum light soaking). To advance this work further, expanding the investigation to different families of MHP semiconductors should be investigated. Further, collaborations with computational chemists could help to unravel why the benefit of benzylammonium bromide is maintained during these harsh ageing conditions, whereas the benefits from similar molecules, namely phenethylammonium iodide, are lost rapidly.

In **Chapter 5**, the methylammonium-free wide bandgap perovskite $FA_{0.83}Cs_{0.17}Pb(I_{0.6}Br_{0.4})_3$ ($E_g = 1.8\,eV$) was investigated in detail due to its suitability for perovskite-on-perovskite tandem solar cells. There had been relatively few investigations on this material, and most had focused on empirical trial-and-error device optimisation. Instead, in this Chapter I investigated the recombination processes occurring within this perovskite, in half-device stacks as well as full photovoltaic devices. I discovered that, contrary to the lower bandgap perovskites (i.e. as investigated in **Chapter 4**), the interface with the hole transport layer is constraining the V_{OC} of these devices. A thorough investigation using time-correlated single photon counting measurements on half-device stacks as well as ultraviolet photoemission sprectroscopy measurements gave a deep understanding of the interfaces in PV devices based on these materials. This understanding informed drift-diffusion simulations which could accurately reproduce the device performance, confirming the validity of this analysis. To reduce the severity of the non-radiative losses, two passivation strategies were used: the incorporation of 1-butyl-1-methylpiperidinium tetrafluoroborate into the perovskite precursor solution and evaporating a ~ 1 nm layer of LiF between the perovskite and the electron transport layer (C60). The influence of these treatments was thoroughly investigated using photoluminescence-based studies, and, together, they enabled PCEs in excess of 16.5% which rivalled the best in the world at the time. Following this, in-depth studies

into the recombination processes in full devices highlighted that charge-transport losses are a major bottleneck for these devices and so an alternative transport layer strategy should be devised, with the HTL being the major focus.

Therefore, in **Chapter 6**, I investigated strategies to improve the hole transport layer / wide bandgap metal halide perovskite interface, again using $FA_{0.83}Cs_{0.17}Pb(I_{0.6}Br_{0.4})_3$ ($E_g = 1.8\,eV$) as the model system. As identified earlier in this thesis, poor energetic alignment between the perovskite and charge transport layers was discovered as a major limiting factor. Therefore, I sought to implement a novel HTL which possessed a deeper HOMO compared to the conventionally implemented PTAA. I decided to use TFB since it meets this requirement, but is still a commercially available polymer and so should not offer a major bottle neck. Motivated by the desire to form a 'tunable' HTL, I decided to blend the two polymers in a hope to form an 'effective material' in which the HOMO could be set by the ratio of one polymer to the other.

The blended polymer system was found to be an extremely promising new HTL candidate, delivering high performance devices with greater reliability than those processed on self-assembled monolayers. There is a clear trend in terms of device open-circuit voltage, with the 2:1 PTAA:TFB blend delivering the highest V_{OC}s and the champion device whose stabilised PCE exceeded 17.5 % after 30 minutes of maximum power point tracking. The basic structure and optoelectronic properties of the perovskite were found to be insensitive of PTAA:TFB ratio of the HTL on which they were deposited.

Investigations into photophysical properties of the polymers were performed using absorption, PL and time-resolved emission spectroscopy measurements. The absorption of the polymer blends can be described accurately as an appropriately weighted linear combination of the PTAA and TFB polymer absorption. In contrast, the PL from the blends seems to entirely originate from the TFB. Enhanced PL intensity was observed in the blended polymer systems. TRES measurements revealed that the HOMO-LUMO transition is accelerated upon increasing TFB addition. However, there is no consistent trend in these photophysical data that would suggest a that the blended

polymers ought to perform better when incorporated as the HTL in PV devices.

To enhance this work, there are a number of currently ongoing investigations: synchrotron based X-ray scattering studies to delve deeper into the structure of the polymer layer; the HOMO level of the blends will be determined through photoelectron spectroscopy to determine if this follows a similar trend to the absorption measurements. Moreover, preliminary investigations have shown that this strategy is adaptable to different bandgap perovskites, and only the ratio of PTAA:TFB needs to be adapted to achieve the benefit to the performance, enhancing the 'tunable HTL' hypothesis.

Future investigations will involve transient absorption measurements. These will be undertaken to understand the charge transfer properties between the perovskite semiconductor and the polymer(s). In addition, these investigations should be able to detect charge transfer between the polymers themselves. As such, this will help us to understand why the PL of the polymer blend system is dominated by the TFB, and how charges are transferred from the perovskite into this novel HTL before being extracted from the device.

Overall, this thesis has provided new insights into the physics of the interfaces within solar cells based on a selection of MHP semiconductors. Understanding and improving the quality of these interfaces is becoming ever more crucial as this family of materials nears real-world deployment. This is especially critical in tandem solar cells which introduce numerous additional interfaces. There have been relatively few investigations focused on understanding these systems holistically, and in my opinion it is critical this work be undertaken urgently. In this thesis, I have shown how understanding the physics occurring at these interfaces can yield outstanding enhancements to the device performance. If similar enhancements can be brought to perovskite-based tandem solar cells, then this will accelerate the arrival of MHP-based PV on rooftops around the world.